Modifying pentamidine blood-brain barrier transport through ion-pair formation

Wang, Hao

Awarding institution:
King's College London

Modifying Pentamidine Blood-Brain Barrier Transport Through Ion-Pair Formation

Hao Wang

In fulfilment of the requirement

for the degree of Doctor of Philosophy (PhD)

in Pharmaceutical Science

Supervisors:

Dr Sarah Thomas

Dr Stuart Jones

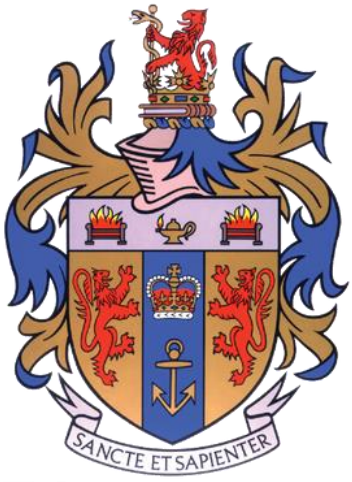

Institute of Pharmaceutical Science
Faculty of Life Sciences and Medicine
King's College London
July 2020

Acknowledgements

First of all, I would like to express my deepest appreciation to my supervisor Dr Sarah Thomas. I'm deeply indebted to the supervision and support that she gave me during my PhD. Without her guidance and constant feedback for my project and my thesis, this project would not have been achievable.

I would also like to extend my deepest gratitude to my supervisor Dr Stuart Jones for his guidance, helpful advice and extensive knowledge in the physicochemical work of this PhD project.

I would like to extend my sincere thanks to my thesis committee members Professor Ben Forbes, Dr David Barlow, Dr Christopher Corpe, and Dr Nic Bury for their invaluable insight into the project. I am extremely grateful to Dr Christopher Corpe for his guidance and knowledge in the oocytes work. I very much appreciate Dr David Barlow for drawing the 3D images of ion-pairs as well as taking me to the Rutherford Appleton Laboratory at Science and Technology Facilities Council in Didcot to perform experiments with Fluorescence Lifetime Imaging Microscopy.

Special thanks to Dr Khondaker Miraz Rahman and Doaa Farag for performing the molecular docking in this project. I also want to thank Dr Andy Ward and Professor Stanley Botchway from the Science and Technology Facilities Council for their help in setting up the Fluorescence Lifetime Imaging Microscopy. I want to express my gratitude to Professor Koepsell Hermann and Dr Valentin Gorboulev from the University of Wuerzburg for providing the hOCT1 vector.

I want to thank all my colleagues at King's College London for bringing joy and happiness to my PhD life. Special thanks to Dr Gayathri Sekhar for teaching me accumulation assay at the beginning of my PhD, Dr Alice Fleckney for teaching me cell culture and western blot, and my colleagues Dr Montserrat Castillo Carrizales, Miss Sevda Boyanova for their support. I want to thank people from the Blood-Brain Barrier Group Dr Ana Giorgian, Dr Svetlana Drndarski and Jane Preston, for their assistance and encouragement during my PhD. I am grateful to Dr Arcadia Woods, Dr Zarif Mohamed Sofian, Dr Mais Saleh, Dr Rober Harper, Dr Hanpeng Chen, Dr Parastoo Masoomi, for their help in my physicochemical experiments. I want to thank all the MSc

and BSc students in the group for their assistance, especially to Ahmed Sedky for his support in the MTT assay.

Finally, I would like to say a heartful thank to my mum Yao Tianmei and my dad Wang Shuigen for supporting me financially and encouraging me to follow my dreams in the UK. I want to thank all my friends for their company and encouragement.

Abstract

Background. Human African trypanosomiasis (HAT) is fatal unless treated. Pentamidine has been used to treat first-stage (hemolymphatic) HAT since the 1940s, but it is ineffective againstsecond-stage (meningoencephalitic, or central nervous system) infection. Research has suggested that hOCT1 and P-gp are involved in the transport of pentamidine across the blood-brain barrier (BBB). The aim of this study was to investigate if through the formation of ion-pairs the passive diffusion and hOCT1 and P-gp mediated BBB transport of pentamidine could be improved.

Methods. Structural properties (stoichiometry, binding sites and binding affinities) of ion-pairs formed between pentamidine and taurodeoxycholate, octanoate and xinafoate (selected to generate an ion-pair with a +1 charge) were examined by HPLC, NMR spectroscopy and fluorescence spectroscopy. The lipophilicity of pentamidine with an excess concentration of the counter-ions was measured by octanol-water shake-flask method at pH 7.4. Hyperquad Simulation and Speciation (HySS) studies predicted the percentage of pentamidine ion pairs that would be formed in plasma and CNS and determined the concentrations utilised in the biological studies. Molecular docking studies were performed using Dock Ligands from Discovery Studio version 4.0 to simulate and confirm the binding of pentamidine with hOCT1 and P-gp. The influence of counterions on the passive permeability properties of pentamidine was explored using a simple membrane *xenopus* oocytes which were injected with water. The influence of counterions on pentamidine transport by hOCT1 was studied using (i) human brain endothelial cells (hCMEC/D3) (ii) a *xenopus* oocytes system in which functional expression of hOCT1 was confirmed using the hOCT1 endogenous substrate acetylcholine (kinetic uptake, 1-120min). The influence of counterions on pentamidine transport by human P-gp (MDR1) was examined using (i) cultured Madin-Darby Canine Kidney (MDCK)-wild-type and MDCK-MDR1 cells and (ii) a *xenopus* oocytes system expressing P-gp and its functional expression of P-gp was confirmed by the efflux of two P-gp substrates [^{3}H]dexamethasone and [^{3}H]corticosterone. Data were analysed by t-test, one-way ANOVA or two-way ANOVA and expressed as mean ± S.E.M. or mean ± S.D. as specified.

Results. The lipophilicity (log D, 7.4) of 33μM pentamidine with 20 times molar ratio of taurodeoxycholate, octanoate by 1.15 and 1.06 units, respectively. The lipophilicity (log D, 7.4) of 8μM pentamidine with 20 times molar ratio of xinafoate increased by 0.82 units compared to pentamidine respectively. NMR revealed that ion-pairing occurred through the pentamidine amidine groups. The binding constants (pK_a) of pentamidine with taurodeoxycholate, octanoate, or xinafoate were determined by HPLC and ranged from 3.1 - 4.1. The binding of pentamidine with counterions is relatively weak, compared to the reported highly stable metal complexes: $pK_{Cu^{2+}\text{-}EDTA}$= 18.8, $pK_{Mg^{2+}\text{-}EDTA}$= 8.8 (Wang and Tomasella, 2016). The percentage bound of pentamidine with 20 molar ratios of xinafoate is predicted to be 0.07% and 38.5% when pentamidine is 9nM and 8μM, respectively. The accumulation of [^{3}H]pentamidine in hCMEC/D3 cells was either unchanged or reduced with all the counterions. Initial molecular docking showed the energy of pentamidine-hOCT1 was -27.0 kcal/mol compared to -27.6 prazosin (substrate) and +26.6 kcal/mol for sucrose (non-substrate). Uptake of [^{3}H]acetylcholine confirmed the functional expression of hOCT1 in oocytes (hOCT1: 2.23±0.73 pmol/oocyte/h vs sham: 1.19±0.28 pmol/oocyte/h n=28-32). Pentamidine utilized hOCT1 to accumulate in the oocyte (hOCT1: 86.35±18.99 vs sham: 40.00±12.06 fmol/oocyte/h, n=23-24 $p<0.05$) and its Km (half-saturation constant) was 279.9±112.4 μM (determined using 2-500 μM of pentamidine; n=6-8). Comparing the uptake of [^{3}H]pentamidine ion-pairs in water-injected oocytes, when pentamidine was in the ion-pair complex, more pentamidine could be passively diffused across the membrane if the counterion had a small molecular weight. This is due to the improved lipophilicity of the pentamidine ion pair compared with pentamidine alone. However, less pentamidine interacted with hOCT1 as the ion-pairs could inhibit pentamidine to be influxed by hOCT1. Molecular docking showed the energy of pentamidine-P-gp was -31.0 kcal/mol compared to -31.8 kcal/mol for the substrate, dexamethasone and +2.9 kcal/mol for the non-substrate, sucrose. The efflux of [^{3}H]pentamidine-xinafoate ion-pair in oocytes expressing P-gp indicated that the efflux of [^{3}H]pentamidine by P-gp was not affected by forming ion-pairs with xinafoate.

Conclusions. The counterions taurodeoxycholate, octanoate, and xinafoate in this study generated an ion-pair complex with pentamidine, which was more lipophilic than the parent drug, presumably due to the shielding of one of pentamadine's two +ve charges. HySS studies predicted that the percentage of ion pairs present in solution would increase dramatically when increasing the concentration of pentamidine regardless of excess of counterions. This structural

modification improved BBB uptake by enhancing the passive transport of pentamidine. The molecular docking studies and the hOCT1 and P-gp expressing oocytes confirmed the role of hOCT1 and P-gp in pentamidine transport. When pentamidine forms ion-pairs with xinafoate, its influx across the BBB by hOCT1 is prevented. Pentamidine is still effluxed by P-gp and its efflux by P-gp is not affected by forming ion-pairs with xinafoate. This may be because the size of pentamidine-xinafoate ion-pair is outside the normal MW range for OCT1, but is within the range for P-gp substrates. It may also because forming ion-pairs with xinafoate affect the binding pocket with hOCT1 but not P-gp.

Contents

List of Figures

List of Tables

Abbreviations

Abbreviations	Meanings
AAV9	Adeno-associated viral 9
ABC	Atp-binding cassette
ADMET	Absorption, distribution, metabolism, elimination and toxicity
AE	Astrocyte endfeet
AHDS	Allan-herndon-dudley syndrome
AMT	Adsorptive-mediated transcytosis
ATP	Adenosine triphosphate
BBB	Blood-brain barrier
BBMEC	Bovine brain microvessel endothelial cell
BCA	Bicinchoninic acid
BCRP	Breast cancer resistance protein
BCSFB	Blood-cerebrospinal fluid barrier
BM	Basement membrane
cDNA	Complementary DNA
CHO	Chinese hamster ovary
CNS	Central nervous system
CNT	Concentrative nucleoside transporter
CP	Chimeric peptides
cRNA	Complementary RNA
CSF	Cerebrospinal fluid
CV	Coefficient of variance
CYP	Cytochromes P450
DAPI	4’,6-diamidino-2-phenylindole
DFMO	Difluoromethylornithine
DLG1	Disks large homolog 1
ECs	Endothelial cells
EDTA	Ethylenediaminetetraacetic acid
EMA	European medicines agency

ENT	Equilibrative nucleoside transporter
FLIM	Fluorescence-lifetime imaging microscopy
HAT	Human african trypanosomiasis
HNAP	1-hydroxy-2-naphthoic acid, xinafoate
HPLC	High performance liquid chromatography
HySS	Hyperquad simulation and speciation
IR	Insulin receptor
JAMs	Junctional adhesion molecules
LATs	L-alpha amino acid transporters
LDLR	Low density lipoprotein receptor
LOD	Limit of detection
Log D	Distribution coefficient
Log P	Partition coefficient
log β	Overall stability constants
LOQ	Limit of quantification
MAGUK	Membrane-associated guanylate kinase
MATE	Multidrug and toxic compound extrusion
MBM	Barth's medium
MCT	Monocarboxylate transporter
MDCK	Madin-darby canine kidney
MOPS	3-(n-morpholino) propanesulfonic acid
MPP	Membrane protein palmitoylated
MRP	Multidrug resistance associate protein
MTT	3-(4,5-dimethylthiazol-2-yl)-2,5-diphenyltetrazolium bromide
MW	Molecular weight
NCBI	National centre for biotechnology information
ND	Neutral density
NECT	Combination of nifurtimox and eflornithine
NMR	Nuclear magnetic resonance
NVU	Neurovascular unit
OATPs	Organic anion transporting polypeptides

OATs/oats	Organic anion transporters
OCT	Organic cation transporters
PBS	Phosphate buffered saline
PC	Pericytes
PEPT	Peptide transporters
PHT1	Peptide/histidine transporter-1
PHT2	Peptide/histidine transporter-2
pK_a	Negative log of the association constant (binding constant) or k_a value
pK_d	Negative log of the acid dissociation constant or k_d value
PMAT	Plasma membrane monoamine transporter
PTRE	Post-treatment reactive encephalopathy
rSGLT	Rat sodium-dependent glucose transporter
SEM	Standard errors
SLC	Solute carrier
SN-38	7-ethyl-10-hydroxycamptothecin
SRA	Serum resistance-associated
TCSPC	Time-correlated single photon counting
TEER	Transepithelial/ transendothelial electrical resistance
TfR	Transferrin receptor
TJ	Tight junctions
Vd	Volume of distribution
VMA	Vanilmandelic acid
WHO	World health organisation
ZO-1	Zonula oocludens-1
ZO-2	Zonula oocludens-2
ZO-3	Zonula oocludens-3

Chapter 1 Drug delivery across the blood-brain barrier

1.1 General introduction

In the last decade, several major pharmaceutical companies had to shut down their centres for central nervous system (CNS) drug development. The main reason behind this phenomenon was the low success rate of CNS drug development. Also, the cost of developing a new drug is high at 10-15 billion US dollars (Wegener and Rujescu, 2013). CNS drugs in general have a higher failure rate than non-CNS drugs and the main obstacle is the blood-brain barrier (BBB) (Gribkoff and Kaczmarek, 2017). It is estimated that 98% of small drug molecules and almost all large drug molecules cannot cross the blood-brain barrier (BBB) (Pardridge, 2005). Therefore, it is of great importance to design CNS drugs that can cross the BBB. The current drug delivery methods, both invasive or non-invasive, suffer multiple issues such as high cost, toxicity, and low efficacy (Lu *et al.*, 2014). Novel drug delivery methods are continually being sought which improve drug delivery across the BBB, are cost-effective and safe.

In this chapter, I will introduce a fatal CNS disease called human African trypanosomiasis (HAT) and how it is treated. I will focus on the drug pentamidine and how its inability to cross the BBB prevents it from treating the CNS stage disease. Then I will explain in detail the structure of the BBB and compare current drug delivery strategies across the BBB. Finally, I will propose a new drug delivery method using an ion-pairing strategy for pentamidine to improve the delivery of pentamidine across the BBB and reformulate pentamidine to treat CNS stage HAT.

1.2 Human African Trypanosomiasis (HAT)

Human African trypanosomiasis (HAT), also known as Sleeping Sickness, is a fatal infectious disease in sub-Saharan Africa. The causative parasite, Trypanosoma brucei, was first identified by David Bruce in 1899 and affects both cattle and humans in sub-Saharan areas (Kennedy, 2013). It was originally called nagana. HAT is a neglected disease that affects 70 million population in sub-Saharan Africa. The treatment of HAT is mainly led by the World Health Organisation (WHO). Due to their efforts, the global incidence of *T.b.gambiense* HAT was reduced to below 3,000 cases in 2015 (Aksoy *et al.*, 2017). According to (WHO, 2019), the number of HAT cases further dropped to less than 1,000 cases in 2018 and of which the majority

were *T.b.gambiense* type. The target for 2030 set by WHO is to completely eradicate the *T.b.gambiense* infection.

Figure 1-1 Number of cases of HAT from 2000 to 2020. The figure was downloaded from (WHO, 2019).

HAT is fatal unless treated. The life cycle of *Trypanosoma brucei,* as summarised by Kennedy (2004), is composed of 8 steps (Figure 1-2): (a) An infected tsetse fly bites humans and injects metacyclic trypomastigotes. (b) The metacyclic trypomastigotes are converted into bloodstream trypomastigotes. (c) The trypomastigotes multiply in the blood, lymph and spinal fluid. (d) The trypomastigotes in blood become infective. (e) The tsetse fly bites infected humans or animal hosts. (f) The trypomastigotes in blood become procyclic trypomastigotes and multiply. (g) The procyclic trypomastigotes become epimastigotes (h) Epimastigotes multiply in salivary gland and become metacyclic trypomastigotes (Aksoy, 2003; Kennedy, 2004).

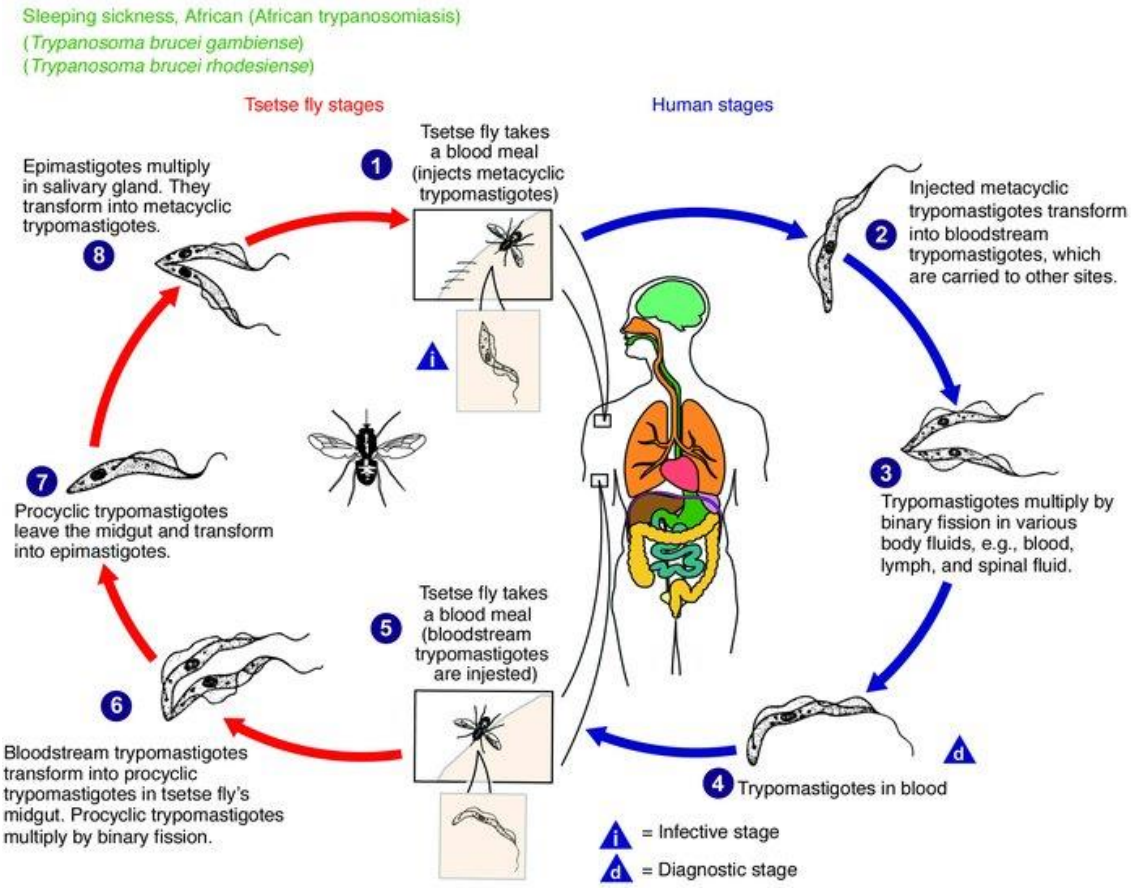

Figure 1-2 The life cycle of Trypanosoma brucei. The image was taken from (Kennedy, 2004) and the image was drawn by Alexander J. da Silva and Melanie Moser, Centers for Disease Control Public Health Image Library.

For humans, the infection of HAT starts with a bite from a tsetse fly. Then after a minimum of five days, the skin area becomes swollen and the disease starts to progress to the first stage, also known as the hemolymphatic stage, where parasites proliferate in the lymphatic system and the blood (Stich, Abel and Krishna, 2002). At this stage, patients usually experience fever for many weeks. Patients in West Africa also have unnoticeable symptoms like lymphadenopathy in the neck and a light rash, while patients in east Africa normally have more severe symptoms with 10% of death rate at the first stage (Stich, Abel and Krishna, 2002). The second stage is the meningo-encephalitic stage where trypanosomes pass through the BBB and infect the brain and the cerebrospinal fluid. The second stage of HAT is difficult to treat, due to the low permeability of drugs across the BBB. If the patients are left untreated, patients will fall into a coma, suffer organ failure, and eventually death (Wenzler *et al.*, 2009; Franco *et al.*, 2014).

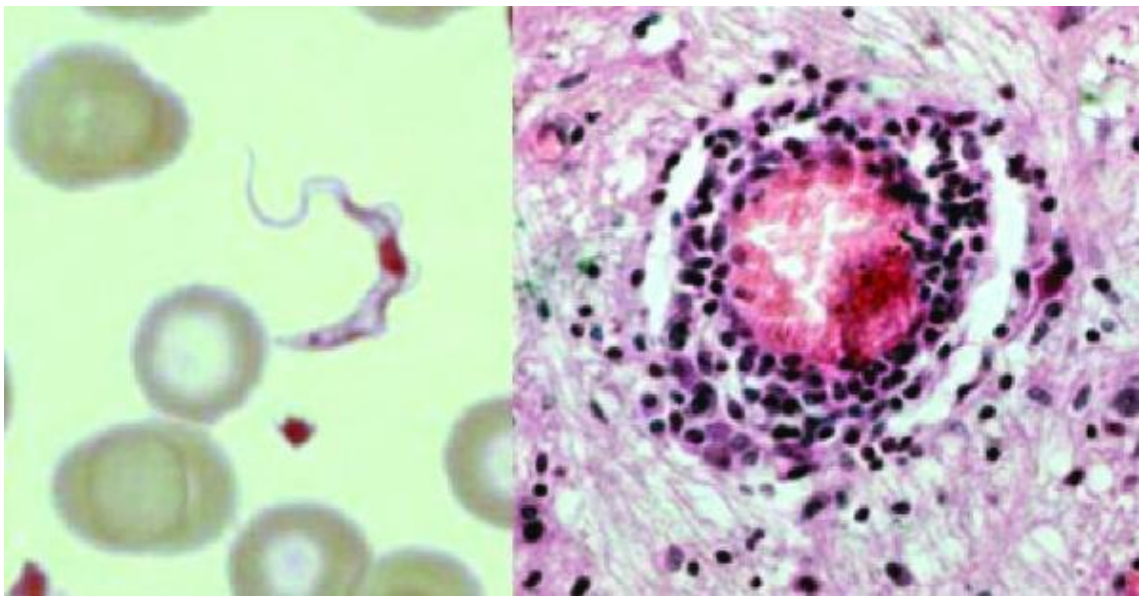

Figure 1-3 Trypanosoma brucei in blood (left) and the brain pathohistological changes of a patient infected with HAT. The image was taken from (Stich, Abel and Krishna, 2002).

There are two types of HAT: *T.b.rhodesience* and *T.b.gambiense*. The two types of HAT differ in the region affected in Africa and have different severity. *T.b.rhodesience* is found in East Africa while *T.b.gambiense* is found in West and Central Africa. The majority (97%) of HAT cases were *T.b.gambiense* while only 3% of cases were *T.b.rhodesience. T.b.rhodesience* is more acute and more severe than *T.b.gambiense.* Therefore, *T.b.rhodesience* is a much more significant concern for European and American travellers who visit East Africa and then return to their countries (Kennedy, 2013). It can take six months from the initial infection for *T.b.rhodesience* to cause death with a more chronic progress of up to 3 years for people infected with *T.b.gambiense* (Franco *et al.*, 2014).

The majority of *T.b.rhodesience* reservoirs are animals, particularly in livestock. When cattle are infected with *T.b.rhodesience*, they become ill and lose milk, and eventually die (Stich, Abel and Krishna, 2002). The human serum resistance-associated (SRA) gene can be isolated from *T.b.rhodesience infected individuals* (Gibson, Backhouse and Griffiths, 2002). Therefore, the SRA gene is often used to diagnose *T.b.rhodesience* in humans since this type of HAT cannot be observed by microscopy (Radwanska *et al.*, 2002). The TgsGP gene can be used as a molecular marker to identify *T.b.gambiense*. TgsGP is a *T. b. gambiense* specific receptor and it can only be found at the first stage of HAT (Berberof, Pérez-Morga and Pays, 2001).

To understand how parasites cross the blood-brain barrier (BBB) and subsequently invade the central nervous system, Mulenga *et al.*, (2001) injected rats with *Trypanosoma brucei (Tb) brucei*., a subspecies of T.brucei which causes disease in cattle, but is nonpathogenic in humans. At late stages post-infection when parasites were found in brain parenchyma, the tight junctional proteins, occludin and zonula occludens 1 (ZO1), were preserved in the cerebral vessels. This implied that parasites pass the BBB without compromising its paracellular integrity. Studies on a murine model of human African Trypanosomiasis also revealed that *Trypanosoma brucei brucei* could reach the blood-CNS interfaces at the early stage of infection when the tight junctions of the BBB were remained (Sanderson et al., 2008). During the course of infection, the concentrations of brain parasites increased. At day-28 post-infection, the blood-brain barrier was dysfunctional, as evidenced by the increased concentration of [^{3}H]eflornithine and [^{14}C]sucrose delivery in brain. The integrity of the blood-brain barrier did not reinstate, and animals died around 5-6 weeks post-infection (Sanderson *et al.*, 2008). Further studies have found that some bloodstream forms of parasites have the capacity to enter the human BMECs. Parasites may permeate into endothelial cells by triggering the G protein-coupled receptor. A study revealed that *T.b. rhodesiense* showed greater efficiency of crossing brain microvascular endothelial cells than *T.b. brucei*. When cathepsin L-like cysteine proteases were inhibited by N-methylpiperazine-urea-Phe-homopheylalanine-vinylsulfone-benzene, *T.b. rhodesiense* was not able to cross the BBB and at the same time did not cause calcium fluxes. In addition, the transport of *T. b. brucei* was enhanced by incubating with supernatants with cathepsin L-like cysteine proteases. This studies indicated that calcium signalling triggered by parasite cysteine protease was involved in the ability of the parasites to cross the BBB (Nikolskaia *et al.*, 2006, 2008).

The options of drugs for HAT are limited and expensive. Currently, there are limited options of drugs for the treatment of human African Trypanosomiasis. All the options are expensive and toxic (Wenzler *et al.*, 2009).

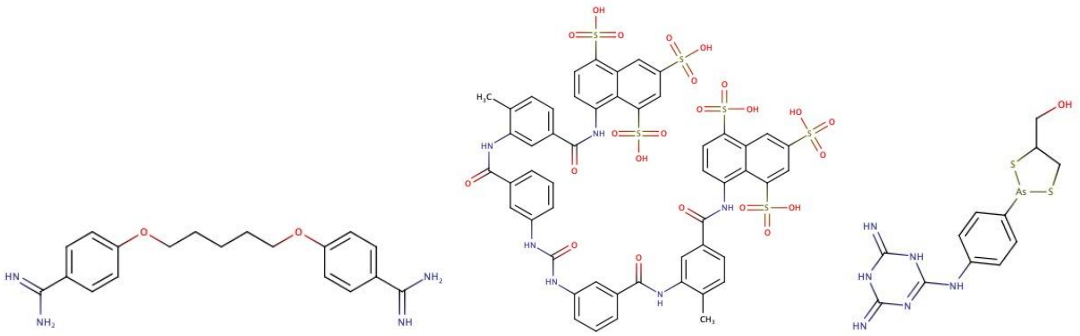

(Pentamidine) (Suramin) (Melarsoprol)

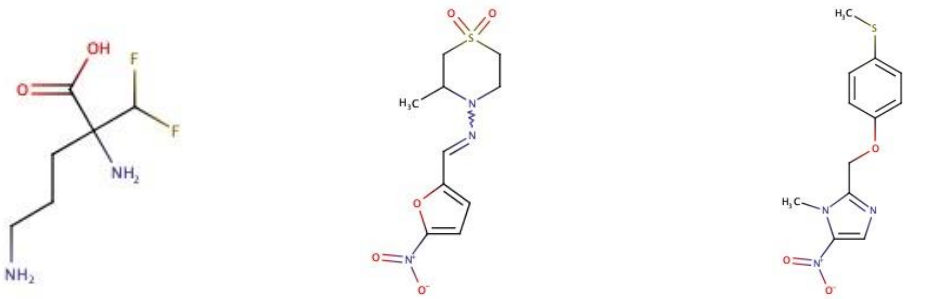

(Eflornithine) (Nifurtimox) (Fexinidazole)

Figure 1-4 Structures of drugs for the treatment of HAT. Pentamidine and Suramin are used for the first stage of HAT. Melarsoprol, eflornithine, nifurtimox, and Fexinidazole can be used for the s (late) stage of HAT (Babokhov *et al.*, 2013).

Pentamidine

Pentamidine (or pentamidine isethionate) is an aromatic diamidine with two positive charges at physiological pH. It is effective against the first stage of *T.b.gambiense* HAT. In clinic, pentamidine is administered through intramuscular injection at the concentration of 4 mg/kg per injection per day for 7-10 days. Pentamidine has a half-life in plasma of 22-47 hs (Babokhov *et al.*, 2013). DAPI staining and TUNEL assay revealed that pentamidine could bind to DNA and disrupt trypanosome mitochondrial, causing the loss of kinetoplast DNA. Kinetoplast DNA is responsible for membrane potential since the A6-subunit of the ATP synthase is encoded by kinetoplast (Bornstein and Yarbro, 1970; Bacchi, 2009; Thomas *et al.*, 2018). The advantage of pentamidine is that it does not cause trypanosomal drug resistance (Babokhov *et al.*, 2013). Pentamidine has several limitations: Firstly, it is ineffective against the s stage of HAT. Sly, it is not convenient for patients

as it has to be administered by intramuscular injection. Thirdly, pentamidine causes side effects, including hepatic toxicity and hypoglycaemia. Despite these, pentamidine is still safer than drugs for stage 2 treatment. It is well tolerated, and most reactions are reversible (Sanderson *et al.*, 2008; Paine *et al.*, 2010).

Suramin

Suramin (Bayer 205), a polysulphonated naphthylamine based compound, is the preferred drug for the treatment of *T.b.rhodesience* HAT (Wenzler *et al.*, 2009). Suramin is administered through intravenous injections at the concentration of 20 mg/kg every 3-7 days for one month. It has a long half-life time of 44-54 days in plasma. The advantages of suramin include its high effectiveness against *T.b.rhodesience*, and not causing drug resistance, resulting from suramin's inhibition of multiple metabolic pathways and enzymes. The disadvantage of suramin is that it can only be used for the early stage of *T.b.rhodesience*, due to its large size (MW)and its inability to cross the BBB (Sanderson, Khan and Thomas, 2007; Babokhov *et al.*, 2013).

Melarsoprol

Melarsoprol is an arsenical and until 1990 it was the only drug available for treating the s stage of both *T.b.gambiense* and *T.b.rhodesience* HAT. It is highly lipophilic and has to be administered intravenously by dissolving in propylene glycol. The dose is 2.2 mg/kg melarsoprol per day for 10 days which has a success rate of 93.9% after treatment and 86.2% after 2 years post-treatment. The arsenic group makes it very toxic with approximately 10% of patients experiencing post-treatment reactive encephalopathy (PTRE) with symptoms of high fever, seizures and dizziness. Up to 50% of patients with PTRE die within 2 days after being administered with melarsoprol. In addition to its toxicity, melarsoprol causes trypanosome resistance, which may arise from the modification of the P2/TbAT1 nucleoside transporter, a transporter for the entry of melarsoprol in trypanosome (Babokhov *et al.*, 2013).

Eflornithine

Eflornithine, also known as alpha-Difluoromethylornithine (DFMO), is effective against both early and late stage of *T. b. gambiense* HAT. It is, however, ineffective for the *T. b. rhodesiense* infection. It was originally an anti-cancer drug, and its anti-trypanosomiasis characteristic was discovered by Cyrus Bacchi in 1980. Eflornithine can inhibit ornithine decarboxylase, thereby

intervening the process of cell division and proliferation. Eflornithine can be administered by both oral and intravenous infusions. However, oral administration shows low efficacy against HAT (Babokhov *et al.*, 2013). Compared to melarsoprol, eflornithine is more effective with a lower death rate (Priotto *et al.*, 2008). Eflornithine has a short half-life of up to 5 hs and limited permeability across the BBB. Thus it needs a prolonged intravenous infusion, which is expensive and inconvenient for patients (Sanderson *et al.*, 2008; Bacchi, 2009). The dose of eflornithine is 100 mg/kg body weight at intervals of 6 hs for two weeks (Burri and Brun, 2003).

Nifurtimox eflornithine combination therapy

Nifurtimox was originally used for treating Chagas disease. It has limited efficacy against the late stage of HAT. However, the combination of nifurtimox and eflornithine, known as NECT, showed lower death rate (0.7%) and a higher cure rate (97.7% at 18 months) for *T.b. gambiense*. NECT is well tolerated among children (Alirol *et al.*, 2013). It is administered by intravenous infusion of eflornithine at 200 mg/kg twice a day for one week and oral administration of nifurtimox three times a day for ten days (Bacchi, 2009).

Fexinidazole

Fexinidazole (Faxinidazole Winthrop) is a DNA synthesis inhibitor and was just approved by European Medicines Agency (EMA) in 2019 for the treatment of HAT. This is the first and only drug available now for the treatment of both haymolymphatic and meningo-encephalitic stage of *T.b.gambiense* and *T.b.rhodesiense* HAT (Deeks, 2019). Fexinidazole has been designed for oral administration therefore it is less invasive for patients and cheaper from a healthcare perspective. Studies showed that a dose of 1,800 mg fexinidazole in tablet per day for four days and then 1200 mg per day for six days provided desired efficacy and was well tolerated by patients. However, late relapse has been observed. Therefore, patients are suggested to have a follow-up check 12 months post-treatment of fexinidazole (Tarral *et al.*, 2014; Pelfrene *et al.*, 2019).

Table 1-1 Current drugs for the treatment of human African Trypanosomiasis. *Log P and charges at pH 7.4 are predicted using the MarvinSketch software

Drugs	Molecular weight (g/mol)	Log P*	Charge at pH 7.4*
Pentamidine	340.4	2.32	+2
Suramin	1297.3	5.58	-6
Melarsoprol	398.3	2.79	+2
Eflornithine	182.2	-0.61	+1
Nifurtimox	287.3	-0.27	0
Fexinidazole	279.3	2.38	0

To summarise, pentamidine is the safest choice for treating HAT because it is well-tolerated and less toxic. It is not effective for the late stage of HAT due to its limited ability to cross the BBB. Therefore, developing a drug delivery method for increasing pentamidine delivery across the BBB would provide a promising treatment option for treating the late stage of HAT. Thus, it is necessary to understand the BBB and how drugs cross the BBB.

1.3 The blood-brain barrier

The neurons in the central nervous system (CNS) play keys roles such as receiving and transferring chemical and electrical signals and require a stable environment in which to function. The BBB plays a critical role in regulating the exchange of ions and molecules between the blood and the brain (Abbott *et al.*, 2010). To maintain the homeostasis of CNS and protect the brain from external toxins, there are several interfaces including the blood-brain barrier (BBB) and the blood-cerebrospinal fluid barrier (BCSFB) which includes the arachnoid barrier (Cipolla, 2009). As the BBB is the interface directly between the blood and the brain tissue, has the largest surface area and limits the entry of pentamidine into the CNS, this chapter will be focused on introducing the BBB. The BCSFB and the arachnoid barrier will only be briefly summarised.

The blood-cerebrospinal fluid barrier (BCSFB) is a barrier which sits between the blood in the choroid plexus capillaries and the cerebrospinal fluid. The walls of the choroidal capillaries are of the fenestrated, non-continuous type. There are discontinuous tight junctions between the capillary endothelium cells which allow the free movement of small molecules as well as large molecules such as horseradish peroxidase. Thus the choroid capillary endothelium does not contribute to the actual physical barrier. However, surrounding the choroid plexus capillaries is a single layer of epithelial cells which is continuous with the ventricular ependyma (the layer of cells between the brain and the CSF). This layer of modified epithelial cells has tight junctions that restrict the intercellular movement of molecules and offer a barrier phenotype (Cipolla, 2009). The meningeal barrier consists of fenestrated dura and outer cells of the arachnoid membrane with tight junctions. The fetal cerebrospinal fluid (CSF)-brain barrier is a membrane between the CSF and brain parenchyma. The fetal CSF-brain barrier is active only during early development when its neuroependymal cells form the physical barrier to restrict large molecules (Cipolla, 2009). The adult (mature) ventricular ependyma does not control the entry of large molecules between the CSF and brain (Cipolla, 2009).

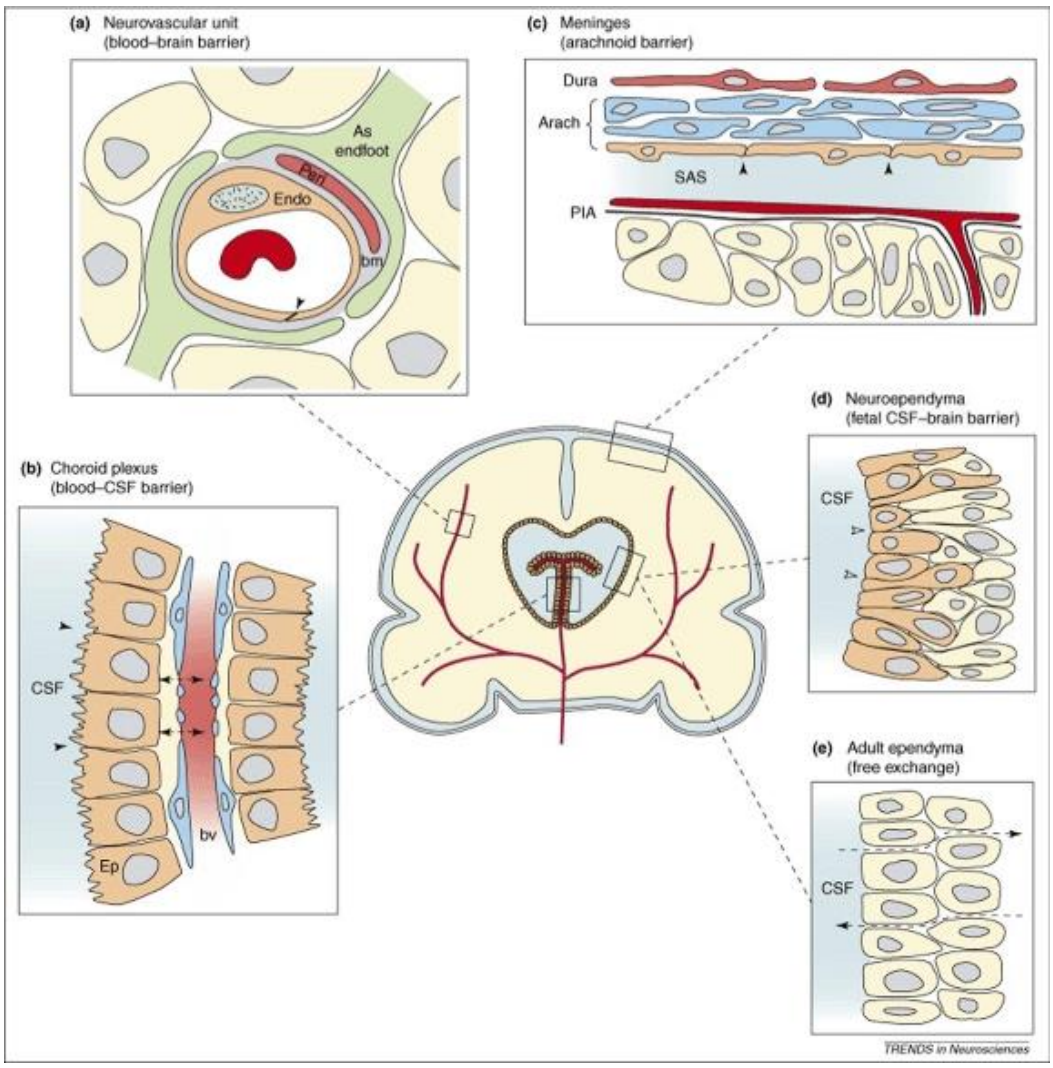

Figure 1-5 Barrier interfaces in the adult brain. The image was taken from (Cipolla, 2009). (a) The blood-brain barrier. (b) The blood-CSF barrier. (c) The meningeal barrier (d) The fetal-CSF barrier (d) The adult ventricular ependyma.

The blood-brain barrier (BBB) is part of the neurovascular unit (NVU) and is located at the walls of the cerebral capillaries (Figure 1-6). The NVU is composed of the endothelial cells, a basement membrane, pericytes, astrocytic endfeet, neurons, microglia, and oligodendrocytes (Warren, 2018). The BBB can regulate the entry of external substances into the brain and is a dynamic barrier responding to the changes of the CNS, through signalling among brain endothelial cells, neurons and astrocytes (Neuwelt *et al.*, 2011; Banks, 2016). The BBB impedes the majority of small molecules and almost all big molecules from entering the central nervous system (CNS) in the brain (Sweeney *et al.*, 2019).

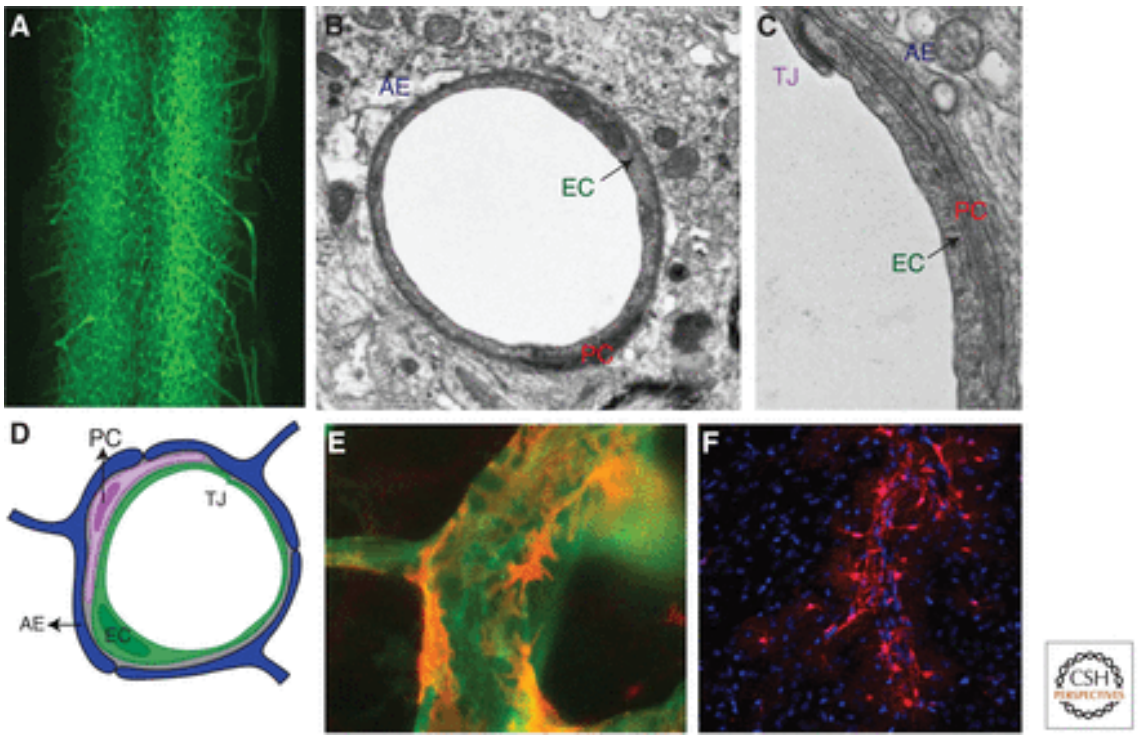

Figure 1-6 Components of the NVU. The image was taken from (Daneman and Prat, 2015). (A) The dense CNS vascular network; (B) and (C) Cross-section image captured by electron micrograph of the endothelial cells (EC) with tight junctions (TJ), pericytes (PC), astrocyte endfeet (AE); (D) The neurovascular unit (NVU); (E) Pericytes (orange) and endothelial cells (green) captured by immunofluorescence. (F) Astrocytes (red) and unstained blood vessels captured by immunofluorescence.

1.3.1 Endothelial Cells (ECs)

The walls of the capillaries are composed of a monolayer of endothelial cells (ECs). The ECs in CNS are 39% thinner than ECs in muscles (Coomber and Stewart, 1985) with a thickness of 0.3-0.5 mm (Zlokovic, 2009). There is a paucity of vesicles and fenestrations found in brain endothelial cells compared to non-cerebral endothelial cells. Endothelial cells are joined together at the paracellular cleft by both tight and adherens junctions. These junctions are intermingled and continuous throughout the paracellular cleft. The BBB tight junctions are complex and restrict the paracellular movement of ions and molecules with electrical resistance (TEER) of ~ 2,000 $\Omega.cm^2$ compared to ~30 $\Omega.cm^2$ in other tissues (Stamatovic, Keep and Andjelkovic, 2008) (Grieb *et al.*, 1985; Sumpio, Riley and Dardik, 2002; Ballabh, Braun and Nedergaard, 2004; Weiss *et al.*, 2009). The endothelial cells at the BBB have a higher density of mitochondria compared to non-cerebral endothelial cells. The electron micrographs of different sections of the rat brain revealed that 8-11% of the endothelial cytoplasmic volume accommodated the mitochondrial content of the BBB, whilst non-BBB tissues had a mitochondrial content of 2-5%. The higher expression of mitochondria is related to the role of the BBB in exchanging ions and molecules between the plasma and the brain and the homeostasis of the CNS fluids. These roles of the BBB require the

use of energy in the form of ATP, which is generated by the mitochondria. ATP is hydrolysed to ADP to provide the energy for primary active transporters to move solutes and ions against their concentration gradients. Primary active transporters set up the ion gradients needed by secondary active transporters to drive solutes and ions against their concentration gradients. Thus secondary active transporters also require ATP, albeit indirectly (Oldendorf, Cornford and Brown, 1977).

There are multiple membrane transporter proteins which are expressed in the endothelial cell plasma membranes and select molecules to cross the endothelial cells and enter the brain and also to cross the endothelial cell and enter the blood. A detailed introduction of these transporters can be found in sections 1.4.2 and 1.4.3. In addition to the membrane transporters, there are a number of metabolising enzymes expressed at the BBB including alkaline phosphatase, γ-glutamyl transpeptidase, and cytochromes P450 (CYP) enzymes (Correale and Villa, 2009). Alkaline phosphatase is used as a biomarker to differentiate capillary endothelial cells in the brain from those in the periphery. It also mediates the transport of compounds across the BBB. When alkaline phosphatase was inhibited with levamisole, the permeability of the BBB to Lucifer Yellow was increased (Deracinois *et al.*, 2015). Both γ-glutamyl transpeptidase and alkaline phosphatase are expressed at the luminal side of the endothelial cells (Persidsky *et al.*, 2006). Cytochromes P450 are situated at mitochondrial membranes or endoplasmic reticulum. They are involved in the metabolism of xenobiotics and endogenous compounds (Ghosh *et al.*, 2011).

1.3.2 Tight junctions (TCs)

The BBB endothelial cells are connected by tight junctions (TJs). These TJs are responsible for regulating the paracellular transport of molecules, preventing the lateral movement of lipids and membrane proteins, and intracellular signalling. The TJs are composed of transmembrane proteins and membrane-associated cytoplasmic proteins (Luissint *et al.*, 2012).

1.3.2.1 Transmembrane proteins

Transmembrane proteins including claudins, occludins, and junctional adhesion molecules (JAMs) form the backbone of the tight junctions of the BBB.

Claudins (20-27 kDa) have over 25 family members and are vital for the paracellular barrier formation. Claudin-3, claudin-5, and claudin-12 are expressed at the BBB. Claudin-3 and claudin-5 are crucial for the formation and integrity of the tight junctions of the BBB (Luissint *et al.*, 2012). It was found that the permeability of small molecules with less than 800 Da was affected in claudin-5 deficient mice, indicating that claudin-5 was vital for the integrity of the BBB (Nitta *et al.*, 2003). Study on claudin-12 knocked out mice revealed that claudin-12 is not essential for the establishment of the integrity of tight junctions of the BBB (Castro Dias *et al.*, 2019)

Occludin (60 kDa) is expressed on both epithelial and endothelial cells in CNS. It contributes to the function of barriers. It is a member of TJ-associated marvel proteins with marvelD2 and marvelD3, both of which consist of four transmembrane helices and coiled-coil cytosolic C-terminus. The structure of occludin contributes to the assembly and redox regulation of tight junctions of the blood-brain barrier (Luissint *et al.*, 2012).

Junctional adhesion molecules (JAMs) are not essential to the tight junctions. They are immunoglobulin proteins that mediate leukocyte extravasation and paracellular permeability (Daneman and Prat, 2015).

1.3.2.2 Membrane-associated cytoplasmic proteins

Cytoplasmic proteins contribute to the integrity of brain endothelial cells and epithelial cells. Among these, the membrane-associated guanylate kinase (MAGUK) family, including zonula occludens (ZO) proteins, disks large homolog 1 (DLG1), and membrane protein palmitoylated (MPP) 1, 5 and 7 have been identified on the tight junctions of brain endothelial cells. The ZO proteins have been extensively studied. ZO proteins are composed of zonula oocludens-1 (ZO-1), zonula oocludens-2 (ZO-2), and zonula oocludens-3 (ZO-3). ZO proteins have a SH3 domain, a guanylate cyclase, and PDZ domains. The SH3 domain interacts with signalling proteins and cytoskeletal elements. The guanylate cyclase is responsible for transforming GMP to GDP. The PDZ domains bind to the C-terminal cytoplasmic ends of transmembrane proteins (Stamatovic *et al.*, 2016). The functions of ZO proteins distinct within their C-terminus. The PDZ-1 domain of ZO proteins interacts with the C-terminal of claudins, the PDZ-3 of ZO proteins interacts with JAMs, the GUK domains of ZO proteins connects with occluding. ZO proteins are vital to the assembly of claudins, occludin, and JAMs which constitute the backbone of the BBB tight junctions (Luissint

et al., 2012). ZO proteins also coordinate the multimolecular complex to the actin cytoskeleton. ZO proteins bind to F-actin binding proteins (cortactin, α-catenin, protein 4.1, and fodrin) which affect the assembly and maintenance of tight junctions. A study on Madin-darby canine kidney (MDCK) cells confirmed that ZO-1 interacts with F-actin and plays an important role in the assembly of tight junctions (Fanning, Ma and Anderson, 2002).

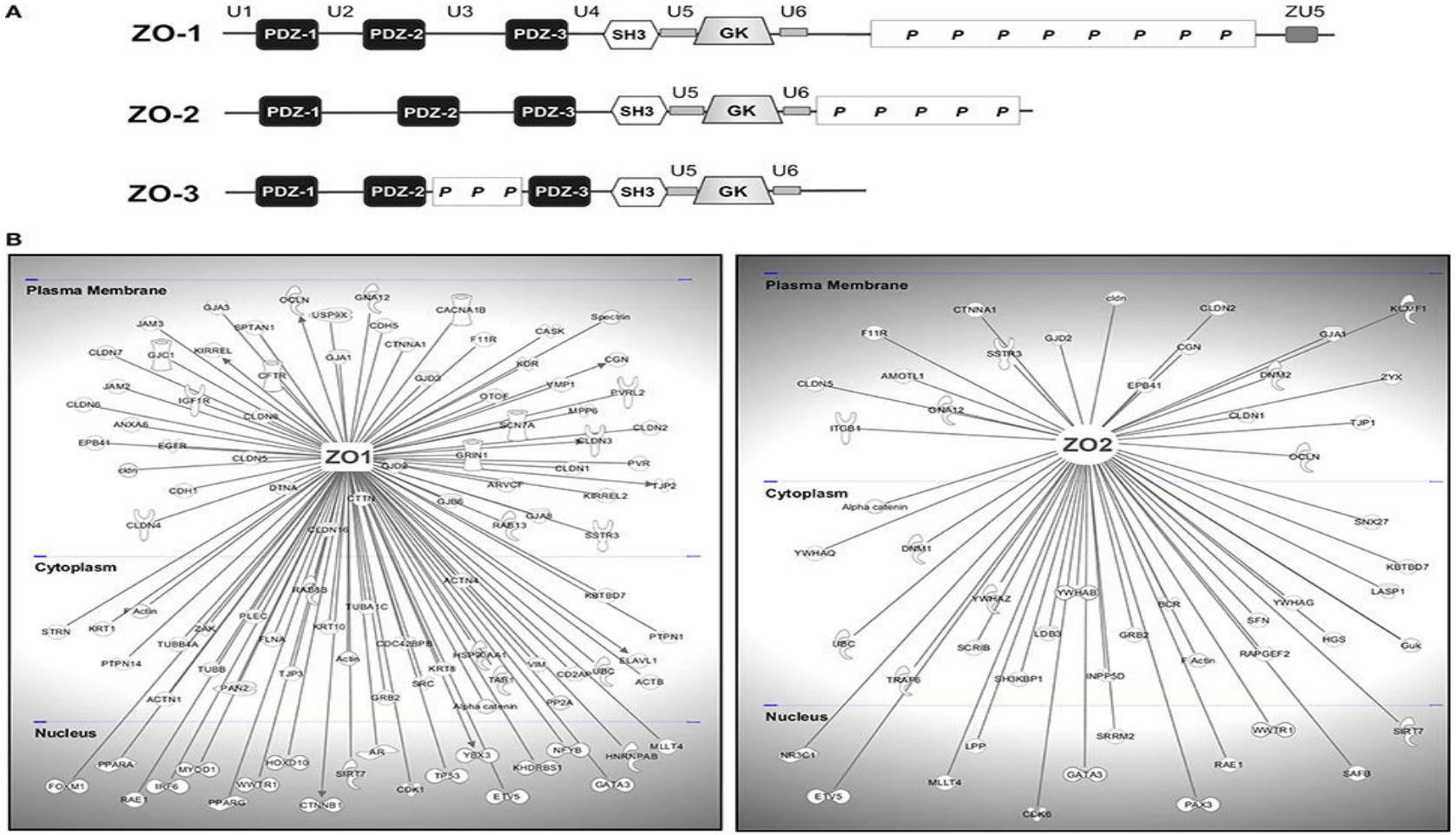

Figure 1-7 Zonula oocludens-1 (ZO-1), zonula oocludens-2 (ZO-2), and zonula oocludens-3 (ZO-3). (A) The structure of ZO-1, ZO-2, and ZO-3. They consist of PDZ domains, SH3, GK (catalytically inactive GUK domain), and various ZO-specific U or P regions. ZU5 is a region that is specifically found on ZO-1. (B) ZO-1 and ZO-2 contain structural and signalling molecules. Proteins that are known to interact with ZO-1 and ZO-2 in endothelial and epithelial cells are shown in the figure. The image was taken from (Bauer et al., 2014)

1.3.3 Pericytes

Pericytes were first identified in the 19th century, but their role was not elucidated until the 21st century, thanks to the development of more sensitive technologies. In CNS, pericytes share a common basement membrane with endothelial cells. Pericytes regulate cerebral blood flow, maintain the stability of the BBB, and perform immune cell functions (Brown *et al.*, 2019). Pericytes are associated with microvasculature and possess antigen properties. Thus they are regarded as the first line of defence in the CNS. In the presence of antigens, pericytes can trigger pro-inflammatory response in the brain, which induces monocyte and lymphocyte recruitment. This process is associated with the increased expression of adhesion molecules on the apical side of brain endothelial cells. A previous study on mouse brains revealed that pericytes produce cytokines, nitric oxide, chemokines and react to immune stimulator lipopolysaccharide. The immune functions of pericytes are crucial for communication within NVU and the neuroinflammatory process in response to infections and neurodegenerative diseases (Kovac, Erickson and Banks, 2011). Pericytes can also produce chemo-attractants and contribute to the transmigration of immune cells to the brain. In addition, pericytes can directly produce multiple inflammatory mediators such as interleukin (IL)-1β, IL-6, and nitric oxide. These inflammatory mediators can potentially cause pericytes to detach and disrupt the BBB (Hurtado-Alvarado, Cabañas-Morales and Gómez-Gónzalez, 2013). Pericytes might directly regulate the BBB. Armulik (*et al.*, 2010) found that in pericyte-deficient adult mice, the BBB permeability of water and a variety of molecular mass tracers was increased, indicating the critical role of pericytes in regulating the BBB. Also, it was shown that a lack of pericytes might lead to disorders such as hypoxia and/or stroke (Liu *et al.*, 2012). Recent studies suggested that pericytes could be a potential drug target for HIV-1 infection (Bertrand, Cho and Toborek, 2019).

1.3.4 Astrocytes

Astrocytes are glial cells in CNS whose endfeet completely enclose the brain microvessels (Mathiisen *et al.*, 2010). Astrocytes serve multiple functions in CNS including facilitation of neurovascular coupling, regulation of brain microenvironment, CNS development and repair, and among others (Cabezas *et al.*, 2014; Oksanen *et al.*, 2019). Astrocytes were shown to induce BBB characteristics, as the tight junctions of endothelial cells were enhanced both in length and width when they were co-cultured with astrocytes (Janzer and Raff, 1987; Tao-Cheng, Nagy and

Brightman, 1987). Astrocytes endfeet are an integral component of the BBB. It provides nutrients from blood vessels to neurons and helps maintain the integrity of the BBB. In a previous study, the role of astrocytic endfeet was observed in a mouse brain. When astrocytes were partially removed by a laser, the remaining astrocytic endfeet contributed to angiogenesis. This indicated that damage to astrocytes caused signalling factors to be secreted, which stimulated the growth of new vessels from existing blood vessels (Kubotera *et al.*, 2019).

1.3.5 Basement membrane

The basement membrane (BM) is a 50-100 nm protein layer that provides structural support, mediation for cell signalling, and maintenance of tight junctions. (Persidsky *et al.*, 2006; Liu *et al.*, 2012; Daneman and Prat, 2015). The BM is composed of type IV collagen, laminin, nidogen and heparan sulfate proteoglycans proteins (LeBleu, Macdonald and Kalluri, 2007). There are two forms of basement membrane in the brain: the inner endothelial BM and the outer parenchymal BM. The two types of BM are isolated by pericytes (Liu et al., 2012), and they have different protein components. A detailed protein components of the endothelial BM and the parenchymal BM can be found in Thomsen, Routhe and Moos (2017).

1.3.6 Microglia

Microglia are immune cells in CNS. In healthy brain, microglia and neurons promote the stability of the brain. Microglia are activated by brain injury and this process includes microglia proliferation, chemotaxis, morphological alternations, and immunomodulatory molecules generation (Yenari *et al.*, 2006; da Fonseca *et al.*, 2014). It was found that the introduction of microglia in the co-culture of endothelial cells and astrocytes double the cell death rate. The increasing cell death rate was avoided by the addition of minocycline, a microglial inhibitor. This suggested that microglial inhibitors could be a potential measure to protect the brain after ischemic stroke and fibrinolysis (Yenari *et al.*, 2006).

1.4 Drug delivery across the blood-brain barrier

Drug molecules can cross the BBB through various routes including passive diffusion, ATP-binding cassette (ABC) transporters, solute carrier (SLC) transporters, and transcytosis (Bhowmik *et al.*, 2015).

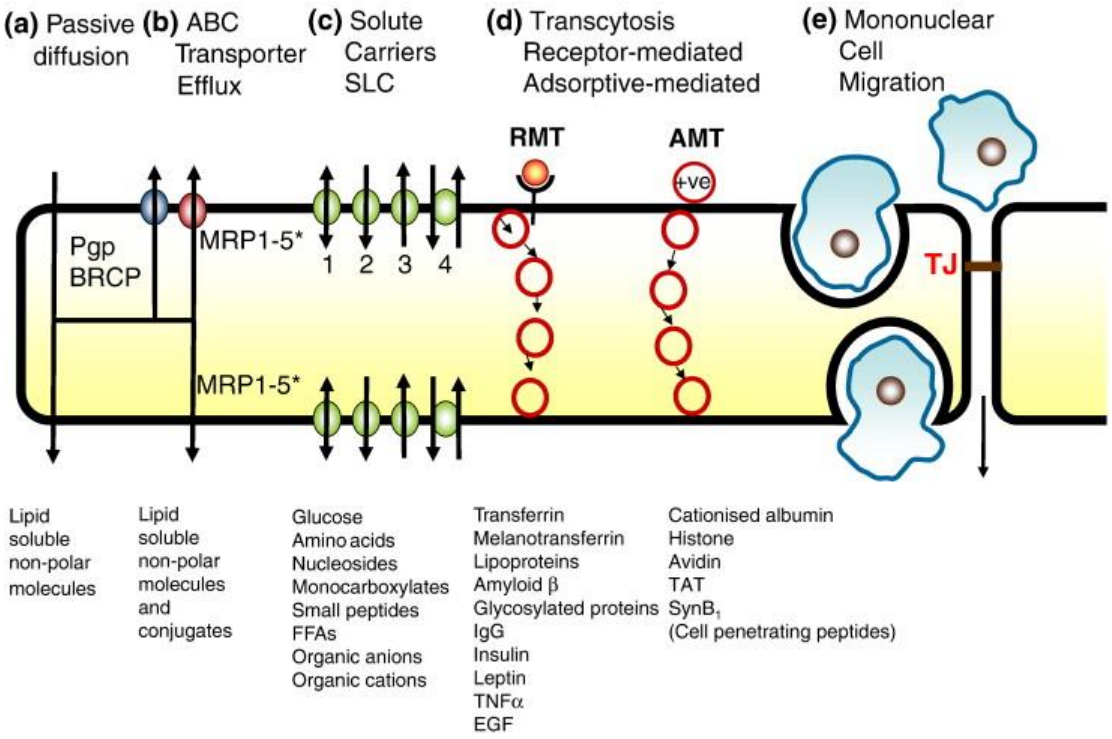

Figure 1-8 Drug transport across the BBB. The image was taken from (Abbott et al., 2010)

1.4.1 Passive diffusion

Passive diffusion is the transport of substances along the concentration gradient across membranes without utilising energy or the assistance of membrane transporters (Sanchez-Covarrubias *et al.*, 2014). Physicochemical properties such as charge and lipophilicity affect the passive transport of drugs across the BBB (Mikitsh and Chacko, 2014). The charge state of a molecule can be predicted by its pK_d value and the pH of the medium where the molecule is dissolved. For lipophilicity, the octanol-water partition coefficient (log P) is a traditional parameter to determine the lipophilicity of neutral molecules. For ionised molecules, the distribution coefficient (log D) is utilised as an indicator for lipophilicity (Avdeef, 2012). Generally, small unionized compound (molecular weight < 400-500 Da) with relatively high lipophilicity (log P ~2) and fewer hydrogen bonds (< 8-10 hydrogen bonds with water) are more likely to cross the BBB (Pardridge, 2012; Kasinathan *et al.*, 2015). A detailed explanation of physicochemical properties can be found in chapter 2.

1.4.2 ABC efflux transporters

Theoretically, the more lipid a drug is, the more likely a drug can cross the lipid membrane. However, many lipid drugs have much lower permeability across the BBB according to their

lipophilicities as they are substrates of ATP-binding cassette (ABC) efflux transporters at the BBB (Löscher and Potschka, 2005b). The transport of substances by ABC transporters is energy-dependent and uses energy from the hydrolysis of ATP. Substances can be moved across the BBB against the concentration gradient (Sanchez-Covarrubias *et al.*, 2014). ABC transporters are categorised into seven subfamilies from A to G. ABC transporters need energy from ATP hydrolysis to pump a broad range of lipophilic and amphipathic drug substrates across the BBB (Qosa *et al.*, 2015). In human, ABCB, ABCC, and ABCG subfamilies efflux metabolic waste, xenobiotics, and drugs out of the brain. The ABC transporters expressing at the BBB include the multidrug resistance proteins (ABCB1, MDR1, P-gp), multidrug resistance-associated proteins (ABCC; MRPs), and breast cancer resistance protein (ABCG2, BCRP) (M.S. Hartz and Bauer, 2011; Miller, 2015; Qosa *et al.*, 2015). ABC transporters have similar ATP-hydrolysing nucleotide-binding domains and a common “coupling helix” which is responsible for conformational changes. It has been suggested that the binding of ABC transporters to ATP causes outward-facing conformation changes while hydrolysis of ATP triggers inward-facing conformation changes (Hollenstein, Dawson and Locher, 2007).

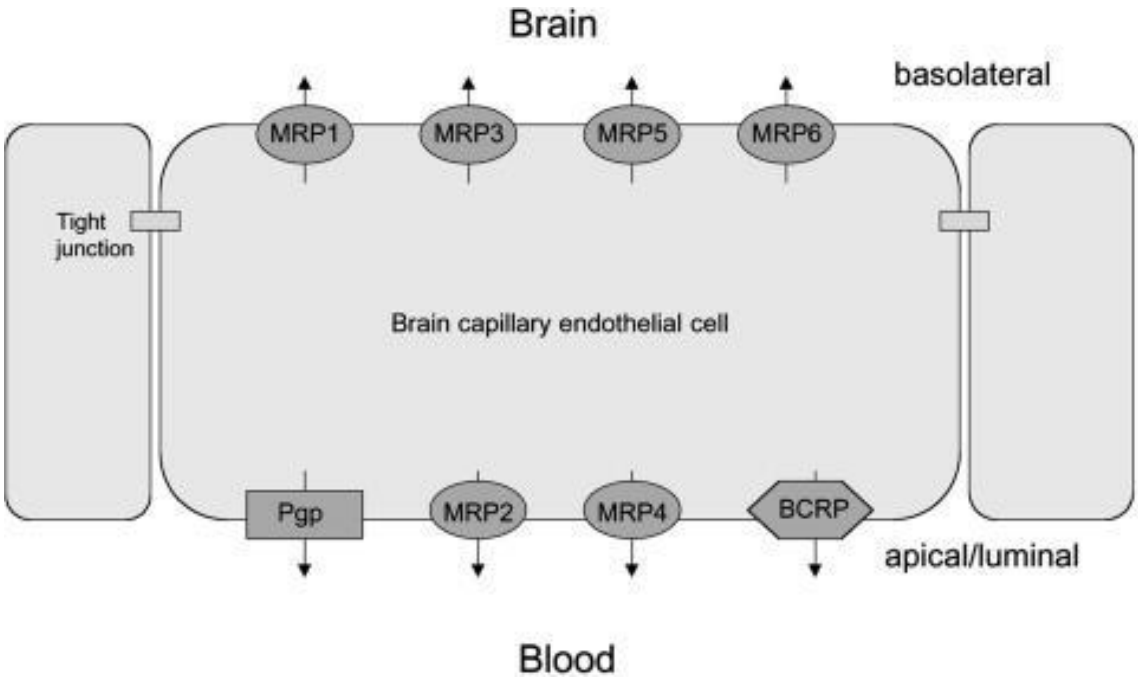

Figure 1-9 Localization of main ABC transporters at the blood-brain barrier. The image was taken from (Löscher and Potschka, 2005a)

Table 1-2 ABC transporters at the BBB

ABC Transporter	Gene encoded	Localization	Substrates	References
P-glycoprotein (P-gp; MDR1/ ABCB1)	*ABCB1*	Apical/luminal	Methotrexate, cyclosporin A, dexamethasone, corticosterone, cortisol, aldosterone, morphine, colchicines, amprenavir, indinavir, saquinavir, loperamide, ivermectin, abamectin, cimetidine, verapamil, phenytoin, carbamazepine, lamotrigine, digoxin	(Schinkel and Jonker, 2003; Sun *et al.*, 2003; Löscher and Potschka, 2005a)
MRP1	*ABCC1*	Basolateral	Etoposide, teniposide, vincristine, doxorubicine, daunorubicine, methotrexate	(Löscher and Potschka, 2005a)
MRP2	*ABCC2*	Apical/luminal	Similar to MRP1	(Löscher and Potschka, 2005a)
MRP3	*ABCC3*	Basolateral	Similar to MRP1	(Löscher and Potschka, 2005a)
MRP4	*ABCC4*	Apical/luminal	Methotrexate, 6-mercaptopurine, thioguanine	(Löscher and Potschka, 2005a)
MRP5	*ABCC5*	Basolateral	cGMP, cAMP, 6-mercaptopurine, thioguanine, fluorescein	(Löscher and Potschka, 2005a)

BCRP/MXR	*ABCG2*	Apical/luminal	Prazosin, anthracyclines, mitoxantrone, estrone 3-sulfate, methotrexate, sulfasalazine, glyburide, hematoporphyrin, 7-ethyl-10-hydroxycamptothecin (SN-38), SN-38-glucuronide	(Löscher and Potschka, 2005a; Ni *et al.*, 2010)

1.4.2.1 P-gp transporter

P-glycoprotein (P-gp, MDR1, ABCB1) was first discovered in the 1970s and the first efflux transporter identified in the brain capillary endothelial cells. P-gp is found in both animals and humans (Tsuji and Tamai, 1997). P-gp is encoded by *ABCB1* in humans and two isoforms (*Abcb1a and Abcb1b*) in rodents (DeMars *et al.*, 2017). The human type of P-gp has a molecular weight of 170 kDa and was found in in the apical (luminal) side of the BBB (Löscher and Potschka, 2005b). The human P-gp is a phosphorylated glycoprotein. It is situated on chromosome 7 and contains 28 exons (Löscher and Potschka, 2005b). It consists of 1280 amino acids. The structure of P-gp is separated into two hydrophobic domains. Each domain has 6 transmembrane segments as well as 2 cytoplasmic nucleotide-binding domains. Also, on the first extracellular loop there are 3 glycosylation sites (Loo and Clarke, 1999; Ramakrishnan, 2003).

The main function of P-gp at the BBB is to protect the brain from external substances and toxins, however, the defensive function of P-gp has made it one of the major obstacles for drug development. For example, HIV-1 protease inhibitors indinavir, nelfinavir, and saquinavir have limited entry into the brain. The plasma concentrations of these HIV-1 protease inhibitors were elevated by 2-5 times in P-gp knocked-out (mdr1a (-/-)) mice after oral administration and 7-36 folds in brain after intravenous administration (Kim *et al.*, 1998). Also, interactions of P-gp with drugs makes it difficult to be predicted in terms of its permeability across the BBB. For example, the permeability of doxorubicin, vincristine, epipodophyllotoxin and cyclosporin A across the BBB was found to be much lower than predicted by octanol-water partition coefficient. This was mainly because P-gp was involved in the transport of these compounds (Levin, 1980). Therefore, understanding the role and interaction of drugs with P-gp is crucial for developing safe and effective drugs for brain diseases.

1.4.2.2 Breast cancer resistance protein (BCRP, ABCG2)

The breast cancer resistance protein (BCRP, ABCG2) was discovered in 1998 using RNA fingerprinting identification in a multidrug-resistant human breast cancer cell line (MCF-7/AdrVp) (Doyle *et al.*, 1998). In the brain, the function of BCRP is to protect the brain from the accumulation of neurotoxic amyloid and carcinogen PhIP (ZHANG *et al.*, 2003; Mahringer and Fricker, 2010). BCRP is localized on the apical (luminal) side of brain capillaries endothelial cells in rats (Hori *et al.*, 2004) and humans (Cooray *et al.*, 2002). The sequence of mouse BCRP and human BCRP

is 81% identical, making mouse BCRP comparable to human BCRP studies (Allen *et al.*, 1999). Human BCRP has 657 amino acids and around 75 kDa for its protein size (Ni *et al.*, 2010). BCRP is a half-transporter which is composed of 6 transmembrane helices and 1 ATP-binding site (Nakanishi and Ross, 2012).

BCRP has a wide range of substrates some of which are also substrates for P-gp. A list of BCRP substrates is summarized in table 1-1. As BCRP inhibits many drugs from crossing the BBB, a few strategies have been developed to overcome this. One method is to use BCRP inhibitors. For example, the accumulation of dasatinib (a substrate for BCRP) was increased in brain of BCRP-knocked out (Abcg2(-/-)) mice compared to wild-type mice. A similar increase of dasatinib was also observed by co-administration of dasatinib and BCRP inhibitor elacridar in wild-type mice brain (Lagas *et al.*, 2009). The other approach of interest is by intervening the signalling mechanisms of BCRP. Mahringer and Fricker (2010) found that both BCRP protein expression and mRNA level were decreased with 17ß-estradiol in isolated rat brain capillaries, suggesting the down-regulation of BCRP by 17ß-estradiol. Other evidence suggested that BCRP may also be regulated by Akt - a regulator of cell survival. It was found that BCRP was regulated by Akt signalling in mice bone marrow (Mogi *et al.*, 2003).

1.4.2.3 Multidrug resistance proteins (MRPs; ABCCs)

Multidrug resistance associate protein (MRPs, ABCCs) is a member of the ABC superfamily transport proteins with a protein size of 190 kDa. The structure of MRP is quite different from P-gp and they only share 15% of amino acid homology. MRPs maintain the homeostasis of the BBB and regulates the transport activity of opioids (Huai-Yun *et al.*, 1998; Su and Pasternak, 2013). In the brain, MRP1, MRP2, MRP4 and MRP5 are particularly important in the transport of drugs (Abbott *et al.*, 2010). The substrates of MRPs are usually organic anions and their metabolites. The expression and localization of MRPs at the BBB are still under examinations, and conflicting results have been reported (Fan and Liu, 2018). Quantitative PCR analyses showed the existence of MRP1-5 in human brain samples, but MRP2 and MRP3 proteins could not be detected under immunofluorescence microscopy. The MRP1, MRP4, and MRP5 were found to be on the apical side of the human brain endothelial cells (Nies *et al.*, 2004). In contrast, other studies showed that the MRP1 was not found on the luminal side of the human and mouse BBB (Cisternino *et al.*, 2003; Daood *et al.*, 2008).

1.4.3 Solute carrier (SLC) transporters

Solute carrier (SLC) transporters are facilitated transporters or secondary active transporters that transport endogenous substances and nutrients such as amino acids, glucose, vitamins, and hormones across the BBB without ATP (Sanchez-Covarrubias *et al.*, 2014; Bhowmik *et al.*, 2015). Up to now, 65 subfamilies (SLC1-SLC65) with 439 members have been discovered (Hu *et al.*, 2019). SLC transporters that are expressed at the BBB include amino acid transporters, monocarboxylate transporters, nucleoside transporters, organic anion transporters, organic anion transporting polypeptides, organic cation transporters, and peptide transporters (Morris, Rodriguez-Cruz and Felmlee, 2017). Generally, SLC transporters are uptake transporters, although some of the SLC transporters can transport substances bidirectionally (Sanchez-Covarrubias et al., 2014).

Table 1-3 Solute transporters expressed at the BBB. The table was taken from (Ohtsuki and Terasaki, 2007) with modifications.

Transporter system	Transporters	Substrates	Localization	Direction
Energy transport system	GLUT1	D-glucose	Luminal, abluminal	Blood-to-brain
	MCT1	L-Lactate, monocarboxylates	Luminal, abluminal	Blood-to-brain
	CRT	Creatine	Luminal, abluminal	Blood-to-brain
Amino acid transport system	LAT1/4F2hc[system L]	Large neutral amino acids	To be confirmed	Blood-to-brain
	CAT1 [system y^+]	Cationic amino acids	To be confirmed	Blood-to-brain
	$EAAT_{1, 2, 3}$	Anionic amino acids	Abluminal	Brain-to-blood
	ASCT2	L-Asp, L-Glu	Abluminal	Brain-to-blood
	ATA_2 [System A]	Small neutral amino acids	To be confirmed	Brain-to-blood
	xCT/4F2hc [System x_c^-]	$_L$-Cystine/$_L$-Glu	To be confirmed	Blood-to-brain
	TAUT [System β]	Taurine, β-alanine	To be confirmed	Both brain-to-blood and blood-to-brain

	System ASC/system B^{0+}	$_{L}$-Ala and others	To be confirmed	Brain-to-blood
Neurotransmitter transport system	GAT_2/BGT_1	γ-Aminobutyric acid	To be confirmed	Brain-to-blood
	SERT	Serotonin	Luminal, abluminal	To be confirmed
	NET	Norepinephrine	Abluminal	To be confirmed
Organic anion transport system	OAT3	PAH, HVA, indoxyl sulfate	Abluminal	Brain-to-blood
	oatp2	Digoxin, organic anions	Luminal and abluminal	Blood-to-brain and brain-to-blood
	oatp14	Thyroid hormones	To be confirmed	Blood-to-brain
	OCTN2	Carnitine	To be confirmed	Blood-to-brain
Nucleoside transport system	CNT2	Nucleosides	To be confirmed	Blood-to-brain

1.4.3.1 L-Alpha Amino Acid Transporters

L-alpha amino acid transporters (LATs) belong to SLC7 and SLC43 subfamilies and 4 L-alpha amino acid transporters have been identified: LAT1 (SLC7A5), LAT2 (SLC7A8), LAT3 (SLC43A1), and LAT4 (SLC43A2) (Morris, Rodriguez-Cruz and Felmlee, 2017). LAT1 was cloned in 1998. Its cDNA was extracted from rat C6 glioma cells. It transport neutral amino acids and the process is Na^+-independent (Kanai *et al.*, 1998). It exists in brain, placenta, and tumours and transports amino acids into cells across endothelial and epithelial membranes. LAT1 was found expressing on both apical and abluminal sides at the human BBB using immunofluorescence staining method (Geier *et al.*, 2013). The cDNA of LAT2 was first isolated from rat small intestine in 1999. LAT2 and LAT1 share an identical of 45-50% DNA sequence, but the transport by LAT2 is not dependent on Na^+-concentrations (Segawa *et al.*, 1999). It mainly exists in the colon, intestine, and kidney. LAT2 has much lower expression at the BBB than LAT1 and barely affects the transport of substrates at the BBB. It transports both large and small amino acids (Morris, Rodriguez-Cruz and Felmlee, 2017).

1.4.3.2 Monocarboxylate Transporters

Monocarboxylate transporters belong to SLC5 and SLC16 subfamilies. There have been 14 members in the proton-dependent family (SLC16; MCTs) and 2 members of the sodium-dependant family: SLC5A8 and SLC5A12 (SMCTs) identified. Only 2 isoforms of MCTs (MCT1 and MCT8) express on the brain capillary endothelial cells (Morris, Rodriguez-Cruz and Felmlee, 2017). MCT1 (SLC16A1) is expressed in almost all tissues, and its main function is to transport L-lactic acid in or out of cells depending on the proton gradient. The substrates of MCT1 include GHB (define), XP13512, butyrate, acetoacetate, lactate, pyruvate, β-hydroxybutyrate (Vijay and Morris, 2014). The amount of MCT1 in the brain was found to be age-related. The amount of MCT1 in the cerebral cortex of suckling and adult rats was quantified using electron microscopic immunogold approach. Furthermore, results showed that the amount of MCT1 in brain capillary endothelial cells suckling rats was 25-fold more than adult rats (Leino, Gerhart and Drewes, 1999), possible because suckling rats were more dependent on MCT1 to supply energy to the

brain (Gerhart *et al.*, 1997). Immunoelectron microscopy revealed that MCT1 was expressed on both apical and basolateral sides of brain endothelial cells in rats (Gerhart *et al.*, 1997). MCT8 (SLC16A2) is a high-affinity thyroid hormones membrane transporter, and its substrates include tri-iodothyronine and pro-hormone thyroxine. In humans, modifications of the SLC16A2 gene could result in Allan-Herndon-Dudley syndrome (AHDS) (Lee *et al.*, 2017).

1.4.3.3 Nucleoside Transporters

Nucleoside transporters regulate the uptake of physiologic nucleosides and play important roles in the disposition and intracellular transport of nucleoside analogues of drugs for cancer and anti-viral drugs. There are two nucleoside transporters: equilibrative nucleoside transporters (ENTs) and concentrative nucleoside transporters (CNTs) (Kong, Engel and Wang, 2004). ENTs belong to SLC29A subfamilies and 4 isoforms have been identified in humans: ENT1 (SLC29A1), ENT2 (SLC29A2), ENT3 (SLC29A3), and ENT4 (SLC29A4). ENT1-4 are expressed in liver, kidney, colon, intestine, placenta and brain. ENT1, ENT2 and ENT3 transport purines and pyrimidines and they have common substrates (Morris, Rodriguez-Cruz and Felmlee, 2017). In the brain, the location of ENT1 is yet to be determined. ENT2 is situated on the apical side of the BBB. Reversed transcriptase PCR and Western blot results showed that ENT1 and ENT2 mRNA and their proteins existed in rat brain endothelial cells. Drug permeability assay confirmed the transport of ENT1 was Na^+ independent (Redzic *et al.*, 2005). CNTs belong to SLC28A subfamilies, and they have 3 isoforms in humans: CNT1 (SLC28A1), CNT2 (SLC28A2), and CNT3 (SLC28A3). CNT1 mainly transports pyrimidine while CNT2 mainly transports purine nucleosides. CNT3 transports pyrimidine and purine nucleosides. All the 3 isoforms of CNTs transport nucleosides against concentration gradients. CNTs are mainly found in epithelial cells in the kidney and liver. The expression of CNTs in the human brain was extremely low and may have very limited functions of transporting nucleosides in human brains (Kong, Engel and Wang, 2004; Morris, Rodriguez-Cruz and Felmlee, 2017).

1.4.3.4 Organic Anion Transporters

The organic anion transporters (OATs/oats) take up approximately half of the SLC22 subfamilies. The OATs have 11 members: OAT1 (SLC22A6), OAT2 (SLC22A7), OAT3 (SLC22A8), OAT4 (SLC22A11), Oat5 (Slc22a19), OAT6 (SLC22A20), OAT7 (SLC22A9), Oat8 (Slc22a9), Oat9 (Slc22a27), OAT10 (SLC22A13), and URAT1 (SLC22A12). OATs are expressed in many tissues including kidney, liver, olfactory mucosa and brain (Nigam *et al.*, 2015). OATs have a broad range of substrates for endogenous and exogenous compounds with a negative charge at physiological pH condition (Morris, Rodriguez-Cruz and Felmlee, 2017). In humans, OAT1 and OAT3 were found in the cytoplasmic membrane and cytoplasm of human choroid plexus using immunohistochemical analysis. OAT1 mediates the transport of a range of neurotransmitter metabolites such as vanilmandelic acid (VMA) and melatonin (Alebouyeh *et al.*, 2003). At the human BBB, the expression of OAT1 was not identified while low expression of OAT3 was found using proteomic analysis. OAT3 expression at the human BBB was over 5-fold smaller than its expression at the mouse BBB (Hoshi *et al.*, 2013).

1.4.3.5 Organic Anion Transporting Polypeptides

Organic anion transporting polypeptides (OATPs) belong to the SLCO (SLC21A) subfamilies. OATPs have 11 isoforms in humans, 14 isoforms in mice, and 15 isoforms in rats. The OATPs mediated transport is ATP and Na^+ independent. The endogenous substrates of OATPs include bile salts, polypeptides, and thyroid hormones. In human brains, a few isoforms of OATPs were identified: OATP1A2 (SLCO1A2), OATP1C1 (SLCO1C1), and OATP2B1 (SLCO2B1) (Morris, Rodriguez-Cruz and Felmlee, 2017). OATP1A2 is expressed at neurons and neuronal processes. OATP2B1 is highly expressed in brain endothelial cells (Gao *et al.*, 2015). In rat brain, Oatp1 and Oatp2 were found at both luminal and abluminal side of the choroid plexus epithelium. The Oatp2 is highly expressed at the rat BBB (Gao *et al.*, 2000).

1.4.3.6 Organic Cation Transporters

Organic cation transporters (OCT) belong to SLC22 subfamilies and three of them have been identified in humans: OCT1 (SLC22A1), OCT2 (SLC22A2), and OCT3 (SLC22A3). There are

three orthologs in rats, mice and humans: OCT1 (SLC22A1), OCT2 (SLC22A2) and OCT3 (SLC22A3). OCT1 is expressed in liver and brain. It is situated at the apical/ luminal side of the brain capillary endothelial cells. OCT2 is expressed in kidney and brain. It is also found at the apical/ luminal side of the brain capillary endothelial cells. OCT3 has a wider distribution, and it is found in liver, heart, kidney, lung, muscle, brain, and placenta (Morris, Rodriguez-Cruz and Felmlee, 2017). A detailed explanation about OCT transporters can be found in Chapter 3.

Three isoforms of OCTN transporters (OCTN1, OCTN2, and OCTN3) have been identified. OCTN transporters are responsible for the transport of organic cations and amino acid carnitine. OCTN1 and OCTN3 have not been identified in human CNS. OCTN2 was found at the luminal side of the BBB in the brain. Its transport of substrates is dependent on Na^+ concentrations (Sanchez-Covarrubias *et al.*, 2014).

1.4.3.7 Plasma Membrane Monoamine Transporter (PMAT)

Plasma membrane monoamine transporter (PMAT) is a polyspecific organic cation transporter that mainly transport amines and xenobiotic cations (Figure 1-10). It was highly expressed in the brain. Human PMAT cDNA is composed of 530 amino acid with 11 membrane-spanning domains. It has an intracellular N-terminus and a C-terminus (Wang, 2016). It was found that the expression of PMAT at the BBB in Alzheimer's patients was reduced compared to healthy patients (Sekhar *et al.*, 2019).

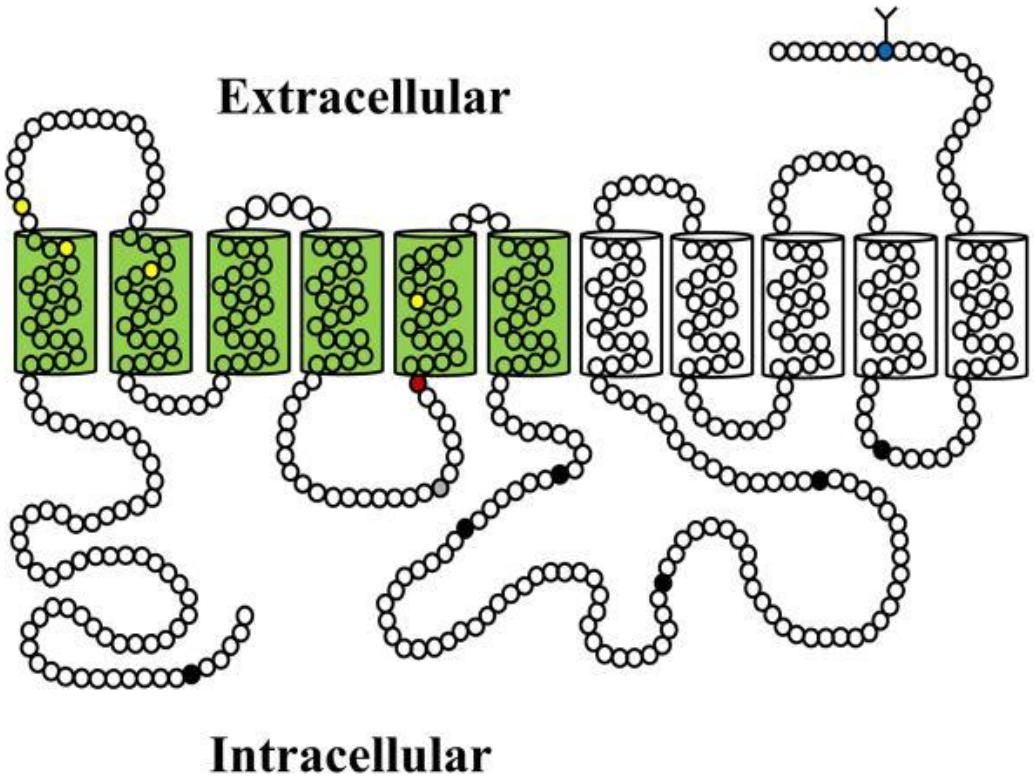

Figure 1-10 Proposed structure of PMAT. The image was taken from (Wang, 2016).

1.4.3.8 Multidrug and toxic compound extrusion (MATE) transporters

Multidrug and toxic compound extrusion (MATE) transporters were first identified as a bacterial drug transporter. It was identified in prokaryotes and eukaryotes. MATE transporters are responsible for eliminating metabolic waste and xenobiotics. It is important for maintaining the homeostasis of the CNS (Moriyama *et al.*, 2008; Sekhar *et al.*, 2019). MATE1 (SLC47A1) was primarily found in human brain microvessels > 10 μm in diameter by western blotting and immunohistochemistry (Geier *et al.*, 2013).

1.4.3.9 Peptide transporters

Peptide transporters belong to the SLC15A superfamily. There are 4 members of SLC15A superfamily: peptide transporter-1 (PEPT1; SLC15A1), peptide transporter-2 (PEPT2; SLC15A2), peptide/histidine transporter-1 (PHT1; SLC15A4), and peptide/histidine transporter-2 (PHT2; SLC15A3). Peptide transporters are proton-dependent oligopeptide transporters and they

transport peptides across membranes. PEPT1 has not been found in the CNS while PEPT2 has been identified in the cerebral cortex, cerebellum, astrocytes, and choroid plexus. PHT1 was found in rat brain at hippocampus, cerebral cortex, and cerebellum. PHT2 has a high affinity for di-peptides and tri-peptides, but its location in the brain is not known (Sanchez-Covarrubias *et al.*, 2014).

1.5 Drug delivery strategies across the BBB

1.5.1 Invasive approaches

In order to increase drugs permeability across the BBB, invasive methods such as intracerebral implants and intraventricular infusion of drugs have been used in the past. Another approach is to open the BBB temporarily with an intracarotid infusion of hypertonic solutions containing mannitol or arabinose. However, these methods can expose the CNS to toxins and may lead to severe side effects (Sanchez-Covarrubias *et al.*, 2014).

1.5.1.1 Disrupting BBB

The BBB can be opened by intracarotid infusion of hypertonic solutes such as arabinose and mannitol solutions. This is also known as the osmotic opening of the BBB. The process is regulated by vasodilation and shrinkage of brain endothelial cells. The inter-endothelial tight junctions can be widened and let therapeutic drugs cross the BBB (Rapoport, 2000).

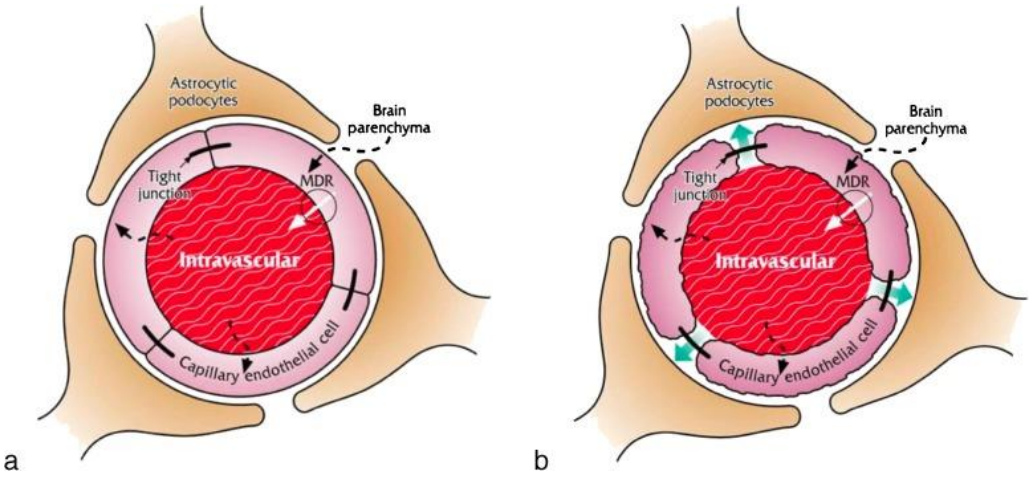

Figure 1-11 Osmotic modification of the BBB. (a). Brain capillary endothelial cells with tight junctions without anatomic space (b) Osmotic modification induces retractions of the cell membrane and the BBB was physically opened. The image was taken from (Bellavance, Blanchette and Fortin, 2008).

Rapoport, Hori and Klatzo (1972) applied several concentrated solutions of electrolytes and nonelectrolytes to the pia-arachnoid surface of rabbit brain. It was found that the less lipophilic electrolytes opened the blood-brain barrier in a reversible manner, while lipophilic propylene glycol opened the barrier irreversibly. Greenwood (*et al.*, 1988) investigated the impacts of hyperosmolar solutions of arabinose and mannitol on the permeability of the BBB. He perfused hyperosmolar solutions into rat brain and he found that within 1 min of perfusion, the BBB was consistently opened. Also, [^{14}C]mannitol and Evans blue were used as indicators of membrane integrity. The accumulation of radiolabeled hyperosmolar solutions, which was expressed as the

ratio of brain tissue to perfusate radioactivity for cerebrum, increased with the increasing concentration of arabinose. He concluded that the opening of BBB by osmotic barrier is caused by the passive shrinkage of brain endothelial cells. Fredericks and Rapoport (1988) infused 1.8 M arabinose in water into the internal carotid artery of mice brain. The process of osmotic opening is concentration-dependent and can be revered within 4 hs with no long-term neurologic deficit.

1.5.1.2 Increasing the permeability of BBB with pharmacological agents

Some pharmacological agents such as histamine and vasoactive peptides can temporarily increase the permeability of the BBB by targeting inflammatory mechanisms. These agents can disrupt the BBB temporarily and create pores that are large enough to let molecules cross through. Disrupting the BBB often cause severe side effects and damage neurons (Kasinathan *et al.*, 2015). Cereport is a bradykinin analogue can increase the permeability of the BBB for chemotherapy drugs. However, clinical studies on patients did not show the improvement of the efficacy of the chemotherapy drug carboplatin by using cereport (Prados *et al.*, 2003). Regadenoson is an adenosine receptor agonist which could disrupt the BBB and increase the BBB permeability of dextran and temozolomide in rodents. However, clinical studies on humans did not exhibit improved permeability of BBB by regadenoson (Jackson *et al.*, 2017).

1.5.1.3 Focused ultrasound

Focused ultrasound with intravenously injected microbubbles can disrupt the BBB and open its tight junctions at the specific location. This method is also known as sonoporation. The injected microbubbles have a diameter of 1-10 μm, wrapped by lipid or protein with heavy gases inside. Compared to other invasive approaches to opening the BBB, focused ultrasound is less invasive because it is focused on specific areas of the brain, does not damage intermediary tissues, and the disrupted membrane integrity of the BBB can recover within a few hs. The disadvantage of the focused ultrasound may cause inflammatory reactions to the targeted area of the brain (Kovacs *et al.*, 2017; Bors and Erdő, 2019). Using focused ultrasound with intravenously injected microbubbles, the BBB in rabbit brain was opened. Trypan blue was injected to rabbits intravenously before the rabbit was killed and could be identified at the sonicated sites in rabbit brains (Hynynen *et al.*, 2003).

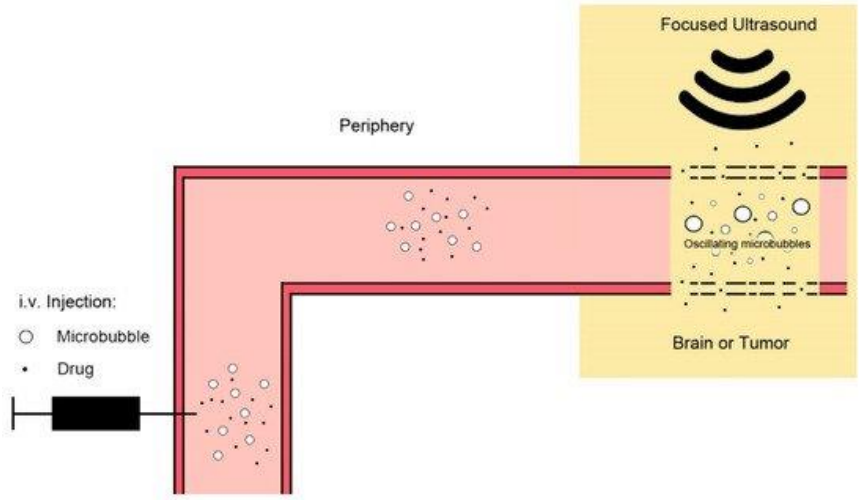

Figure 1-12 Sonoporation with focused ultrasound. Microbubbles can target the specific area in brain and improve the efficiency of sonoporation. The image was taken from (Bors and Erdő, 2019).

1.5.2 Non-invasive methods

1.5.2.1 Changing the solubility of drugs

Improving the lipid solubility of a drug can enhance its passive diffusion across the BBB. Although the octanol-water shake flask method has been a traditional method to determine the lipophilicity of a drug, the number of hydrogen bonds may be a better determinant. Low hydrogen bonds indicate high lipophilicity. Chikhale (*et al.*, 1994) investigated the permeability of a series of model peptides using an *in vitro* model of the BBB - bovine brain microvessel endothelial cell (BBMEC) monolayers and *in situ* method with rat brain perfusion. The results indicated that there was no correlation between the octanol-water partition coefficients of those peptides and BBB permeability; instead, inverse correlations ($r=0.837$ *in vitro* and $r=0.906$ *in situ*; $P<0.05$) were found between the hydrogen bonds of peptides with permeability.

With medicinal chemistry methods, the hydrogen bond on drug molecules can be modified or removed in order to improve their lipophilicity. Modifying hydrogen bond account number is in effect generating a new drug entity. For example, heroin shares a similar structure with morphine, but the hydroxy groups of morphine were acetylated to form heroin. This resulted in a higher log P of heroin at 2.3 versus the log P of morphine at 0.99 consequently the brain uptake of heroin was 100 times higher than that of morphine (Oldendorf *et al.*, 1972; Pardridge, 2012; Mikitsh and Chacko, 2014). However, modifying the hydrogen bond may also reduce the efficacy of the drugs and can increase the instability of the hydrogen blocking groups (Pardridge, 2012). Also,

increasing the lipophilicity of drugs will also increase its permeation into other tissues rather than brain (Tsuji and Tamai, 1997).

1.5.2.2 Prodrug

Prodrugs are bioreversible derivatives of drug molecules that exhibit pharmacological action after enzymatic or chemical biotransformation. Depending on how the prodrug is designed, the release rate of active drug can be controlled. As many parent drugs are unstable after administration into the human body or suffer from poor solubility issues, using a prodrug can resolve these issues. It is possible to design a prodrug which can modify the distribution, toxicity and affect the efficacy of the parent drugs (Rautio, Laine, *et al.*, 2008).

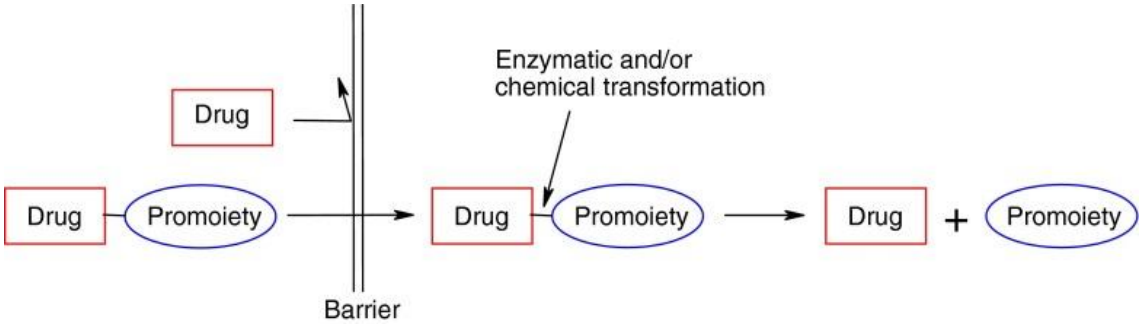

Figure 1-13 Concept of prodrug (Rautio, Kumpulainen, et al., 2008; Rautio, Laine, et al., 2008). Promoiety is an inactive component of a prodrug. The figure was taken from (Rautio, Laine, et al., 2008).

1.5.2.3 Viral vectors

Viral vectors can infect genes including small-interfering RNA, short-hairpin RNA, and decoy RNA into cells and change the expression of proteins for the treatment of diseases (Mohammed *et al.*, 2018). The transfection of viral vectors is high at around 80% (Pérez-Martínez, 2012). Several viral vectors including herpes simplex virus, adenovirus, lentivirus, and adeno-associated virus vectors have achieved gene transduction in the brain. The major concerns of using viral vectors are their safety issues and high cost. As viruses normally cannot cross the BBB by passive diffusion, invasive approaches such as stereotaxic injection and direct injection into the cerebrospinal fluid are needed for the delivery of viral vectors. These delivery methods are invasive to patients and can result in severe side effects (Dong, 2018).

Among the viral vectors developed, adeno-associated viral 9 (AAV9) is a promising one as it is well-tolerated and is able to cross the BBB through active transport while not damaging the integrity of the BBB (Bors and Erdő, 2019).

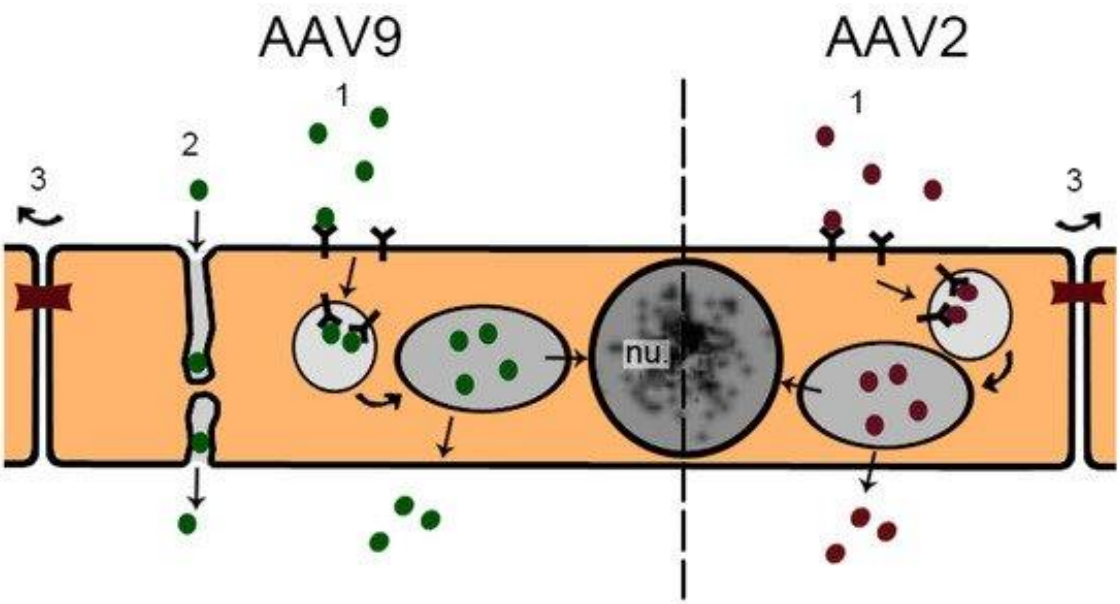

Figure 1-14 The transport of Adeno-associated viral 9 (AAV9) and adeno-associated viral 2 (AAV2) across the BBB. AAV9 can cross the BBB by active transport. AAV2 cannot cross the BBB by itself. It can be provided with a receptor for the ligand in order to use the receptor-mediated transport. The image was taken from (Bors and Erdő, 2019).

1.5.2.4 Nanoparticles

Nanoparticles are colloidal carriers which originated naturally or have been synthesised. Their sizes vary ranging from 1 nm to 1000 nm (Saraiva *et al.*, 2016). Nanoparticles offer several advantages for drug delivery across the BBB such as chemical and biological stability, flexibility to be administered via different routes and the capability of containing both water and lipid-soluble drug molecules. Nanoparticles have a large surface-area-to-volume ratio so they can also be conjugated with antibodies for targeted drug delivery. Commonly used nanoparticles include lipid-based nanoparticles (liposomes, solid lipid nanoparticles) and polymer-based nanoparticles (polymeric nanoparticles, polymeric micelles, dendrimers) (Masserini, 2013). Nanoparticles can cross the BBB through interendothelial diffusion, transcytosis and endocytosis. How a nanoparticle passes through the BBB is dependent on the design of its size, charge, and surface (Ceña and Játiva, 2018).

1.5.2.5 Drug delivery by adsorptive-mediated transcytosis

Adsorptive-mediated transcytosis (AMT) does not involve specific receptors but requires a net positive charge on the molecule to make it cationic, to allow interaction with negative charges on the cell surface binding sites. This interaction induces endocytosis and subsequent transcytosis (Hervé, Ghinea and Scherrmann, 2008). With the growing evidence of successful drug delivery across the BBB through cationic proteins and cell-penetrating peptides, adsorptive-mediated transcytosis has gained more attention in recent years. Cell-penetrating peptides are amphipathic. They can pass through cells without generating any cytolytic effects, so they can be used to deliver drugs without being effluxed by efflux transporters across the BBB (Chen and Liu, 2012). One of the examples of utilising AMT for drug delivery across the BBB is the synthesis of chimeric peptides (CP). CP can be used to deliver peptides across the BBB. CPs are composed by coupling a non-transportable peptide to a peptide through covalent binding that can transport across the BBB by receptor mediated-transcytosis or absorptive-mediated transcytosis. For example, β-endorphin can be coupled to cationised albumin via its disulfide linkage and get transported across the BBB through adsorptive-mediated transport (Pardridge, Kumagai and Eisenberg, 1987).

1.5.2.6 Drug delivery by receptor-mediated transcytosis

Drug delivery strategy using receptor-mediated transcytosis (RMT) involves the production of a complex between the drug of interest and a ligand or an antibody that can target an endogenous receptor at the BBB (Pulgar, 2019). Receptor-mediated transcytosis is an important pathway to enter the brain for peptides, including insulin and transferrin (Chen and Liu, 2012). Common targets for drug delivery via RMT include the transferrin receptor (TfR), insulin receptor (IR), low-density lipoprotein receptor (LDLR), FC5, Rabies Virus Glycoprotein among others (Lajoie and Shusta, 2015). An interesting example of drug delivery by RMT is ANG2002, a conjugate of Angiopep-2 and neurotensin. Neurotensin is a strong analgesic with limited ability to cross the BBB. However, combining neurotensin, with the brain delivery vehicle, angiopep-2 to form ANG2020 improves brain delivery by 10 fold. This is due to the interaction of Angiopep-2 with low-density lipoprotein receptor-related protein-1. (Demeule, Currie, *et al.*, 2008; Demeule, Régina, *et al.*, 2008; Demeule *et al.*, 2014). By developing a brain shuttle of an anti-Aβ antibody which binds to the TfR, the efficiency of the antibody targeting the β-amyloid in a mouse model of Alzheimer's was enhanced by 55 times (Niewoehner et al., 2014). Inhibitors of β-secretase and

γ-secretase APP processing enzymes for treating Alzheimer's disease have limited transport across the BBB. By developing an antibody that targets BACE1 (an inhibitor of the β-secretase), it reduced Aβ concentrations in vitro and in vivo of mouse brains (Atwal et al., 2011). IgG fusion protein can be used as Trojan horse to transport proteins across the BBB into brain. AGT-181 is an engineered protein against the human insulin receptor. It can be used to treat Hurler's Syndrome in humans. AGT-181 is currently studied in Phase II clinical trials by ArmaGen (Boado et al., 2009).

1.5.2.7 Target influx and efflux membrane transporters

Both influx and efflux membrane transporters can be targeted for drug delivery. As endogenous substances could pass through the BBB with the assistance of SLC transporters, the structure of a drug compound can be modified to mimic the substrates of SLC transporters. For example, levodopa used to Parkinson's disease is a prodrug of dopamine. Dopamine cannot cross the BBB while levodopa can pass the BBB through using an amino acid transporter (Oldendorf and Szabo, 1976). The limitation of this method is that the drug has to be a similar size and structure of the SLC transporter substrate (Patel and Patel, 2017).

For drugs that are substrates of efflux transporters at the BBB, a transporter inhibitor can be co-administered with substrate drugs. The third generation of P-gp inhibitors including tariquidar, zosuquidar, laniquidar, and ONT-093 have been used in chemotherapy regimens (Thomas and Coley, 2003). Co-administration of probenecid, an inhibitor of OAT, MRP, and OATP transporters, improved the distribution of cefadroxil in rat brains (Chen *et al.*, 2014)

1.6 Ion-pairing method for pentamidine

A drug can be paired with a counterion to form an ion pair. Ion-pair drugs are formed non-covalently by a positively charged therapeutic drug and a negatively charged counterion or a negatively charged therapeutic drug and a positively charged counterion. This ion-pairing method is a useful strategy to facilitate the delivery of ionised hydrophilic therapeutic drugs across biological membranes. The ion-pair formation could improve the lipid solubility of the therapeutic drug thereby enhancing its permeability across biological membranes (Neubert, 1989). At the molecular level, the positively charged group of the therapeutic drug is masked and coated by the hydrophobic group on the counterion through ion-pairing (Ristroph and Prud'homme, 2019).

The ion-paring method has advantages of improving the lipophilicity of drugs while not affecting their efficacies (Suresh and Paul, 2011a). For a therapeutic drug to be suitable for ion-paring, the drug needs at least one charged group on its structure, such as compounds with positively charged amine groups or negatively charged carboxylic acid groups at physiological pH. It is straightforward to pair with molecules with only positive or only negative charges. For a zwitterionic molecule with both positive and negative charges on its structure, ion-pairing could be complicated. One way to make it easier is to change the pH environment so that only one type of charge is shown. In addition to the charges on molecules, the charge density which is calculated by the charge per molecular weight would also affect ion-pairing. Normally, pairing a counterion with a single charged molecule with smaller molecular weight will be more effective than pairing the same counterion to a single charged molecule with an extremely large molecular weight (Ristroph and Prud'homme, 2019).

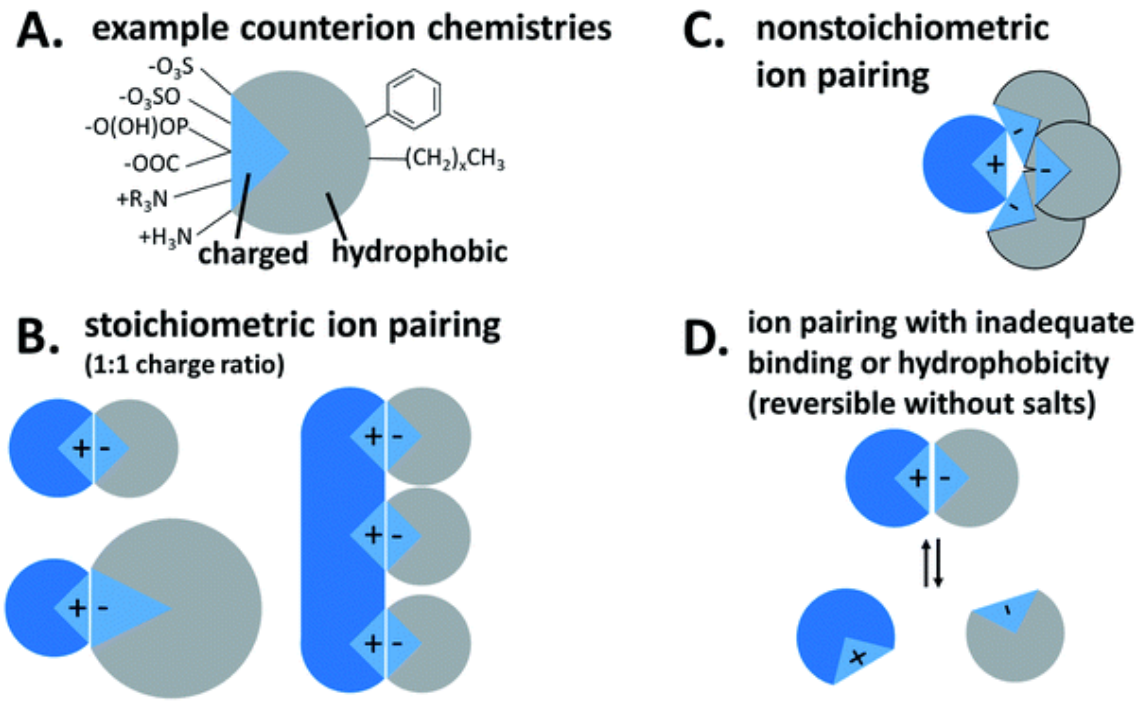

Figure 1-15 The concept of ion-pairing method. The image was taken from (Ristroph and Prud'homme, 2019). (A) Common charged groups (left) and hydrophobic moieties for counterions (B) Stoichiometry of ion pairs, 1:1 charge ratio (C) Non-stoichiometric ion pairing. (D) Reverse of ion-pairing with inadequate binding or hydrophobicity

The ion-pairing strategy has successfully improved delivery across transdermal, ocular, oral, parenteral and nasal routes (Suresh and Paul, 2011a). Tan (*et al.*, 2009) found that the permeation of glipizide across rat skin was enhanced by ion-pairing with amine counterions such as diethylamine and triethylamine. This study showed that ion-pairing was a useful method to enhance the skin permeation of glipizide. Miller (*et al.*, 2010) selected 1-hydroxy-2-naphthoic acid (HNAP) as the counterion to pair with the antiviral drugs, zanamivir heptyl ester and guanidino oseltamivir, and increased the log P of antiviral drugs by up to 3.7 log units. He also found that ion-pairs with stronger binding were more likely to be effective *in vivo*, as the rat jejunal of zanamivir heptyl ester-HNAP ion-pair with higher binding affinity had higher permeability than the guanidino oseltamivir-HNAP ion-pair with lower binding affinity.

Studies on ion-pairing had been focused on the physicochemical properties of drugs until the last decade. In recent years, the involvement of membrane transporters in the transport of ion pairs has been examined. ElShaer, Hanson and Mohammed (2014) found that the lipophilicity of indomethacin was increased by forming ion-pairs with the counterions, arginine and lysine, as measured by octanol-water partitioning. An *in vitro* study on Caco-2 monolayers revealed that the transcellular uptake of indomethacin was saturable when counterions were present, with the

highest accumulation being observed at the 60-min time-point. This suggested a transporter could be involved, although the specific transporter was not identified. Benaouda (*et al.*, 2018) showed that theophylline ion-pairing with a polyamine transporter system substrate spermine could increase theophylline delivery to the lungs. A 3.6-fold increase in the accumulation of theophylline in lungs was observed after vascular administration by ion-pairing theophylline with spermine. She also suggested that the ion-pair formation could change dramatically with pH as the ion-pair dissociated completely when the pH dropped from 9.6 to 7.4 according to *in silico* simulation.

In this study, we selected pentamidine as a drug for reformulation. Pentamidine has pK_{d1} and pK_{d2} of 12.13 and 11.53 (MarvinSketch version 17.28, ChemAxon). It can be classed as a strong basic and has two positive charges at physiological pH. The two amidine groups on pentamidine have the potential to pick up protons from acids in solutions, which makes pentamidine an ideal drug candidate for the ion-pairing method.

1.7 Summary

- Pentamidine is a safe and effective drug for treating sleeping sickness. However, it cannot be used for the late-CNS stage of HAT due to its inability to cross the BBB.
- Ion-pairing method is a cost-effective and non-invasive method to improve drug transport across biological membranes. This method, however, has not previously been used to improve drug delivery across the blood-brain barrier.

The physicochemical characterisation of pentamidine ion-pairs will be discussed in Chapter 2. In Chapter 3 and Chapter 4, we will examine the influence of OCT1 and P-gp, respectively on the transport of pentamidine ion-pairs. In chapter 5 we will have a general discussion of the PhD project.

1.8 General aim and hypothesis of this PhD project

The aim of this study was to investigate if reformulating pentamidine with a counterion to form an ion pair would improve the ability of pentamidine to cross the BBB by passive diffusion and/or by interaction with specific transporters (i.e. hOCT1 and P-gp). There were three hypotheses tested in this project:

1. The passive diffusion of pentamidine across the blood-brain barrier is improved by ion pairing.
2. The ion-pairing of pentamidine increases the transport of pentamidine by hOCT1.
3. Pentamidine ion-pairs inhibit the efflux of pentamidine by P-gp transporter expressed at the blood-brain barrier.

The three hypotheses are addressed in Chapters 2, 3 and 4 of this thesis, respectively.

Chapter 2 Physicochemical Characterisation of Pentamidine Ion-pairs

2.1 Chapter overview

In this chapter, we will discuss the selection of counterions to form ion pairs with pentamidine to improve the delivery of pentamidine to the CNS and examine the specific physicochemical characteristics of the pentamidine ion-pairs by various methods.

2.2 Introduction

Physicochemical properties are crucial in predicting the pharmacokinetics process, which involves Absorption, Distribution, Metabolism, Elimination and Toxicity (ADMET) of compounds. The understanding of physicochemical properties of molecules, including lipophilicity, molecular weight (MW), hydrogen bonding and charges enables scientists to develop drugs with high efficacy and minimal side effect. Drugs with optimal ADMET properties are potent molecules that can reach target tissues selectively with adequate concentrations (Guan *et al.*, 2019).

2.2.1 Physicochemical characteristics for drug development

2.2.1.1 Lipophilicity

One of the most important physicochemical characteristics is lipophilicity. Lipophilicity reflects the ability of compounds to permeate from the aqueous phase to the organic phase and thus serves as an indicator for passive transport of drugs across lipid membranes. Lipophilicity is often measured by partition coefficient (log P) for unionised compounds, or by distribution coefficient (log D) for pH-dependent ionised solutes between octanol and water using the shake-flask method (Arnott, Kumar and Planey, 2013). According to literature reviews, compounds with a log P at 1-3 have optimal ADMET properties. Therefore they are more likely to progress through the different stages of the drug development process (Lipinski *et al.*, 2001; Gleeson, 2008; Waring, 2010). Compounds with too low log P values often have poor ADMET; If the lipophilicity of a compound is too high (log P > 5), it will have poor solubility, a higher chance of eliciting toxicity, and poor clearance (Arnott, Kumar and Planey, 2013).

2.2.1.2 Molecular Weight

Drugs with molecular weight > 500 Da generally have poor absorptions, according to the “Rule of Five” (Lipinski *et al.*, 2001). It was found that the permeation of drugs at the blood-brain barrier decreased 100-fold when the molecular weight increased by 150 Da from 300 Da (Pardridge, 2012).

2.2.1.3 Hydrogen bonding

Hydrogen bonding reflects the water solubility of molecules. The higher the number of hydrogen bonds, the lower the membrane permeability. It has been shown that an increase of one pair of hydrogen bonds will decrease membrane permeability 10 fold (Pardridge, 2012). Lipinski (et al., 2001) suggested that the drug membrane permeation was poor when hydrogen accepter count was > 10, or hydrogen donor count was >5. It was also found that the central nervous system active drugs had less than 7 hydrogen bonds when dissolved in water (Ajay, Bemis and Murcko, 1999).

2.2.1.4 Charges

The charge state of a molecule influences the absorption of drugs across membranes. For drugs that can successfully pass through the blood-brain barrier (BBB), most of them have one positive charge at pH 7-8. Many CNS drugs share a common tertiary nitrogen on their structure which allows them to be positively charged at physiological pH environment (Clark, 2003). As brain endothelial cells have a negatively charged glycocalyx (Ribeiro *et al.*, 2012), drugs molecules with one positive charge at physiological pH are facilitated across the BBB as their charges are neutralised when they cross the BBB. Molecules that are classed as a strong base or as a strong acid have a limited ability to cross the BBB (Pajouhesh and Lenz, 2005). The charge state of drugs could be predicted by its dissociation constant pK_d (Avdeef, 2012). It was found that successful CNS drugs have a pK_d value at 4-10 (Fischer, Gottschlich and Seelig, 1998).

2.2.2 Pentamidine ion-pairing strategy

In this study, we selected pentamidine as a drug for reformulation. Pentamidine is an aromatic diamidine and has been used for treating early-stage of *gambiense* HAT since the 1940s (Yang *et al.*, 2014). Pentamidine has pK_{d1} and pK_{d2} of 12.13 and 11.53 (MarvinSketch version 17.28, ChemAxon). It has a molecular weight of 340.19 g/mol. It can be classed as a strong base and has two positive charges at physiological pH (See Table 2-1 for pentamidine structure and characteristics). The two amidine groups on pentamidine have the potential to pick up protons from acids in solutions, which makes pentamidine an ideal drug candidate for ion-pairing method.

In this study, we tested the hypothesis that a -1 charged counterion can bind to the +2 pentamidine and form a +1 charged ion-pair and in doing so make pentamidine more lipophilic and more likely to be transported across the BBB by passive diffusion.

2.2.2.1 Counterions for pentamidine ion-pairs

We selected four counterions which have -1 charge at pH 7.4. They included taurodeoxycholate, octanoate, quercetin and xinafoate. They are described in more detail in the following section and their physicochemical properties are summarized in Table 2.1.

(1) Taurodeoxycholate: is an anionic bile salt and has been used to treat multiple diseases such as neurological disorders (Gronbeck *et al.*, 2016), ocular diseases (Boatright *et al.*, 2009), regulate apoptosis (Amaral *et al.*, 2009) and relieve inflammation in throat (Wang and Carey, 2014). Taudeoxycholate has previously been used for ion-pairing. For example, Lee (*et al.*, 1988) used taurodeoxycholate to pair with isopropamide iodide. The partition coefficient of isopropamide iodide which was measured using the n-octanol and phosphate buffer shake flask method at pH 7.4 was improved through ion-pairing with isopropamide iodide. The octanol-phosphate buffer (pH 7.4) shake flask method was also used to confirm the increased partition coefficient of methylene blue with sodium taurodeoxycholate (Shim 1986). Also, when sodium taurodeoxycholate with methylene blue was infused into rats, the systemic distribution of methylene blue in the whole blood of rats was increased.

(2) Octanoate (octanoic acid), also called caprylic acid: has been found in coconut, babassu and milk fat (Beare-Rogers, Dieffenbacher and Holm, 2001). It has been proven to be a cheap option

to treat frequent urination. It also has the potential to treat infections, ageing and cancer (Omura *et al.*, 2011). Salbutamol is a beta$_2$-adrenergic receptor antagonist to treat asthma and chronic obstructive pulmonary disease. It is rapidly eliminated after being administered, so patients have to take it several times a day. Octanoate has been explored as a counterion for the ion-pair drug delivery of salbutamol to the lung. The ion-pair formation of salbutamol-octanoate has been confirmed by Fourier Transformed infra-red spectroscopy. In vivo study indicated that ion-pairing salbutamol with octanoate could prolong half-life by extending the duration of salbutamol to stay in the lung (Dutton, 2018).

(3) Quercetin: is a natural flavonoid that has been found extensively in vegetables, fruits, and herbs. It has been used to treat rheumatoid arthritis and reduce the risk of infections (Davis, Murphy and Carmichael, 2009; Ji *et al.*, 2013). Quercetin is also an anticancer agent as it can suppress cyclin-dependent kinases, induce apoptosis, inhibit enzymes that cause carcinogenesis, modify signal transduction pathways, among others (Pangeni *et al.*, 2018).

(4) Xinafoate (1-hydroxy-2-naphthoic acid): has been used to form a salt with salmeterol, a beta-adrenergic agonist, for chronic obstructive pulmonary disease. This salt form can improve the lipophilicity of salmeterol and extend the time at the site of action (Ticehurst and Marziano, 2015; Gupta *et al.*, 2018). Xinafoate has also been used for ion-pairing with antivirals which have poor oral absorption and limited intestinal permeability. It was found that the use of xinafoate to form ion-pairs with two antiviral compounds heptyl ester and guanidino oseltamivir could enhance their lipophilicity (log P) by up to 3.7 log units. In addition, the permeability of heptyl ester and guanidino oseltamivir across Caco-2 cell monolayers was enhanced by the increasing concentration of xinafoate (Miller *et al.*, 2010). (Patel *et al.*, 2016) found salbutamol-xinafoate ion-pairs exhibit significant bronchodilator effect compared to salbutamol base. When salbutamol-xinafoate ion-pair was tested on guinea pig tracheal parts, a faster ($p<0.05$) distribution rate was observed than salbutamol alone.

Table 2-1. Molecular weight, log D, log P, charge and structures of pentamidine and selected counterions

Compound	MW (g/mol)	*Predicted Log D, pH 7.4	*Predicted Log P	Charge, pH 7.4	Structure
Pentamidine	340.4	-2.50	2.32	+2	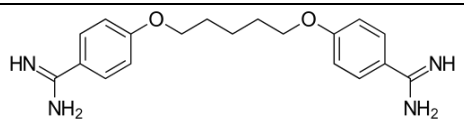
Taurodeoxycholate	521.7	2.23	2.33	-1	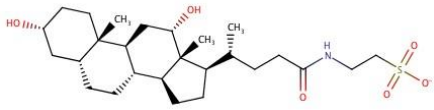
Octanoate	166.2	2.70	2.70	-1	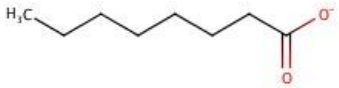
Quercetin	302.2	2.16	2.16	-1	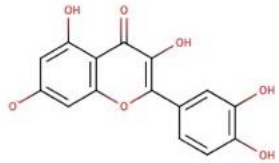
Xinafoate	188.2	2.97	2.97	-1	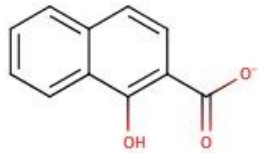

*Log D and Log P were predicted using MarvinSketch (version 17.28, ChemAxon)

The hypothesis of this chapter is that the passive diffusion of pentamidine across the blood-brain barrier is improved by ion pairing. The aim of this chapter is to examine the physicochemical properties of pentamidine ion-pairs. The specific objectives are as follows:

- To measure the lipophilicity (Log D) of pentamidine alone and when bound to a counterion (i.e. the ion-pair) by shake-flask and fluorescence methods;
- To investigate the binding site of the counterion with pentamidine with ^{13}C-NMR and ^{1}H-NMR by assessing the chemical shift of H and C assigned to pentamidine in the presence of counterions;
- To determine the association constants (binding constants, pK_a) of pentamidine ion-pairs using HPLC and fluorescence methods;
- To estimate the percentage of pentamidine (%) bound with counterions (taurodeoxycholate, octanoate and xinafoate) in solutions using Hyperquad Simulation and Speciation (HySS) software;
- To further confirm the presence of pentamidine ion-pairs and understand the dissociation (pK_d) of pentamidine ion-pairs with fluorescence-lifetime imaging microscopy (FLIM).

2.3 Materials and methods

2.3.1 Materials

Pentamidine isethionate (>=98%), xinafoate (1-Hydroxy-2-naphthoic acid) (>=97.0%), Dimethyl sulfoxide-d6 (>=99.9 atom % D), sodium chloride (>=99.5%), phosphoric acid (ACS reagent, >=85%, wt % in H_2O) were purchased from Sigma-Aldrich (Dorset, UK), sodium octanoate (>=99.0%), quercetin (>=95.0%), sodium taurodeoxycholate hydrate (>=95.0%) were from Sigma Life Science, deuterium Oxide (>=99.90%) was purchased from Fluorochem Ltd (Derbyshire, UK), DAPI (hydrochloride) was purchased from Cayman Chemical (Cambridge, UK). Tris base (for Molecular Biology) was purchased from Fisher Scientific (New Jersey, US). 1-Octanol (99%, pure) was purchased from Acros Organics UK. Potassium phosphate monobasic for HPLC (>=99.5%), hydrochloric acid (p.a.>=32%), sodium hydroxide standard solution (1.001 mol/L) were purchased from Fluka, Japan. Acetonitrile (>=99.9%) was purchased from Honeywell Riedel-de Haen, Germany.

Table 2-2 Concentrations of pentamidine used in different methods

Methods	Concentrations of pentamidine
HPLC calibration curves	0 - 168.9 μM
Chemical stability by HPLC	0 - 168.9 μM
*Octanol-saline shake-flask	*Pentamidine was used at two concentrations depending on the solubility of the counterion. 33 μM of pentamidine was used with taurodeoxycholate and octanoate and 8 μM of pentamidine was used for quercetin and xinafoate. The molar ratios of pentamidine: counterion are 1:0 - 1:20
Fluorescence	Pentamidine was utilised at a concentration of 8 μM for xinafoate
NMR	Pentamidine was utilised at a concentration of 11.2 mM for xinafoate
HySS	Pentamidine was set at 9 nM, 8 μM, or 8 mM with equal or 20 times molar ratio of each counterion
FLIM	The concentration of pentamidine was 8 mM or 8 μM with 20 times molar ratio of xinafoate

* The solubility of the counterions was estimated by dissolving each of the counterions in saline and then increasing the amount of counterions gradually until sediment was visually seen in the solution.
* Quercetin and xinafoate have limited solubility (< 200 μM) in saline, therefore, the concentrations of quercetin and xinafoate utilised were 8 - 160 μM, which were much lower than taurodeoxycholate and octanoate (33 - 660 μM) used in the octanol-saline shake-flask method.
* In order to compare the results, the concentrations of pentamidine were 1/20 - 1 folds of the molar concentration of each counterions. So, 33 μM of pentamidine was used with taurodeoxycholate and octanoate and 8 μM of pentamidine was used for quercetin and xinafoate.

2.3.2 High Performance Liquid Chromatography (HPLC) analysis of pentamidine

Pentamidine was quantified isocratically by HPLC (Spectra-Physics P4000 Quaternary Pump, Waters™ 996 Photodiode Array Detector, Waters 717plus Auto Sampler) with an μBondapak C18 Column (Waters, 3.9 mm X 300 mm). The mobile phase consisted of 0.025M monobasic potassium phosphate and acetonitrile (76%:24%, v/v; pH 3.2 regulated by phosphoric acid). The solution was filtered through a 0.45 μm pore size membrane filter (Hewlett Packard®, Germany) and then degassed by sonication. The flow rate was set at 1 ml/min. The UV determination wavelength was set at 264 nm. The injection volume was 50 μl. The experiment was conducted at room temperature (around 20 °C). The running time was 10 mins for each injection.

In order to evaluate the suitability of HPLC method for the quantification of pentamidine in the following saline-octanol shake flask method, pentamidine standard solutions in different concentrations ranging from 2 µg/ml (3 µM) to 100.0 µg/ml (168.9 µM) were prepared in mobile phase and in physiological saline saturated with octanol. The samples were measured in triplicates by HPLC. Then a calibration curve was generated by plotting the peak area from HPLC (y-axis) against the concentrations of pentamidine. The results were fit into a regression model in GraphPad7, where an equation for the relationship between peak area and concentrations of pentamidine, and R-squared value were acquired. The Limit of Detection (LOD), the Limit of Quantification (LOQ) were calculated using the following equations:

$$LOD = \frac{3.3\,\sigma}{S} \qquad \text{(Equation 2-1)}$$

$$LOQ = \frac{10\,\sigma}{S} \qquad \text{(Equation 2-2)}$$

In the above equations, σ and S represent the standard deviation of the response and the slope of the calibration curve, respectively.

The coefficient of variance (CV) was calculated as follows:

CV% = 100% * standard deviation of peak area / mean of peak area (Equation 2-3)

2.3.3 Chemical stability of pentamidine solutions

The standard pentamidine solutions (5.88 µM - 293.75 µM) in HPLC capped vials were kept at both room temperature and 37°C water bath. After 2, 7, 14 and 28 days, the concentrations of pentamidine in these samples were measured in triplicates by HPLC as described in 2.3.2. Data were analysed by two-way ANOVA with GraphPad 7. Results were compared to the initial concentrations of pentamidine (control) and expressed as a percentage of recovery:

Recovery (%) = Pentamidine $Conc_{(t)}$ / Pentamidine $Conc_{(Initial)}$, where $_{(t)}$ is sampling times at 2, 7, 14, 28 days (Equation 2-4)

2.3.4 Octanol-saline shake flask method

2.3.4.1 Ion-pairing theory

Miller (et al., 2009) established the quasi-equilibrium mass transport analyses for hydrophobic molecules in octanol-buffer shake-flask method. Based on his theory, we assume that pentamidine and the counterion could form ion-pairs in the aqueous phase (saline) and these ion-pairs are in equilibrium with pentamidine and the counterion alone (Figure 2-1). Also, it is assumed that the pentamidine in the organic phase (octanol) exists in the form of ion-pairs only, since the free pentamidine in octanol is very limited due to its poor lipophilicity.

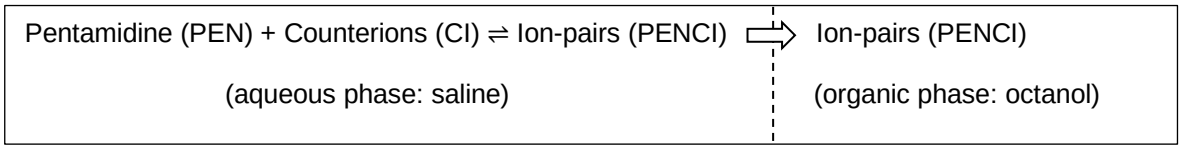

Figure 2-1 The equilibrium of pentamidine, counterions and ion-pairs in octanol and saline.

The logarithm distribution coefficient (Log D) of pentamidine can be calculated as follows:

$$\text{Log D} = \text{Log}\left[([\text{PEN}]_{\text{In}} - [\text{PEN}]_{\text{aq}}) / [\text{PEN}]_{\text{aq}}\right] \qquad \text{(Equation 2-5)}$$

$[\text{PEN}]_{\text{In}}$ represents the initial concentrations of pentamidine added to the octanol-saline system; $[\text{PEN}]_{\text{aq}}$ stands for the total concentration of pentamidine in the aqueous phase. The result of $([\text{PEN}]_{\text{In}} - [\text{PEN}]_{\text{aq}})$ is the concentration of pentamidine in octanol. The $[\text{PEN}]_{\text{aq}}$ is measured by HPLC following the shake-flask method. HPLC is a precise, convenient and well-established method. However, the limitation of using HPLC in this study is that it can only detect free pentamidine rather than pentamidine ion-pairs in the aqueous phase saline.

2.3.4.2 Shake-flask method

In order to determine the lipophilicity of pentamidine and pentamidine ion pairs, the shake-flask method was utilised. 2 ml of 0.9% saline (pH=7.4) was pre-saturated with 2 ml of octanol for 48 hs before experiments. Pentamidine and the counterions were dissolved in 2 ml of octanol saturated saline (pH 7.4) at the following molar ratios: 1:0, 1:1, 1:2, 1:4, 1:8, 1:12 and 1:20. The pentamidine concentration was 20 µg/ml (33 µM) for ion-pairing with taurodeoxycholate and octanoate, or 5 µg/ml (8 µM) for pairing with xinafoate and quercetin. The ion-pairs in pre-saturated saline solutions were equilibrated with an equal volume of pre-saturated octanol at 37 °C shaker for 24 hs. After the equilibrium, the bottom aqueous layer was carefully extracted by a fine tip glass pipette and measured by HPLC. Each sample was measured by HPLC for three times. The concentration in the octanol layer was calculated by mass balance method. Then the

distribution coefficient of pentamidine (Log D) was calculated as Equation 2-5 by dividing the concentration of pentamidine in the octanol phase by the concentration in the aqueous phase, saline, and converted to the logarithm. The experiments were repeated (n=3) and results were expressed as the mean ± standard deviation.

2.3.5 ^{1}H NMR and ^{13}C NMR spectroscopy

Nuclear magnetic resonance (NMR) can provide information on the binding sites of pentamidine with the counterion to form the ion pair. Since xinafoate has the largest predicted Log P value among the four counterions, it was selected as a template compound in the NMR method to study pentamidine ion-pairs. NMR spectra were measured by Bruker AscendTM 400 MHz Spectrometer at 298.0 K. Data were processed and analysed by TopSpin 3.5pl7 software. Samples were loaded into the Wilmad® 5 mm Thin Wall Precision NMR tubes. The chemical shifts were relative to the DMSO residual signal at 2.5 ppm for ^{1}H-NMR and at 39 ppm for ^{13}C-NMR.

The concentration of pentamidine was 11.2 mM with or without equal or 20 times molar ratios of xinafoate. Xinafoate has very low solubility in pure D_2O. Only 228.7 mg/l xinafoate can dissolve in water at 25°C. Therefore, DMSO-d6 and mix solution of DMSO-d6 and D_2O (1%) were used as the solvent instead. This allows us to determine if there were the differences in the pentamidine spectra with the presence of water. A volume of 700 µl for each sample was loaded into NMR tubes for detection.

2.3.6 Fluorescence spectroscopic characterisation of ion-pairs

2.3.6.1 Method validation for DAPI and Pentamidine

The NMR study described above revealed that the amidine groups on pentamidine interacted with the counterion, xinafoate. In order to confirm the binding sites and to determine the binding constants of pentamidine - xinafoate ion-pairs, both DAPI (4′,6-diamidino-2-phenylindole) and pentamidine were used to form an ion-pair with xinafoate for the fluorescence study. DAPI (4',6-diamidino-2-phenylindole) has been used as a useful DNA-specific fluorescent probe for decades (Kapuscinski, 1995). It has a similar structure as pentamidine with two amidine groups and +2 charges at physiological pH 7.4 (Figure 2-2).

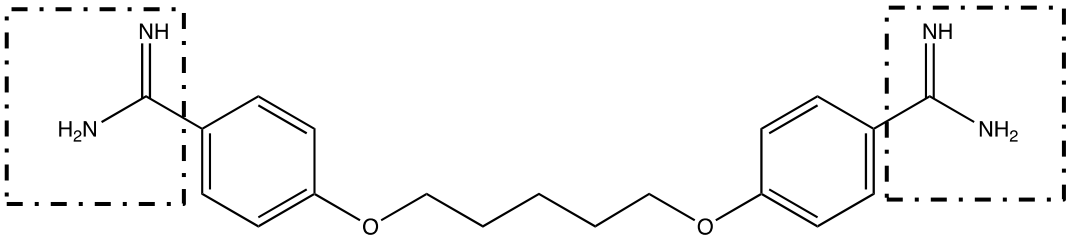

(Pentamidine)

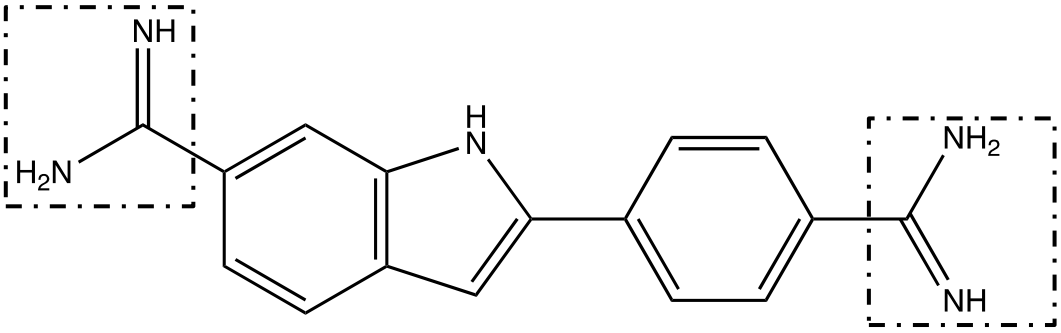

(DAPI)

Figure 2-2 Chemical structures of pentamidine and DAPI. The two amidine groups are highlighted in the figures.

The fluorescence intensity of DAPI and pentamidine was measured by Cary Eclipse fluorescence spectrophotometer with Hellma® fluorescence ultra-micro cuvette (path length 3x3 mm) with a 200-2500 nm spectra range. Samples were dissolved in 50 nM Tris-buffer at pH 7.4. Each sample's pH was checked by Hanna Checker pH Meter and regulated at 7.4 for measurement.

DAPI was excited at 358 nm and the maximum emission was at 461 nm. The excitation slit and emission slit were set at 5 nm. The scan rate was set at 600 (nm/min) with averaging time at 0.1 s and data interval at 1.0 nm. The detector voltage was set at 800 v. Pentamidine was excited at 270 nm and its maximum emission was at 340 nm. The excitation slit and emission slit were set at 5 nm. The scan rate was set at 120 (nm/min) with an averaging time of 0.5 s and 1 nm data interval. The detector voltage was set at 800 v. Standard solutions (2-10 μg/ml) of DAPI and pentamidine were prepared and calibration curves were plotted using the maximum fluorescence intensity against the concentrations of drugs. The R-squared value, Limit of Detection (LOD) and Limit of Quantification (LOQ) were acquired by regression analysis.

2.3.6.2 Fluorescence quenching in the presence of xinafoate

DAPI was utilised as an alternative for pentamidine in order to confirm the binding of amidine groups with xinafoate. The fluorescent intensity for a concentration of 4 μg/ml (11.4 μM) DAPI in 50 nM Tris buffer (pH 7.4) was measured with equal and 20 times molar ratios of xinafoate at 358 nm excitation wavelength. The concentration of pentamidine in 50 nM Tris buffer was 8 μM with different molar ratios (1:2,1:4, 1:6, 1:8, 1:16,1:20) of xinafoate at pH 7.4. The sample was excited at 270 nm and the maximum emission intensity of pentamidine was measured.

2.3.7 Binding constants of pentamidine ion-pairs

The binding constants here measure how tightly pentamidine is bound to each of the counterions. The binding constants (pK_a) of ion-pairs were generated by (a) HPLC and (b) fluorescence spectroscopy. As pentamidine has two amidine groups which could allow it to bind to one or two -1 charged counterion, both 1:1 and 1:2 stoichiometries were assumed:

$$PEN + \alpha Cl \rightleftharpoons PEN \bullet Cl \qquad \text{(Equation 2-6)}$$

where α=1 or 2; PEN, Cl, PEN•Cl represents pentamidine, counterion, pentamidine ion-pair complex.

2.3.7.1 The binding constants of pentamidine-taurodeoxycholate, pentamidine-octanoate, pentamidine-xinafoate, and pentamidine-quercetin ion-pairs determined by HPLC

The percentage bound of pentamidine with different molar ratios of counterions was estimated based on the lipophilicity (distribution coefficients) of pentamidine determined by HPLC. It is assumed that the two potential binding sites on pentamidine are fully bound when there are 20 times molar ratio of counterions in the solution.

The percentage bound of pentamidine:

$$PEN_{BOUND}\% = (LogD_1 - LogD_0) * 100\% / (LogD_{20} - LogD_0) \quad \text{(Equation 2-7)}$$

where $LogD_1$ represents the logarithm distribution coefficients of pentamidine with different molar ratios of counterions (1:1,1:2, 1:4, 1:8, 1:12, 1:20), $LogD_0$ represents the logarithm distribution coefficients of pentamidine without any counterion, $LogD_{20}$ represents the logarithm distribution coefficient of pentamidine with 20 molar ratios of counterions.

To calculate the percentage bound of counterions to pentamidine:

(a) under the 1:1 stoichiometry assumption,

$$CI_{Bound}\% = PEN_{Bound}\% \quad \text{(Equation 2-8)}$$

(b) under the 1:2 stoichiometry assumption,

$$CI_{Bound}\% = PEN_{Bound}\% / 2 \quad \text{(Equation 2-9)}$$

where $PEN_{Bound}\%$ and $CI_{Bound}\%$ represent the percentage bound of pentamidine and percentage bound of counterions, respectively.

Then the free unbound concentrations of counterions are calculated by subtracting the counterions bound to pentamidine:

$$[CI]_{free} = [CI]_{Initial} * (1 - CI_{Bound}\%) \quad \text{(Equation 2-10)}$$

where $[CI]_{Initial}$ is the initial concentration of counterions added in the solution and $CI_{Bound}\%$ is the percentage bound of counterions.

Then the percentage bound of pentamidine ($PEN_{Bound}\%$) and the concentrations of free unbound counterions ($[CI]_{free}$) were fit into the Sigmoidal model where the binding constants of pentamidine-counterion ion pairs were generated.

2.3.7.2 Fluorescence binding studies of pentamidine - xinafoate ion pairs

The percentage bound of pentamidine with different molar ratios of xinafoate was calculated based on the change of fluorescence intensity of pentamidine with xinafoate. It is assumed that pentamidine is fully bound when there is 20 times molar ratio of counterions in the buffer.

The percentage binding of pentamidine:

$$PEN_{Bound}\ \% = (I_0 - I_1) * 100\% / (I_0 - I_{20}) \qquad \text{(Equation 2-11)}$$

where I_0 represents the fluorescence intensity of pentamidine without xinafoate, I_1 represents the fluorescence intensity of pentamidine with certain molar ratios (1, 2, 4, 8, 12, or 20) of xinafoate, I_{20} represents the fluorescence intensity of pentamidine with 20 molar ratios of xinafoate.

The percentage binding of counterions was calculated by Equations 2-8, 2-9. The free unbound concentrations of xinafoate are calculated by subtracting the counterions bound to pentamidine:

$$[CI]_{free} = [CI]_{Initial} * (1 - CI_{Bound}\%) \qquad \text{(Equation 2-12)}$$

where $[CI]_{Initial}$ is the initial molar concentration of xinafoate added in the solution and $CI_{Bound}\%$ is the percentage bound of xinafoate

Then the percentage bound of pentamidine ($PEN_{Bound}\%$) and the concentrations of free unbound counterion xinafoate ($[CI]_{free}$) were fit into Sigmoidal model in GraphPad 7 to calculate the binding constants of pentamidine-xinafoate ion pairs.

2.3.8 Hyperquad Simulation and Speciation (HySS)

The percentage of pentamidine bound with the selected counterions (taurodeoxycholate, octanoate and xinafoate) in the various physiological compartments was predicted using Hyperquad Simulation and Speciation (HySS2009, Protonic Software), a computer programme for titrations and speciation (Alderighi *et al.*, 1999). This software has been developed for the determination of stability constants and is a powerful tool to estimate ratios of multiple microspecies when complexes are formed in solutions. For example, Benaouda (et al., 2018) estimated the microspecies of spermine-theophylline ion-pair complexes for drug delivery to the lungs. Fazary & Ramadan (2014) utilised HySS to gain equilibria information on complexes of metal ions with vitamin B9 and glycine.

The HYSS computer program requires the following information: the pH range used for determination of microspecies, knowledge of the molar concentrations and molar ratios of pentamidine to counterion, and binding constants for each pentamidine-counterion complex.

2.3.8.1 Pentamidine: counterion ion-pair complexes

For the purposes of our study, microspeciation was determined over the pH range of 2-12. Pentamidine concentration was set at 9 nM or 8 µM, while the concentrations of taurodeoxycholate, octanoate, xinafoate were set at equal (i.e. 1:1 molar ratio) and 20 times molar ratios of pentamidine (i.e. 1:20 molar ratio). The counterions were assumed to bind with pentamidine at 1:1 molar ratio to one of the amidine groups of pentamidine. Binding constants were determined experimentally by HPLC for each pentamidine-counterions complex (Section 2.3.7.1).

In order to utilise the HySS software for simulations, three requirements need to be met and they are: (1) A chemical model needs to be hypothesised. (2) The logarithms of the overall stability constants (log β) of the complexes and any micro-species formed need to be determined. (3) The experimental procedure needs to be defined (Alderighi *et al.*, 1999). As for the pentamidine complexes in our study, our assumptions for each requirement are explained as follows:

(1) Requirement 1: A chemical model needs to be hypothesised.

For the pentamidine ion-pairs, we assumed that one 2+ ionised pentamidine (PENH2) bound to one negatively charged counterion (CI) and formed an ion-pair (PENCIH2) at pH 7.4. In addition to the ion-pair complexes (PENCIH2) in solution, the +2 ionised pentamidine (PENH2) self-dissociates and exists in the forms of +1 ionised pentamidine (PENH) and uncharged pentamidine (PEN). Therefore, the stepwise association equilibria of pentamidine ion-pairs at pH 7.4 are as follows:

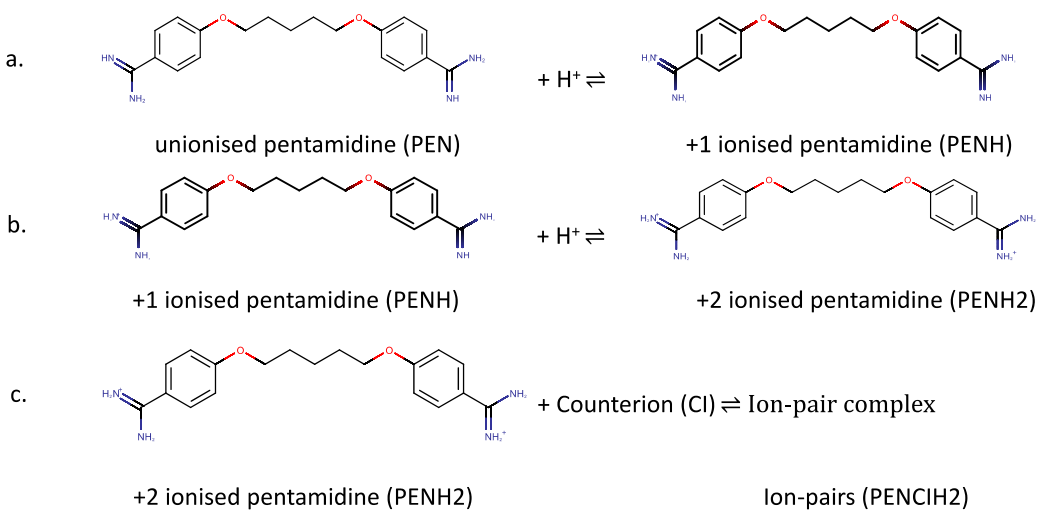

Figure 2-3 The stepwise association equilibria of pentamidine ion-pairs. (a). Unionised pentamidine (PEN) and one proton from water form into +1 ionised pentamidine (PENH). The association constant (K_{a1}) of this step Ka1=(PENH)/[(PEN)x(H)]. (b). The +1 ionised pentamidine (PENH) further binds with one proton from water and then forms into +2 ionised pentamidine (PENH2). Its association constant K_{a2}=(PENH2)/[(PENH)x(H)]. (c). The +2 ionised pentamidine (PENH2) further binds to negatively charged counterions (Cl) and become ion-pair complex (PENClH2). The association constant K_{a3}=(PENClH2)/[(PENH2)x(Cl)].

Thus, it is assumed that pentamidine exists in four microspecies in solution (i.e. unionised pentamidine (PEN), +1 ionised pentamidine (PENH), +2 ionised pentamidine (PENH2) and pentamidine ion pair (PENClH2). The association constant (K_a), or binding constant, is a special form of the dissociation constant (K_d), a measure of the strength of an acid in solutions, and has an inverse relationship with dissociation constants of complexes.

The pK_d values are the logarithm of dissociation constant ($pK_d = -\log_{10}K_d$). The higher the pK_d, the stronger the base is. For the pentamidine, its self-dissociation pK_{d1} (i.e. 12.13) and pK_{d2} (i.e. 11.53) in solutions are known values acquired from MarvinSketch (version17.28, ChemAxon), as shown at the two amidine groups of pentamidine in the figure below. Therefore, the amidine group with 12.13 pK_d has a higher binding affinity with counterions in solutions. The 3-D structures of pentamidine and taurodeoxycholate, octanoate, and xinafoate are shown in the discussion section of this chapter.

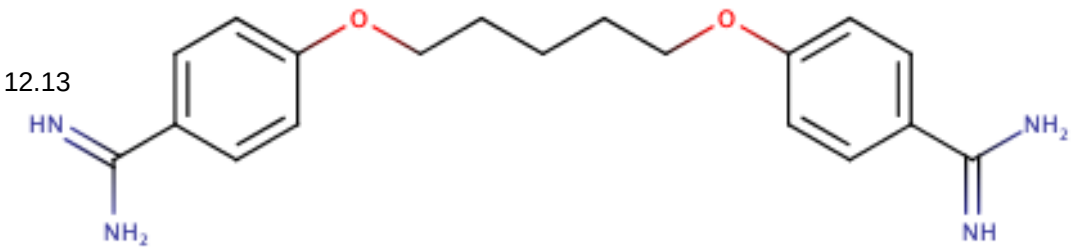

Figure 2-4 The self-dissociations of pentamidine in water. The pK_{d1} and pK_{d2} of the two amidine groups on pentamidine are 12.13 and 11.53, respectively.

(2) Requirement 2: The logarithms of the overall stability constants (log β) of the complexes and any micro-species formed need to be calculated or determined.

For HySS simulation, the logarithms of the overall stability constants (log β) are required for the HySS software. From the three equilibria (a) (b) and (c) in Figure 2-3, we can deduct the logarithms of the overall stability constants (log beta also called log β). And then the logarithms of the overall stability constant (log β_1) of +1 ionised pentamidine (PENH) from unionised pentamidine (PEN) and a proton (H^+) is calculated by Equation 2-13, the logarithms of the overall stability constant (log β_2) of +2 ionised pentamidine (PENH2) from unionised pentamidine (PEN) and two protons (H^+) can be calculated by Equation 2-14, and the logarithms of the overall stability constant (log β_3) of pentamidine ion-pairs (PENCIH2) from unionised pentamidine (PEN) and two protons (H^+) and counterions (Cl) can be calculated by Equation 2-15.

$\log \beta_1 = pK_{a3} = 12.13$ (Equation 2-13)
$\log \beta_2 = pK_{a3} + pK_{a2} = 12.13 + 11.53 = 23.65$ (Equation 2-14)
$\log \beta_3 = pK_{a3} + pK_{a2} + pK_{a1} = 12.13 + 11.53 + pK_{a1}$ (Equation 2-15)

In the above equations, log β_1, log β_2, log β_3 represent the logarithms of the overall stability constants (log β) of +1 ionised pentamidine (PENH), +2 ionised pentamidine (PENH2), and pentamidine ion-pairs (PENCIH2). pK_{a1}, pK_{a2}, pK_{a3} are the logarithm of binding constants of +1 ionised pentamidine, +2 ionised pentamidine and pentamidine ion-pairs, respectively.

For the pentamidine ion-pairs, the binding constants of pentamidine ion-pairs (pK_{a3}) were determined by octanol-saline shake-flask experiments and HPLC analysis, as described in section 2.3.7.1.

The $\log \beta_1, \log \beta_2, \log \beta_3$ were then inputted in the HYSS software, as shown in Figure 2-5. The Log Beta for PENH, PENH2, H_{-1} is the same for different counterions, while the PENCIH2 is calculated by Equation 2-15. H_{-1} represents the measured pK_a value of water and is a set value for ion-pair HySS simulations.

Model

Add B | Remove B

Formula	Log Beta	PEN	Cl	H	
PENH	12.13	1	0	1	const.
$PENH_2$	23.66	1	0	2	const.
$PENClH_2$	27.46	1	1	2	const.
H_{-1}	-13.77	0	0	-1	const.

Figure 2-5. HYSS screen to input the log beta and formula information

(3) Requirement 3: The experimental method needs to be considered

The pH range and the range of pentamidine concentrations that would be used in the studies need to be defined and these values inputted into the simulation software (Figure 2-6). For the simulation of ion-pairs speciation, the pH limits were set at 2 and 12. Then the result of the percentage of pentamidine bound to the counterion was extracted at pH 7.4, corresponding to the experimental and physiological conditions used in this study. The range of pentamidine concentrations was set at 4 nM - 9 mM and the ratios of each counter ion to pentamidine were fixed at 20:1 and 1:1 for comparison. A screenshot of the experimental conditions inputted into HYSS is shown as follows:

Model | Conditions | Solids

Conditions

Titration simulation | Species Distribution

Reagent	initial concentration	final concentration	start pH	final pH
PEN	8.000E-06	8.000E-06		
XIN	1.600E-04	1.600E-04		
H			2.0	12.0

Figure 2-6. A screenshot of the HYSS simulation software. Experimental conditions for HySS modelling. PEN and XIN represent pentamidine and the counterion (CI) xinafoate (XIN), respectively. The molar concentrations of pentamidine and the counterion xinafoate are input in the software.

2.3.9 Measurement of dissociation constants of pentamidine - xinafoate ion pairs using fluorescence-lifetime imaging microscopy (FLIM)

2.3.9.1 Multiphoton fluorescence lifetime measurement microscope system

The experiment was performed in the Rutherford Appleton laboratory of the science and technology facilities council in Didcot. All the samples were dissolved in 50 nM Tris buffer, pH 7.4. The experiments were undertaken with an existing FLIM system based on a Nikon E-C2 confocal system. Excitation sources for multiphoton lifetime measurements was achieved using a Mira 900F Ti-sapphire laser pumped by a CW Verdi 532 nm laser (Coherent Ltd) (tunable 700-980 nm, pulse length 180-200 fs) pumping an OPO (Optical Parametric Oscillators APE, Germany) with a selectable centre wavelength-tunable between 550-650 nm, pulse length 180 fs. Photons were detected by a Becker and Hickl, SPC 830 TCSPC unit. Briefly, multiphoton excitation using 580 ± 5 nm or 600 ±5 nm was used in this study from a tunable mode-locked titanium sapphire (Ti: Sapphire) laser (Mira 900, Coherent Lasers, UK) that generated 180 fs pulses at 76 MHz pumped by a 532 nm solid-state Neodymium Vanadate laser source (Verdi, Coherent Lasers). Excitation was performed using an x60 water immersion objective, NA 1.2. Collected fluorescence emission was passed through a UV filter, U340 to eliminate the visible excitation wavelength. A high-speed hybrid detector (HPM-100) with a sense in the UV was used, connected to a Time-Correlated Single Photon Counting (TCSPC) module, SPC830 (Becker-Hickl, GmbH). Excitation laser power was controlled using a circular Neutral Density (ND) filter, and the setup is depicted in the figure below.

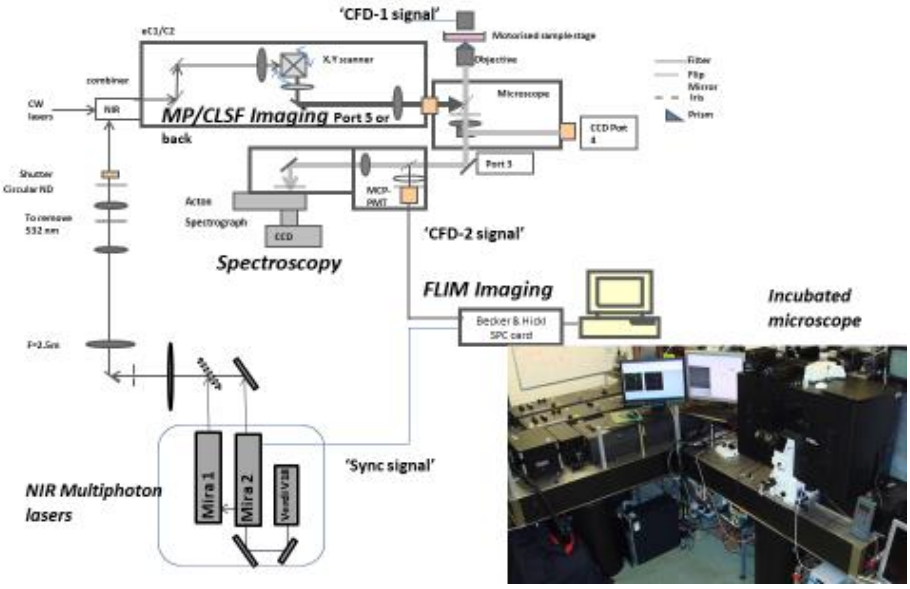

Figure 2-7 Multiphoton excitation confocal and 4-channel confocal set up (BOTCHWAY et al., 2015).

2.3.9.2 Post image processing and analysis

Time-correlated Single Photon Counting (TCSPC) decay traces were exported to a Becker and Hickl SPCImage software and fluorescence lifetime analysed using an internally generated instrument response function.

2.3.10 Data analysis

Data were expressed as the mean ± standard deviation. Statistics were performed by ANOVA or t-test in GraphPad7. Statistical significance was assumed when $p<0.05$.

2.4 Results

2.4.1 Verification of HPLC analysis for pentamidine

The calibration curve (Figure 2-8, 2-9) for pentamidine shows a high degree of linearity (R^2=0.9999). The Limit of Detection (LOD) and Limit of Quantification (LOQ) for pentamidine assay are 2.30 µg/ml (3.88 µM) and 6.98 µg/ml (11.78 µM), respectively.

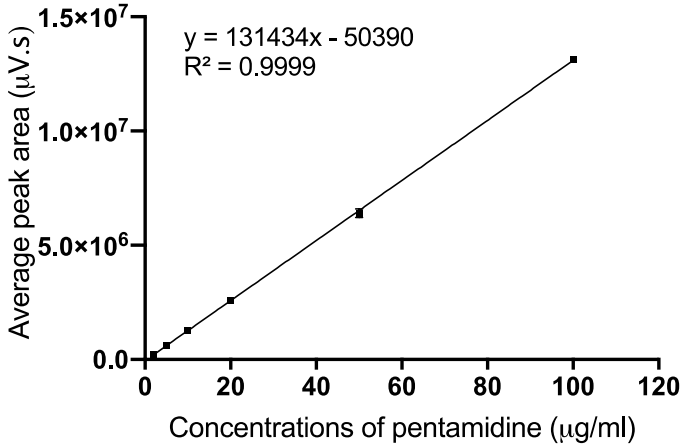

Figure 2-8 Calibration curve of pentamidine (0-100 µg/ml; 0-168 µM) in mobile phase (0.025 M monobasic potassium phosphate: acetonitrile = 76%: 24%, v/v; pH 3.2 regulated by phosphoric acid). Data represent the mean ± standard deviation (n=3). The standard deviation of some points in the figure was too small to be visualised.

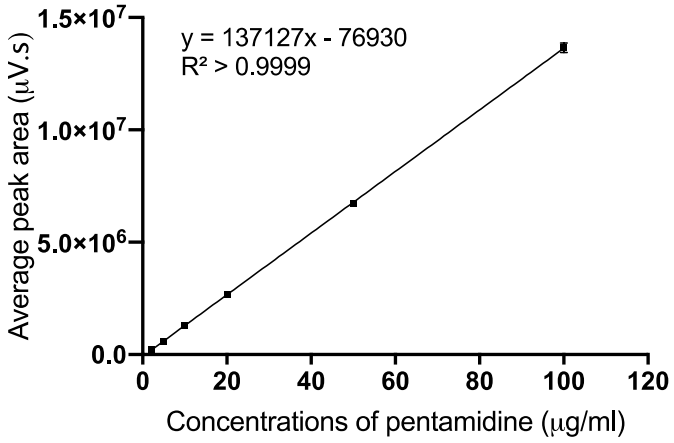

Figure 2-9 Calibration curve of pentamidine (0-100 µg/ml; 0-168 µM) in 0.9% saline (pH 7.4) saturated with octanol. Data represent the mean ± standard deviation (n=3). The standard deviation of some points in the figure was too small to be visualised.

The peak for pentamidine appeared within 4.68-4.72 mins as indicated by the retention time in the table 2-3. The peak area of pentamidine increased in proportion with the concentrations of pentamidine. The coefficient of variance (CV), a measure of precision, varied from 0.32 - 2.90%, although the majority is within 2%.

Table 2-3 Retention time, peak area and Coefficient of Variance (CV) of pentamidine dissolved in the HPLC mobile phase (0.025 M monobasic potassium phosphate: acetonitrile = 76%: 24%, v/v; pH 3.2 regulated by phosphoric acid) was measured by HPLC. The results represent the mean ± standard deviations (n=3). CV was calculated by the standard deviations/ mean of peak areas.

Concentrations (µg/ml)	**Retention Time (min)**	**Peak area (µV.s)**	**CV (%)**
100	4.70	13148678 ± 111752	0.85
50	4.68	6402594 ± 185439	2.90
20	4.70	2581060 ± 25262	0.98
10	4.71	1285323 ± 4162	0.32
5	4.71	616741 ± 3833	0.62
2	4.72	242165 ± 1534	0.63

The peak for pentamidine appeared within 4.77-4.86 mins as indicated by the retention time in the table 2-4 for pentamidine dissolved in octanol saturated saline. The peak area of pentamidine increased in proportion with the concentrations of pentamidine. The coefficient of variance (CV) varied from 0.33 - 3.47%.

Table 2-4 Retention time, peak area and Coefficient of Variance (CV) of pentamidine dissolved in octanol saturated saline and then measured by HPLC. The results represent the mean ± standard deviations (n=3). CV was calculated by the standard deviations/ mean of peak areas.

Concentrations (µg/ml)	**Retention Time (min)**	**Peak area (µV.s)**	**CV (%)**
100	4.86	13653188 ± 209946	1.54
50	4.81	6747010 ± 27371	0.41
20	4.84	2654747 ± 13771	0.52
10	4.84	1300928 ± 15902	1.22
5	4.81	606280 ± 2011	0.33
2	4.77	219032 ± 7592	3.47

2.4.2 Chemical stability of pentamidine solutions

The stability of pentamidine solutions (2-100 µg/ml, pH 7.4) at both room temperature and 37 °C was assessed by HPLC for up to 28 days. At room temperature (Table 2-5), there were no significant degradations at the lower concentrations and degradation could only be detected when the pentamidine concentration was initially 100 µg/ml (168 µM) and dropped to 94.60% ($P<0.001$). At 37 °C (Table 2-6), the pentamidine solutions at 50 µg/ml (84 µM) and 100 µg/ml (168 µM) degraded after 7 days, dropping from 100% to 93.00% ($P<0.001$) and 90.48% ($P<0.001$), respectively.

Table 2-5 Stability of pentamidine standards in 0.9% saline (pH 7.4) saturated with octanol. Samples were stored at room temperature for 2, 7, 14 and 28 days.

Concentrations of pentamidine µg/ml (µM)	Time (days)	Retention time (min) (n=3 ± SD)	Peak area (µV*s) (n=3 ± SD)	% Recovery
100 µg/ml	0	4.48 ± 0.03	11945414 ± 37126	100.00%
(168 µM)	2	4.48 ± 0.02	11939444 ± 17978	99.95%
	7	4.40 ± 0.00	11890057 ± 11107	99.54%
	14	4.51 ± 0.07	11760900 ± 481279	98.46%
	28	4.49 ± 0.02	11300331 ± 524264	94.60%
50 µg/ml	0	4.48 ± 0.00	5930977 ± 12227	100.00%
(84 µM)	2	4.49 ± 0.03	5932881 ± 23250	100.03%
	7	4.46 ± 0.04	5942533 ± 49969	100.19%
	14	4.46 ± 0.03	5810347 ± 63036	97.97%
	28	4.50 ± 0.03	5884931 ± 80213	99.22%
20 µg/ml	0	4.51 ± 0.02	2327521 ± 14771	100.00%
(33 µM)	2	4.50 ± 0.01	2331281 ±17252	100.16%
	7	4.42 ± 0.04	2358955 ± 7055	101.35%
	14	4.48 ± 0.03	2361669 ± 8711	101.47%
	28	4.52 ± 0.02	2364060 ± 3130	101.57%
10 µg/ml	0	4.51 ± 0.02	1154026 ± 19326	100.00%
(16 µM)	2	4.55 ± 0.03	1166975 ± 4926	101.12%
	7	4.44 ± 0.03	1167062 ± 3511	101.13%
	14	4.46 ± 0.01	1175839 ± 8647	101.89%
	28	4.52 ± 0.02	1159798 ± 19805	100.50%
5 µg/ml	0	4.53 ± 0.04	566584 ± 2424	100.00%
(8 µM)	2	4.54 ± 0.02	575535 ± 3365	101.58%
	7	4.45 ± 0.06	575969 ± 2958	101.66%
	14	4.46 ± 0.01	594522 ± 2013	104.93%
	28	4.52 ± 0.02	589663 ± 8407	104.07%
2 µg/ml	0	4.51 ± 0.02	227108 ± 2299	100.00%
(3 µM)	2	4.58 ± 0.02	225923 ± 2128	99.48%
	7	4.43 ± 0.01	227798 ± 860	100.30%
	14	4.51 ± 0.07	230204 ± 1016	101.36%
	28	4.53 ± 0.01	233766 ± 1988	102.93%

Table 2-6 Stability of pentamidine standards in 0.9% saline (pH 7.4) saturated with octanol. Samples were stored at 37°C for 2, 7, 14 and 28 days.

Concentrations of pentamidine µg/ml (µM)	Time (days)	Retention time (min) (n=3 ± SD)	Peak area (µV*s) (n=3 ± SD)	% Recovery
100 µg/ml	0	4.48 ± 0.03	11945414 ± 37126	100.00%
(168 µM)	2	4.53 ± 0.05	11923725 ± 75496	99.82%
	7	4.40 ± 0.02	11517138 ± 74832	96.41%
	14	4.44 ± 0.04	11413168 ± 232233	95.54%
	28	4.49 ± 0.02	10808348 ± 179213	90.48%
50 µg/ml	0	4.48 ± 0.00	5930977 ± 12227	100.00%
(84 µM)	2	4.50 ± 0.01	5885856 ± 57257	99.24%
	7	4.41 ± 0.03	5659399 ± 6879	95.42%
	14	4.47 ± 0.06	5567208 ± 23125	93.87%
	28	4.50 ± 0.01	5515947 ± 6544	93.00%
20 µg/ml	0	4.51 ± 0.02	2327521 ± 14771	100.00%
(33 µM)	2	4.23 ± 0.44	2351282 ± 9481	101.02%
	7	4.44 ± 0.02	2284371 ± 19071	98.15%
	14	4.46 ± 0.02	2293498 ± 15963	98.54%
	28	4.54 ± 0.03	2241901 ± 1165	96.32%
10 µg/ml	0	4.51 ± 0.02	1154026 ± 19326	100.00%
(16 µM)	2	4.51 ± 0.04	1151453 ± 7586	99.78%
	7	4.45 ± 0.02	1094396 ± 3532	94.83%
	14	4.48 ± 0.02	1096031 ± 3313	94.97%
	28	4.54 ± 0.02	1072813 ± 18515	92.96%
5 µg/ml	0	4.53 ± 0.04	566584 ± 2424	100.00%
(8 µM)	2	4.53 ± 0.03	576866 ± 4090	101.81%
	7	4.45 ± 0.06	547407 ± 2083	96.62%
	14	4.48 ± 0.01	543093 ± 13314	95.85%
	28	4.54 ± 0.03	541672 ± 10154	95.60%
2 µg/ml	0	4.51 ± 0.02	227108 ± 2299	100.00%
(3 µM)	2	4.55 ± 0.06	228224 ± 4492	100.49%

2.4.3 Octanol-water distribution coefficient

The lipophilicity (log D, 7.4) of pentamidine (33 μM of pentamidine was used with taurodeoxycholate and octanoate and 8 μM of pentamidine were used for quercetin and xinafoate) in the presence of 20 times molar ratio of taurodeoxycholate, octanoate, quercetin, and xinafoate increased by 1.15, 1.06, 0.06 and 0.82 compared to pentamidine respectively.

Table 2-7 The lipophilicity (log $D_{7.4}$) of pentamidine with counterions

Concentrations of pentamidine (μM)	Counterion	Concentrations of counterion (μM)	Log $D_{7.4}$ of pentamidine (n=3)	standard deviation
33	Taurodeoxycholate	0	-1.192	0.093
		33	-0.774	0.023
		66	-0.573	0.009
		132	-0.368	0.015
		264	-0.158	0.002
		396	-0.091	0.001
		660	-0.042	0.001
33	Octanoate	0	-1.194	0.091
		33	-0.927	0.028
		66	-0.785	0.016
		132	-0.632	0.054
		264	-0.388	0.005
		396	-0.238	0.010
		660	-0.133	0.010
8	Xinafoate	0	-1.194	0.091
		32	-1.022	0.041
		64	-0.811	0.023
		96	-0.557	0.008
		160	-0.371	0.016
0	Quercetin	0	-1.194	0.091
		32	-1.136	0.175
		64	-1.272	0.079
		96	-0.920	0.077
		160	-1.137	0.048

For taurodeoxycholate (Figure 2-10), the log $D_{7.4}$ of pentamidine improved continually when increasing the concentration of taurodeoxycholate in the solution. Compared to the log $D_{7.4}$ of pentamidine without taurodeoxycholate, it was 96.5% higher when adding 20 times molar ratio (660 µM) of taurodeoxycholate.

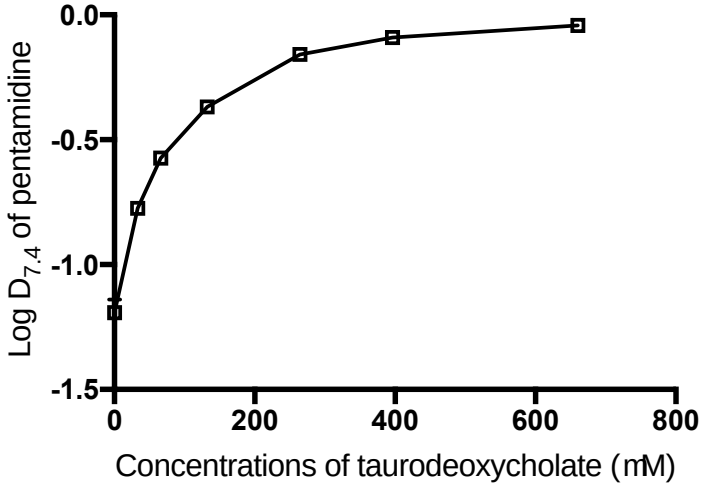

Figure 2-10 Distribution coefficient of pentamidine at pH 7.4 with the presence of taurodeoxycholate. The experiment was performed at 37 °C. Results were expressed as mean ± standard deviation at each point (n=3, with 3 replicates each). Some of the error bars were too small to be seen in the figure.

For octanoate (Figure 2-11), the distribution coefficient of pentamidine at pH 7.4 also increased with the presence of octanoate, although the magnitude of change was not as significant compared to taurodeoxycholate. The log $D_{7.4}$ of pentamidine was 89.1% higher when adding 20 times molar ratios (660 µM) of octanoate.

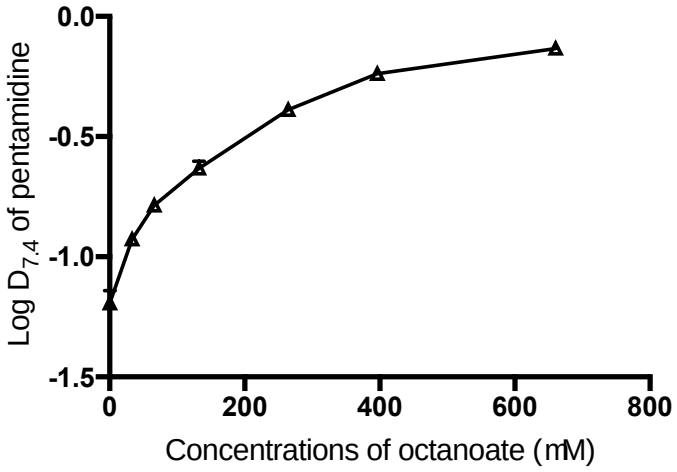

Figure 2-11 Distribution coefficient of pentamidine at pH 7.4 with the presence of octanoate. The experiment was performed at 37 °C. Results were expressed as mean ± standard deviation at each point (n=3, with 3 replicates each). Some of the error bars were too small to be seen in the figure.

The log $D_{7.4}$ of pentamidine dramatically fluctuated when introducing quercetin to the solution, and no significant increase was observed. This indicated that quercetin did not form a stable ion pair that improved lipophilicity of the parent drug and/or an ion-pair that could be measured using HPLC.

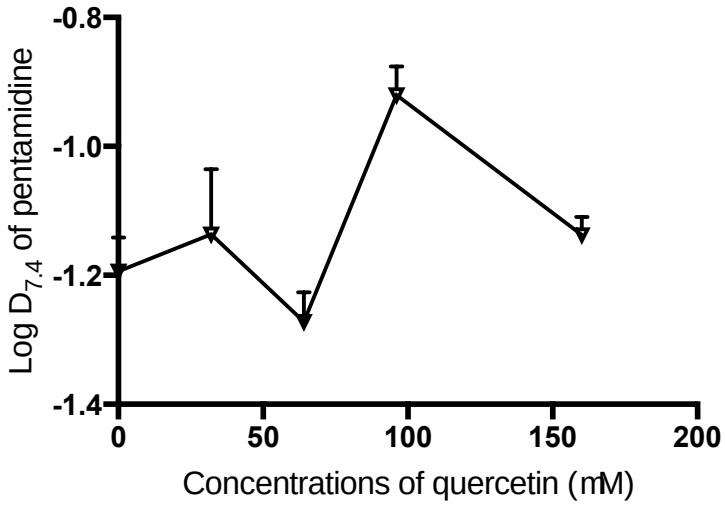

Figure 2-12 Distribution coefficient of pentamidine at pH 7.4 with the presence of quercetin. The experiment was performed at 37 °C. Results were expressed as mean ± standard deviation at each point (n=3, with 3 replicates each).

For xinafoate (Figure 2-13), the lipophilicity of pentamidine increased proportionally when adding 1-12 times molar ratios of xinafoate. After that, the magnitude of change was milder, and the log $D_{7.4}$ of pentamidine reached 68.9% higher compared to the original value without xinafoate when adding 20 times molar ratios (160 μM) of xinafoate.

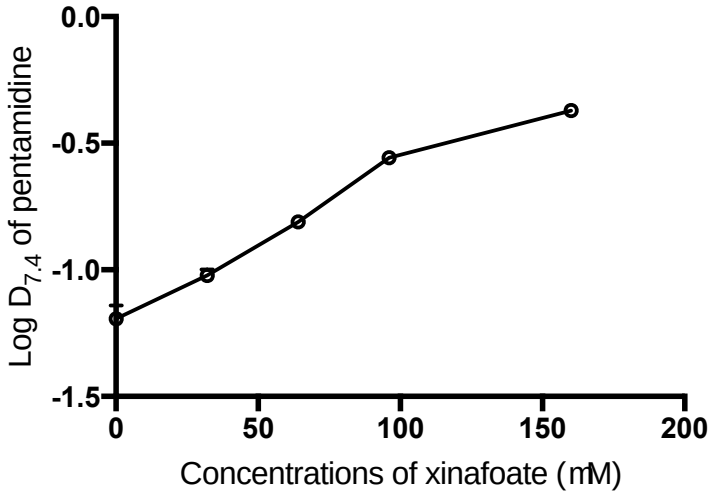

Figure 2-13 Distribution coefficient of pentamidine at pH 7.4 with the presence of xinafoate. The experiment was performed at 37 °C. Results were expressed as mean ± standard deviation at each point (n=3, with 3 replicates each). Some of the error bars were too small to be seen in the figure.

2.4.4 Nuclear magnetic resonance (NMR) spectroscopy

The binding site of the counterion with pentamidine is determined by assessing the chemical shift of H and C assigned to pentamidine in the presence of the counterion xinafoate using nuclear magnetic resonance (NMR) spectroscopy. The principle of NMR explained in detail can be found (Koutcher and Burt, 1984). In simple terms, nuclei in different chemical structures share electrons with other electrons. Thesis electrons have magnetic fields and resonate different frequencies. When nuclei samples are excited, they generate signals with different frequencies which are reflected as different chemical shift on NMR spectra. The NMR spectra can be used to identify chemical structures of molecules (Chatham and Blackband, 2001).

2.4.4.1 ^{13}C NMR spectra

^{13}C-NMR measures the spin changes of carbon nuclei. The number of protons carbons and the backbones of molecules can be directly observed from ^{13}C-NMR spectra. Although ^{13}C-NMR is less sensitive than ^{1}H-NMR, it has the advantage of specificity. The chemical shifts of ^{13}C-NMR spectra range from 0 to 240 ppm and are not sensitive to the change of environment. Thus the

protons for carbons are easier to be distinguished and specified to carbons of molecules (Pieters and Vlietinck, 1989; Thompson, 1990).

For the carbons of pentamidine in DMSO-d6 (Figure 2-15), an upfield shift was observed on the carbon (P6, P7, P8) near the C-O-C linkage. A minor upfield shift was also seen on the carbons assigned to the two benzene rings (P2, P3, P4, P5). The carbons (P1) located in the amidine groups experienced a downfield shift with the presence of xinafoate at 1:20 molar ratio. For the carbons of xinafoate in DMSO-d6, no obvious carbon shift was observed.

Similar shifts in the majority of carbons were observed when pentamidine and xinafoate were dissolved in DMSO-d6 with 1% D_2O (Figure 2-16). Exceptions included the carbon (P2) adjacent to the amidine groups assigned to the benzene ring of pentamidine shifted downfield and the carbons (X9, X10) in the naphthalene functional group of xinafoate which shifted upfield.

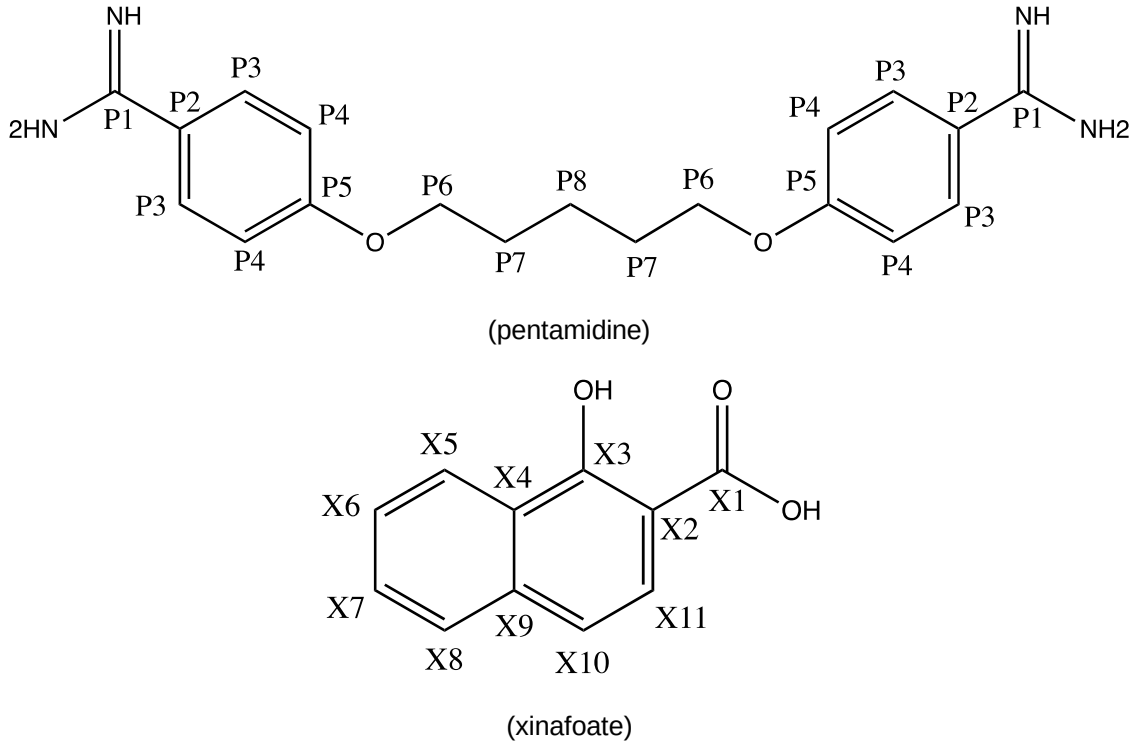

Figure 2-14 Carbon labelled structures of pentamidine and xinafoate

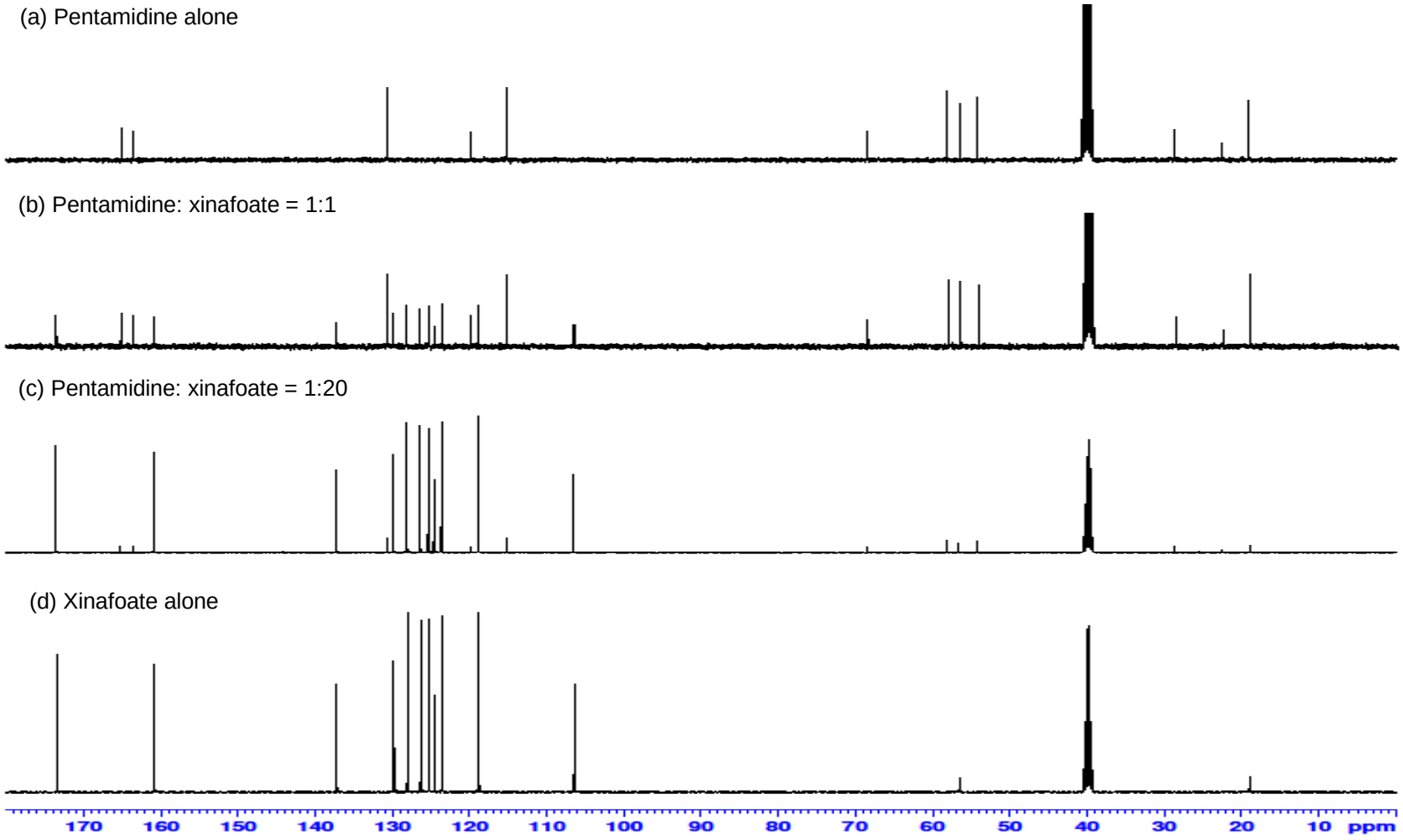

Figure 2-15 The ^{13}C NMR spectra of pentamidine free, and pentamidine xinafoate mixture (1:1 and 1:20) and xinafoate free dissolved in DMSO-d6

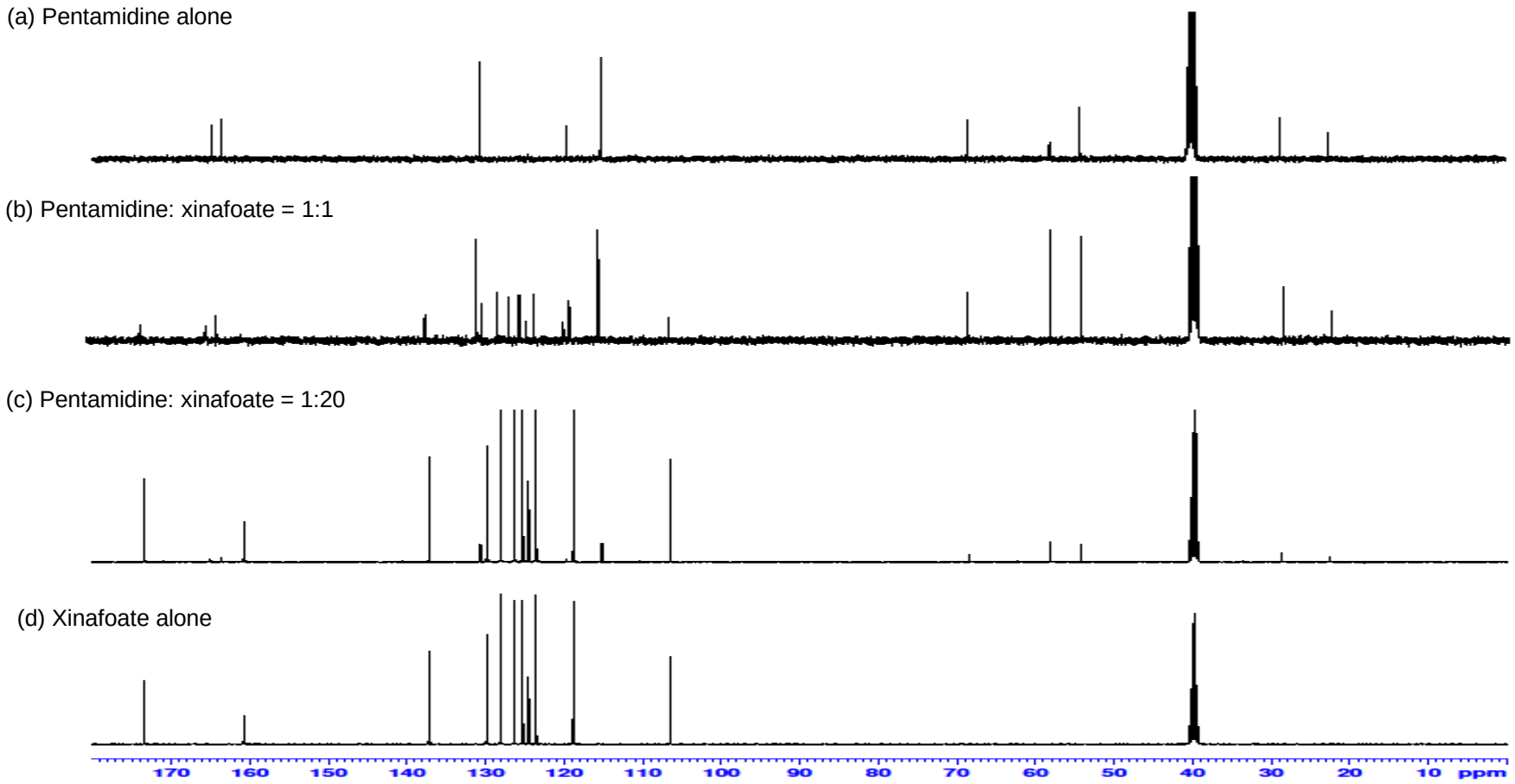

Figure 2-16 The ^{13}C NMR spectra of pentamidine free, and pentamidine xinafoate mixture (1:1 and 1:20) and xinafoate free dissolved in DMSO-d6 (99%) with D2O (1%) mixed solution

Table 2-8 Chemical shifts (δ, ppm) of pentamidine from ^{13}C-NMR spectra dissolved in DMSO-d6

Molar ratio (Pentamidine:Xinafoate)	Chemical shift, δ(ppm)							
	P1	P2	P3	P4	P5	P6	P7	P8
1:0 (pentamidine only)	165.04	119.85	130.65	115.26	163.54	68.51	28.65	22.54
1:1	165.04	119.85	130.65	115.25	163.54	68.50	28.65	22.53
1:20	165.10	119.80	130.61	115.15	163.51	68.39	28.62	22.48

Table 2-9 Chemical shifts (δ, ppm) of xinafoate from ^{13}C-NMR spectra dissolved in DMSO-d6

Molar ratio (Pentamidine:Xinafoate)	Chemical shift, δ(ppm)				
	X1	X2	X3	X9	X10
0:1 (xinafoate only)	173.47	106.45	160.80	137.19	118.78
1:1	173.42	106.48	160.72	137.20	118.86
1:20	173.47	106.45	160.79	137.18	118.77

Table 2-10 Chemical shifts (δ, ppm) of pentamidine from 13C-NMR spectra dissolved in DMSO-d6 (99%) with D2O (1%) mixed solution

Molar ratio (Pentamidine:Xinafoate)	Chemical shift, δ(ppm)							
	P1	P2	P3	P4	P5	P6	P7	P8
1:0 (pentamidine only)	164.89	119.71	130.67	115.28	163.56	68.52	28.64	22.53
1:1	164.92	119.78	130.66	115.27	163.56	68.51	28.64	22.53
1:20	165.11	119.79	130.60	115.14	163.51	68.38	28.62	22.47

Table 2-11 Chemical shifts (δ, ppm) of xinafoate from ^{13}C-NMR spectra dissolved in DMSO-d6 (99%) with D_2O (1%) mixed solution

Molar ratio	Chemical shift, δ(ppm)				
(Pentamidine:Xinafoate)	X1	X2	X3	X9	X10
0:1 (xinafoate only)	173.37	106.40	160.70	137.45	118.80
1:1	173.25	106.41	160.57	137.20	119.72
1:20	173.39	106.41	160.72	137.18	119.72

2.4.4.2 ^{1}H NMR spectra

^{1}H-NMR is more sensitive than ^{13}C-NMR. The information on the total number and types of the chemical environment of protons can be acquired from the ^{1}H-NMR spectra. Its chemical shift ranges from 0 to 14 ppm. ^{1}H-NMR spectra are generally more complicated than ^{13}C-NMR spectra, and it is affected by proton resonance with water (Pieters and Vlietinck, 1989; Thompson, 1990).

The protons on pentamidine and xinafoate were labelled, as shown in Figure 2-17. The chemical shifts of these protons are shown in Figure 2-18 and Figure 2-19.

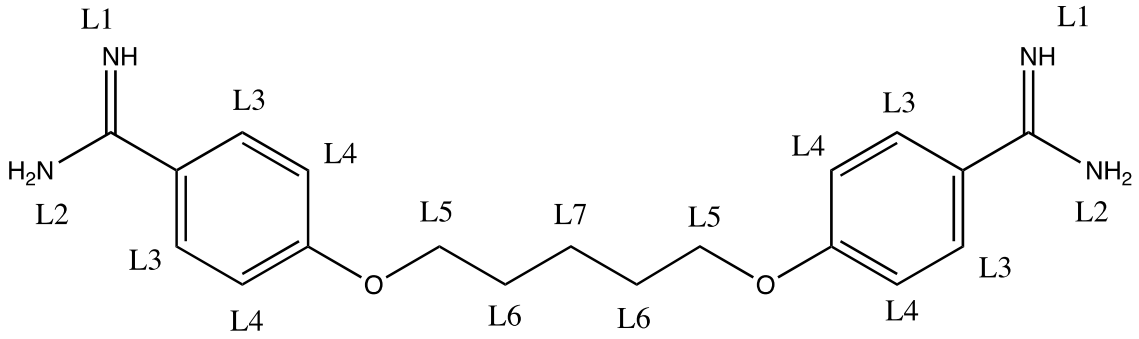

(pentamidine)

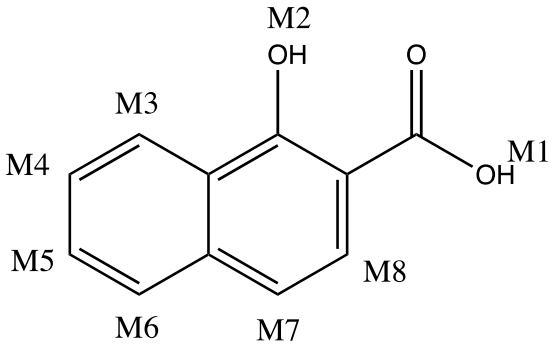

(xinafoate)

Figure 2-17 Proton labelled structures of pentamidine and xinafoate

For ^{1}H-NMR, the pentamidine concentration was 11.2 mM without or with different molar ratios of xinafoate (1:1, 1:20). As shown in Figure 2-18 and Figure 2-19, the peak for the proton (L2) assigned to the amidine groups on pentamidine split into two peaks with both equal and 20 times molar ratio of xinafoate, and another peak for the proton on amidine groups (L1) disappeared with the presence of xinafoate. No chemical shift changes were observed for protons on the benzene rings or carbon chains of pentamidine with xinafoate at a 1:1 molar ratio. However, at a 1:20 molar ratio of xinafoate the protons (L4, L5, L6, L7) shifted upfield while the proton located near the amine groups shifted downfield. For xinafoate, it was expected to see a chemical shift of protons -COOH (M1) and -OH (M2) on xinafoate. Unfortunately, these signals were not detected. For the rest of the protons on xinafoate, only a slight upfield shift was observed for the proton (M6) of naphthalene. The ^{1}H-NMR spectra in both DMSO-d6 and DMSO-d6/D2O mixed solutions showed the same patterns as discussed earlier.

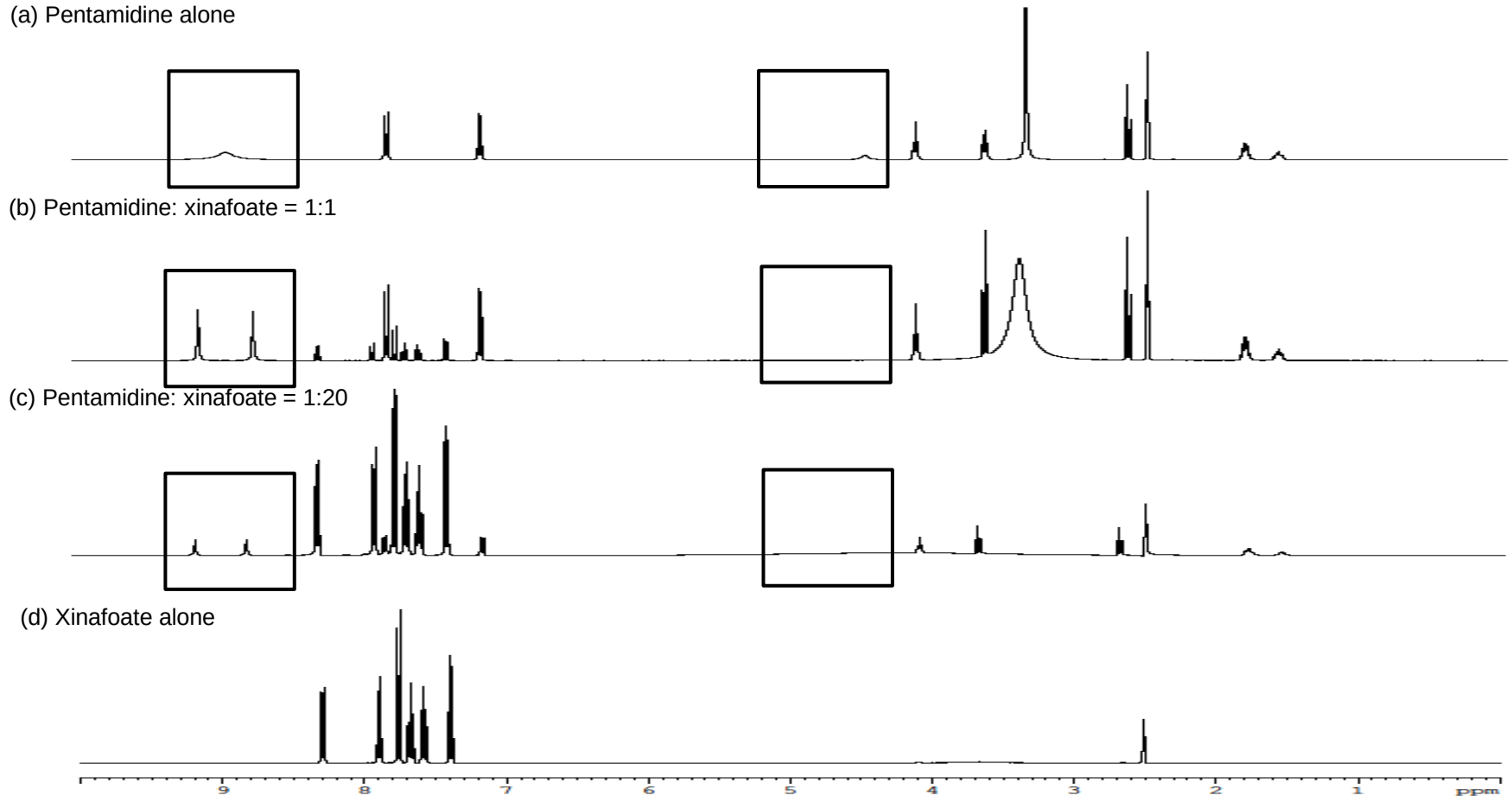

Figure 2-18 The ^{1}H NMR spectra of pentamidine free, and pentamidine xinafoate mixture (1:1 and 1:20) and xinafoate free dissolved in DMSO-d6 (99%) and D2O (1%) mixed solution. The concentration of pentamidine was 11.2 mM in (a) (b) (c). The concentration of xinafoate alone was 224 mM in (d). The peak for the proton assigned to the amidine groups on pentamidine (L2) split into two peaks, and another proton peak on pentamidine (L1) disappeared with the presence of xinafoate.

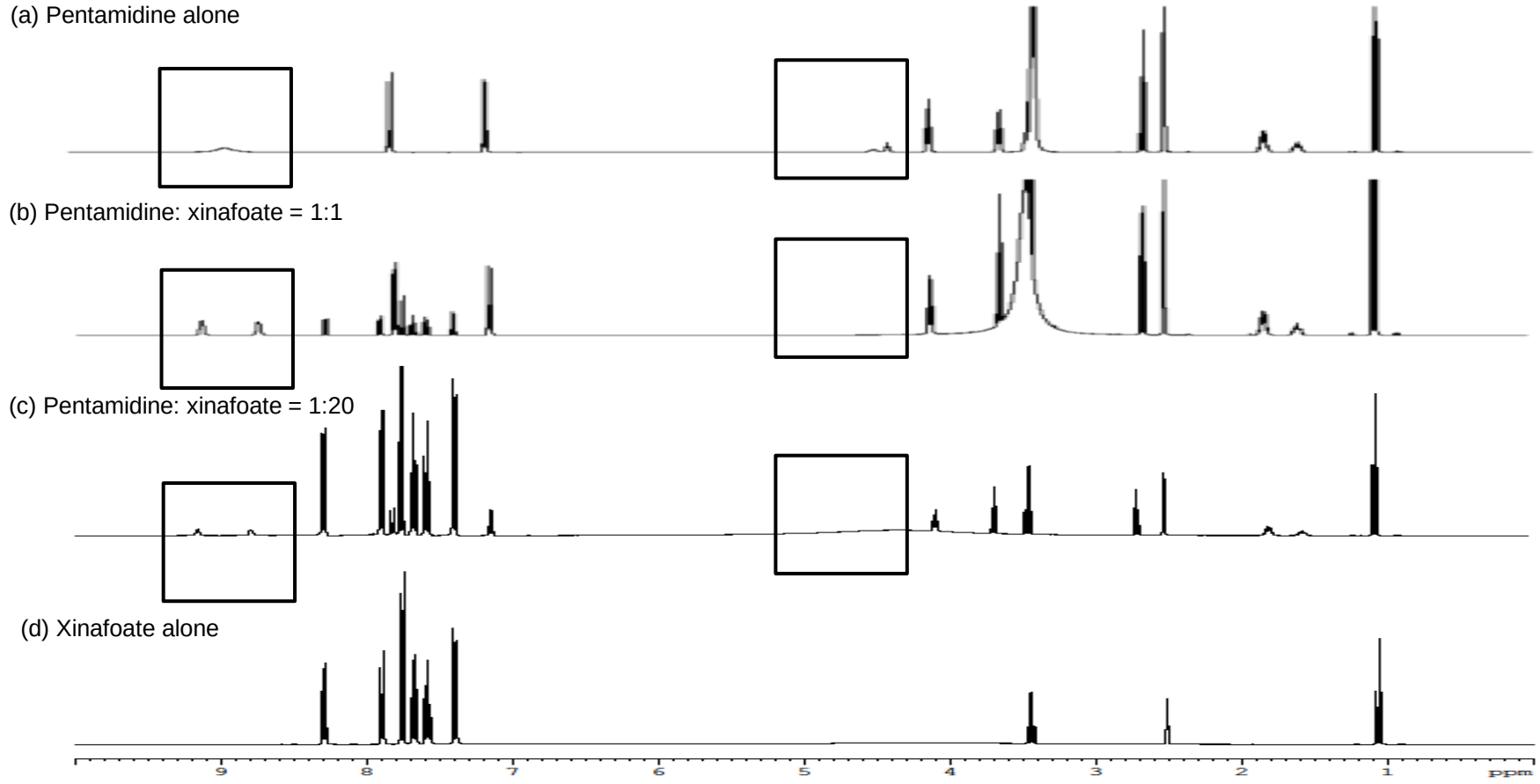

Figure 2-19 The ^{1}H NMR spectra of pentamidine free, and pentamidine xinafoate mixture (1:1 and 1:20) and xinafoate free dissolved in DMSO-d6 (99%) and D2O (1%) mixed solution. The concentration of pentamidine was 11.2 mM in (a) (b) (c). The concentration of xinafoate alone was 224 mM in (d). The peak for the proton assigned to the amidine groups on pentamidine (L2) split into two peaks, and another proton peak on pentamidine (L1) disappeared with the presence of xinafoate.

Table 2-12 1H NMR chemical shifts of pentamidine protons in DMSO-d6

Molar ratio (Pentamidine:Xinafoate)	Chemical shift, δ(ppm)						
	L1	L2	L3	L4	L5	L6	L7
1:0 (pentamidine only)	4.48	8.93	7.81	7.16	4.13	1.83	1.59
1:1	disappeared	split into 2 peaks (8.74, 9.13)	7.81	7.16	4.12	1.83	1.59
1:20	disappeared	split into 2 peaks (8.79, 9.14)	7.82	7.14	4.09	1.79	1.56

Table 2-13 ^{1}H NMR chemical shifts of pentamidine protons in DMSO-d6 (99%) and D_2O (1%) mixed solution

Molar ratio (Pentamidine:Xinafoate)	Chemical shift, δ(ppm)						
	L1	L2	L3	L4	L5	L6	L7
1:0 (pentamidine only)	4.49	8.94	7.81	7.16	4.12	1.83	1.59
1:1	disappeared	split into 2 peaks (8.75, 9.14)	7.81	7.16	4.12	1.83	1.59
1:20	disappeared	split into 2 peaks (8.79, 9.16)	7.82	7.14	4.08	1.79	1.56

Table 2-14 ^{1}H NMR chemical shifts of xinafoate protons in DMSO-d6

Molar ratio (Pentamidine:Xinafoate)	Chemical shift, δ(ppm)					
	M3	M4	M5	M6	M7	M8
0:1 (xinafoate only)	8.29	7.67	7.58	7.90	7.39	7.76
1:1	8.29	7.69	7.59	7.91	7.40	7.76
1:20	8.29	7.67	7.58	7.89	7.39	7.76

Table 2-15 ^{1}H NMR chemical shifts of xinafoate protons in DMSO-d6 (99%) and D_2O (1%) mixed solution

Molar ratio (Pentamidine:Xinafoate)	Chemical shift, δ(ppm)					
	M3	M4	M5	M6	M7	M8
0:1 (xinafoate only)	8.29	7.67	7.58	7.89	7.39	7.76
1:1	8.29	7.69	7.59	7.91	7.41	7.76
1:20	8.28	7.67	7.58	7.89	7.39	7.75

2.4.5 Fluorescence spectroscopic characterisation of ion-pairs

2.4.5.1 Method validation for DAPI

The maximum emission of DAPI appeared at 460 nm, and its intensity increased proportionally with the concentrations of DAPI (Figure 2-20).

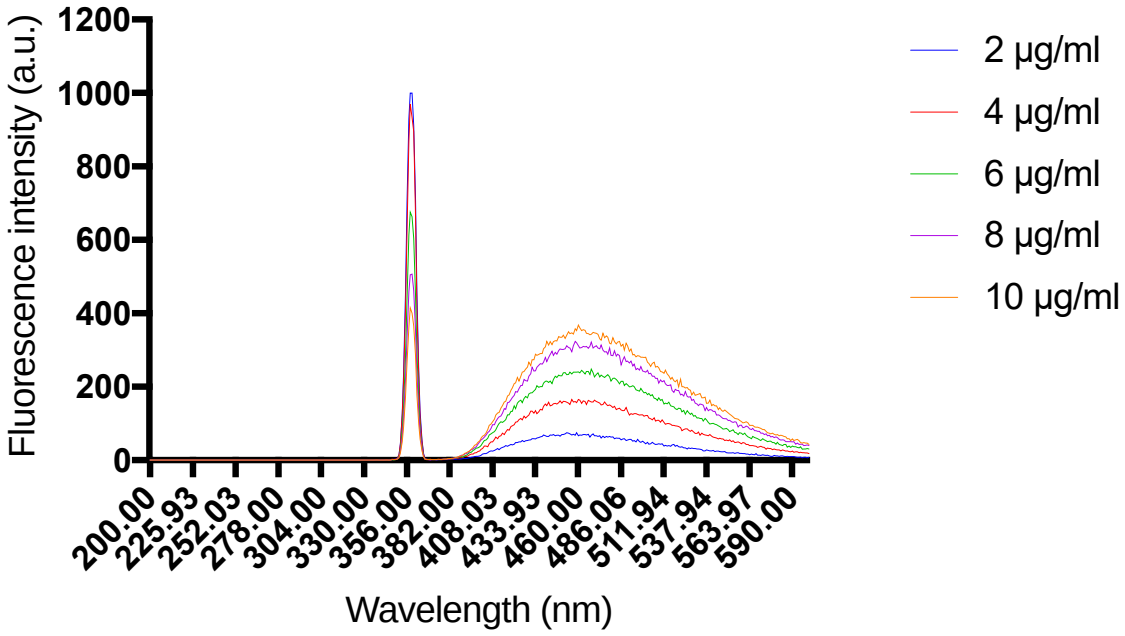

Figure 2-20 Fluorescence spectra of 2-10 µg/ml (7-36 µM) DAPI (emission spectra from bottom to top) in 50 nM Tris-buffer at pH 7.4. The excitation was set at 358 nm, and the emission was scanned for the full range from 200 to 600 nm (maximum emission at 460 nm).

As shown in Figure 2-21, the standard curve of DAPI has an R-squared value of 0.9902. Its Limit of Detection (LOD) is 1.25 μg/ml (3.57 μM) and its Limit of Quantification (LOQ) is 3.80 μg/ml (10.85 μM).

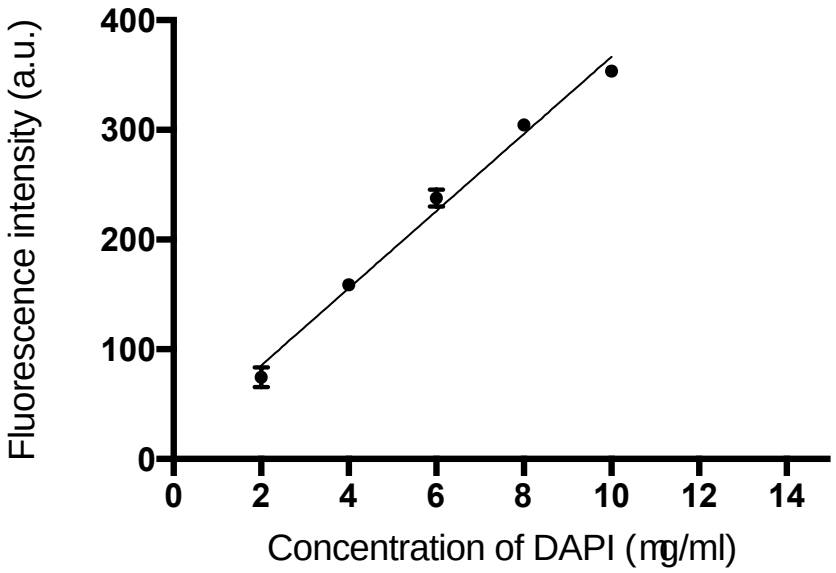

Figure 2-21 Calibration curve of DAPI in Tris buffer at pH 7.4. The average fluorescence intensity (n=3, background value subtracted) was plotted as a function of 2-10 μg/ml (7-36 μM) DAPI. Data were expressed as mean ± S.D (n=3 samples/ replicates). The S.D. of some points is too small to be seen in the figure.

Table 2-16 Statistical parameters for DAPI linearity with regression analysis

Parameters	Value
Wavelength(nm) of excitation	358
Wavelength(nm) of emission	460
Linear range (μg/ml)	2-10
Intercept	13.42
Slope	35.31
R-squared	0.9902
LOD	1.25 μg/ml (3.57 μM)
LOQ	3.80 μg/ml (10.85 μM)

2.4.5.2 Method validation for pentamidine

The maximum emission of pentamidine was at 340 nm, and its intensity was enhanced with the increasing concentrations of pentamidine (Figure 2-22).

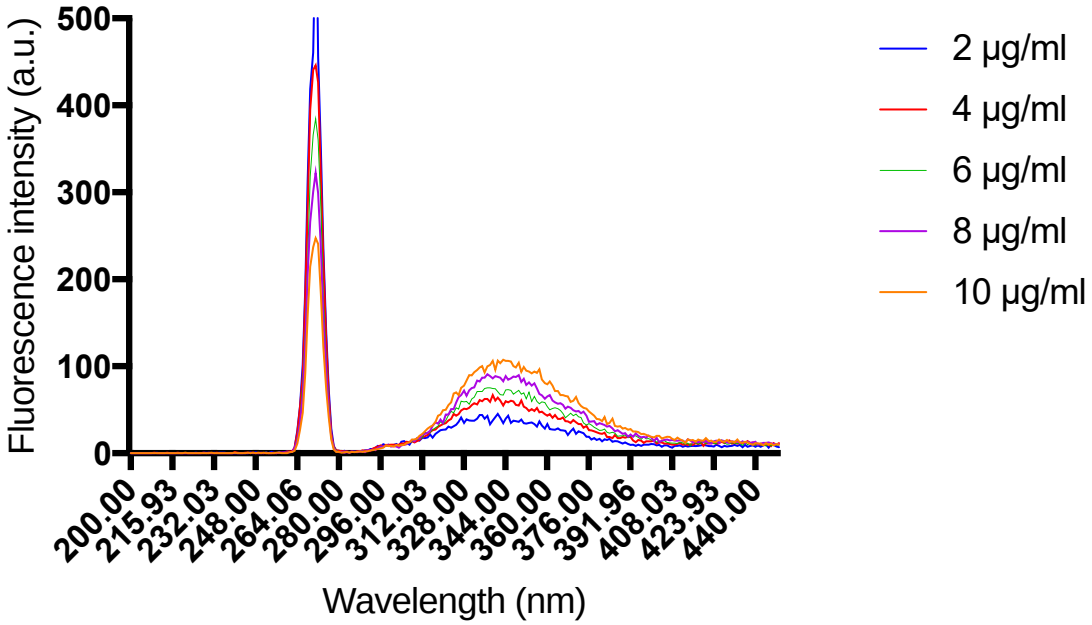

Figure 2-22 Fluorescence spectra of 2-10 μg/ml (3-17 μM) pentamidine (emission spectra from bottom to top) in 50 nM Tris-buffer at pH 7.4. The excitation was set at 270 nm, and the emission was scanned for the full range from 200 to 600 nm (maximum emission at 340 nm).

As shown in Figure 2-23, the standard curve of pentamidine in tris buffer has an R-squared value of 0.9979. Its Limit of Detection (LOD) is 0.58 μg/ml (0.98 μM) and its Limit of Quantification (LOQ) is 1.76 μg/ml (2.97 μM).

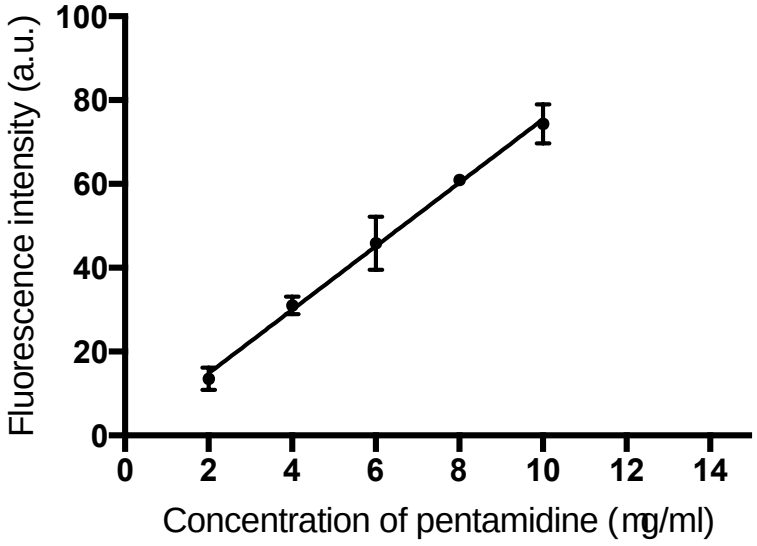

Figure 2-23. Calibration curve of 2-10 μg/ml (3-17μM) pentamidine in 50nM Tris buffer at pH 7.4. The average fluorescence intensity (n=3, background value subtracted) was plotted as a function of the pentamidine concentration (2-10 μg/ml). Data were expressed as the mean ± S.D.

Table 2-17 Statistical parameters for pentamidine linearity with regression analysis

Parameters	Value
Wavelength(nm) of excitation	270
Wavelength(nm) of emission	340
Linear range (μg/ml)	2-10
Intercept	-0.30
Slope	7.58
R-squared	0.9979
LOD (μg/ml)	0.58
LOQ (μg/ml)	1.76

2.4.5.3 Fluorescence spectra of DAPI-xinafoate and pentamidine-xinafoate ion-pairs

The fluorescence intensity of DAPI quenched slightly when adding an equal molar ratio of xinafoate (Figure 2-24). When adding a 20 times molar ratio of xinafoate, the emission intensity of DAPI increased. This occurred as xinafoate itself had a wavelength of emission overlapping with the emission of DAPI. There was also a blue shift of the DAPI's peak when adding equal and 20 times molar ratio of xinafoate. The new peaks of DAPI appeared when xinafoate was presented in the solution. This indicated that ion-pairs of DAPI and xinafoate were formed.

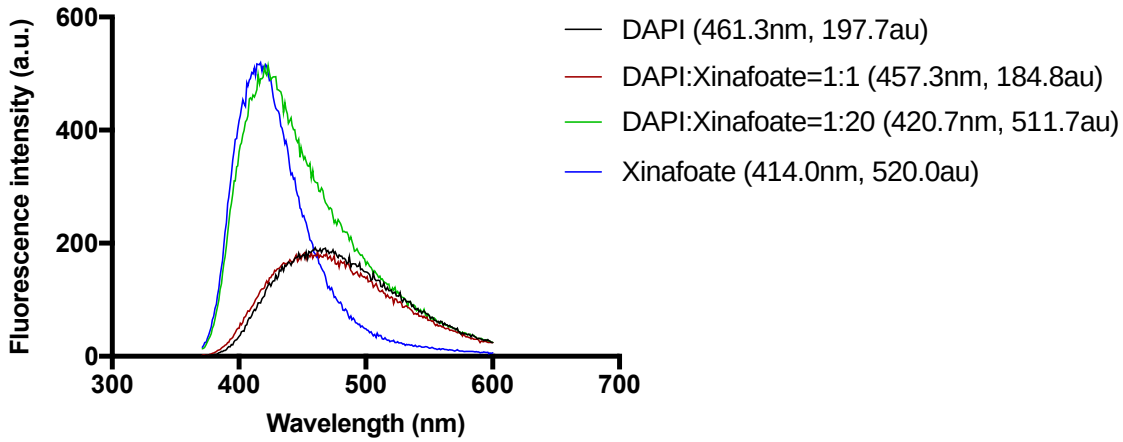

Figure 2-24 Fluorescence excitation and emission of 11.4 μM DAPI (4 μg/ml), 11.4μM Xinafoate and DAPI-Xinafoate ion-pairing solution (DAPI: xinafoate = 1:1 and 1:20). The excitation was set at 358 nm and a full emission scan at 200-600 nm.

The intensity of pentamidine was quenched with the increasing molar ratios of xinafoate (Figure 2-25). Also, there was a red shift in the spectra of pentamidine with xinafoate. This indicated that pentamidine formed ion-pairs with xinafoate.

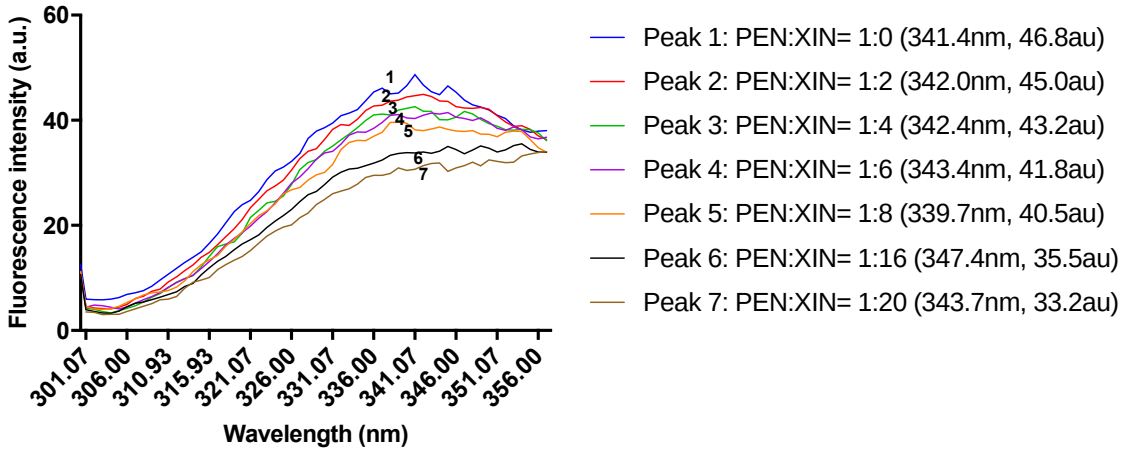

Figure 2-25 Emission spectra of 8 µM pentamidine (PEN) with increasing molar ratios of xinafoate (XIN) in 50 nM Tris buffer at pH 7.4. The excitation was set at 270 nm and a full emission scan at 200-600 nm. The maximum emission for pentamidine was at 340 nm.

2.4.6 Binding constants of ion-pairs

2.4.6.1 (a) Binding constants of pentamidine ion-pairs determined by HPLC

Binding constants were determined by measuring the concentrations of pentamidine in the saline phase with increasing concentrations of counterions using the octanol-saline shake flask method followed by HPLC. The R-squared values for pentamidine – taurodeoxycholate, pentamidine – octanoate, and pentamidine – xinafoate are > 0.99, which suggested a good fit for the regression curves (Figure 2-26, Figure 2-27, Figure 2-29). The regression curve for pentamidine – quercetin showed a poor fit, which could be caused by multiple steps of reactions or non-ion-pairing process between pentamidine and quercetin (Figure 2-28). Among pentamidine – taurodeoxycholate, pentamidine – octanoate, and pentamidine – xinafoate, pentamidine has the strongest binding with taurodeoxycholate ($pK_{pen\text{-}tau}$ = 4.1), followed by xinafoate ($pK_{pen\text{-}xin}$ = 3.6), and octanoate ($pK_{pen\text{-}oct}$ = 3.1).

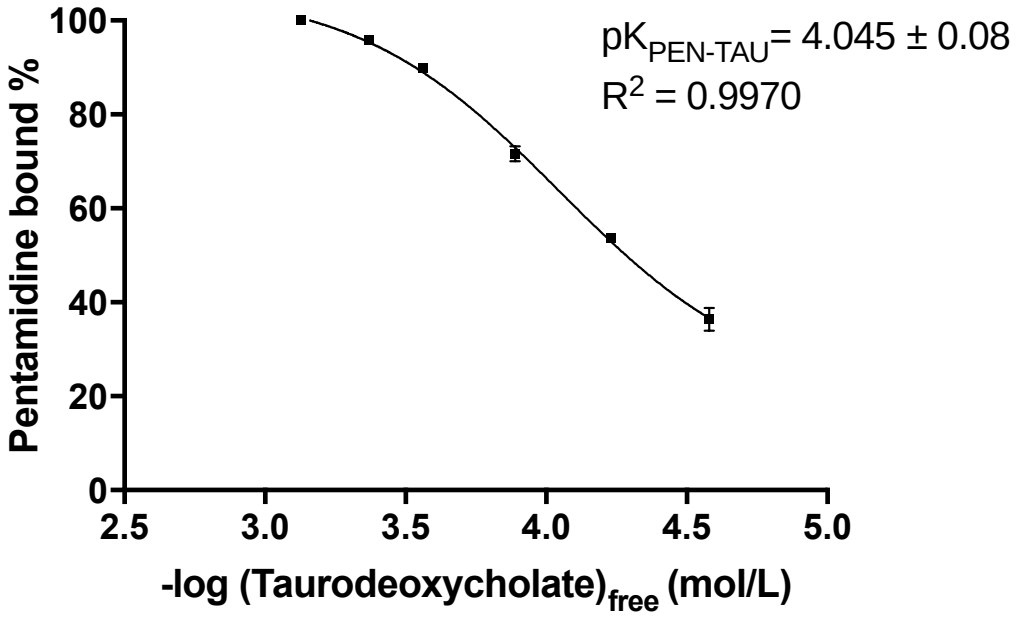

(a)

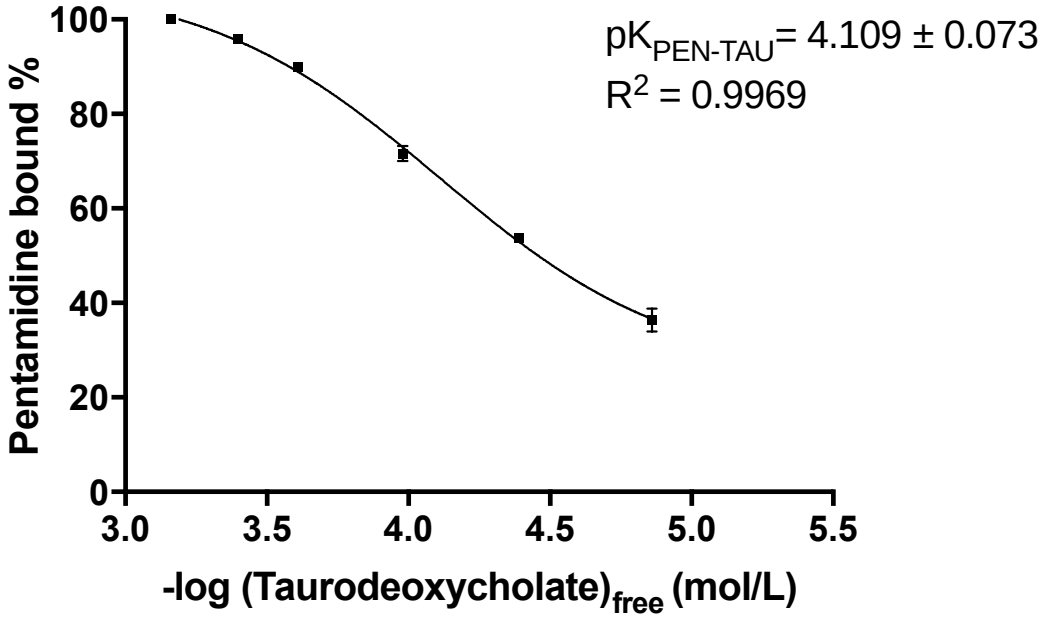

(b)

Figure 2-26 The binding constants of pentamidine with taurodeoxycholate based on 1:1 (a) and 1:2 (b) stoichiometry determined by HPLC. Data were expressed as mean ± S.D. (n=3) and fit into the Sigmoidal regression model in GraphPad7.

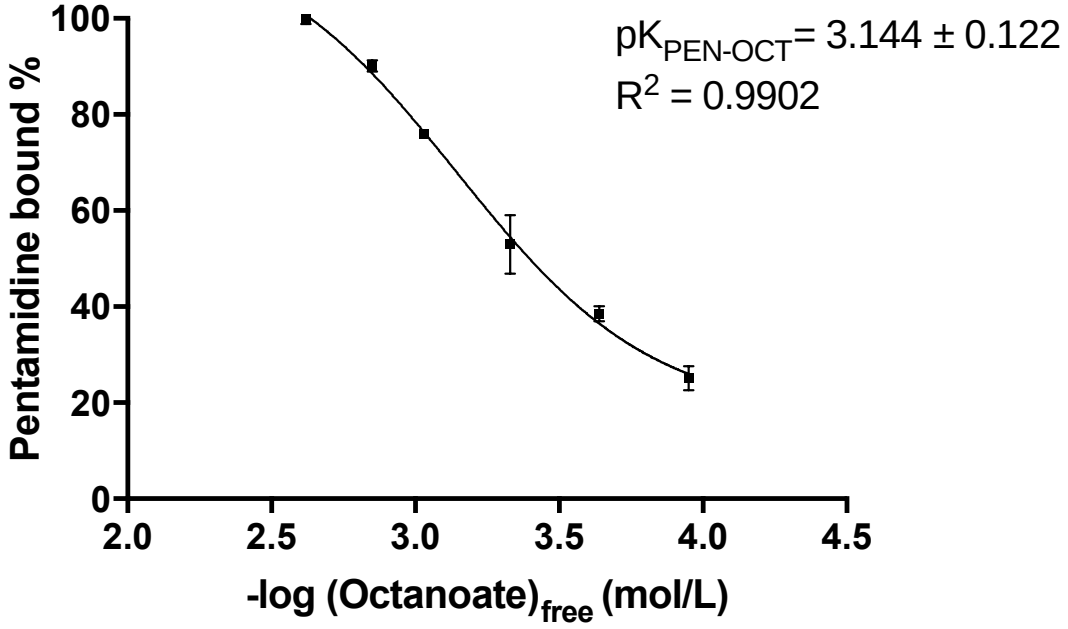

(a)

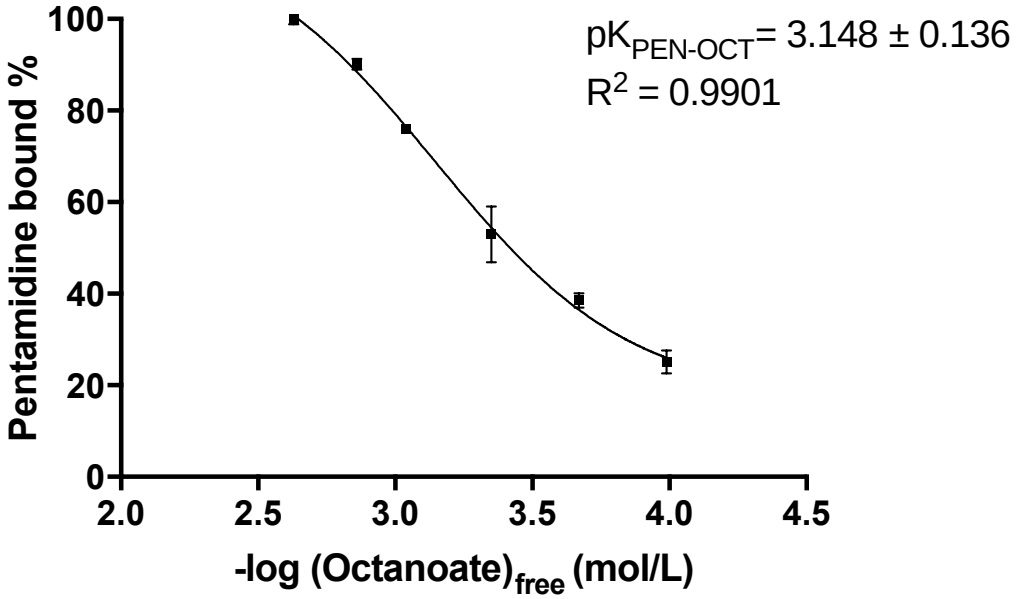

(b)

Figure 2-27 The binding constants of pentamidine with octanoate based on 1:1 (a) and 1:2 (b) stoichiometry determined by HPLC. Data were expressed as mean ± S.D. (n=3) and fit into the Sigmoidal regression model in GraphPad7.

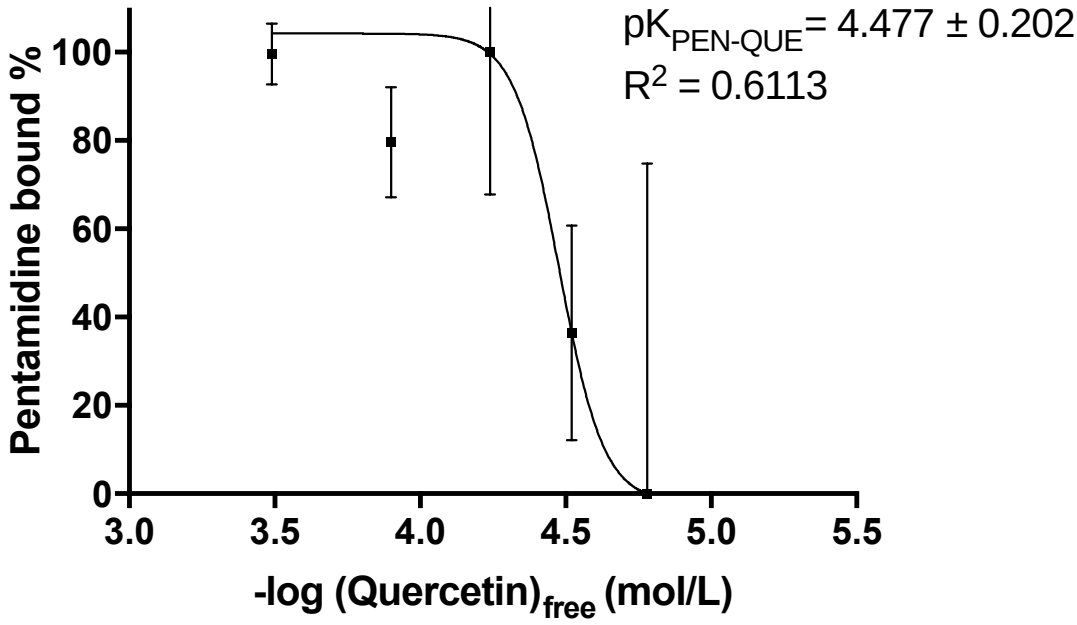

(a)

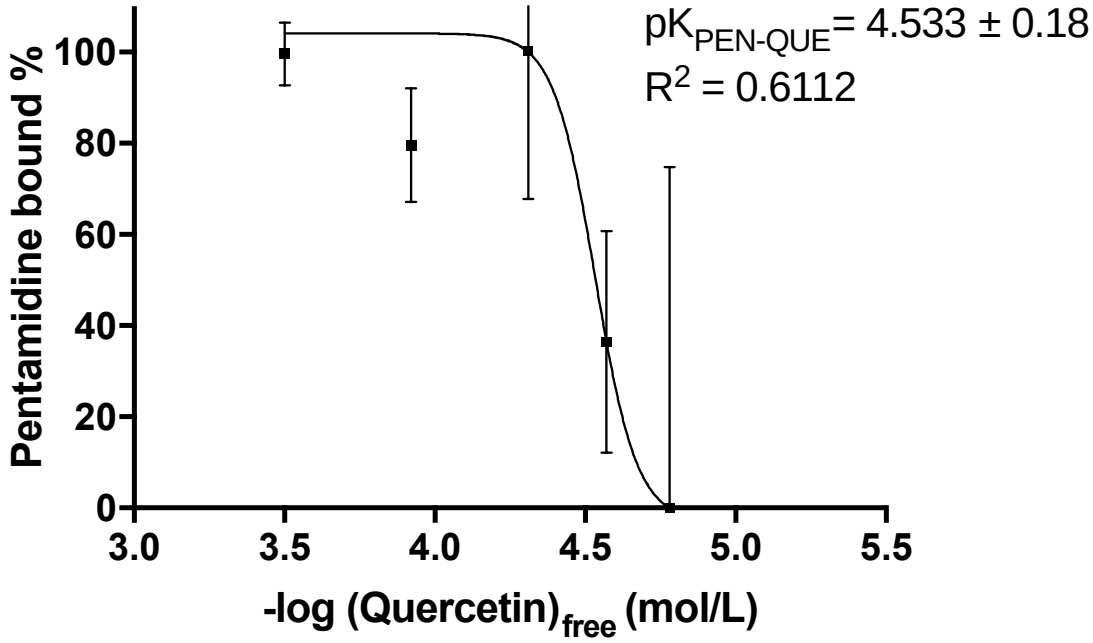

(b)

Figure 2-28 The binding constants of pentamidine with quercetin based on 1:1 (a) and 1:2 (b) stoichiometry determined by HPLC. Data were expressed as mean ± S.D. (n=3) and fit into the Sigmoidal regression model in GraphPad7. The regression curve for pentamidine – quercetin shows poor fit, which could be caused by multiple steps of reactions or non-ion-pairing process between pentamidine and quercetin.

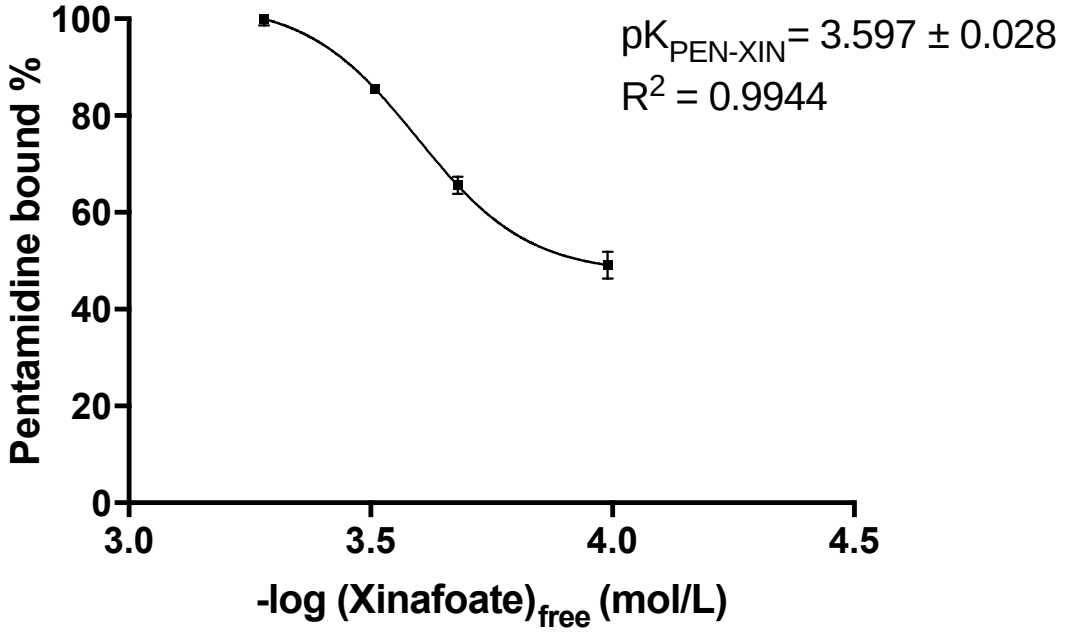

(a)

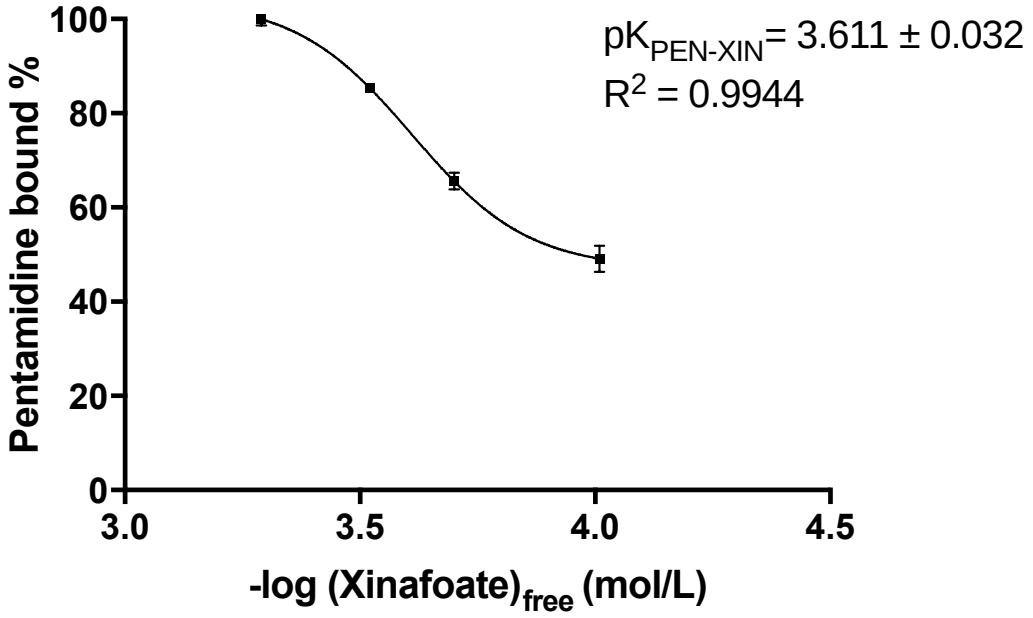

(b)

Figure 2-29 The binding constants of pentamidine with xinafoate based on 1:1 (a) and 1:2 (b) stoichiometry determined by HPLC. Data were expressed as mean ± S.D. (n=3) and fit into the Sigmoidal regression model in GraphPad7.

2.4.6.2 (b) Binding constants determined by fluorescence spectroscopy

The binding constants of pentamidine – xinafoate ion pairs calculated from fluorescence quenching method are 3.922 ± 0.234 and 3.959 ± 0.238 for 1:1 and 1:2 binding ratios of pentamidine and xinafoate (Figure 2-30).

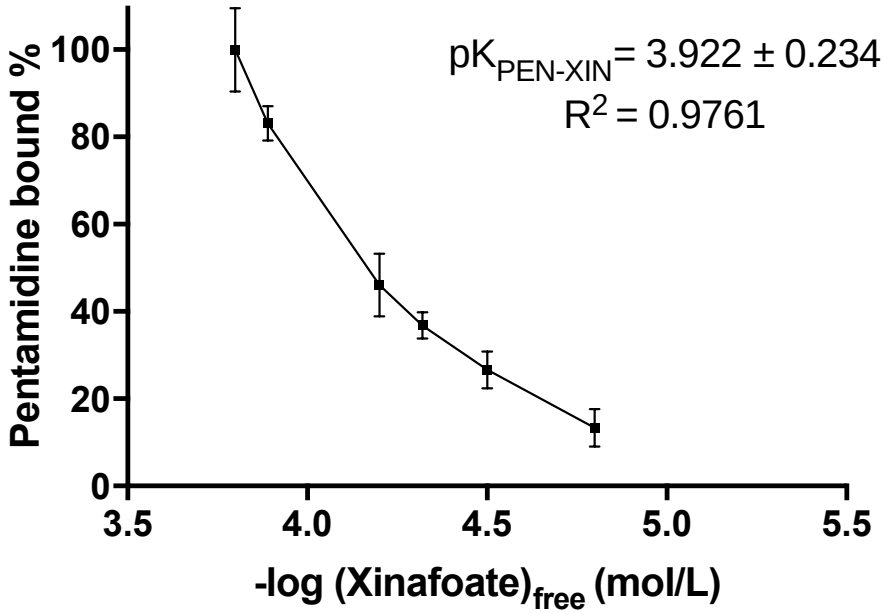

(a)

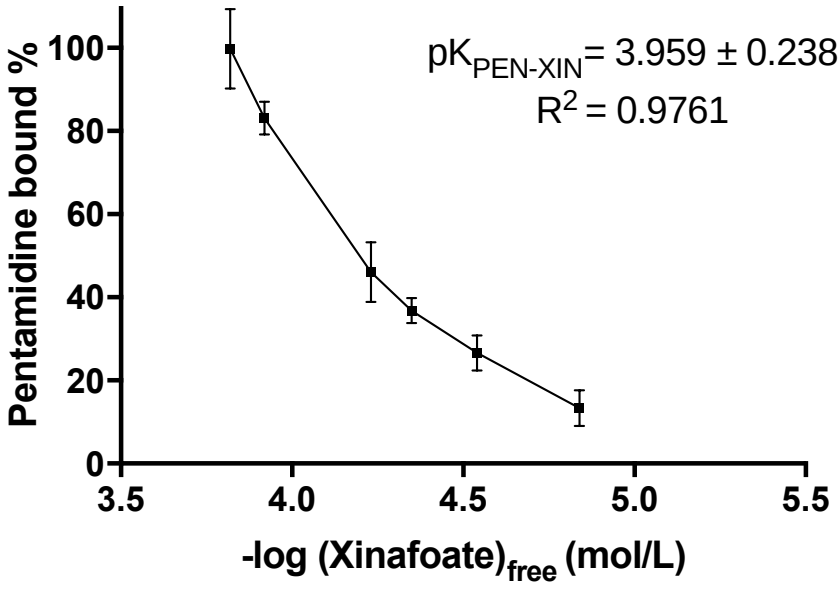

(b)

Figure 2-30 The binding constants of pentamidine with xinafoate based on 1:1 (a) and 1:2 (b) stoichiometry. Data were expressed as mean ± S.D. (n=3) and fit into the Sigmoidal regression model in GraphPad7.

These binding constants calculated from fluorescence method are around 0.3 higher than the binding constants acquired from the previous HPLC method, as shown in Table 2-17.

Table 2-18 A comparison of the binding constants of pentamidine-xinafoate ion-pairs ($pK_{pen\text{-}xin}$) determined by HPLC and fluorescence methods

	$pK_{pen\text{-}xin}$ (Pentamidine:xinafoate = 1:1)	$pK_{pen\text{-}xin}$ (Pentamidine:xinafoate = 1:2)
HPLC	3.597 ± 0.028	3.611 ± 0.032
Fluorescence	3.922 ± 0.234	3.959 ± 0.238
Difference	0.325	0.348
*Statistical significance?	No	No

* Data were analysed by t-test with GraphPad 7 (P<0.05 is considered significantly different).

2.4.7 HySS micro-speciation of pentamidine ion-pairs

2.4.7.1 HySS micro-speciation of pentamidine and taurodeoxycholate

As simulated by HySS, when pentamidine and taurodeoxycholate were added into the solution, +2 ionised pentamidine (PENH2), +1 ionised pentamidine (PENH), +2 ionised pentamidine (PENH2), and pentamidine-taurodeoxycholate ion pair formation (PENTAUH2) were present in the equilibria (Figure 2-31). The concentration of pentamidine was set at 9nM (representing the concentration in the brain) or 8μM (representing the concentration in plasma) (Bronner *et al.*, 1991), and taurodeoxycholate was set at equal or 20 times molar ratios of pentamidine.

When the concentrations of pentamidine and taurodeoxycholate were both at 9nM, pentamidine was predicted to be in the form of +2 ionised (almost 100.0%) at pH 2-8, and there would be almost no (0.01%) ion-pairs in the solution (Figure 2-31a). In the 8-12 pH range, +2 ionised pentamidine would start to decrease, while +1 ionised pentamidine and non-charged pentamidine would increase gradually with the increase of pH. No pentamidine (<0.01%) would be in the form of ion-pairs at pH 8-12. When pentamidine was fixed at 9nM and taurodeoxycholate was increased to 180nM, 0.22% of pentamidine would be in ion-pairs, and the rest vast majority of pentamidine (>99%) would be +2 ionised at pH 2-9. +2 ionised pentamidine would start to decrease from pH above 9 and until 20% at pH 12, while the total of +1 ionised pentamidine and non-charged pentamidine would increase gradually to 80% (Figure 2-34b).

When the concentration of pentamidine was increased to 8µM and taurodeoxycholate was increased to 8 µM or 160 µM, the main forms of pentamidine would be ion-paired and +2 ionised (Figure 2-31c and d). At pH 7.35-7.45, there would be 8.4% of pentamidine and 66.1% of pentamidine in ion-pairs for 8 µM and 160 µM taurodeoxycholate, respectively (Table 2-19). Both ion-pairs and +2 pentamidine would start to decrease from pH above 10, while unionised and uncharged pentamidine decreased.

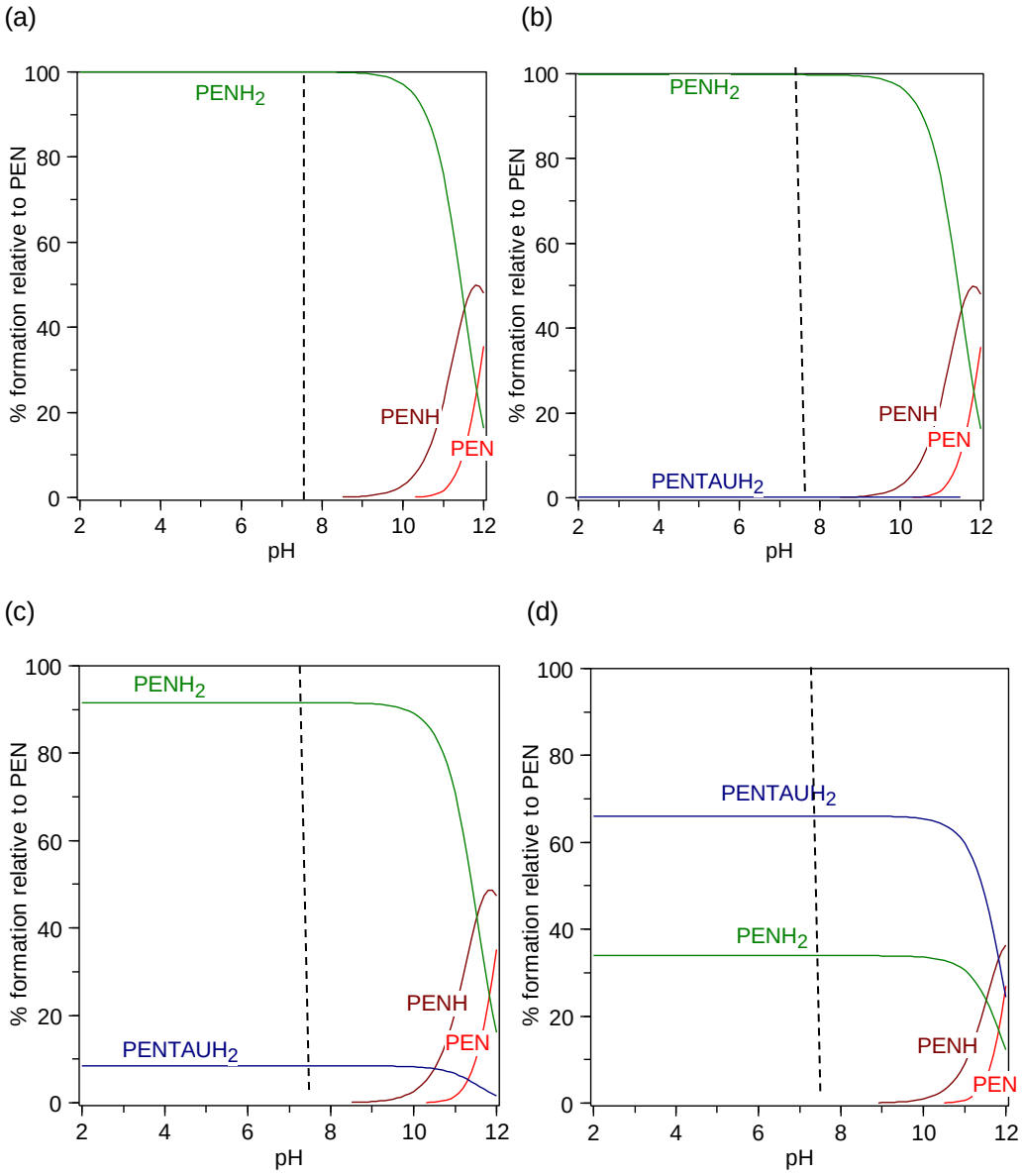

Figure 2-31 HySS speciation plots of (a) 9 nM pentamidine and 9 nM taurodeoxycholate, (b) 9 nM pentamidine and 180 nM taurodeoxycholate, (c) 8µM pentamidine and 8µM taurodeoxycholate, (d) 8 µM pentamidine and 160 µM taurodeoxycholate in solutions as a function of pH range at 2-12. Microspecies of +2 ionised pentamidine (PENH2), +1 ionised pentamidine (PENH), and pentamidine-taurodeoxycholate ion pair formation (PENTAUH2) are present in the equilibria.

2.4.7.2 HySS micro-speciation of pentamidine and octanoate

There would be almost no ion-pairs (<0.01%) in the solution for pentamidine (9 nM) – octanoate (9 nM), and only 0.2% for pentamidine (9 nM) – octanoate (180 nM) in the solution at pH 7.4.

Almost 100% of pentamidine was +2 ionised at pH 2-9. From pH above 9, +2 pentamidine started to decrease while non-charged and +1 pentamidine started to increase in the solution. The percentage of ion-pairs was too low (<0.3%) throughout pH 2-12 therefore it remained invisible in Figure 2-35.

When both pentamidine and octanoate were increased to 8 µM, there were 0.99% of pentamidine in ion-pairs and 99% of pentamidine in +2 ionised form at pH 2-9. More ion-pairs (16.6%) and less +2 ionised pentamidine (83.4%) were present in the solution (pH 2-9) when the concentration of octanoate was increased to 160 µM. Both ion-pairs and +2 ionised pentamidine started to decrease at pH above 9, and until pH 12 where the majority (80%) of pentamidine were neutral or +1 ionised.

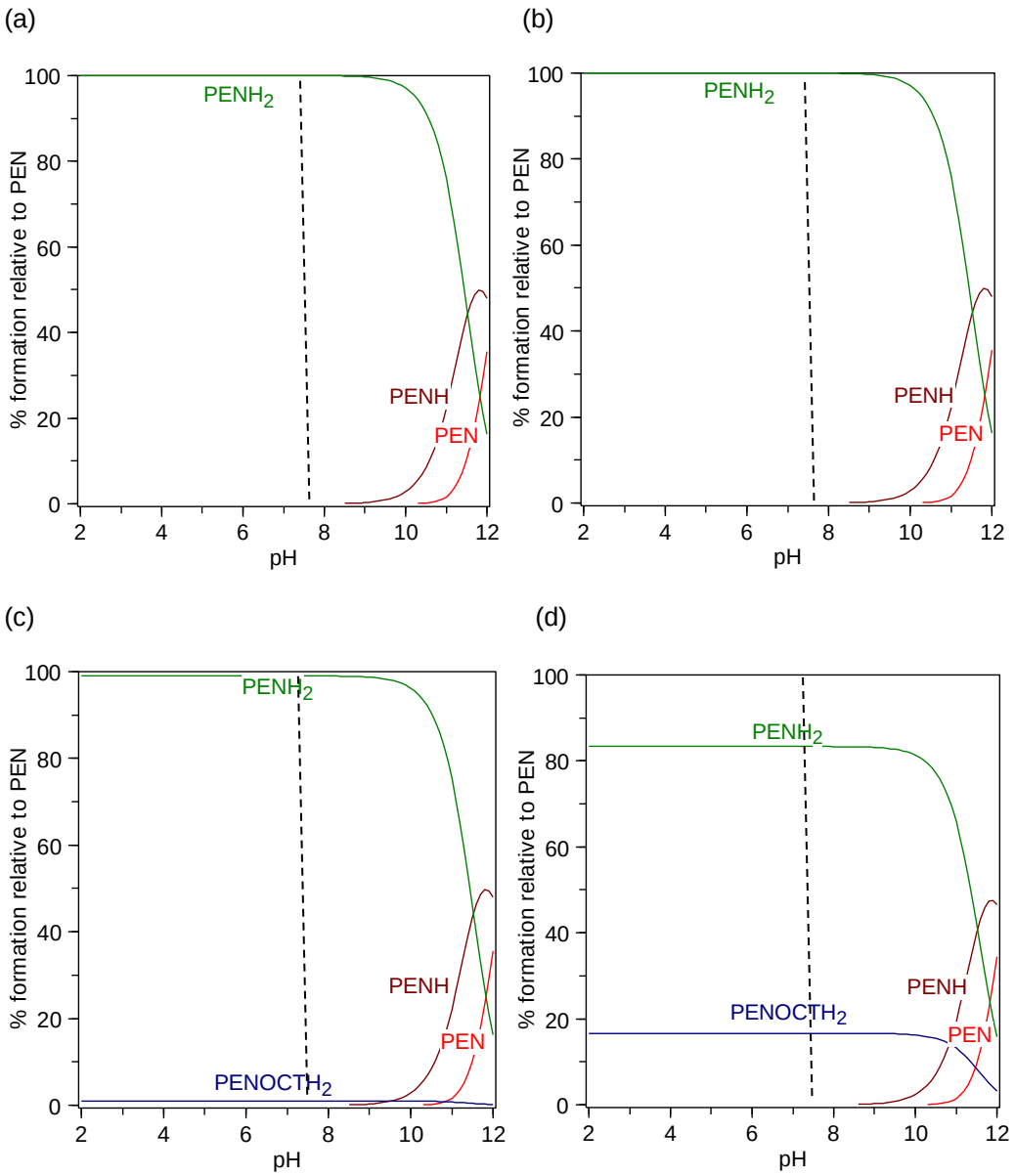

Figure 2-32 HySS speciation plots of (a) 9 nM pentamidine and 9 nM octanoate, (b) 9 nM pentamidine and 180 nM octanoate, (c) 8 µM pentamidine and 8 µM octanoate, (d) 8 µM pentamidine and 160 µM octanoate in solutions as a function of pH range at 2-12. Microspecies of +2 ionised pentamidine (PENH2), +1 ionised pentamidine (PENH), and pentamidine-octanoate ion pair formation (PENOCTH2) are present in the equilibria.

2.4.7.3 HySS micro-speciation of pentamidine and xinafoate

There were almost no ion-pairs (<0.01%) for pentamidine (9 nM) – xinafoate (9 nM) and only 0.07% for pentamidine (9 nM) – xinafoate (180 nM) at pH 2-10. Within this pH range, over 99% of pentamidine were +2 ionised. From pH 10-12, the +2 ionised pentamidine and ion-pairs decreased, while +1 ionised and uncharged pentamidine increased.

For pentamidine (8 µM) – xinafoate (8 µM), there were 3.0% ion-pairs formed and the rest 97.0% of pentamidine +2 ionised at pH 2-10. These two forms started to decrease in the solution at pH

above 10, and +1 and uncharged pentamidine were formed. When changing the concentration of xinafoate from 8 µM to 160 µM, the percentage of ion-pairs increased from 3.0% to 38.5% at pH 2-10. The major forms of pentamidine existed in +2 ionised for pH 2-10, and in +1 ionised and uncharged for pH 10-12.

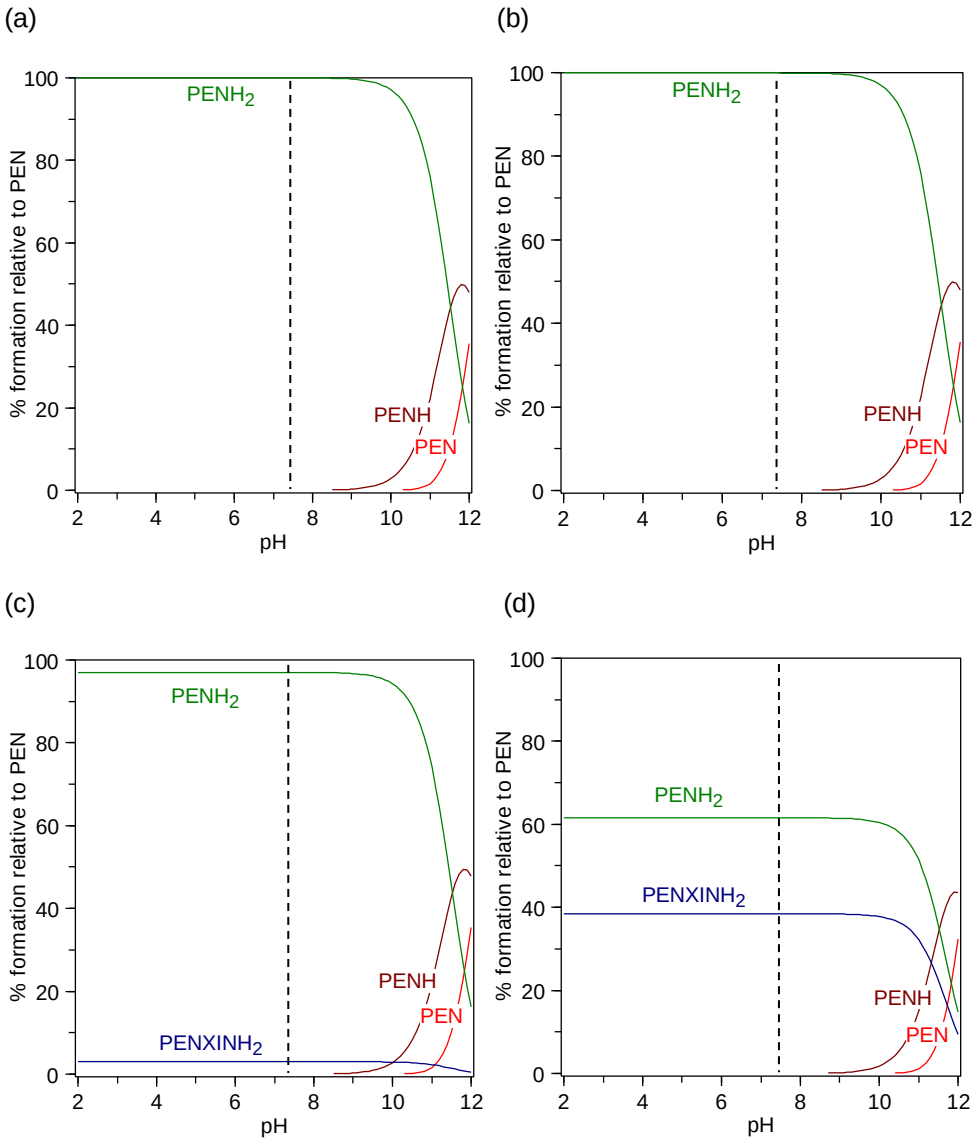

Figure 2-33 HySS speciation plots of (a) 9nM pentamidine and 9nM xinafoate, (b) 9nM pentamidine and 180nM xinafoate, (c) 8µM pentamidine and 8µM xinafoate, (d) 8µM pentamidine and 160µM xinafoate in solutions as a function of pH range at 2-12. Microspecies of +2 ionised pentamidine (PENH2), +1 ionised pentamidine (PENH), and pentamidine-xinafoate ion pair formation (PENXINH2) are present in the equilibria.

2.4.7.4 Simulation of whole-body distribution for pentamidine ion-pairs

The HySS speciation was also utilised in this study to simulate the clinical body distribution upon administration by pentamidine ion-pairs. To treat HAT, pentamidine isethionate (4 mg/kg) is given to patients daily for 2-3 weeks by intramuscular injection or intravenous administration (Burri and Blum, 2017). Given the average human body weight worldwide is 62 kg (average body weight in Africa is 60.7 kg) (Walpole *et al.*, 2012), the dose of pentamidine isethionate on average is 248 mg. Assuming that the 248mg of pentamidine isethionate is dissolved in 50 ml of saline for dilution, then the calculated molar concentration of pentamidine is 8 mM. The detailed calculation process was shown below:

Table 2-19 Simulated concentration of pentamidine in saline for injection

Conditions /assumptions	Molecular weight of pentamidine base = 340 g/mol	Molecular weight of pentamidine isethionate salt = 592 g/mol	The volume of saline for dilution =50 ml	Weight of pentamidine isethionate salt = 248 mg
Calculation of pentamidine concentration =142 mg/(340 g/mol*50 ml)= 0.142 g/(340 g/mol*0.05 L)=0.008 mol/L=8 mM				

After injection, the plasma concentration of pentamidine peaked at 1 h after administration and varied from 0.42 µM (142.8 µg/L) to 13.42 µM (4562.8 µg/L). The median plasma concentration of pentamidine isethionate at day 7 was 4 nM (2.4 µg/L) (Bronner *et al.*, 1991). Pentamidine is highly ionized in a physiological environment so will not cross membranes well and therefore, only achieves a very limited concentration within the central nervous system (Bardal *et al.*, 2011). However, it can be detected within the human cerebrospinal fluid with a concentration of 1.7-3.9 nM (Bronner *et al.*, 1991). To simulate the process of pentamidine ion pairs distribution within the body, the concentration of pentamidine was set at 8 mM (pentamidine in the solution for injection), 8 µM (pentamidine in the plasma) and 4 nM (pentamidine in the brain) in the presence of 20 molar excess of counterions and then analysed by HYSS simulation software.

For pentamidine-xinafoate ion-pairs, the results showed that 99.9% of pentamidine was ion-paired at 8 mM, 38.5% of pentamidine was in ion-pair formation at 8 µM and no (<0.1%) ion pairs existed at 4 nM.

(a) Before Injection (b) In plasma (c) In brain

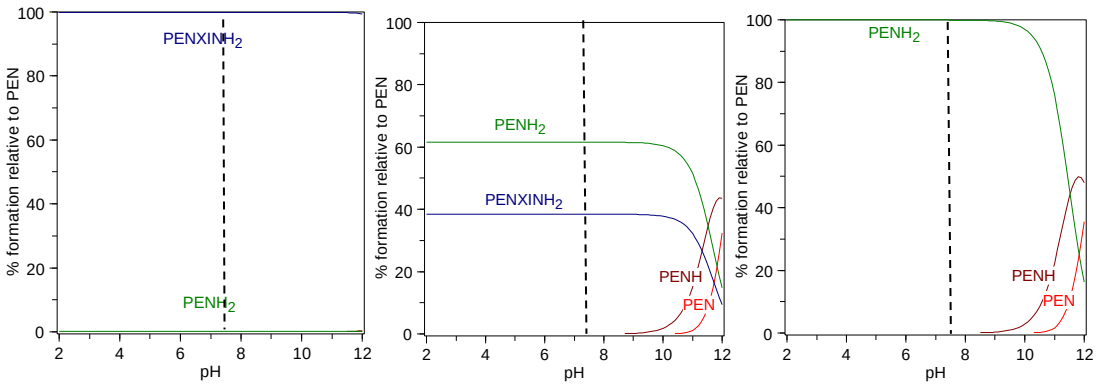

Figure 2-34. HYSS simulation of microspecies percentage as a function of pH range 2-12. PENCIH2 represents the pentamidine ion pair formation, PENH2, PENH, PEN represents +2 pentamidine, +1 pentamidine and uncharged pentamidine respectively. (a) Pentamidine microspeciation in the solution for injection with 8 mM pentamidine and 160 mM counter ions (1:20). 99.9% of pentamidine is formed in ion-pairs at physiological pH. The lines for the PENXINH2 and PENH2 are very close to 100% and 0% in the figure, therefore they are too close to be seen. (b) Pentamidine ion pair ratios in the plasma. Concentrations were set at 8 µM for pentamidine and 160 µM for counter ions. 38.5% of pentamidine is in ion-pair formation at pH 7.4 (c) Pentamidine microspeciation calculated with 4 nM pentamidine and 80 nM counterions in the brain. Less than 0.1% of pentamidine is in ion-pair formation.

2.4.8 Measurement of dissociation constants of pentamidine – xinafoate ion pairs using fluorescence-lifetime imaging microscopy (FLIM)

2.4.8.1 Limitation of detection of pentamidine by FLIM.

Pentamidine was diluted from 8 mM in order to confirm the minimum concentration that could be detected by FLIM method. The decrease of the total number of photons (emission) is related to the dilution of pentamidine. The fluorescence decay curves suggest that pentamidine at 0.8 µM or lower cannot be detected by FLIM (Figure 2-35). In general, the lifetime (τ) does not change with the concentration of molecules. The shorter lifetimes (τ) at higher concentrations of pentamidine can be explained by the self-quench of pentamidine.

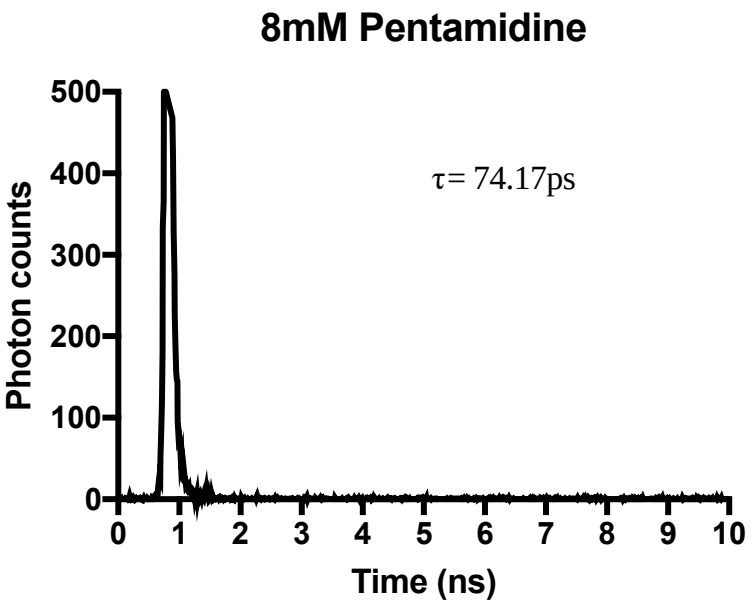
8mM Pentamidine
τ= 74.17ps
Photon counts
Time (ns)
0
100
200
300
400
500
0 1 2 3 4 5 6 7 8 9 10

(a)

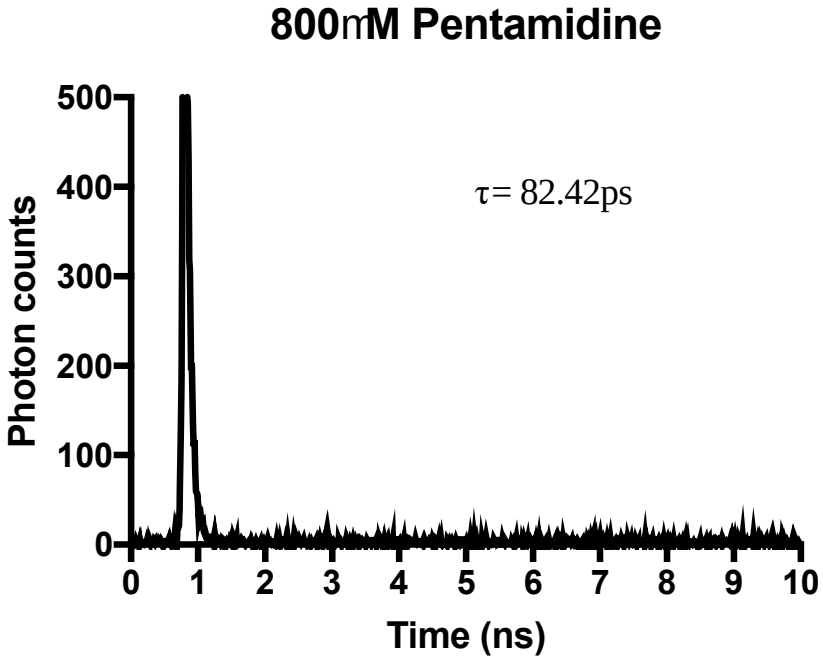
800mM Pentamidine
τ= 82.42ps
Photon counts
Time (ns)
0
100
200
300
400
500
0 1 2 3 4 5 6 7 8 9 10

(b)

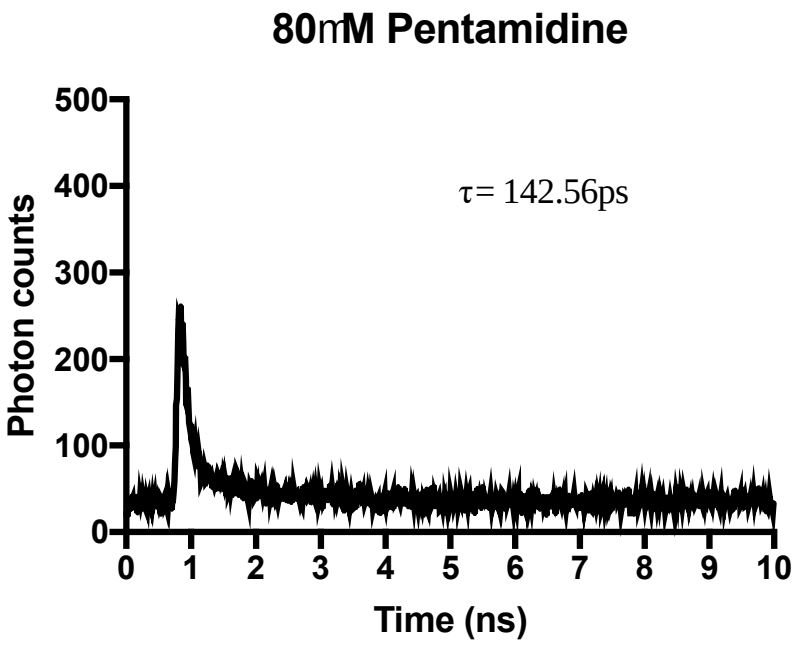
80mM Pentamidine
τ= 142.56ps
Photon counts
Time (ns)
0
100
200
300
400
500
0 1 2 3 4 5 6 7 8 9 10

©

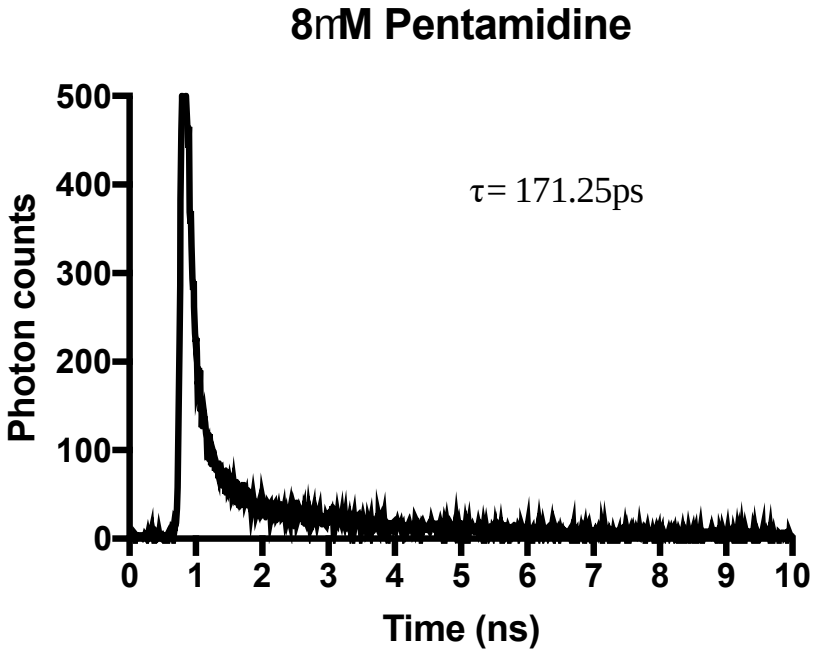
8mM Pentamidine
τ= 171.25ps
Photon counts
Time (ns)
0
100
200
300
400
500
0 1 2 3 4 5 6 7 8 9 10

(d)

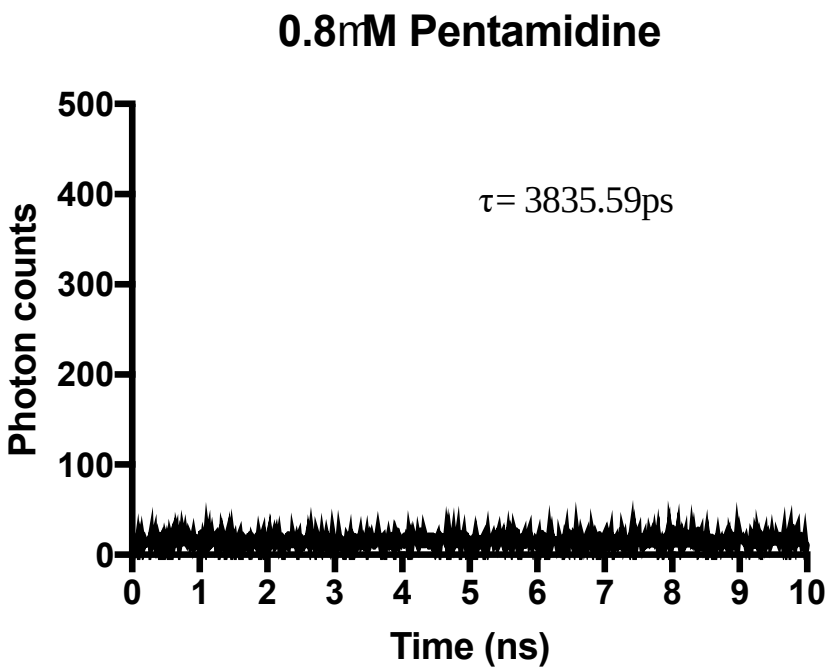

(e)

Figure 2-35 Fluorescence lifetime (τ) of different concentrations of pentamidine dissolved in 50 nM tris buffer (pH 7.4). (a) 8 mM pentamidine, 16329 traced photons in 10 ns, τ= 74.17 ps, χ2= 8.42 (b) 800 µM pentamidine, 12266 traced photons in 10 ns, τ= 82.42 ps, χ2= 1.55. (c) 80 µM pentamidine, 31672 traced photons in 10 ns, τ= 142.56 ps, χ2= 1.24. (d) 8uM pentamidine, 28852 traced photons in 10ns, τ= 171.25, χ2= 1.60 (e) 0.8uM pentamidine, 16132 traced photons in 10ns, τ= 3835.59 ps, χ2= 2.46

2.4.8.2 FLIM detection of pentamidine and xinafoate ion-pairs

The increase of lifetime upon xinafoate addition may suggest a stabilization of the excited state of pentamidine, as shown in Table 2-20. This means that the pentamidine is more stable when it is bound to a counterion. Either or both of the radiative and non-radiative rates of the electrons in the excited state have reduced. The increase of lifetime (τ) for 8 µM/ 8 mM pentamidine and xinafoate ion-pairs may result from the self-quenching of pentamidine.

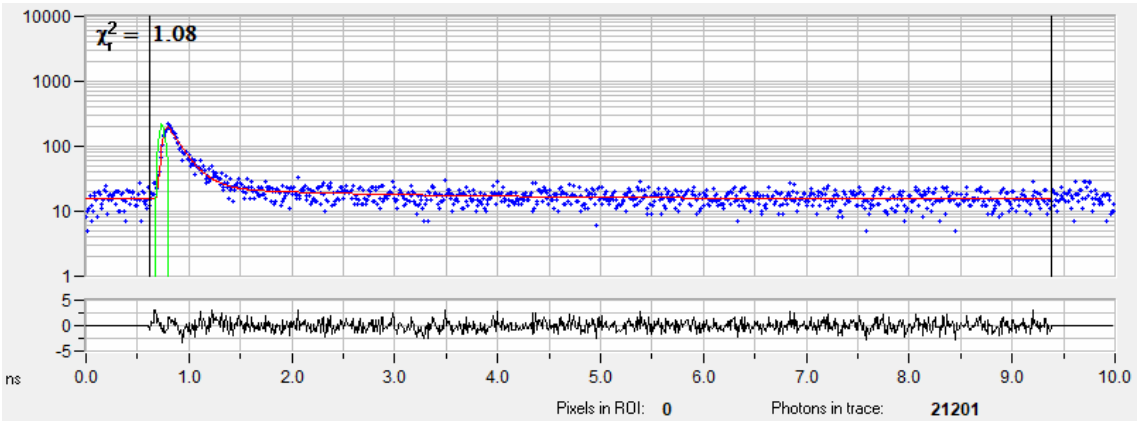

(a)

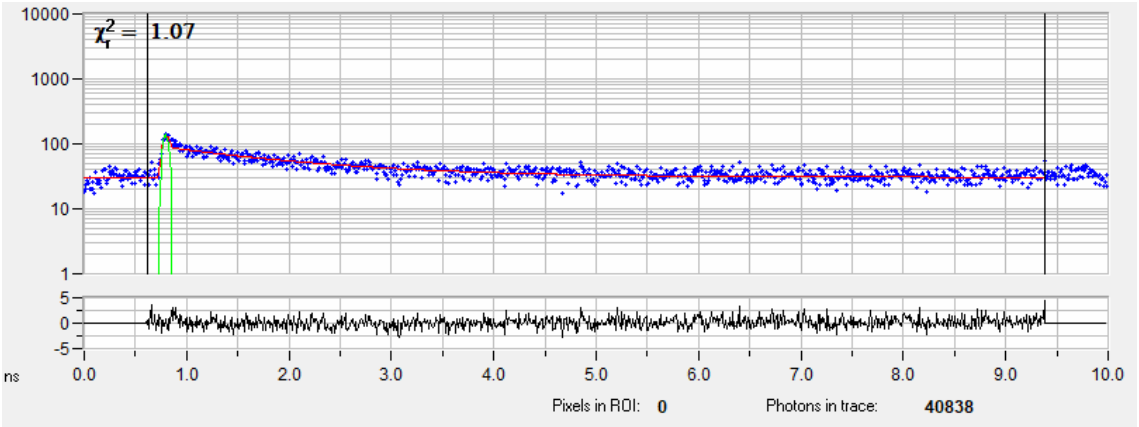

(b)

Figure 2-36 Fluorescence decay curve of pentamidine with xinafoate. (a) 8 mM pentamidine with 160 mM xinafoate in 50 nM Tris buffer (pH 7.4). 21201 traced photons in 10 ns, τ= 147.62 ps, χ2= 1.08. (b) 8 µM pentamidine with 160 µM xinafoate in 50 nM Tris buffer (pH 7.4). 40838 traced photons in 10 ns, τ= 1351.67 ps, χ2= 1.07.

Table 2-20 The lifetime of 8 mM pentamidine with 160 mM xinafoate (pentamidine: xinafoate = 1:20) and 8 µM pentamidine with 160 µM xinafoate (pentamidine: xinafoate = 1:20)

Solutions	Lifetime τ (ps)
8 mM Pentamidine	74.17
8 mM Pentamidine + 160 mM Xinafoate	147.62
8 µM Pentamidine	171.25
8 µM Pentamidine + 160 µM Xinafoate	1351.67

2.5 Discussion

2.5.1 Method validation of HPLC

Pentamidine solutions were measured by HPLC over 10 min at the wavelength of 264 nm. The HPLC method was verified by determining the correlation coefficient and the relative standard deviations of peak areas. The correlation coefficient for the pentamidine calibration curve is higher than 0.9999, which meets the requirement of above 0.99, according to the ICH guideline (*ICH*, 1995). The relative standard deviations of peak areas were within the acceptable limit of 5%. These results confirmed that the HPLC method was a reliable method to quantify pentamidine in aqueous solutions.

2.5.2 Chemical stability of pentamidine solutions

The chemical stability measurement of pentamidine was critical for the octanol and saline shake-flask study, as the pentamidine: counterion solutions would be heated at 37 °C for 24 h, and both degradations of pentamidine and formation of complexes with counterions would contribute to the reduction of pentamidine peak areas by HPLC. The recovery of pentamidine at both 37 °C and at room temperature did not significantly decrease until the 7-days point. In addition, the standard deviations of the retention time of pentamidine were <0.1 min for all the data points. These results confirmed the stability of pentamidine in solutions during the octanol and saline shake-flask study.

2.5.3 Lipophilicity and percentage bound of pentamidine with counterions

The lipophilicity of pentamidine was determined by octanol-saline shake flask method, and the pentamidine concentration was measured in the saline phase by HPLC. The change of pentamidine lipophilicity was explored in the presence of 1:1 to 1:20 of counterions over the time course of 24 h at 37 °C. The possibility of pentamidine self-degradation was excluded as no significant change in pentamidine stability was observed during 7 days.

The result from octanol-saline shake flask experiment revealed that the counterions taurodeoxycholate, octanoate, and xinafoate improved the lipid solubility of pentamidine. Its magnitude of change was the most significant with taurodeoxycholate, followed by octanoate and xinafoate. Also, the increasing concentrations of taurodeoxycholate, octanoate and xinafoate increased the distribution coefficient of pentamidine at pH 7.4 gradually. This magnitude of

change was likely linked to increases in the percentage of pentamidine bound in ion-pairs, as pentamidine ion-pair has higher lipophilicity than pentamidine itself.

Quercetin did not show a similar pattern of change as those three counterions and did not improve the lipophilicity of pentamidine. Also, the lipophilicity of pentamidine in the presence of an excess of quercetin fluctuated dramatically. This indicated that the change of pentamidine lipophilicity with quercetin was a multi-step process and may not result from ion-pairing. Quercetin was chosen as a counterion as it was predicted by MarvinSketch (version 17.28, ChemAxon) to have one negative charge at pH 7.4. Further evaluation revealed that the negatively charged state of quercetin is weak and it is mainly neutral at pH 7.4 (pK_{d1}=7.10 ± 0.12, pK_{d2}=9.09 ± 0.11, pK_{d3}=11.12 ± 0.36 (Herrero-Martínez *et al.*, 2005)). This may be the reason why quercetin could not form ion-pairs with pentamidine, thereby not being able to improve the lipophilicity of pentamidine.

2.5.4 Confirmation of pentamidine-xinafoate ion-pairs with fluorescence method

In the fluorescence spectroscopy study, the correlation coefficients of DAPI and pentamidine standard curves are greater than 0.99, which verified the reliability of the fluorescence method. In addition, the calculated Limit of Quantification was necessary for selecting the concentrations for pentamidine and DAPI with xinafoate in the quenching study. The fluorescence quenching of pentamidine titration with xinafoate further confirmed the formation of ion-pairs. The new peaks and the shift in maximum emission wavelength of DAPI in the presence of xinafoate further confirmed that the amidine groups could bind to xinafoate and form ion-pairs.

2.5.5 The binding affinity of pentamidine ion-pairs

The binding constants calculated from HPLC and fluorescence methods are crucial to understanding the binding affinity of pentamidine ion-pairs. Pentamidine has the strongest binding with taurodeoxycholate, followed by xinafoate, and octanoate. Interestingly, this ranking is different from the predicted Log P (pLog P) of these three counterions: Xinafoate (pLog P = 2.97) > Octanoate (pLog P = 2.70) > Taurodeoxycholate (pLog P = 2.33).

For taurodeoxycholate, its hydroxyl group and sulfonyl hydroxide can both act as hydrogen bond acceptors to attract pentamidine. This may explain the strongest binding of taurodeoxycholate -

pentamidine ion-pairs. A predicted 3D molecular modelling for pentamidine and taurodeoxycholate is shown in Figure 2-37 (a).

For xinafoate and octanoate, only the carboxyl group on their structures can interact with the amidine groups of pentamidine. Xinafoate is more polar than octanoate. Thus it has a stronger binding affinity with pentamidine than octanoate. Their predicted 3D pentamidine ion pair structures are shown in Figure 2-37 (b) and (c).

It is reasonable to conclude that pentamidine is unable to form significant numbers of ion-pairs with quercetin, due to the very limited lipophilicity improvement of pentamidine with quercetin in the shake-flask experiment, as well as the unfit regression of pentamidine - quercetin binding constants analysis. They may, however, have other forms of interaction, rather than ion-pairing.

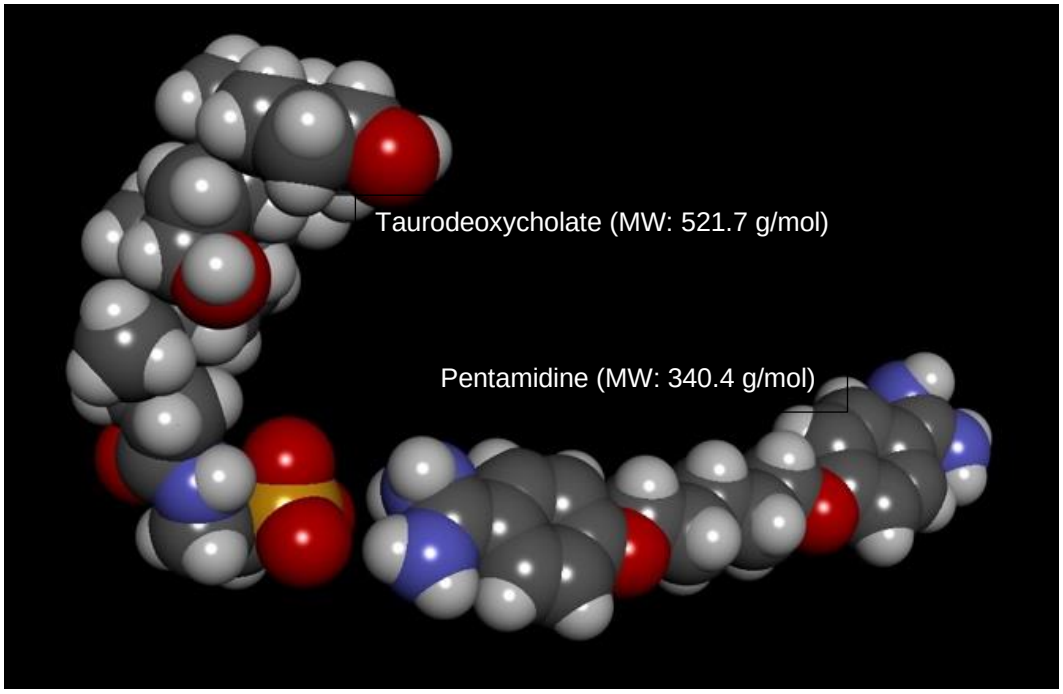

(a)

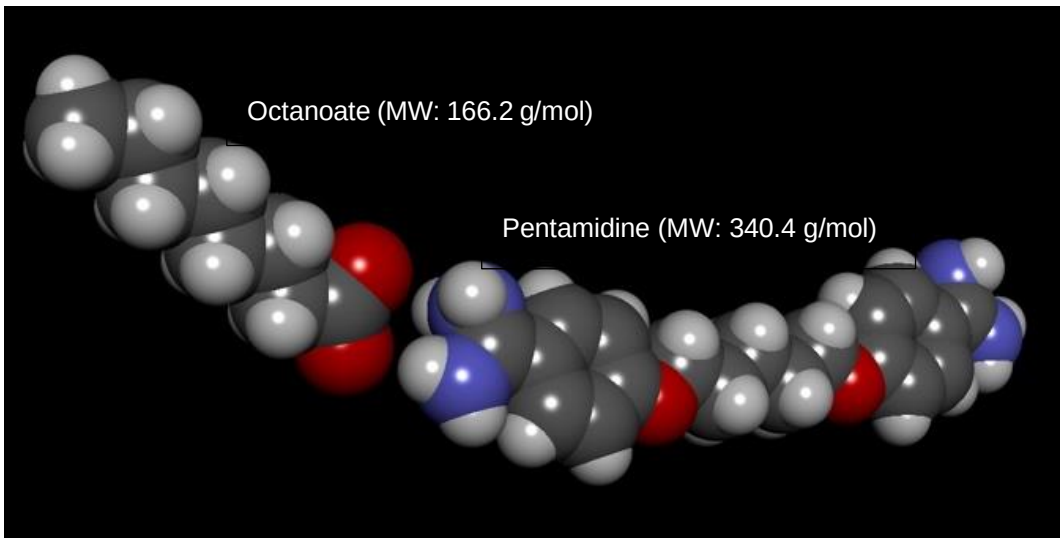

(b)

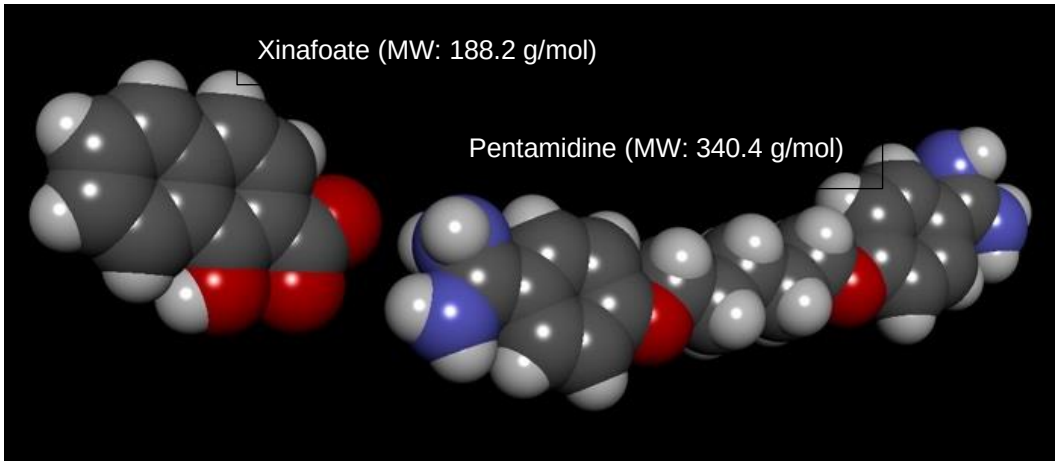

(c)

Figure 2-37 The predicted 3D structures of (a) pentamidine - taurodeoxycholate, (b) pentamidine - octanoate, and (c) pentamidine - xinafoate. The elements were labelled in different colours: red = hydrogen (O), blue = Nitrite (N), orange = sulfate (S), light grey = hydrogen (H), dark grey = carbon (C). The images of pentamidine ion pairs were manually created by Dr David Barlow and displayed using Discovery Studio Visualizer 4.0 (Accelrys Software Inc, San Diego, CA, USA), with the atomic co-ordinates for the individual molecules downloaded from the NIH PubChem resource.

The binding constants (pK_a) of pentamidine with taurodeoxycholate, octanoate, and xinafoate range from 3.1 - 4.1 in this study. Their binding constants much smaller than the reported highly stable metal complexes: $pK_{Cu2+\text{-}EDTA}$= 18.8, $pK_{Mg2+\text{-}EDTA}$= 8.8 (Wang and Tomasella, 2016). Therefore, the strength of pentamidine ion-pairs binding is relatively weak. Therefore, it is important to understand the dissociation of pentamidine ion-pairs for their potential applications in drug development.

2.5.6 Binding sites of pentamidine-xinafoate ion-pair

The NMR data provided insight into the specific binding sites information of pentamidine-xinafoate ion-pair. In the ^{1}H NMR experiment, the splitting and disappearance of the proton peaks assigned to the amidine group of pentamidine provided evidence that pentamidine could bind to xinafoate at the site of its amidine group through hydrogen bonding, a strong non-covalent interaction. In the ^{13}C NMR study, the down shield shift of pentamidine peaks associated with the carbons on the benzene ring indicated that pentamidine might also interact with xinafoate through π-systems interaction.

2.5.7 Percentage of pentamidine bound in ion-pairs by HySS simulation

The HySS simulation results showed that the percentage of ion-pairs (pentamidine in ion-pairs/ total pentamidine) varied with the pH of solutions, the binding constant of pentamidine- counterion complexes, the concentration of initial pentamidine, and the concentration of initial counterions added in the solution. The percentage bound of pentamidine with taurodeoxycholate, octanoate, and xinafoate was predicted by HySS. Percentage bound of pentamidine with quercetin was not predicted as the lipophilicity and binding studies showed that pentamidine would unlikely to form ion-pairs with quercetin. This information will help interpret the results gained from *in vitro* studies in Chapter 3 and Chapter 4. Table 2-21 summarises the percentage of pentamidine bound in ion-pairs with different concentrations of taurodeoxycholate, octanoate, xinafoate at pH 7.4.

Table 2-21 Summary of percentage of pentamidine bound in ion-pairs with different concentrations of taurodeoxycholate, octanoate and xinafoate at pH 7.4

% Pentamidine bound in ion-pairs at pH 7.4	Pentamidine (9 nM)	Pentamidine (8 µM)	Pentamidine (8 mM)
Taurodeoxycholate (9 nM)	0.01%		
Taurodeoxycholate (180 nM)	0.22%		
Taurodeoxycholate (8 µM)		8.4%	
Taurodeoxycholate (160 µM)		66.1%	
Octanoate (9 nM)	<0.01%		
Octanoate (180 nM)	0.2%		
Octanoate (8 µM)		0.99%	
Octanoate (160 µM)		16.6%	
Xinafoate (9 nM)	<0.01%		
Xinafoate (180 nM)	0.07%		
Xinafoate (8 µM)		3.0%	
Xinafoate (160 µM)		38.5%	
Xinafoate (160 mM)			99.9%

2.5.8 Dissociation of pentamidine-xinafoate ion-pair

The florescence lifetime imaging microscopy were utilized in this study to understand the dissociation of pentamidine ion-pairs upon dilutions in physiological compartments. Three concentrations (8 mM, 8 µM, and 8 nM) of pentamidine were selected for the dissociation of pentamidine - xinafoate ion-pair study in order to mimic the concentrations range of pentamidine in clinic. For pentamidine, the human plasma concentration of pentamidine peaked at 1 h after administration at a varied range from 0.42 µM (142.8 µg/L) to 13.42 µM (4562.8 µg/L) with a median plasma concentration of pentamidine isethionate at day 7 was 4 nM (2.4 µg/L) after injection (Bronner *et al.*, 1991). Unfortunately, pentamidine at 0.8 µM or less was not detectable by fluorescence lifetime imaging microscopy. Nevertheless, the change of lifetime of pentamidine upon the addition of xinafoate further proved the formation of pentamidine - xinafoate ion pairs at 8 mM and 8 µM.

2.6 Conclusion

The different methods utilised in this study helped us to understand the lipophilicity, binding affinity, binding sites, percentage bound, and dissociation of pentamidine upon forming ion-pairs with taurodeoxycholate, octanoate, quercetin and xinafoate. A summary of changes to the properties of pentamidine is listed in Table 2-22 below.

Table 2-22 The change of pentamidine physicochemical parameters through ion-pairing with taurodeoxycholate, octanoate, quercetin, and xinafoate

Physicochemical parameters	**Effect**
Lipophilicity (log D)	The magnitude of change: taurodeoxycholate > octanoate > xinafoate > quercetin
Binding constants (pK_a)	Pentamidine-taurodeoxycholate > pentamidine-xinafoate> pentamidine-octanoate
Binding sites (only xinafoate was assessed)	The amidine groups on pentamidine could bind to xinafoate and form ion-pairs
Percentage bound	The percentage of pentamidine existing as an ion pair is extremely low (<1%) when pentamidine is at 9 nM, even in the presence of excess counterions; The percentage of pentamidine bound with counterions ranges from 1% to 66%, depending on the type and concentrations of counterions.
Dissociation rate (only xinafoate was assessed)	Not determined due to method limitations, however, FLIM confirmed the formation of ion-pairs

Xinafoate was selected as a model counterion for pentamidine, and it has been extensively studied with multiple techniques in this chapter. The HPLC, fluorescence, binding studies and NMR results confirmed the formation of pentamidine-xinafoate ion-pairs. Based on the improved lipophilicity of pentamidine with taurodeoxycholate, octanoate, and xinafoate in the octanol-saline shake-flask study, we can predict that pentamidine could also form ion-pairs with taurodeoxycholate and octanoate. The improved lipophilicity of pentamidine by forming ion-pairs

with taurodeoxycholate, octanoate, and xinafoate should be able to enhance the passive diffusion of pentamidine across lipid membranes. The results from the octanol-saline shake-flask and binding studies indicate that quercetin does not improve the lipophilicity of pentamidine and that quercetin cannot form ion-pairs with pentamidine.

The results of the transport of pentamidine ion-pairs across biological membranes and their interactions with hOCT1 and P-gp are explained in chapter 3 and chapter 4, respectively.

Chapter 3 Interactions of Pentamidine Ion-pair Complexes with hOCT1 Transporter at the Blood-Brain Barrier

3.1 Chapter overview

In this chapter, we will examine the interaction of pentamidine ion-pairs with biological membranes using human blood-brain barrier cells and *xenopus* oocytes expressing hOCT1. We will first establish and verify these cell models and then study the accumulation of pentamidine ion-pairs across the blood-brain barrier as well as their interactions with hOCT1.

3.2 Introduction

The blood-brain barrier (BBB) is critical for maintaining homeostasis and preventing toxins from entering the central nervous system (CNS). As a result, this protective barrier remains the biggest obstacle in the development of effective therapies for treating neurological disorders. It is estimated that more than 98% of small molecules (<500 Da) and nearly all large molecules are extruded by the BBB. Thus they cannot reach the CNS at an effective therapeutic concentration (Pardridge, 2005). Increasing doses of drugs administered systemically could improve the final concentrations reached at the CNS. However, this can cause serious side effects and potentially irreversible brain damage (Pardridge, 2012). Therefore, for molecules that are effective but unable to reach the CNS at high enough concentrations, the focus of drug development is to increase their permeability across the BBB whilst not eliciting toxicity.

As mentioned in Chapter 2, for drugs to reach the CNS in the brain, ideal drug candidates usually possess certain physicochemical properties (e.g., sufficient lipid solubility, small size) and a preferable pharmacokinetic profile (e.g., low efflux by P-gp transporter). According to Lipinski's "Rule of Five" (Lipinski *et al.*, 2001; Pajouhesh and Lenz, 2005), for molecules to be successful in penetrating the CNS they must have the following physical properties: (1) molecular weight ≤ 500 Da, (2) Log P (lipophilicity) ≤ 5, (3) sum of OHs and NHs ≤ 5, (4) sum of Ns and Os ≤ 10 and (5) rotatable bonds ≤ 10.

In addition to the physicochemical characteristics, membrane transporters play crucial roles in the pharmacokinetics (absorption, distribution, metabolism, and excretion) of drugs and ultimately

influence their therapeutic efficacy. It is often assumed that improving the lipophilicity of molecules can enhance their lipid solubility. However, this may inhibit drugs from utilising influx transporters such as OCT1 (Ahlin *et al.*, 2008) and therefore decrease their therapeutic efficiencies.

Generally, membrane transporters are divided into two super-families: ATP-binding cassette (ABC) transporters and carrier solute (SLC) transporters. Locations and levels of expression of membrane transporters vary in different organs. Transporters that have been identified at the human BBB are the ABC transporters (P-gp, BCRP, MRPs) and the SLC solute carriers (amino acid transporters, glucose transporters, OATPs, OATs, OCTs, OCTNs, nucleosides transporter, peptide Transporters, MCTs, MATE, PMAT). A comprehensive description of membrane transporters at the BBB can be found in Chapter 1.

Some efflux membrane transporters such as P-gp have been selected as drug targets. For example, in order to eliminate the extrusion by P-gp transporter at biological membranes, a P-gp inhibitor may be co-administered with a P-gp substrate. Kemper (*et al.*, 2004) found that the absorption of paclitaxel into wild-type mice brain was 5-fold higher with LY335979 (a P-gp inhibitor), although the process of inhibiting P-gp was reversible and its effect faded rapidly when the plasma concentration of the inhibitor declined.

More recently, there has been an increasing interest in selecting SLC transporters as drug targets (Lin *et al.*, 2015). One way of enhancing the absorption of drugs is to mimic the structures of influx transporter substrates. As dopamine could not cross the BBB, L-DOPA (a prodrug of dopamine) was developed to target LAT-1 (SLC3A2) transporter at the BBB for the treatment of Parkinson's disease (Sanchez-Covarrubias *et al.*, 2014). Despite the emerging opportunities in targeting SLC transporters for drug delivery, the mechanisms of transport are still being understood.

For pentamidine, its limited efficacy in treating the *Trypanosoma brucei gambiense* type of Human African Trypanosomiasis (HAT) after parasites have invaded the CNS is due to its limited ability to cross the BBB. This process involves multiple influx and efflux transporters (L. Sanderson *et al.*, 2009). Pentamidine has been found to be effluxed by P-gp and MRP transporters at the BBB (L. Sanderson et al. 2009). In addition, Ming (et al. 2009) found that pentamidine is a substrate of hOCT1 in transfected Chinese hamster ovary (CHO) cells. Sekhar (et al. 2017) found that

pentamidine is influxed across the BBB by the OCT1 expressed in human brain endothelial cells (hCMEC/D3) and mouse blood-brain barrier cells (bEnd.3).

Ion-pairing strategy has been shown to improve drug delivery across skin, lung and intestinal membranes (Miller *et al.*, 2009b; Suresh and Paul, 2011b; Hui *et al.*, 2016; Song *et al.*, 2016; Benaouda *et al.*, 2018). It has been proved in Chapter 2 section 2.4.3 that the selected counterions could improve the lipophilicity of pentamidine. However, it is not yet known if the presence of the counter ion in the solution or the ion-pair complex itself would also affect the ability of pentamidine to interact with the membrane transporter hOCT1. By analysing 26 published OCT1 substrates (Figure 3-1) we found that the majority of OCT1 substrates have one positive charge at physiological pH and a relatively small molecular weight (<400 Da).

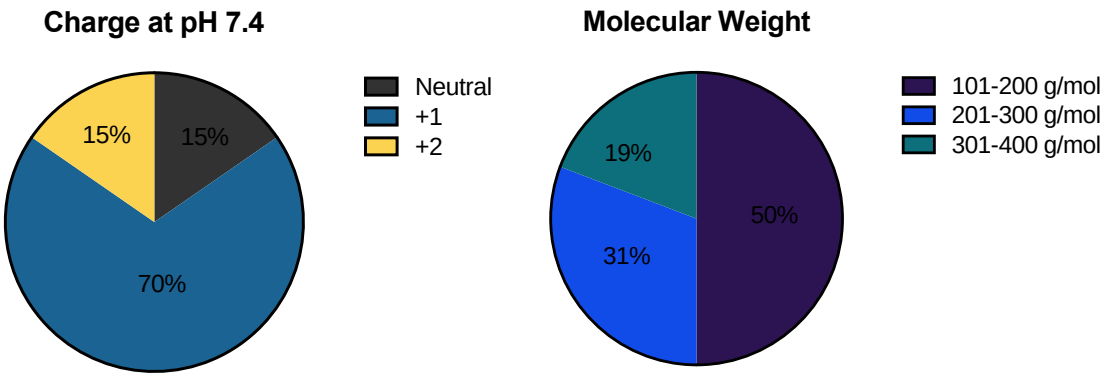

Figure 3-1 Charge and molecular weight of 26 published OCT1 substrates (source: NCBI database, 1989-2016).

In the physicochemical study (Chapter 2 section 2.4.5), we found that one of the selected counterions, xinafoate, bound to the amidine group of pentamidine through hydrogen bonding and increased its log $D_{7.4}$ by 68.9%. While the physicochemical profile of ion-pairs seems promising for enhancing the permeability of drugs across lipid membranes of the BBB, their biological interactions with membrane transporters at the BBB are not understood. In fact, few drug molecules that were discovered at the early stage of drug discovery crossed cell membranes without interacting with transporters (Lee, Lean and Limenta, 2009). Further clarification of this issue will contribute to the design of a safe and effective ion-pair drug delivery method for pentamidine and other diamidines across the BBB.

The hypothesis of this study is that the interaction of pentamidine with hOCT1 at the BBB would be altered through ion-pairing. The *lavies xenopus* oocyte system was selected to examine the

interaction of pentamidine ion-paired complexes with hOCT1. The *xenopus* oocyte is an established single-cell model for expressing heterologous proteins. Its robust translational capacity makes it an ideal model to study proteins (e.g., membrane transporters, ion channels and receptors (Markovich, 2008a; Lin-Moshier and Marchant, 2013; Marchant, 2018; Pike *et al.*, 2019).

The overall aim of this chapter is to examine if the ion-pairing of pentamidine increases the transport of pentamidine by hOCT1.

The objectives are as follows:

- To measure the toxicity of pentamidine-taurodeoxycholate, pentamidine-octanoate, pentamidine-quercetin, and pentamidine-xinafoate in hCMEC/D3 cells with MTT assay.
- To determine the retention of [^{3}H]pentamidine with taurodeoxycholate, octanoate, quercetin, and xinafoate in hCMEC/D3 cells by measuring the volume of distribution (V_d) of [^{3}H]pentamidine with drug accumulation assay and the concentrations of protein with bicinchoninic acid (BCA) assay.
- To simulate the interaction of pentamidine with hOCT1 membrane transporter using *in silico* molecular docking.
- To establish a hOCT1 single transporter expressing model utilising *xenopus* oocytes
- To confirm the identity and functional expression of hOCT1 in *xenopus* oocytes through DNA sequencing, gel electrophoresis of DNA and RNA, and influx of the hOCT1 substrate - [^{3}H]acetylcholine into *xenopus* oocytes expressing hOCT1
- To determine the interaction of [^{3}H]pentamidine ion-pairs with hOCT1 by measuring the influx of [^{3}H]pentamidine into *xenopus* oocytes expressing hOCT1

3.3 Materials and Methods

3.3.1 Materials

Ampicillin sodium salt was purchased from Calbiochem, gentamicin sulphate from Apollo Scientific, HiSpeed Plamid Midi Kit was purchased from Qiagen (Manchester, UK), mMESSAGE mMACHINE T7 Transcription Kit, 3M Sodium Acetate (pH 5.5), 100mm square petri dishes were purchased from Thermo Fisher Scientific (Paisley, UK), 100mM Sodium Pyruvate, tris base were

purchased from Fisher Scientific (Leicestershire, UK), Collagenase Type IV was purchased from Gibco, UltraPure Agarose from Invitrogen Life Technologies, 0.5M EDTA solution was purchased from Severn Biotech (Worcestershire, UK), magnesium sulphate heptahydrate (>=99.5%), potassium chloride were bought from AnalaR, calcium chloride dihydrate (>=99.0%), sodium chloride (>=99.5%), sodium dodecyl sulfate (>=92.5%), quinine were purchased from Sigma-Aldrich, sodium octanoate (>=99.0%), calcium nitrate tetrahydrate, quercetin (>=95.0%), HEPES (>=99.5%), sodium taurodeoxycholate hydrate (>=95.0%), LB Agar, boric acid (>=99.5%) were from Sigma Life Science, 1-Hydroxy-2-naphthoic acid (>=97.0%) from Aldrich Chemistry. Ethidium Bromide Solution (10mg/ ml) was bought from Alfa Aesar, 3.5'' tubes from Drummond Scientific, Ultima Gold was purchased from PerkinElmer (Bucks, UK), 1kb DNA ladder, 6x loading dye, NotI enzyme, HindIII enzyme and EcorI enzyme were purchased from Promega, hydrochloric acid and sodium hydroxide standard solution were purchased from Fluka Analytical.

Radiolabelled chemicals

[^{14}C]sucrose (2.5 mCi in 25 ml, 536 mCi/mmol) was purchased from Moravek Biochemicals and [^{3}H]pentamidine (5 mCi in 5 ml, 31.9 Ci/mmol) was custom radiolabelled by Moravek Biochemicals, [^{14}C] D-glucose (250-360 mCi/mmol) and [^{3}H]acetylcholine iodide (50-100 mCi/mmol) were purchased from PerkinElmer (Bucks, UK).

3.3.2 Cell Culture

The immortalized human brain capillary endothelial cell line, hCMEC/D3 is a commercially available *in vitro* BBB model (Poller *et al.*, 2008; Sekhar *et al.*, 2017, 2019). It was previously utilised to explore the transport of pentamidine and its interaction with OCT1 and P-gp (Sekhar et al., 2017) as well as the effect of pentamidine reformulation with Pluronics (Sanderson *et al.*, 2019). To examine if pentamidine, in the presence of counterions, would be able to cross the BBB more efficiently, we utilised this well-established BBB model. In order to do this, we first needed to confirm that the cells remained viable during the exposure with counterions with a cytotoxicity assay. We could then assess the effect of each of the counterions on the human BBB accumulation of pentamidine.

Culturing method

All the hCMEC/D3 cells used in this study were between passage 29-35. The hCMEC/D3 cells were cultured in T-75 (75 cm^2) flasks or 96-well plates in cell medium at 37 °C with 5% CO_2. The cell media was composed of sterile-filtered Clonetics EGM Endothelial Cell Growth Medium, 1M HEPES (1%), Penicillin-Streptomycin (100 units/ml of penicillin, 100 µg/ml of streptomycin), Foetal Bovine Serum (2.5%), and growth factors (RhfGF-B, R3-IGF-1, VEGF, rhEGF and hydrocortisone). The cell medium was changed every 2-3 days.

For splitting, the hCMEC/D3 cells were passaged when they were 80-90% confluent (areas of cells covered/areas of the T-75 flask), judged by visual observation under the microscope. The T-75 flasks and 96-well plates were pre-coated with rat collagen type I (0.1 mg/ml) for 2 h at 37 °C. Then the residual collagen was removed with three times of wash by PBS^+. The seeding density was 25,000 cells/cm^2, and the hCMEC/D3 cells usually reached 80-90% confluency around 3-4 days. For cell accumulation assay, the cells were left for further 3-4 days to differentiate.

3.3.3 Cytotoxicity Assay

The viability of hCMEC/D3 cells in the presence of taurodeoxycholate, octanoate, quercetin and xinafoate was measured using the MTT (3-(4,5-dimethylthiazol-2-yl)-2,5-diphenyltetrazolium bromide) assay. This assay is a widely used colourimetric assay to determine cell viability or cytotoxicity. This assay measures cell viability through the determination of the mitochondrial function of cells by measuring the activity of mitochondrial enzymes. In this assay, MTT is reduced to purple formazan by NADH. The purple formazan can be measured by light absorbance at a particular wavelength. MTT assay is convenient, reproducible, and safe to use. However, the MTT formazan could interfere with the background, which causes overestimation of the cell viability (Aslantürk, 2018). To account for the inaccurate estimation of cytotoxicity caused by varied numbers of viable cells, the cytotoxicity of hCMEC/D3 cells was investigated by MTT assay and BCA assay (see 3.3.5).

Confluent monolayers of hCMEC/D3 cells (passage 29-33) were incubated with different concentrations (0, 0.1, 1, 10, 20, 50, 100 and 200 µM) of each of the counterions in the accumulation buffer for 2 h at 37 ˚C. At the end of this incubation time, the buffer was aspirated,

and the wells were refilled with pre-warmed MTT (1 mg/ml) in DMEM without phenol red and the plates placed in an incubator with 5% CO_2 at 37 ˚C for 4 h. Following this, the MTT solutions were replaced with 100 µl of propan-2-ol. After 5 min, the viability of cells could be determined by measuring the absorbance of samples at 540 nm using a Labsystems Multiscan reader with the Ascent software. The absorbance was corrected by protein concentrations with BCA assay (See section 3.3.5 for details of BCA assay). Cells viability was compared to the control (i.e. 0 µM of counterions in the accumulation buffer) and results were expressed as percentage viability.

3.3.4 Accumulation of [^{3}H]pentamidine ion-pairs in hCMEC/D3 cells

The accumulation of [^{3}H]pentamidine and [^{14}C]sucrose (0.9 µM), was measured by cell accumulation assay on a single monolayer of hCMEC/D3 cells in 96-well plates. The [^{14}C]sucrose here acted as a marker for non-specific binding, membrane integrity and measurement of extracellular space. Two different test concentrations of pentamidine were utilised in the absence and presence of 20 times molar ratios of counterions: a low concentration (9 nM) of just [^{3}H]pentamidine in the accumulation buffer and a higher concentration (8 µM) which was composed unlabelled and radiolabelled pentamidine together. The buffer was shaken at 120 rpm over 2 h at 37°. The selected concentrations of pentamidine were based on the clinical concentration of pentamidine achieved in plasma after intramuscular injections at 3.5 - 4.5 mg pentamidine base per kg body weight. The plasma concentration of pentamidine peaked at 1h after administration, ranging from 0.42 µM (142.8 µg/L) to 13.42 µM (4562.8 µg/L), and the median plasma concentration of pentamidine isethionate at day 7 was 4 nM (2.4 µg/L) (Bronner *et al.*, 1991).

The accumulation buffer was removed at 5, 20, 30, 60 and 120-min time points, immediately followed with three washes with ice-cold PBS^+ to terminate the transport. Then the cells were lysed in 200 µl 1% Triton x-100 and shaken at 120 rpm for 1 h. The 100 µl of the lysates were transferred to a scintillation vial with 4 ml of scintillation solution to count for radioactivity. The radioactivity was measured as disintegration per min (dpm) by Packard Tri-Carb 2900TR liquid scintillation counter (Perkin-Elmer, Beaconsfield, UK). The radioactivity of the lysates was corrected with protein concentrations measured by BCA and background dpm of the accumulation buffer.

3.3.5 BCA protein assay

The bicinchoninic acid assay (BCA assay) was introduced by Paul K. Smith in 1985, and since then, this method has become one of the most popular methods to quantify total protein. Basically, the chelation of copper with protein formed a blue complex and cuprous cation (Cu^{1+}) in an alkaline environment. Then the BCA reagent reacts with Cu^{1+} and generates a water-soluble copper complex in purple colour. This purple complex can be measured at 550-570 nm with less than 10% loss signal, and it has the strongest signal at 562 nm (Smith *et al.*, 1985).

A standard curve was generated using the following bovine serum albumin (BSA) concentrations (0, 100, 150, 200, 250, 300 g/ml) and prepared in triplicate and absorption measured on a Labsystems Multiscan reader at 562 nm. In this study, the rest of the 100 µl cell lysates from the accumulation assay were used to quantify the total protein by BCA protein assay. The absorption of proteins was measured at 562 nm on a Labsystems Multiscan reader with Ascent software. Then the measured absorptions of cells lysates were converted to protein (mg/ml) from the standard curve.

3.3.6 Calculations and expression of results

Results of accumulated radioactivity were expressed as a volume of distribution (V_d), which was calculated by the ratio of dpm/mg protein to dpm/µl buffer (Equation 3-1) (Watson *et al.*, 2012; Sekhar *et al.*, 2017).

$$V_d = \frac{DPM/mg\ protein}{DPM/\mu l\ accumulation\ buffer} \qquad \text{(Equation 3-1)}$$

Background values of the accumulation buffer and V_d values of [^{14}C]sucrose were subtracted in order to correct the V_d of [^{3}H]pentamidine. The protein amount (mg) was acquired from BCA protein assay. The results were expressed as mean values in 6 replicates/wells per 96-well plate from at least 3 different passages of cells. The effect of the counterion was expressed as a percentage change.

3.3.7 Molecular Docking of pentamidine onto hOCT1

The Molecular Docking for pentamidine into hOCT1 transporter was completed by Dr Khondaker Miraz Rahman's group from Medicinal Chemistry at King's College London. Molecular docking

was performed using CDOCKER (Discovery studio version 4.0), a CHARMm based docking tool, where annealing molecular dynamics were simulated to each orientation. Based on the CDOCKER energy, the ligand poses were sorted, and then the most favourable binding (the most negative value) was retained. Due to the unavailability of the structure for hOCT1, 4ZW9 (the crystal structure for human GLUT3) (Deng *et al.*, 2015) from Protein Data Bank was selected. The crystal structure of 4ZW9 is similar to the structure of hOCT1. The binding site of pentamidine to 4ZW9 was chosen based on the least energies needed for docking into different binding cavities.

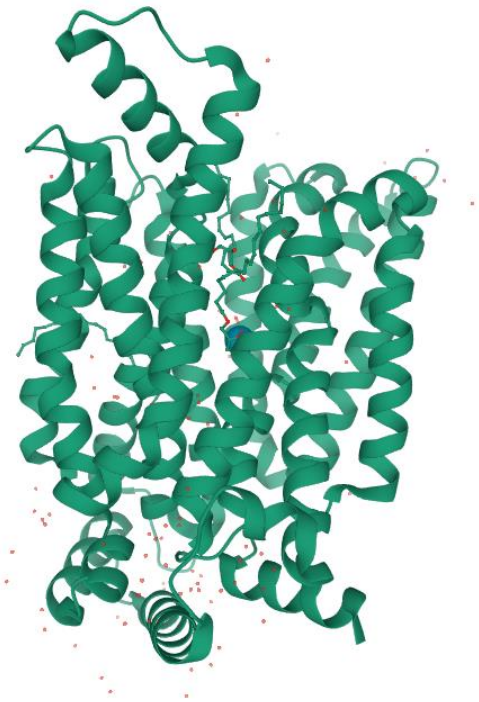

Figure 3-2 Crystal structure of human GLUT3 (4ZW9) bound to D-glucose in the outward-occluded confirmation (Deng *et al.*, 2015).

3.3.8 Using *xenopus laevis* oocytes to functionally characterise the interaction of ion pairs with hOCT1 transporter

Compared to eukaryotic cell lines, the advantages of the *xenopus laevis* oocytes are: (1) they can rapidly express proteins within one week; (2) they can produce a large number of foreign proteins through microinjections; (3) they provide a controllable environment with high-signal-to-noise ratio; (4) they can clone cDNAs with unknown sequence (Markovich, 2008b; Pike *et al.*, 2019). The disadvantages of the *xenopus laevis* oocytes include: (1) some proteins such as aquaporins (van Balkom *et al.*, 2004) affect the viability and will cause swelling or bursting of oocytes; (2) proteins with multiple subunits may not be able to be isolated (Markovich, 2008b).

3.3.9 Uptake of [^{14}C]D-glucose into rSGLT1 expressing oocytes

In this study we utilised an established rat sodium-dependent glucose transporter (rSGLT1) expressing oocyte method and the radiolabelled substrate D-glucose to act as an internal control. The preparation method of *rSGLT* cRNA has been published in the thesis of Dr Corpe MSc student Reshma Suresh (Suresh, 2013). In brief, the prepared *rSGLT* cRNA and [^{14}C] D-glucose (250-360 mCi/mmol, PerkinElmer) were provided by Dr Christopher Corpe from King's College London. Oocytes were injected with 36 nl *rSGLT1* cRNA or water and then incubated in MBM with 1 mM pyruvate at 20 ˚C. MBM was changed daily, and broken oocytes were disposed of. For uptake assay, the 1 mM [^{14}C] D-glucose uptake media was composed of 1 mM unlabelled D-glucose and 0.2 µCi/ml (~ 1 µM) [^{14}C]D-glucose in MBM. 11-13 *rSGLT1* cRNA or water-injected oocytes were placed per vial and incubated for 10 min before washed three times with ice-cold PBS. Then each of the oocytes was lysed in 500 µl 10% (w/v) sodium dodecyl sulfate (SDS). 4 ml of scintillation fluid was then added, and the DPM (disintegrations per min) was counted by Packard Tri-Carb 2900TR liquid scintillation counter (Perkin-Elmer, Beaconsfield, UK). The DPM of 10 µl uptake media was also counted. The results were expressed as the average uptake of [^{14}C]D-glucose (pmol) in each of the 11-13 oocytes during the 10 min incubation time.

3.3.10 *Laevis xenopus* oocyte as a model system to study hOCT1 transporter

There are a few steps of preparing *xenopus* oocytes expressing hOCT1. At first, the cDNA of *hOCT1* vector was amplified and verified through DNA sequencing and restriction enzyme digestion. Then the *hOCT1* cRNA was synthesised and verified by gel electrophoresis. Finally, the *hOCT1* cRNA was injected into oocytes, and the functional expression of hOCT1 was confirmed by radiotracer uptake assay.

3.3.10.1 Materials

3.3.10.1.1 Plasmid and inserts

hOCT1 cDNA was kindly provided by Professor Hermann Koepsell (University of Wurzburg, Würzburg, Germany). *hOCT1* cDNA (Accession: BC126364) was cloned in vector pOG1 using the restriction site 5'HindIII >>>EcoR1 3' containing a 1861kb insert and an ampicillin selection marker (Gorboulev *et al.*, 1997; van Montfoort *et al.*, 2001; Arimany-Nardi *et al.*, 2014).

3.3.10.1.2 Oligonucleotides

The oligonucleotide (sequence: TTA CTC CGC TCT GGT CGA AAT, 25 nmole, desalted) was purchased from Sigma-Aldrich Company Ltd (Dorset, UK) for DNA sequencing for the *hOCT1* vector.

3.3.10.2 Preparation of Agar plates

LB Agar solution (15%) was autoclaved and cooled down to 37 ˚C. Then a small amount of ampicillin (100 µg/ml) was mixed into the LB Agar solution. After that, the solution was immediately poured into petri dishes and left overnight for the agar to solidify.

3.3.10.3 Amplification of *hOCT1* cDNA

One vial of *E.coli* cells (Subcloning Efficiency™ DH5α™ Competent Cells from Invitrogen) was thawed on ice. Then 100 ng of hOCT1 DNA vector was gently mixed with the cells and left on ice for 30 min. After that, the cells went through a heat-shock at 42 ˚C without shaking for 30 s before immediately transferred on ice for 2 min. The cells were then added into 250 µl 20% pre-warmed LB broth shaken at 225 rpm and incubated at 37 ˚C for 1 h. Following the incubation, 20 µl of transformation samples were plated on pre-made selective antibiotics (ampicillin, 100 µg/ml) selective LB agar plates and incubated at 37 ˚C for overnight. The next day, a single colony was picked up and inoculated in 250 ml of LB medium with 100 µg/ml ampicillin. Then the solution was shaken at 225 rpm for overnight at 37 ˚C. After the amplification, the hOCT1 cDNA was purified with the HiSpeed Plasmid Midi Kit (Qiagen, Germany).

3.3.10.4 DNA sequencing of *hOCT1* vector

The *hOCT1* plasmid was diluted to 100 ng/µl. Then the *hOCT1* plasmid and oligonucleotides were sent to Beckman Coulter Genomics (Essex, UK) for sequencing. The DNA sequencing result was compared to the dataset in the National Center for Biotechnology Information (NCBI) of U.S. National Library of Medicine (Link to website: https://www.ncbi.nlm.nih.gov).

3.3.10.5 Restriction Enzyme Digestion of cDNA

The *hOCT1* cDNA plasmid was digested by enzymes to confirm the identity of the insert. *hOCT1* cDNA was digested by EcoRI and HindIII, or Not1 enzymes at 37 ˚C overnight. Then sizes of the fragments were checked by agarose gel electrophoresis. The agarose was dissolved in 75 ml of

1xTBE buffer at a final concentration of 1% (m/v). Ethidium Bromide (4 µl) was added into the gel and used to stain the DNA. 1 kb DNA ladder was loaded in parallel with the samples as a reference. 500 ng DNA samples in loading buffer were loaded in each well and run at 100 V for 1 h. Then results were visualized under UV and images were captured by GeneSnap.

3.3.10.6 Plasmid linearization

The *hOCT1* plasmid was linearized with the restriction enzyme Not1 at 37 ˚C overnight. The linearization process was terminated with 1/20th volume of 0.5 M EDTA, 1/10th volume of 3 M Na acetate and 2 volumes of ethanol. Then the sample was mixed well and chilled at -20 ˚C overnight for precipitation.

3.3.10.7 Synthesis of RNA

The *hOCT1* cDNA was centrifuged at maximum speed (16,000 g) at 4 ˚C for 30 min. Then the pellet was washed three times by 70% ethanol before re-suspended in 10µl nuclease-free water. The concentration of cDNA was determined by NanoDrop Microvolume Spectrophotometer (ND-1000 Spectrophotometer). Then the cDNA sample was used for synthesis with the T7 mMESSAGE mMACHINE kit (Ambion). Briefly, a mixed solution consisting of the precipitated *hOCT1* cDNA (5 µg), nuclease-free water, 2xNTP/CAP, 10xReaction buffer and Enzyme was prepared and then incubated at 37 ˚C for 2 h. Then the reaction was terminated by adding 30 µl lithium chloride and 30 µl nuclease-free water. Then the sample was stored at -20 ˚C to precipitate for at least 12 h. The sample was then removed from the freezer and left to defrost at room temperature (~20 ˚C). It was then centrifuged at 16,000 g at 4 ˚C for 30 min. The supernatant was carefully discarded, and the pellet was washed three times with 70% ice-cold ethanol. The pellet was left at room temperature for 5 min to air-dry the residual ethanol before re-suspension in 10 µl of nuclease-free water. The concentration of the RNA was spectrophotometrically determined by NanoDrop Microvolume Spectrophotometer (ND-1000 Spectrophotometer). Typically, the yield of cRNA was ~10 µg.

Calculation of cRNA yield:

1000 ng/µl (1 µl of the stock cRNA concentration determined by NanoDrop) x 10 µl (total volume of the stock cRNA) = 10 µg cRNA

3.3.10.8 Verification of *hOCT1* RNA

The size and integrity of the synthesised *hOCT1* total RNA were characterised using Agilent RNA 6000 Nano Kit and 2100 Bioanalyzer. Firstly, the gel was prepared. The RNA 6000 gel matrix (550 µl) was pipetted into a spin filter and then centrifuged at 1,500 g for 10 min. Sly, the gel-dye mix was prepared. The RNA 6000 Nano dye concentrate was taken out of the -80 ˚C freezer and allowed to equilibrate to room temperature for half an h. Then the dye concentrate was vortexed for 10 s and spun down. The gel-dye solution was prepared by mixing 1 µl of the dye concentrate into 65 µl aliquot of filtered gel. The solution was vortexed, spun at 13,000 g for 10 min, and used within 24 h. Thirdly, the prepared gel-dye mix was loaded into an RNA 6000 Nanochip. The RNA 6000 Nanochip was placed into the chip priming station and 9 µl gel-mix was loaded into the designated well of the chip. The plunger of the chip priming station was pressed from its initial 1 ml position until it was held by the clip. After 5 s, the plunger was slowly pulled back to its 1 ml position. Finally, the gel-dye mix, RNA 6000 Nano marker, ladder and RNA samples were pipetted into the wells of the chip. The chip was vortexed horizontally at 2,400 rpm for 1 min before it was put into the Agilent 2100 bioanalyzer for analysis.

3.3.10.9 Isolation of Oocytes

Modified Barth's Medium (MBM) was prepared and it consisted of 88 mM NaCl, 1 mM KCl, 0.82 mM $MgSO_4$, 0.33 mM Ca $(NO_3)_2$, 10 mM HEPES, 0.41 mM $CaCl_2$ (pH 7.4 regulated by HCl/ NaOH) and was utilized to store the oocytes. The *lavies xenopus* oocyte ovary (27 months old) was delivered overnight in ice from the European Xenopus Resource Centre (Portsmouth, UK). Upon arrival, the ovary was placed into a petri dish and washed 4-6 times with MBM without Ca $(NO_3)_2$ and $CaCl_2$. The ovary was teased apart and the oocytes were released from the ovary. Then the oocytes were incubated in 25 ml of collagenase (2 mg/ml) in MBM without Ca $(NO_3)_2$ and $CaCl_2$ for 30 min and the whole process was repeated. The collagenase activity was terminated by washing with MBM for 2-3 times. The intact oocytes at stage V or VI were selected under the microscope (Figure 3-3). The oocytes were stored at 19-20 ˚C and protected from light (i.e. covered with foil).

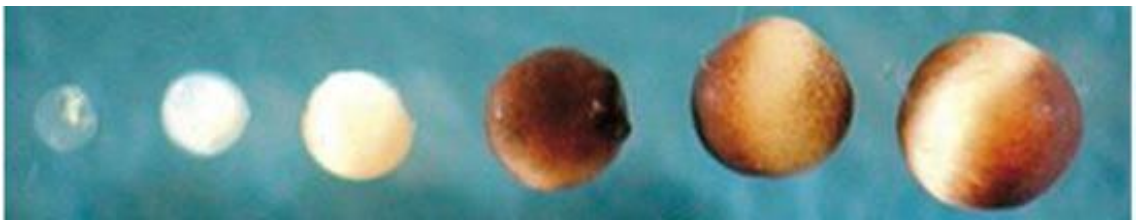

I II III IV V VI

Figure 3-3 Stage I-VI of xenopus oocytes. Picture was modified from Allen (*et al.*, 2007). The oocytes in stage V or VI were selected for injections.

3.3.10.10 Oocytes injection

The micropipettes (Drummond Nanoject™ II Replacement Bores, length: 88.9 mm, outer diameter: 1.14 mm, inner diameter: 0.53 mm, Alpha Laboratories Limited, UK) for injection were prepared by pulling with a needle puller (Sutter Instruments Co. Model-87, Flaming/Brown Micropipette puller) as shown in Figure 3-4. These micropipettes were loaded with *hOCT1* RNA to inject into each oocyte.

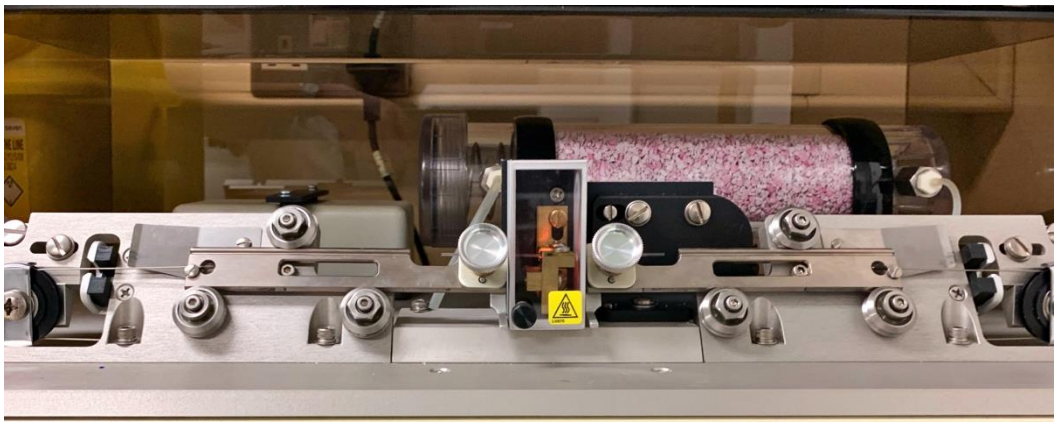

Figure 3-4 Sutter Instruments Co. Model-87, Flaming/Brown Micropipette puller with the setting of heat (749; range 0-999), pull (63: range 0-255), velocity (45, range 0-255) and time (210 millis). The units of the heat, pull, and velocity settings are arbitrary. Heat setting will affect the length and tip size of the pipette. Generally speaking, higher heat settings tend to give longer and finer tips. Low values of pull strength win the range 40-75 will give larger tips appropriate for injection needles, while settings between 120-250 give smaller tips appropriate for micropipettes. Velocity is typically set between 80 to 120 for micropipettes or 50-80 for microinjection needles. The instruction manual is available here: https://www.americaninstrument.com/pdf/3889-PIPETTOR.pdf (accessed 27.5.2020).

Prior to injection, one side of micropipettes was cut by micro tweezers to make the final length between 10 to 15 mm. Then *hOCT1* RNA was loaded into micropipettes with a micro-loader and sealed with mineral oil. Each oocyte was observed under the microscope and the ones that were broken or with unclear edges were disposed of. Each oocyte was injected with 50 nl RNA-free water or *hOCT1* RNA, then placed in MBM solution with 1 mM sodium pyruvate. The injected oocytes were stored at 19-20 ˚C for 3 days before the uptake assay. The MBM buffer was changed every day and broken oocytes were discarded.

Figure 3-5 The RNA injector (NanoJect II, Leica) used in this study. The micropipettes were connected to the injector. The oocytes were placed under the microscope, and one injection to each oocyte contained 50 nl of RNA-free water or *hOCT1* RNA.

3.3.11 Verification of the method

3.3.11.1 Uptake of [^{3}H]acetylcholine in hOCT1 expressed oocytes

In order to confirm the functionality of hOCT1 transporter in oocytes, acetylcholine, an endogenous substrate for hOCT1 (Lips *et al.*, 2005), was utilised. In 8-12 of water-injected oocytes or hOCT1 expressed oocytes were placed in vials with MBM. The MBM was aspirated just before 500 µl of transport buffer (7.6 µM [^{3}H]acetylcholine and 0.9 µM [^{14}C]sucrose in MBM) was pipetted into the vials. Each group of oocytes was incubated with the transport buffer for 1, 30, 60 and 120 min and then stopped with three times of wash with ice-cold MBM containing 100 µM quinine (hOCT1 inhibitor (Lips *et al.*, 2005)). Each of the oocytes was lysed in 500 µl 10% SDS. Then 4 ml of scintillation fluid was added to the each of the oocyte lysates and the DPM was counted by Packard Tri-Carb 2900TR liquid scintillation counter (Perkin-Elmer, Beaconsfield, UK).

3.3.12 Uptake of [^{3}H]pentamidine in oocytes expressing hOCT1

The uptake of [^{3}H]pentamidine in hOCT1 expressed oocytes was performed in order to confirm the role of hOCT1 in the uptake of [^{3}H]pentamidine. Water-injected oocytes and *hOCT1* injected

oocytes were incubated with 31 nM [^{3}H]pentamidine and 0.9 µM [^{14}C]sucrose in 500 µl MBM for 1, 20, 30, 60 and 120 min. The uptake was terminated by three times of wash with ice-cold MBM containing 100 µM quinine (hOCT1 inhibitor). Then each oocyte was lysed in 500 µl 10% SDS solution and 4 ml of scintillation solution. The DPM was counted by Packard Tri-Carb 2900TR liquid scintillation counter (Perkin-Elmer, Beaconsfield, UK).

3.3.13 Self-saturation of [^{3}H]pentamidine in hOCT1 expressed oocytes

[^{3}H]pentamidine (31 nM) was incubated with unlabelled pentamidine (0, 2, 5,10, 20, 50, 100, 250, 500 µM) for 1 h. The uptake of [^{3}H]pentamidine in oocytes was terminated by 3 times of wash with ice-cold MBM buffer containing 100 µM quinine (hOCT1 inhibitor). Then each oocyte was lysed in 500 µl 10% SDS solution and 4 ml of scintillation solution. The DPM was counted by Packard Tri-Carb 2900TR liquid scintillation counter (Perkin-Elmer, Beaconsfield, UK). To calculate the Km of pentamidine by hOCT1 in oocytes, the molar concentrations of [^{3}H]pentamidine (µM) and the net uptake of [^{3}H]pentamidine (fmol/oocyte) by hOCT1 in oocytes were fit into the Michaelis-Menten model in GraphPad 7.

3.3.14 Uptake of [^{3}H]pentamidine ion-pairs in hOCT1 expressed oocytes

To understand how counterions including taurodeoxycholate, octanoate, quercetin and xinafoate affect the uptake of [^{3}H]pentamidine by hOCT1, the uptake of [^{3}H]pentamidine ion-pairs in oocytes expressing hOCT1 was performed. Water-injected (sham) or hOCT1 expressed oocytes were incubated in transport buffer containing 8µM [^{3}H]pentamidine (8 µM unlabelled pentamidine and 31 nM [^{3}H]pentamidine), 0.9 µM [^{14}C]sucrose, and 8 µM or 160 µM of each counterion (taurodeoxycholate, octanoate, quercetin, and xinafoate) for 60 min. The uptake was terminated by 3 times of wash with ice-cold MBM buffer containing 100 µM quinine (hOCT1 inhibitor). Each oocyte was lysed in 500 µl 10% SDS solution and 4 ml of scintillation. The DPM was counted by Packard Tri-Carb 2900TR liquid scintillation counter (Perkin-Elmer, Beaconsfield, UK). Results were expressed as mean ± standard errors of n=21-26 oocytes from 3 different batches/ independent experiments.

3.3.15 Calculation methods

The specific activity of the uptake media was calculated by the moles of the radiolabelled compound in 10 µl uptake media. Together with the counted DPM of 10 µl uptake media, the ratio

of DPM to the molar amount of each radiolabelled compound was calculated. Then this ratio (DPM/moles) was used to determine the uptake of the radiolabelled compound in each oocyte.

3.3.16 Statistical analysis

Results were expressed as mean ± standard errors (S.E.M). The data of the uptake assay were analysed by one-way ANOVA or two-way ANOVA with GraphPad 7. Significant differences were assumed when $p<0.05$.

3.4 Results

3.4.1 Cytotoxicity of taurodeoxycholate, octanoate, xinafoate and quercetin on hCMEC/D3 cells

The four counterions did not cause significant changes on the mitochondrial function or cell viability of hCMEC/D3 cells after 120 min exposure when compared to the negative control of accumulation buffer only. As expected, the positive control caused a decrease by approximately 70% (***p<0.001) with 1% triton (Figure 3-6).

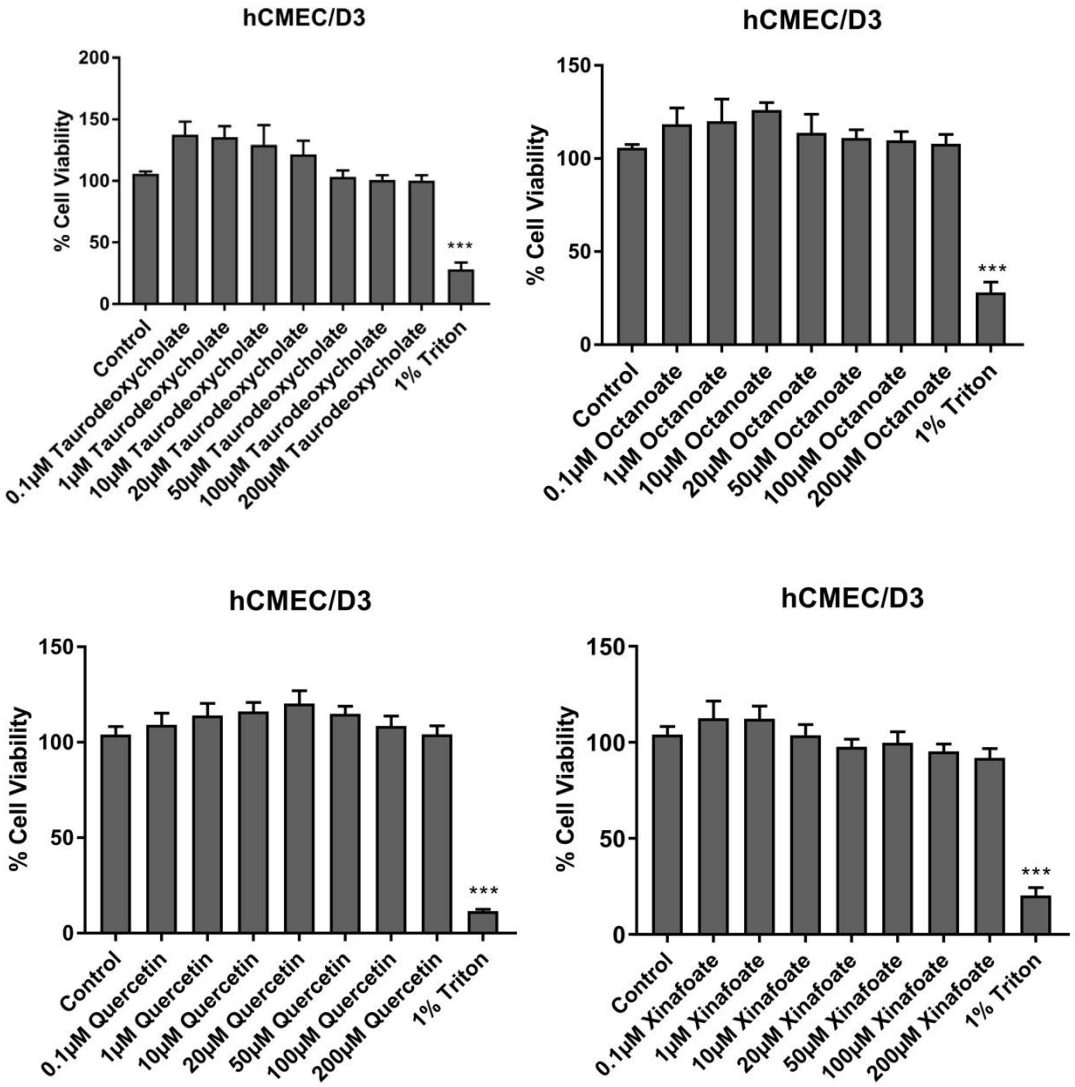

Figure 3-6 Cytotoxicity of taurodeoxycholate, octanoate, quercetin, and xinafoate (0.1- 200 µM) in hCMEC/D3 cells at 2 h incubation time point. Results were corrected by protein from BCA assay and expressed as percentage viability of cells ± SEM (n=3 passages from P29-35/ independent experiments with 6 replicates per plate) compared to the untreated cells (control). Data were analysed by one-way ANOVA with GraphPad Prism 7 (p*<0.05, p**<0.01, p***<0.001).

3.4.2 Uptake of [^{3}H]pentamidine with taurodeoxycholate in hCMEC/D3 cells

The concentration of [^{3}H]pentamidine was set at 9 nM in order to mimic the clinical concentration (4 nM) in the brain, as explained earlier. The results in Figure 3-7 (a) indicated that the presence of 9 nM and 180 nM of taurodeoxycholate did not improve the uptake of [^{3}H]pentamidine. No significant difference of [^{14}C]sucrose was observed (Figure 3-7, b)

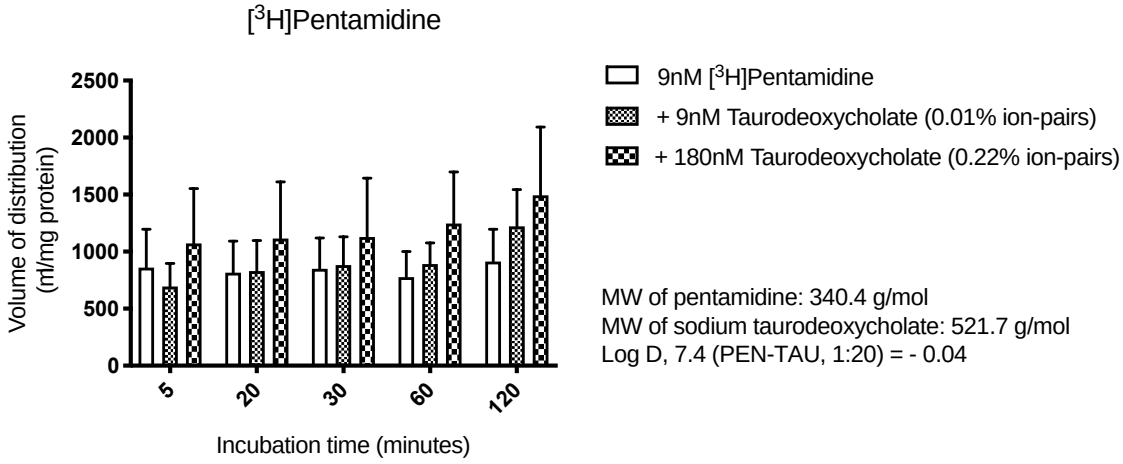

(a)

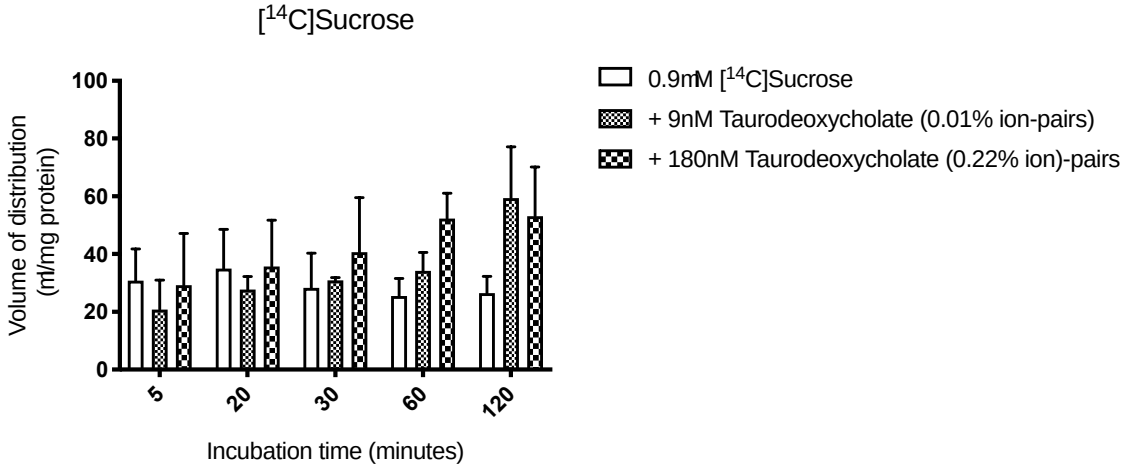

(b)

Figure 3-7 The effect of taurodeoxycholate (9 nM and 180 nM) on the accumulation of [^{3}H]pentamidine (9 nM) corrected by sucrose, and [^{14}C]sucrose (0.9 µM) in hCMEC/D3 cells. Results were expressed as mean ± SEM from 3 passages of cells/ independent experiments (n=3 from passage 31-33) with 6 replicates per time point. Data were analysed by two-way ANOVA with Dunnett multiple comparison test by GraphPad Prism 7. The percentage of [^{3}H]pentamidine in ion-pair form was predicted from the HYSS simulations (Chapter 2 Section 2.4.7.1). The Log D was measured by shake flask method and HPLC analysis (chapter 2 Section 2.4.3). For ease of comparison, these values have been included in this figure.

The presence of taurodeoxycholate (160 µM) suppressed the uptake of [^{3}H]pentamidine and caused significant decrease by 42.4% ($p<0.05$) at the 120 min time point, but there was no effect observed at the earlier time points (Figure 3-8, a). No significant differences of [^{14}C]sucrose with

160 μM taurodeoxycholate compared to the control were observed within the 2 h incubation time (Figure 3-8, b).

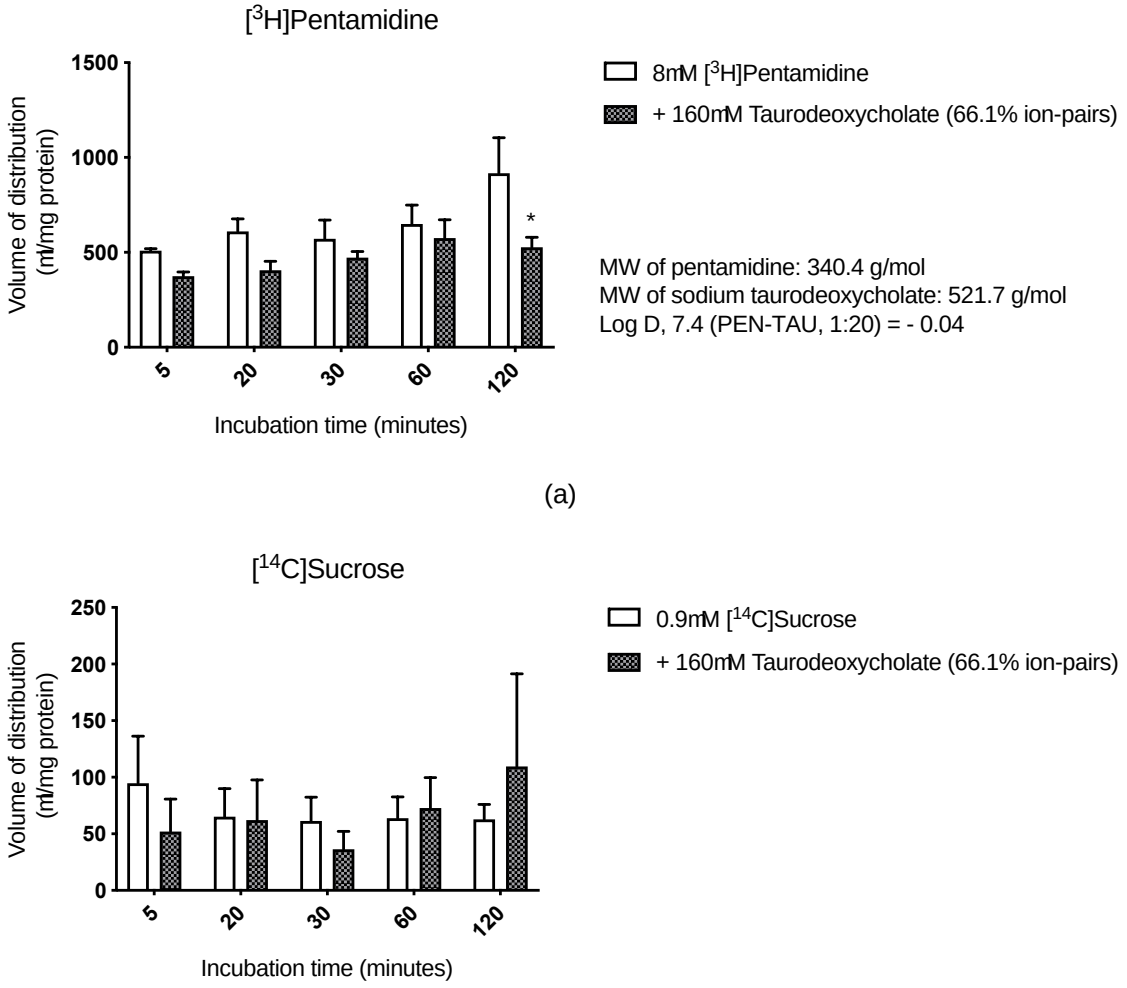

Figure 3-8 The effect of taurodeoxycholate (160 μM) on the accumulation of [^{3}H]pentamidine (9 nM [^{3}H]pentamidine+ 8 μM unlabelled pentamidine) corrected by sucrose and 0.9 μM [^{14}C]sucrose in hCMEC/D3 cells. Results were expressed as mean ± SEM from 3 passages of cells/ independent experiments (n=3 from passage 30, 31 and 34) with 6 replicates per time point. Data were analysed by two-way ANOVA with Sidak's multiple comparison test by GraphPad Prism 7 ($p^*<0.05$). $P^*<0.05$ represents a significant difference between the treatment and control group at a specific time point. The percentage of [^{3}H]pentamidine in ion-pair form was predicted from the HYSS simulations (Chapter 2 Section 2.4.7.1). The Log D was measured by shake flask method and HPLC analysis (Chapter 2 Section 2.4.3). For ease of comparison, these values have been included in this figure.

3.4.3 Uptake of [^{3}H]pentamidine with octanoate in hCMEC/D3 cells

The presence of 20 times of octanoate (180 nM) significantly increased the accumulation of [^{3}H]pentamidine at the 120 min time point ($P<0.05$) by 98.1% (Figure 3-9, a). No significant differences were seen in the uptake of [^{14}C]sucrose over the 120 min incubation time course (Figure 3-9, b).

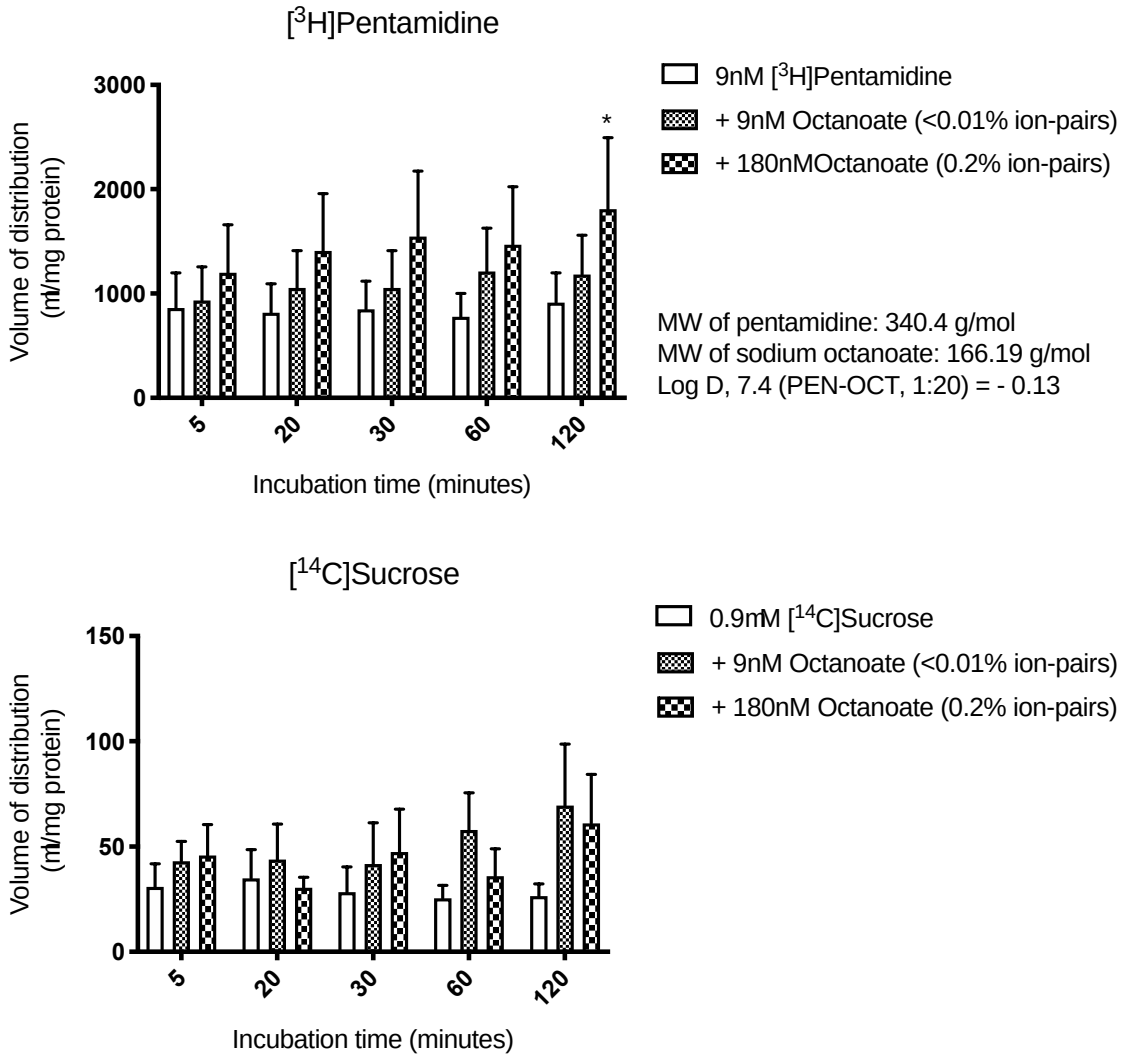

Figure 3-9 The effect of octanoate (9 nM and 180 nM) on the accumulation of [^{3}H]pentamidine (9 nM) corrected by sucrose and [^{14}C]sucrose (0.9 μM) in hCMEC/D3 cells. Results were expressed as mean ± SEM from 3 passages of cells/ independent experiments (n=3 from passage 31-33) with 6 replicates per time point. Data were analysed by two-way ANOVA with Dunnett multiple comparison test by GraphPad Prism 7 (p*<0.05). P*<0.05 represents significant difference between the treatment and control group at a specific time point. The percentage of [^{3}H]pentamidine in ion pair form was predicted from the HYSS simulations (Chapter 2 Section 2.4.7.2). The Log D was measured by shake flask method and HPLC analysis (Chapter 2 Section 2.4.3). For ease of comparison these values have been included in this figure.

The 160 μM octanoate significantly decreased the uptake of [^{3}H]pentamidine by 52.1% at the 20 min ($P<0.05$) and by 54.4% at the 120 min ($P<0.01$) time points (Figure 3-10, a). No statistical differences were seen in the [^{14}C]sucrose uptake over the 2 hs compared to the control (Figure 3-10, b).

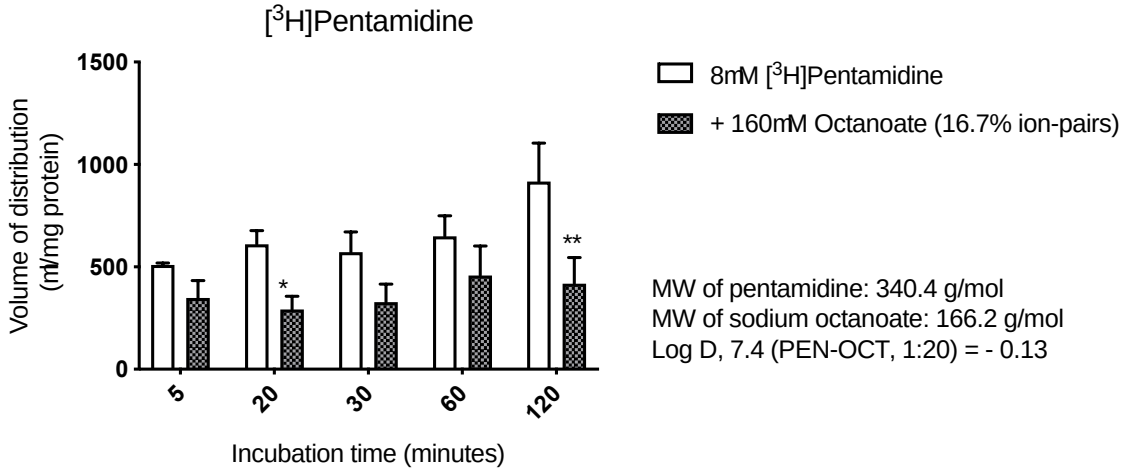

(a)

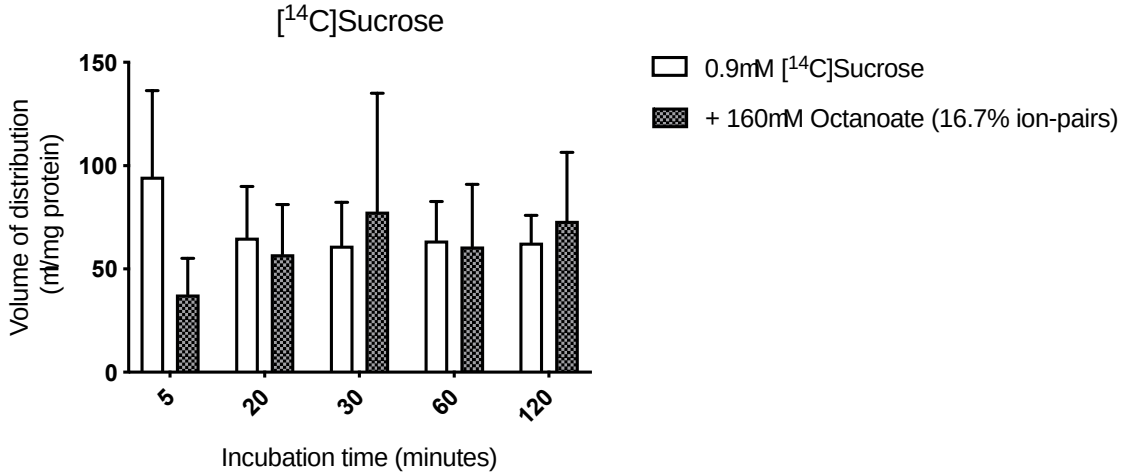

(b)

Figure 3-10 The effect of octanoate (160 μM) on the accumulation of [^{3}H]pentamidine (9 nM [^{3}H]pentamidine+ 8 μM unlabelled pentamidine) corrected by sucrose and 0.9 μM [^{14}C]sucrose in hCMEC/D3 cells. Results were expressed as mean ± SEM from 3 passages of cells/ independent experiments (n=3 from passage 30, 31 and 34) with 6 replicates per time point. Data were analysed by two-way ANOVA with Sidak's multiple comparison test by GraphPad Prism 7 (p*<0.05, p**<0.01). P**<0.01 represents a significant difference between the treatment and control group at a specific time point. The percentage of [^{3}H]pentamidine in ion-pair form was predicted from the HYSS simulations (Chapter 2 Section 2.4.7.2). The Log D was measured by shake flask method and HPLC analysis (Chapter 2 Section 2.4.3). For ease of comparison, these values have been included in this figure.

3.4.4 Uptake of [^{3}H]pentamidine with quercetin in hCMEC/D3 cells

The presence of 9 nM and 180 nM of quercetin did not cause significant changes in the uptake of [^{3}H]pentamidine over the 120 min incubation time (Figure 3-11, a). The uptake of [^{14}C]sucrose increased significantly over 2 folds at the 60 min ($P<0.05$) and the 120 min ($P<0.05$) time points with 9 nM quercetin (Figure 3-11, b).

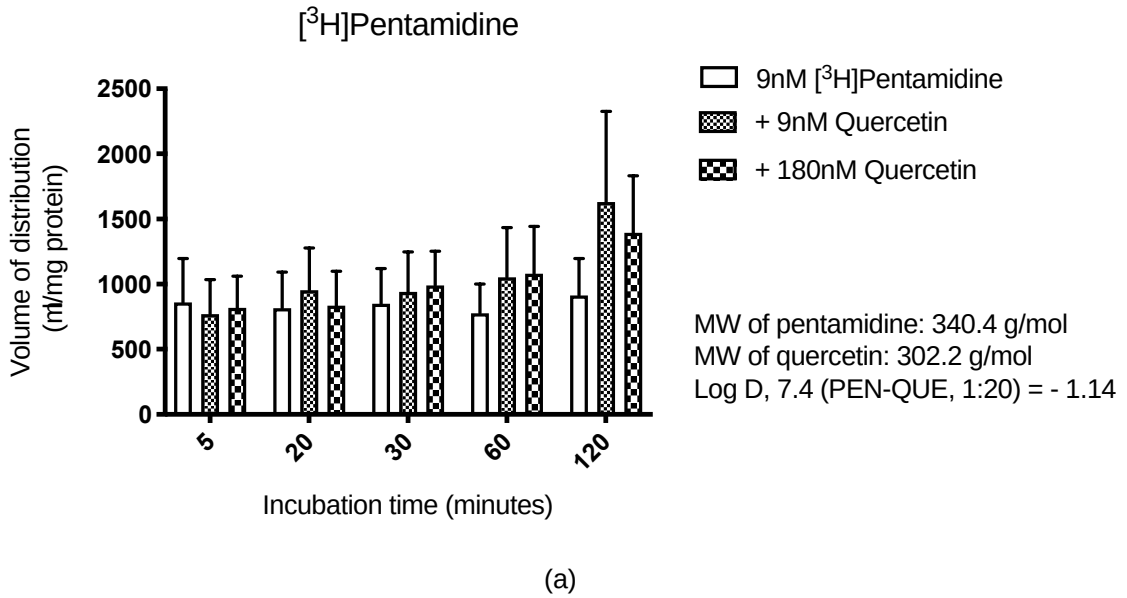

(a)

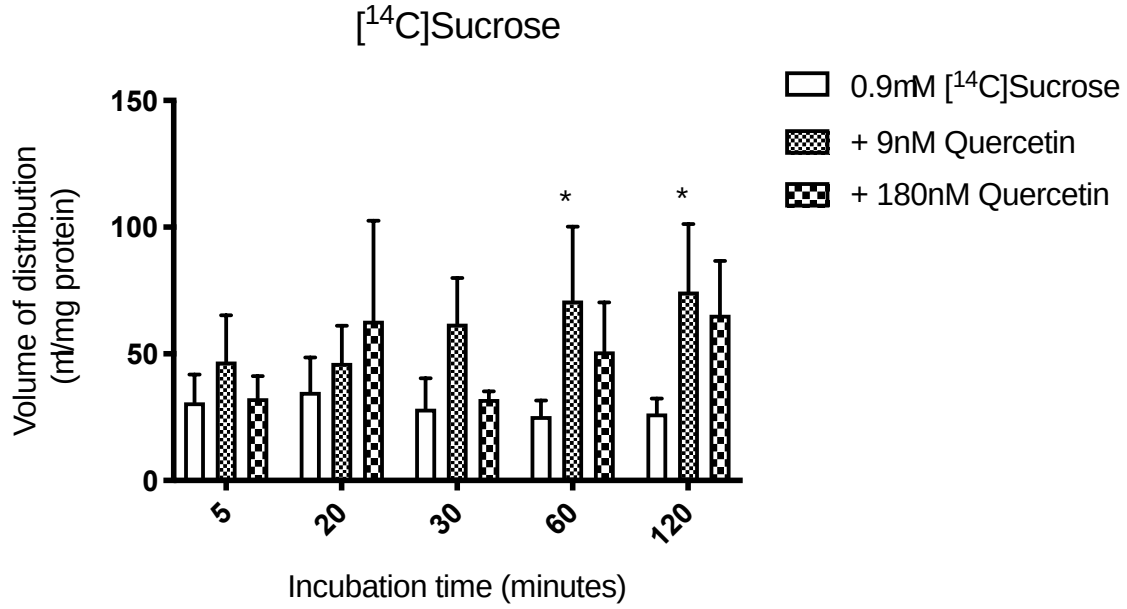

(b)

Figure 3-11 The effect of quercetin (9 nM and 180 nM) on the accumulation of [^{3}H]pentamidine (9 nM) corrected by sucrose and [^{14}C]sucrose (0.9 µM) in hCMEC/D3 cells. Results were expressed as mean ± SEM from 3 passages of cells/ independent experiments (n=3 from passage 31-33) with 6 replicates per time point. Data were analysed by two-way ANOVA with Dunnett multiple comparison test by GraphPad Prism 7 (p*<0.05). P*<0.05 represents a significant difference between the treatment and control group at a specific time point. The Log D was measured by shake flask method and HPLC analysis (Chapter 2 Section 2.4.3). For ease of comparison, these values have been included in this figure.

3.4.5 Uptake of [^{3}H]pentamidine with xinafoate in hCMEC/D3 cells

Significant increases of [^{3}H]pentamidine were observed by 9 nM xinafoate at the 60 min ($P<0.01$) and the 120 min ($P<0.001$) time points (Figure 3-12, a). However, the increases may be explained by the damage of membrane integrity as the uptake of [^{14}C]sucrose showed significant increases ($P<0.05$ and $P<0.01$) at these two time points (Figure 3-12, b).

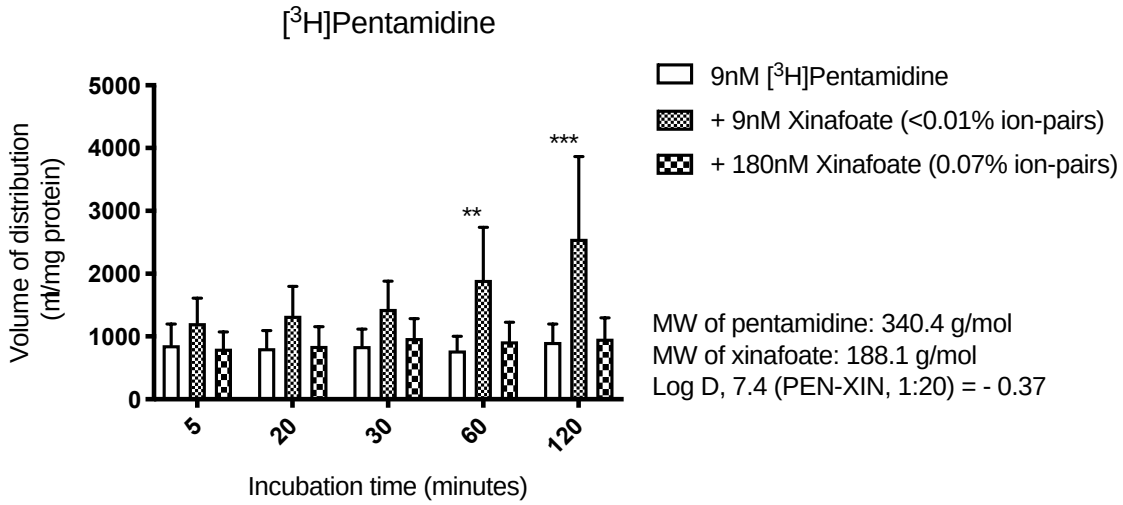

(a)

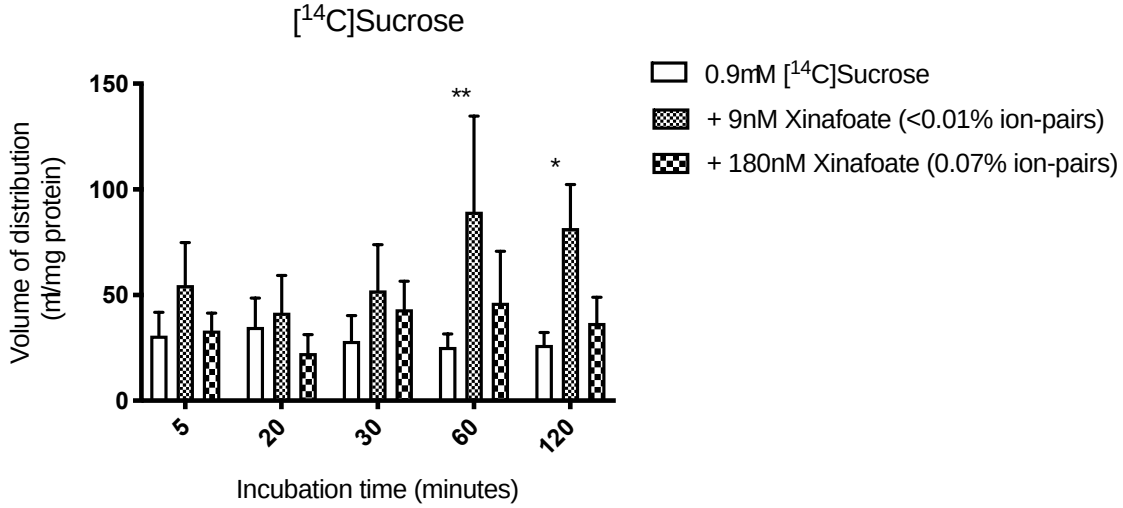

(b)

Figure 3-12 The effect of xinafoate (9 nM and 180 nM) on the accumulation of [^{3}H]pentamidine (9 nM) corrected by sucrose and [^{14}C]sucrose (0.9uM) in hCMEC/D3 cells. Results were expressed as mean ± SEM from 3 passages of cells/ independent experiments (n=3 from passage 31-33) with 6 replicates per time point. Data were analysed by two-way ANOVA with Dunnett multiple comparison test by GraphPad Prism 7 (p*<0.05, p**<0.01). P*<0.05 and P**<0.01 represent a significant difference between the treatment and control group at a specific time point. The percentage of [^{3}H]pentamidine in ion-pair form was predicted from the HYSS simulations (Chapter 2 Section 2.4.7.3). The Log D was measured by shake flask method and HPLC analysis (Chapter 2 Section 2.4.3). For ease of comparison, these values have been included in this figure.

There were no significant differences in the uptake of [^{3}H]pentamidine or [^{14}C]sucrose by 180 μM xinafoate compared to the control, as shown in Figure 3-13.

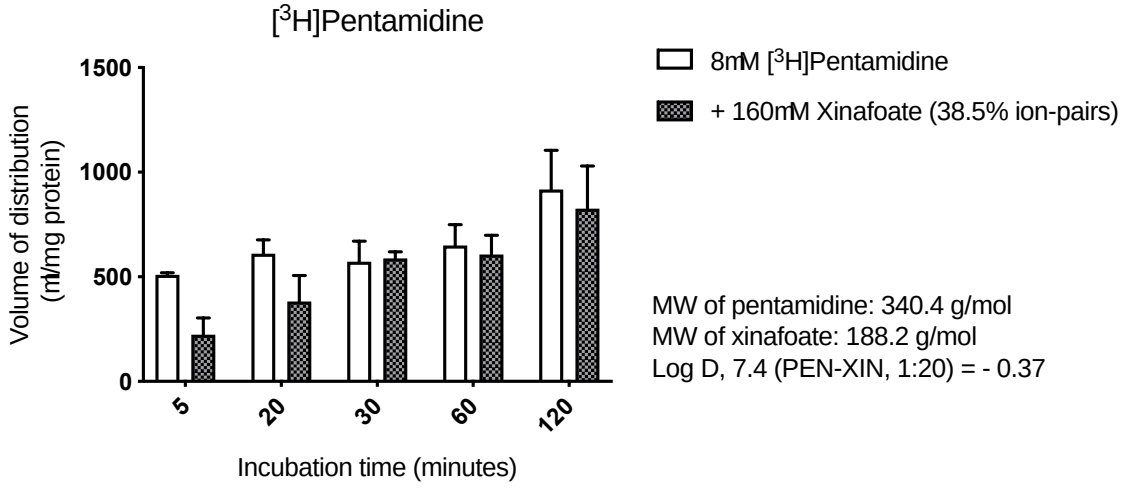

(a)

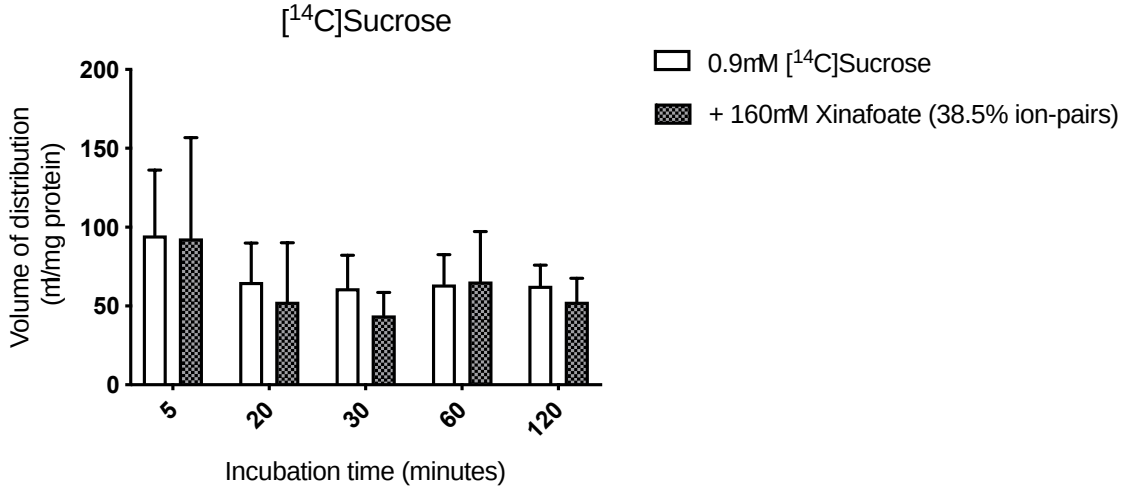

(b)

Figure 3-13 The effect of xinafoate (160 μM) on the accumulation of [^{3}H]pentamidine (9 nM [^{3}H]pentamidine+ 8 μM unlabelled pentamidine) corrected by sucrose and 0.9 μM [^{14}C]sucrose in hCMEC/D3 cells. Results were expressed as mean ± SEM from 3 passages of cells/ independent experiments (n=3 from passage 30, 31 and 34) with 6 replicates per time point. Data were analysed by two-way ANOVA with Sidak's multiple comparison test by GraphPad Prism 7. The percentage of [^{3}H]pentamidine in ion-pair form was predicted from the HYSS simulations (Chapter 2 Section 2.4.7.3). The Log D was measured by shake flask method and HPLC analysis (Chapter 2 Section 2.4.3). For ease of comparison, these values have been included in this figure.

3.4.6 Molecular docking of pentamidine, mannitol and sucrose into hOCT1

The *in silico* simulations revealed that the hydrogens on the amidine groups of pentamidine interact with the ASN286 of hOCT1 (Figure 3-14). The hydrogen on the chain between the ether groups in pentamidine interacts with THR293 of hOCT1. The benzene rings of pentamidine are attracted to PHE289 and ILE166 on hOCT1 through hydrophobic interaction.

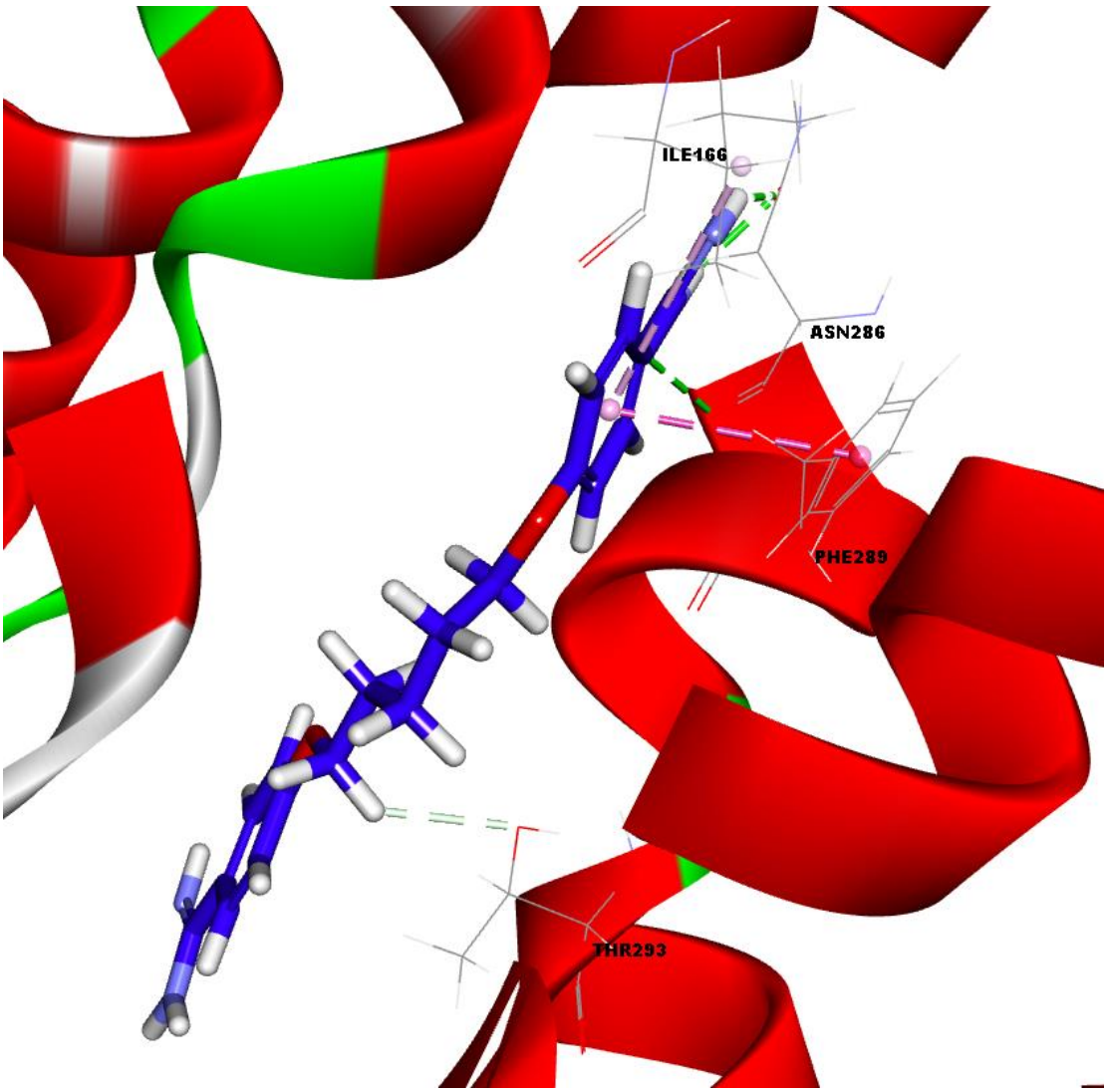

Figure 3-14 Molecular docking of pentamidine into 4ZW9. The green and pink dotted lines in the 3D figure represent hydrogen bonds and hydrophobic interactions, respectively. The image was provided by Dr Khondaker Miraz Rahman's group from Medicinal Chemistry at King's College London.

The docking results showed that the hydroxyls of mannitol interact with the PHE289, THR293, ASN32, TYR290, ASN32, GLU35 on hOCT1 only through hydrogen bond (Figure 3-15).

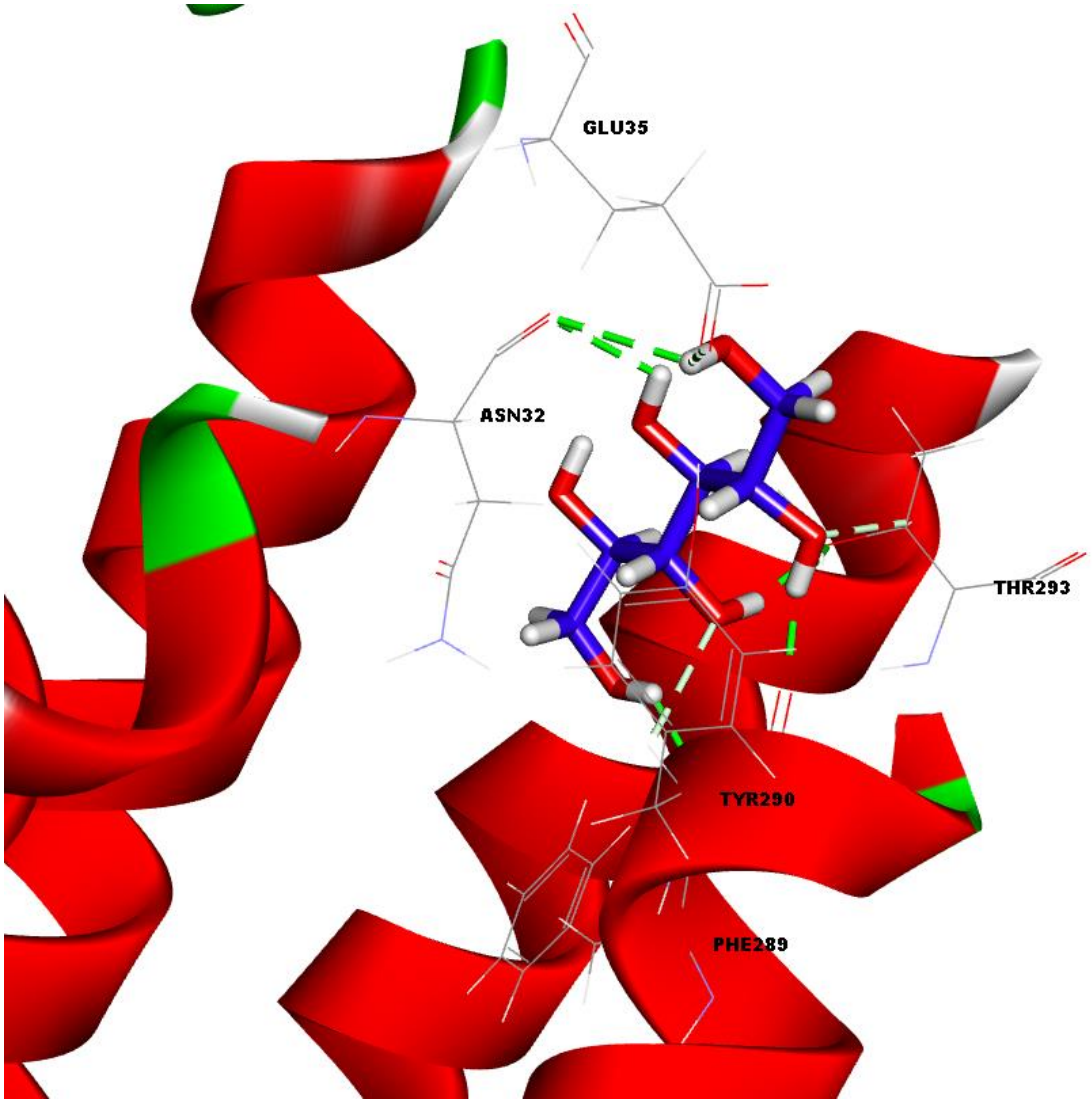

Figure 3-15 Molecular docking of mannitol into 4ZW9. The green dotted lines in the 3D figure represent hydrogen bonds. The image was provided by Dr Khondaker Miraz Rahman's group from Medicinal Chemistry at King's College London.

The molecular docking results indicated that the hydroxyls of sucrose interact with the ASN32, PHE289, TYR290, GLY29, GLU35, ALA33, THR293 on hOCT1 only through hydrogen bond (Figure 3-16).

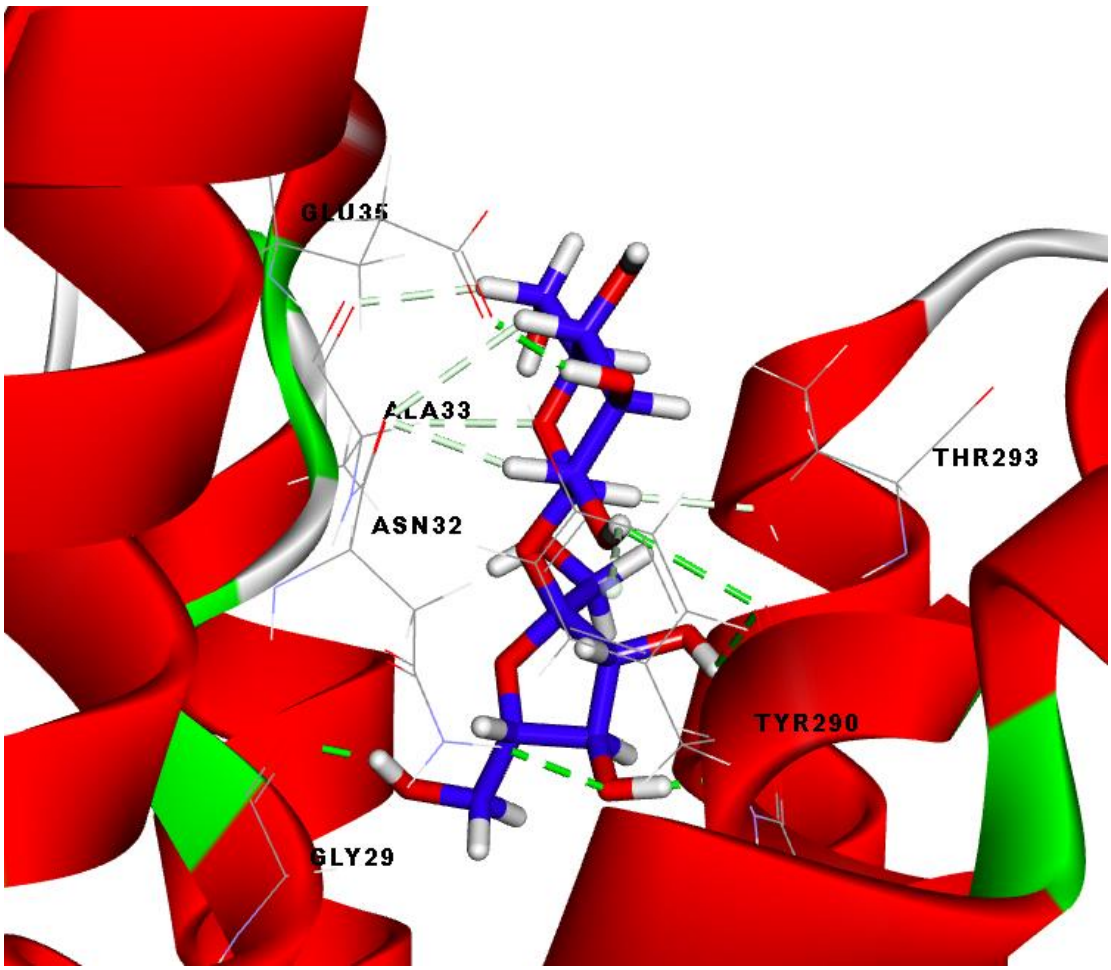

Figure 3-16 Molecular docking of sucrose into 4ZW9. The green dotted lines in the 3D figure represents hydrogen bonds. The image was provided by Dr Khondaker Miraz Rahman's group from Medicinal Chemistry at King's College London.

The free energy with higher negative value implies a more favourable binding between the molecule and the transporter. A substrate is defined as one with a free energy binding lower than -5 kcal/mol (from personal communication with Dr Miraz Rahman from King's College London December 2019). The best pose of pentamidine interacted with the binding site of 4ZW9 with a free energy of -35.22 kcal/mol, while sucrose has a free energy of +19.93 kcal/mol.

3.4.7 Method verification

The hOCT expressing *lavies xenopus* oocyte model was verified in three ways: (a) Confirming the transporter assay methodology using rSGLT, (b) Confirming the identity of hOCT1 DNA and RNA, and (c) Confirming the functional expression of the hOCT1 transporter in *lavies xenopus* oocyte using hOCT1 substrate acetylcholine

3.4.7.1 [^{14}C]D-glucose uptake in established rSGLT expressing oocyte model

The rat sodium-dependent glucose transporter (*rSGLT*) RNA injected oocytes saw significant increases (P<0.001) in [^{14}C] D-glucose compared to both non-injected and water-injected oocytes (Figure 3-17). No significant differences were seen between the non-injected and the water-injected oocytes, which indicated the intact membrane integrity by injections.

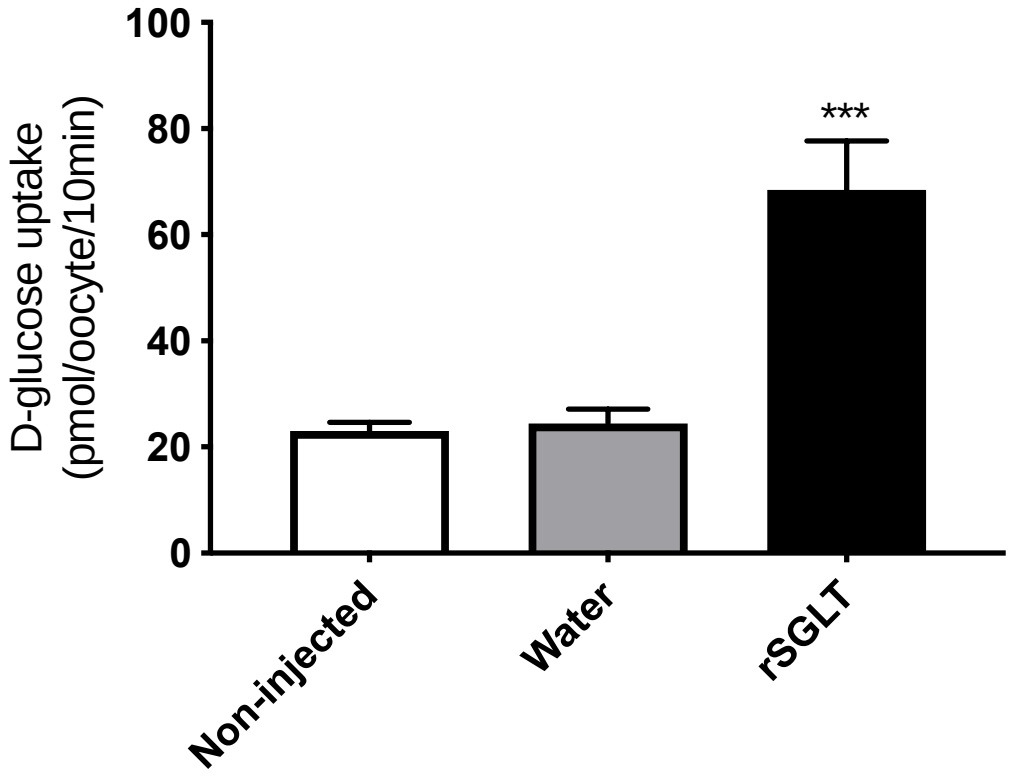

Figure 3-17 [^{14}C]D-glucose (1 mM) uptake in non-injected oocytes, water-injected oocytes, and oocytes expressing rSGLT. Oocytes were incubated in transport buffer with [^{14}C] D-glucose for 10 min. Data represents mean ± standard errors of 11-13 oocytes (1 batch) per group. Results were analysed by one-way ANOVA using GraphPad Prism 7.03 (P<0.001***).

3.4.7.2 *hOCT1* vector sequencing

The amino acid sequences of the *hOCT1* vector were aligned to the published *hOCT1* sequences (BC126364.1) from the National Centre for Biotechnology Information (NCBI) database. The alignment indicated that the *hOCT1* vector sequences were 100% identical to the published cDNA sequences which confirmed the identity of the vector (Figure 3-18). After sequencing, this vector was used for all the following steps to prepare *hOCT1* RNA.

Figure 3-18 Comparison of the *hOCT1* vector sequences to *hOCT1* sequence (BC126364.1) from the NCBI database. A (adenine), T (thymine), C (cytosine), G (guanine) are the four bases of DNA. The upper rows of the alignment are the *hOCT1* vector cDNA sequences and the lower rows are the sequences from NCBI database (BC126364.1).

3.4.7.3 Restriction enzyme digestion of *hOCT1* cDNA

The uncut *hOCT1* cDNA ran in the forms of both supercoiled and open-circular thus it appeared in two fragments on the gel at around 8 kb (band 2, Figure 3-19). The *hOCT1* cDNA linearised by NotI had one single band at around 8 kb (band 3, Figure 3-19), while the double digested *hOCT1* cDNA had two bands (band 4, Figure 3-19), of which the first band appeared at around 1.8 kb and the other at around 6 kb. The sizes of bands for the uncut, linearised, and double digested *hOCT1* on the gel were expected. This verified the identity of the *hOCT1* vector.

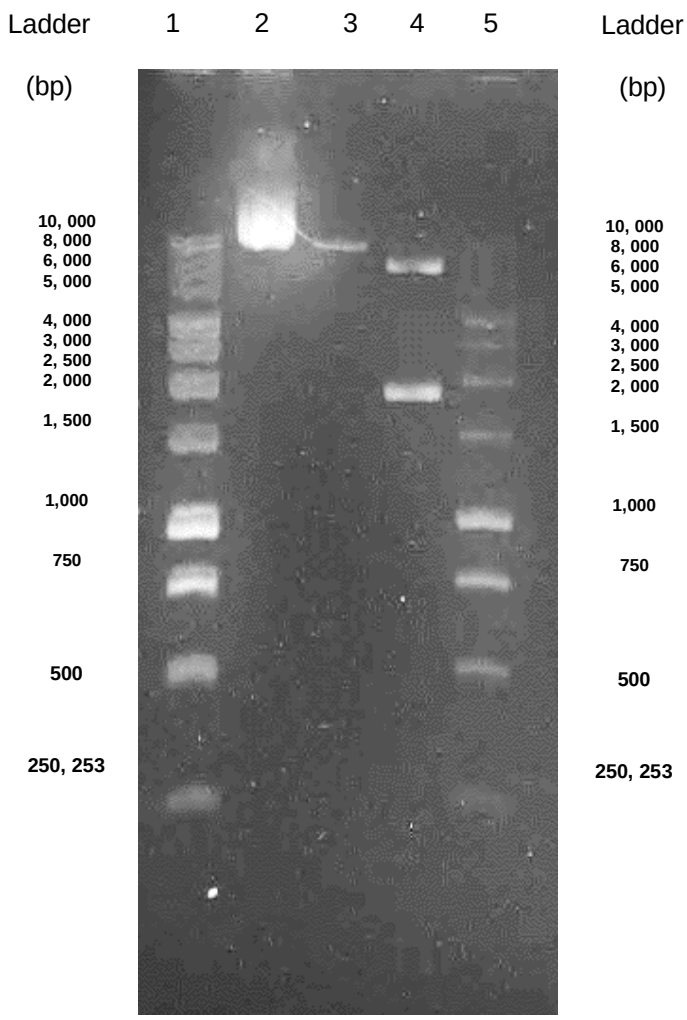

Figure 3-19 Restriction enzyme digestion of *hOCT1*. Lane 1: 1 kb DNA ladder, lane 2: uncut *hOCT1* cDNA, lane 3: *hOCT1* linearised by NotI, lane 4: *hOCT1* digested by HindIII and EcoRI, lane 5: 1 kb DNA ladder. The digestion was repeated each time of cDNA preparation.

3.4.7.4 cRNA Verification by Nano Chip

The size and integrity of the synthesized *hOCT1* cRNA were verified by Agilent RNA 6000 Nano Kit with 2100 Bioanalyzer. As shown in Figure 3-20, the size of *hOCT1* RNA band on the RNA gel was at around 1.7 kb, corresponding to the expected size of the *hOCT1* inserted clone (1.75 kb). The pTRI-Xef, a control RNA provided in the Invitrogen MEGAscript® T7 Kit, appeared at the expected transcript size of 1.89 kb on the gel.

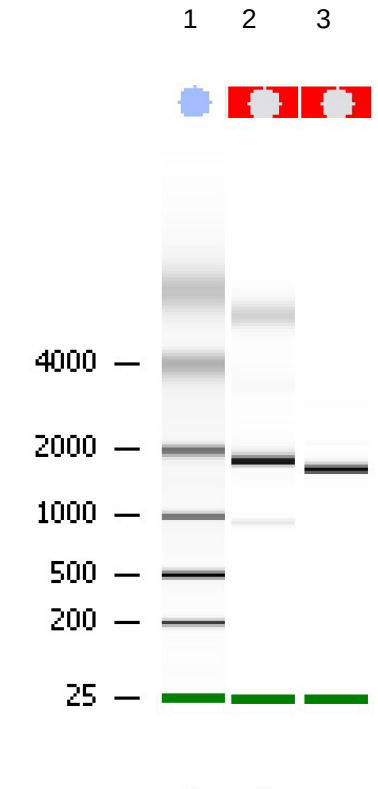

(A)

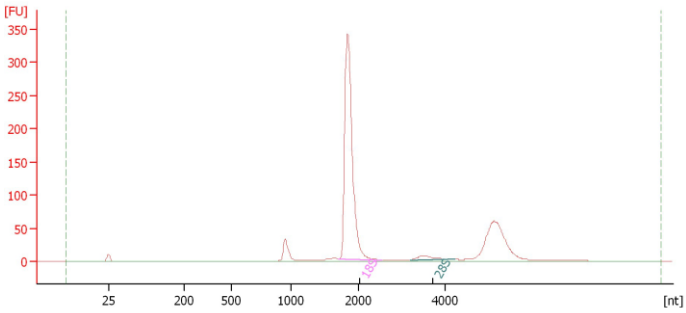

(B)

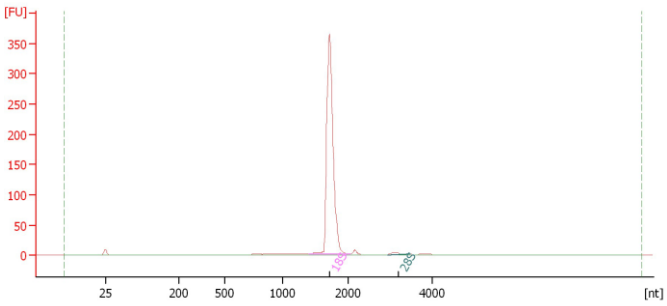

(C)

Figure 3-20 RNA Nano chip electrophoresis of *hOCT1* cRNA. (A) Image of the RNA chip. Band 1: RNA ladder, band 2: *pTRI-Xef* control RNA, band 3: *hOCT1* RNA; (B) Electropherogram of *pTRI-Xef* control RNA; (C) Electropherogram of *hOCT1* cRNA.

3.4.7.5 Uptake of [^{3}H]acetylcholine in oocytes expressing hOCT1

The function of the hOCT1 transporter was verified using the endogenous substrate, acetylcholine. As shown in Figure 3-21, there were significant increases ($P<0.05$) of [^{3}H]acetylcholine uptake in *hOCT1* RNA injected oocytes compared to the water-injected oocytes (control). The uptake of [^{3}H]acetylcholine in oocytes expressing hOCT1 was 80.7% and 87.1% higher than the water-injected oocytes at the 30-min and 60-min time points, respectively.

No significant differences were observed between the non-injected oocytes and water-injected oocytes at all the time points tested (1 min, 30 min and 60 min). [^{14}C]sucrose was co-administered with [^{3}H]acetylcholine and its uptake was an indicator of passive transport and membrane integrity level for the study. No significant differences among the non-injected, water-injected and *hOCT1* injected groups were found at 1 min, 30 min or 60 min time points.

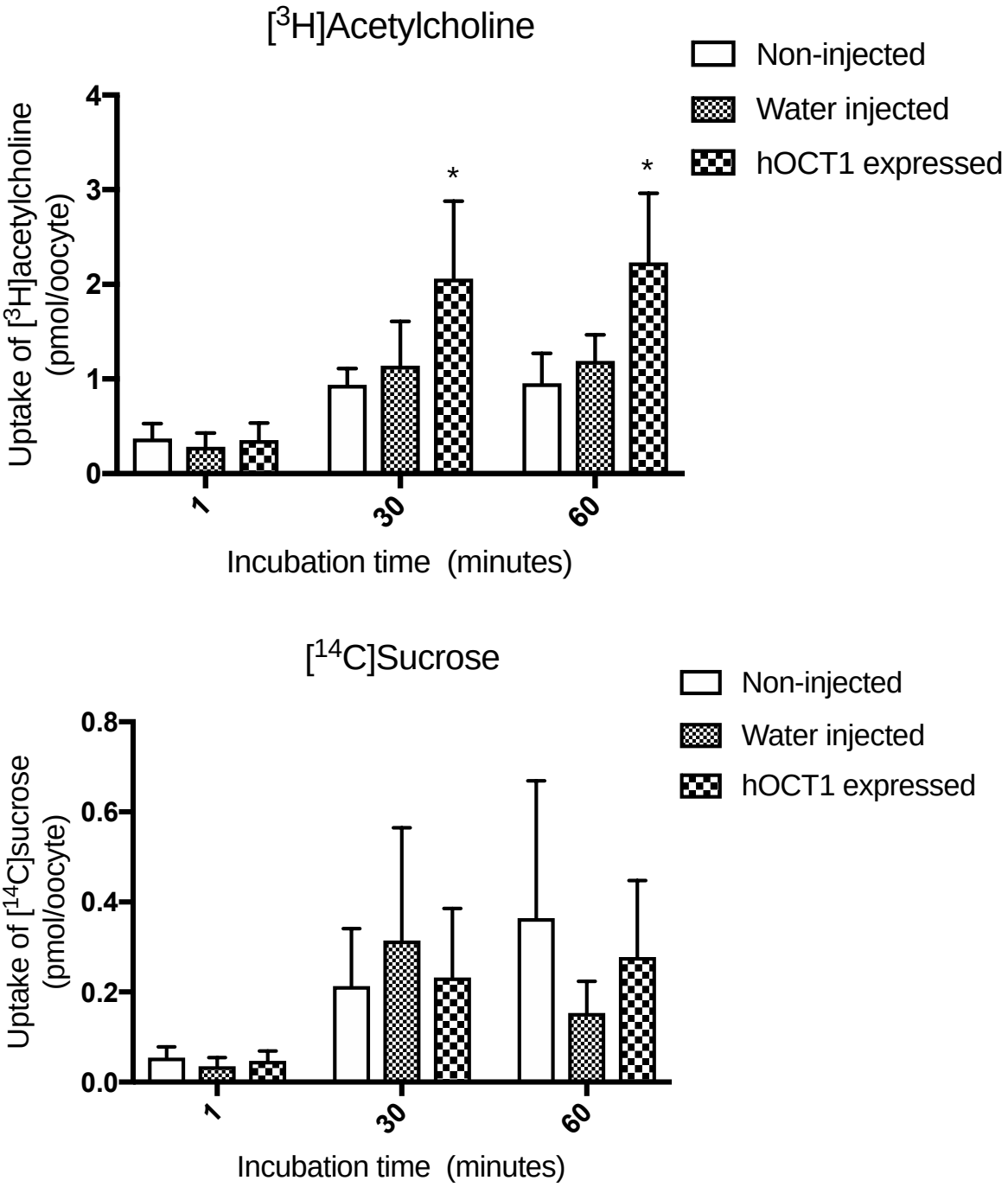

Figure 3-21 [^{3}H]Acetylcholine (7.6 µM) corrected by [^{14}C]sucrose and [^{14}C]sucrose (0.9 µM) uptake in non-injected oocytes, water-injected oocytes and hOCT1 RNA injected oocytes. Data were expressed as the mean ± standard errors of 30-40 oocytes from 4 different batches/ independent experiments. Results were analysed by two-way ANOVA using GraphPad Prism 7.03 (P*<0.05).

3.4.8 Uptake of [^{3}H]pentamidine in oocytes expressing hOCT1

Uptake of [^{3}H]pentamidine (31 nM) in oocytes expressing hOCT1 was significantly higher than water-injected oocytes (control) at 30 min ($P<0.05$), 60 min ($P<0.05$) and 120 min ($P<0.01$) time points (Figure 3-22). [^{14}C]Sucrose uptake between the control group and hOCT1 expressed group was not significantly different until the 120 min time point ($P<0.05$). Based on the results, the 1h incubation time was selected for the following studies in order for the hOCT1 to transport [^{3}H]pentamidine while not damaging the membrane integrity of oocytes.

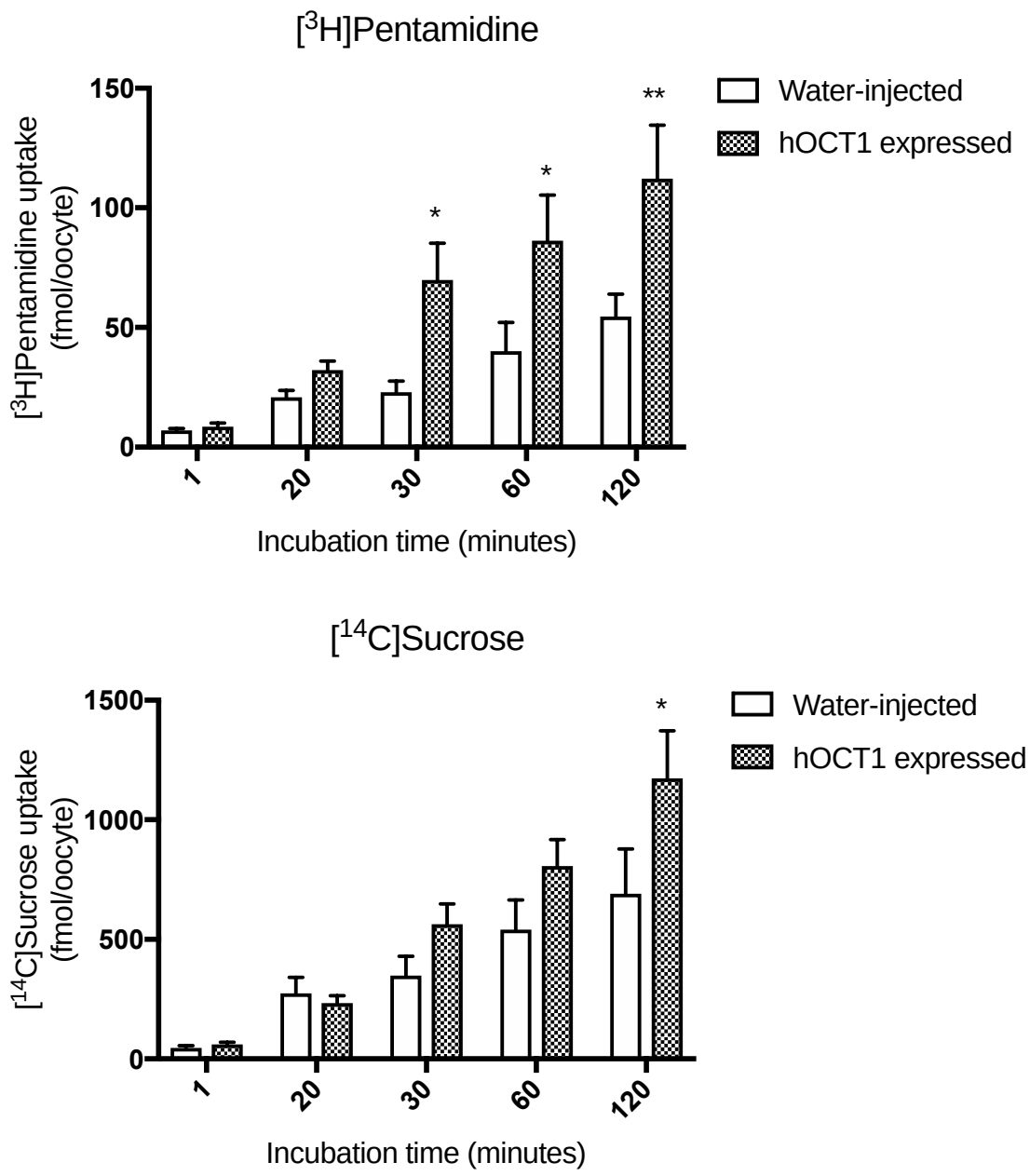

Figure 3-22 [^{3}H]Pentamidine (31 nM) uptake, and [^{14}C]Sucrose (0.9 µM) uptake in water-injected oocytes and oocytes expressing hOCT1. Data represent mean ± standard errors of 23-24 oocytes from 3 different batches/ independent experiments. Statistical analysis was conducted by two-way ANOVA with GraphPad Prism 7.03 (P*<0.05, P**<0.01).

When 8 µM of unlabelled pentamidine was mixed with 31 nM [^{3}H]pentamidine, the difference of [^{3}H]pentamidine uptake in oocytes expressing hOCT1 compared to the water-injected oocytes were not statistically significant until the 120-min time point (Figure 3-23). However, the variations of [^{14}C]sucrose uptake indicated that the membrane integrity of oocytes might have been compromised at the 120-min time point (Figure 3-23). Compared to the results with [^{3}H]pentamidine alone (Figure 3-23), the uptake of [^{3}H]pentamidine with unlabelled pentamidine in hOCT1 expressed oocytes was less, which may be caused by partially self-saturation of pentamidine to the hOCT1 transporter in oocytes.

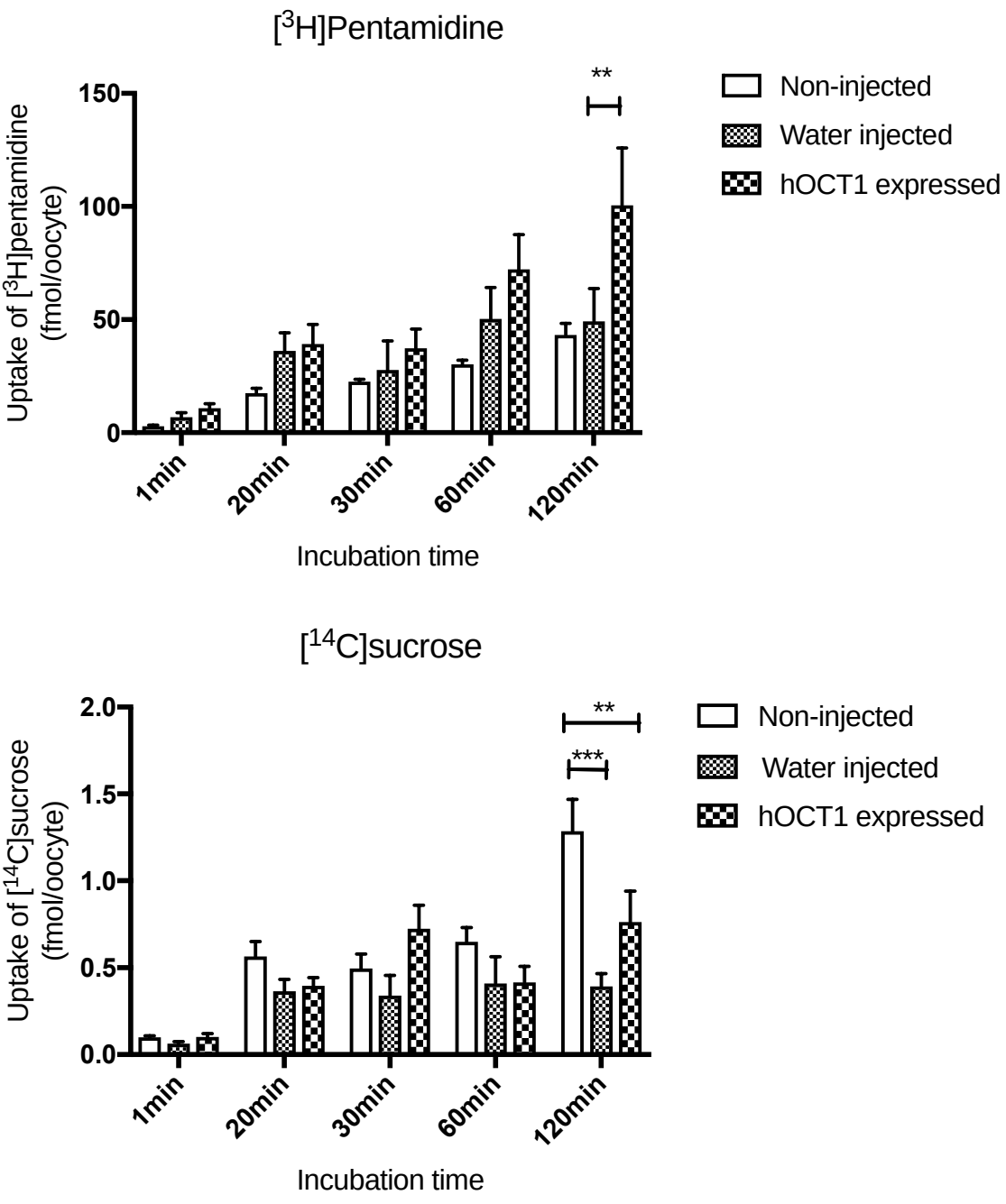

Figure 3-23 Uptake of [^{3}H]Pentamidine (31 nM [^{3}H]pentamidine + 8 µM unlabelled pentamidine) corrected with sucrose, and [^{14}C]Sucrose (0.9 µM) in water-injected oocytes and oocytes expressing hOCT1. Data represent mean ± standard errors of 6-8 oocytes from 1 batch of oocytes. Statistical analysis was conducted by two-way ANOVA with GraphPad Prism 7.03 (P*<0.05, P**<0.01, P***<0.001).

3.4.9 Kinetics of pentamidine uptake by hOCT1 in oocytes

As shown in Figure 3-24, the K_m of [^{3}H]pentamidine uptake by hOCT1 in oocytes was 279.9±112.4 µM and the Vmax was 93.1±18.3 mM (n=6-8 from one batch of oocytes). [^{3}H]pentamidine (31 nM) was incubated with different concentrations of unlabelled pentamidine (0, 2, 5,10, 20, 50, 100, 250, 500 µM) for 1h. Data were fit into the non-linear Michaelis-Menten model using GraphPad7.

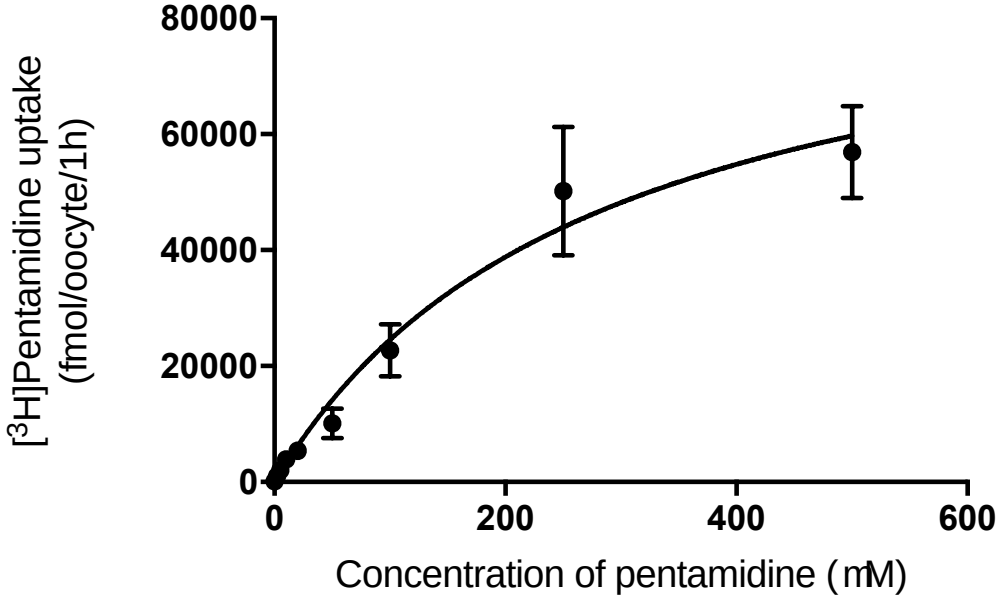

Figure 3-24 Kinetics of pentamidine uptake in oocytes expressing hOCT1. The uptake of [^{3}H]pentamidine in water-injected oocytes was subtracted from oocytes expressing hOCT1. The incubation time was 60 min. Results were expressed as mean ± standard errors of 6-8 oocytes from 1 batch of oocytes.

3.4.10 Uptake of [^{3}H]pentamidine ion pairs by hOCT1

To understand how ion-pairs affect [^{3}H]pentamidine to be transported by hOCT1, the uptake [^{3}H]pentamidine ion-pairs in oocytes expressing hOCT1 were performed. The concentration of pentamidine in the buffer was 8 µM (31nM [^{3}H]pentamidine mixed with 8 µM unlabelled pentamidine) with different concentrations of counterions (8 µM and 160 µM) in MBM.

Three sets of comparison were shown for each counterion: (a) Uptake of [^{3}H]pentamidine ion-pairs in water-injected oocytes, utilised as a control for oocytes expressing hOCT1. This set of results is also an indicator of passive permeability properties in simple cell membranes since no membrane transporters were involved. (b) Uptake of [^{3}H]pentamidine ion-pairs in oocytes expressing hOCT1. This set of results showed the overall results from both passive diffusion and active transport with hOCT1 transporter. (c) Net uptake of [^{3}H]pentamidine ion-pairs by hOCT1 in oocytes. The net uptake by hOCT1 was calculated by subtracting the uptake of [^{3}H]pentamidine

with each counterion in water-injected oocytes from the values in oocytes expressing hOCT1. This was calculated so that the net uptake of [^{3}H]pentamidine with counterions by hOCT1 only, without the influence of passive diffusion, could be revealed.

3.4.10.1 Uptake of [^{3}H]pentamidine-taurodeoxycholate ion pairs by hOCT1 in oocytes

Increasing pentamidine-taurodeoxycholate ion-pairs did not affect the influx of [^{3}H]pentamidine in either water-injected or oocytes expressing hOCT1 (Figure 3-25). The net uptake of [^{3}H]pentamidine by hOCT1 (hOCT1 - water) in oocytes also did not change significantly by the different percentage of pentamidine-taurodeoxycholate ion-pairs.

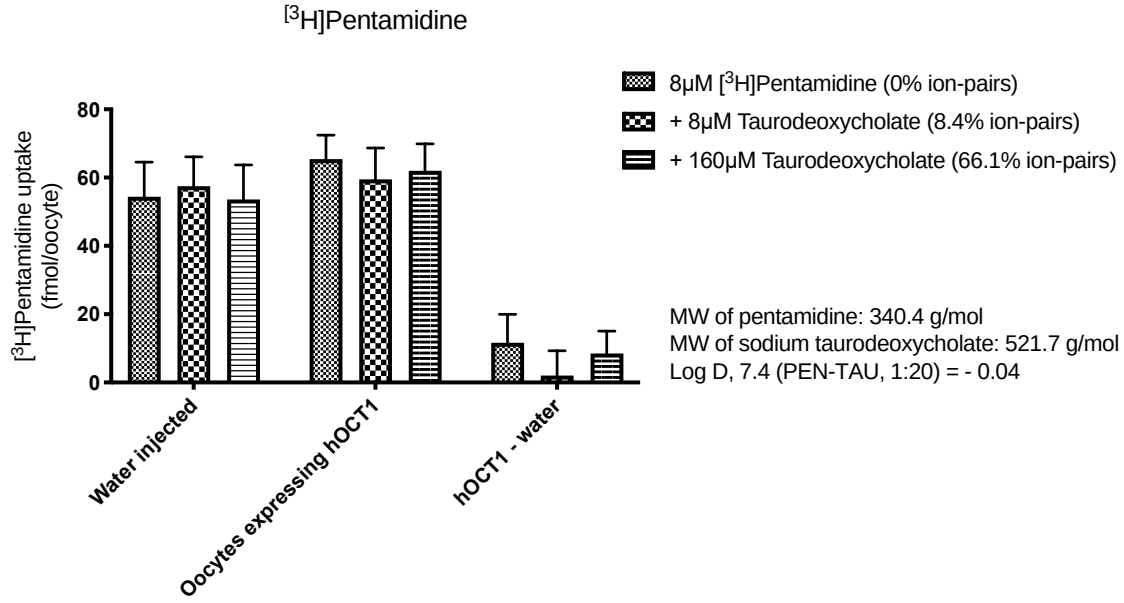

Figure 3-25 The uptake of [^{3}H]pentamidine by hOCT1 transporter. The concentration of pentamidine was 8 μM (31 nM [^{3}H]pentamidine and 8 μM unlabelled pentamidine) and the concentration of taurodeoxycholate was 8 μM or 160 μM. The uptake of [^{3}H]pentamidine in water-injected oocytes was subtracted from oocytes expressing hOCT1 in order to compare the net influence of hOCT1 transporter on pentamidine-taurodeoxycholate ion-pairs. Results were expressed as mean ± SEM, n=24-26 oocytes from 3 different batches/ independent experiments. Data were analysed by one-way ANOVA with GraphPad7. The percentage of [^{3}H]pentamidine in ion-pair form was predicted from the HYSS simulations (Chapter 2 Section 2.4.7.1). The Log D was measured by shake flask method and HPLC analysis (Chapter 2 Section 2.4.3). For ease of comparison, these values have been included in this figure.

3.4.10.2 Uptake of [^{3}H]pentamidine-octanoate ion pairs by hOCT1 in oocytes

The pentamidine-octanoate ion-pairs did not significantly increase the uptake of [^{3}H]pentamidine in both water-injected and oocytes expressing hOCT1 (Figure 3-26). The net effect of hOC1 on the uptake of [^{3}H]pentamidine with octanoate was positive, but the values were very close. This indicated that the pentamidine-octanoate ion-pairs did not influence the [^{3}H]pentamidine to be transported by hOCT1.

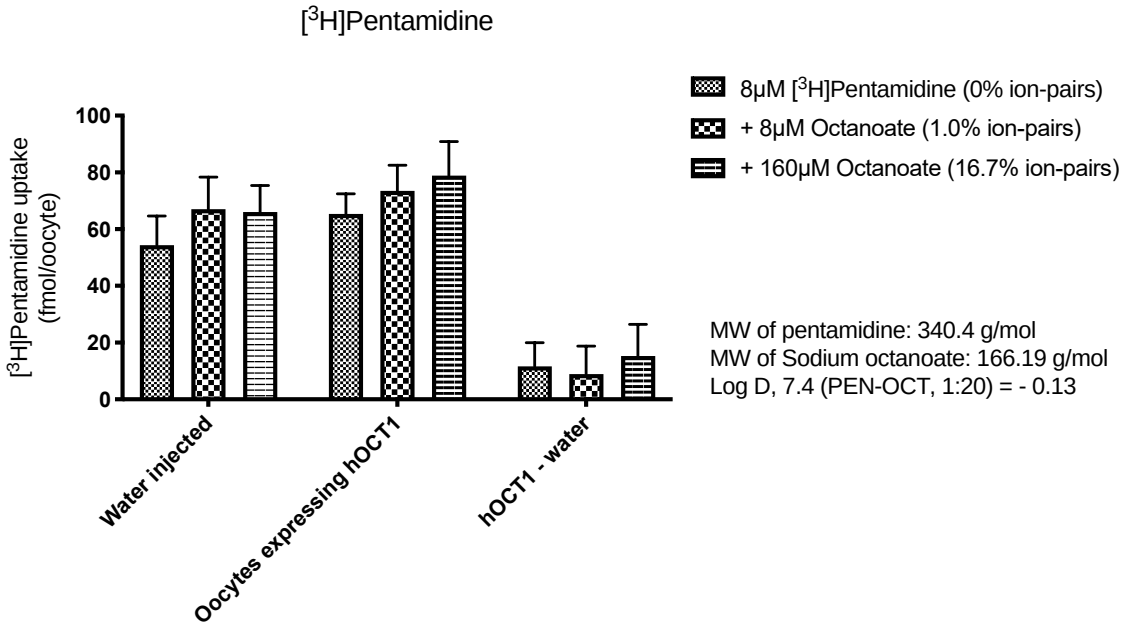

Figure 3-26 The uptake of [^{3}H]pentamidine by hOCT1 transporter. The concentration of pentamidine was 8 μM (31 nM [^{3}H]pentamidine and 8 μM unlabelled pentamidine) and the concentration of octanoate was 8 μM or 160 μM. The uptake of [^{3}H]pentamidine in water-injected oocytes was subtracted from oocytes expressing hOCT1 in order to compare the net influence of hOCT1 transporter on different percentages of pentamidine-octanoate ion-pairs. Results were expressed as mean ± SEM, n=21-26 oocytes from 3 different batches/ independent experiments. Data were analysed by one-way ANOVA with GraphPad7. The percentage of [^{3}H]pentamidine in ion-pair form was predicted from the HYSS simulations (Chapter 2 Section 2.4.7.2). The Log D was measured by shake flask method and HPLC analysis (Chapter 2 Section 2.4.3). For ease of comparison, these values have been included in this figure.

3.4.10.3 Uptake of [^{3}H]pentamidine-xinafoate ion pairs by hOCT1 in oocytes

As shown in Figure 3-27, pentamidine-xinafoate ion-pairs increased the uptake of [^{3}H]pentamidine in water-injected oocytes, although it was not statistically significant. The net uptake of [^{3}H]pentamidine by hOCT1 in oocytes significantly decreased by 154.8% with 38.5% pentamidine-xinafoate ion-pairs compared to 3% of pentamidine-xinafoate ion-pairs.

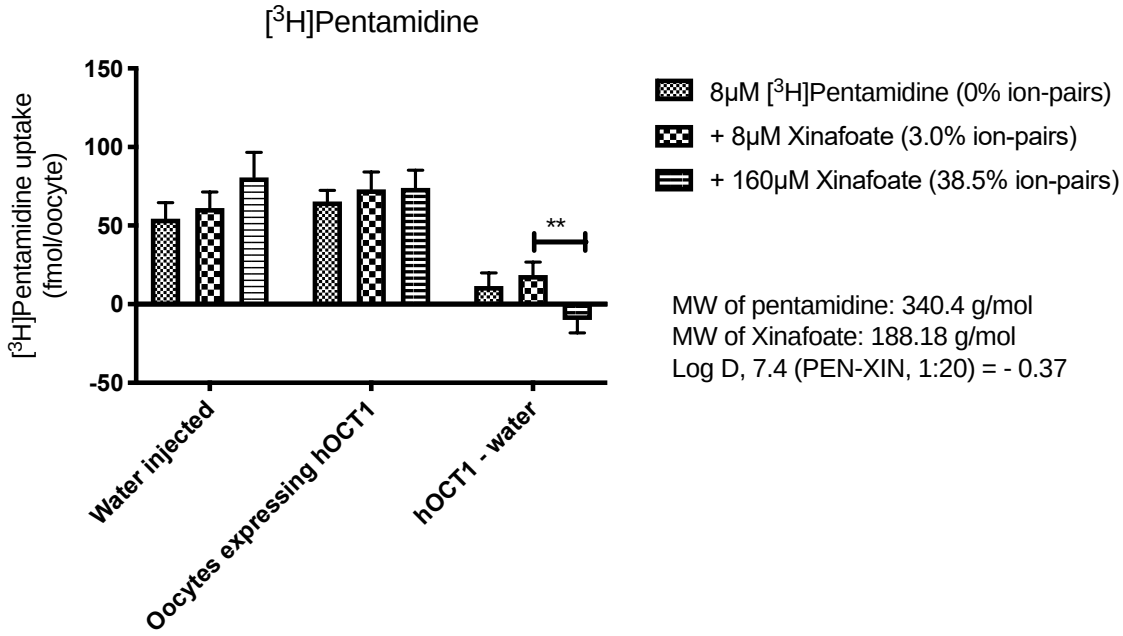

Figure 3-27 The uptake of [^{3}H]pentamidine by hOCT1 transporter. The concentration of pentamidine was 8 μM (31 nM [^{3}H]pentamidine and 8 μM unlabelled pentamidine) and the concentration of xinafoate was 8 μM or 160 μM. The uptake of [^{3}H]pentamidine in water-injected oocytes was subtracted from oocytes expressing hOCT1 in order to compare the net influence of hOCT1 transporter on different percentages of pentamidine-xinafoate ion-pairs. Results were expressed as mean ± SEM, n=21-26 oocytes from 3 different batches/ independent experiments. Data were analysed by one-way ANOVA with GraphPad7. The percentage of [^{3}H]pentamidine in ion-pair form was predicted from the HYSS simulations (Chapter 2 Section 2.4.7.3). The Log D was measured by shake flask method and HPLC analysis (Chapter 2 Section 2.4.3). For ease of comparison, these values have been included in this figure.

3.4.10.4 Uptake of [^{14}C]sucrose in oocytes expressing hOCT1

The purpose of [^{14}C]sucrose uptake assay in oocytes was to evaluate if hOCT1 would affect the membrane integrity of oocytes. The result showed that there were no significant differences of [^{14}C]sucrose uptake between water-injected and oocytes expressing hOCT1 for each counterion. However, the water-injected oocytes had varied [^{14}C]sucrose uptake for different concentrations of octanoate and xinafoate.

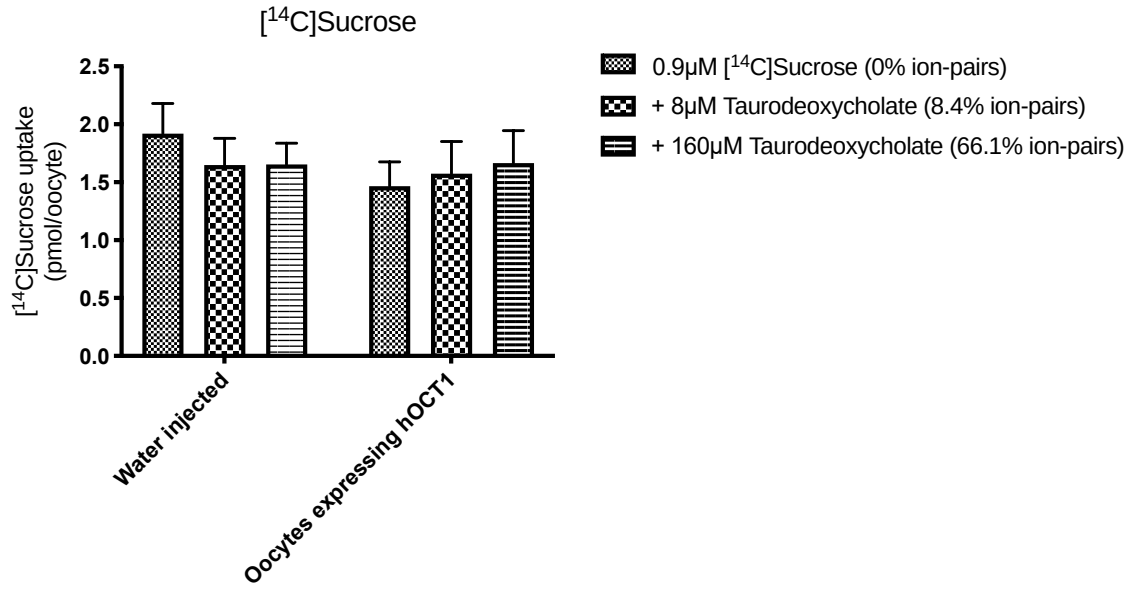
[14C]Sucrose
[14C]Sucrose uptake (pmol/oocyte)
2.5
2.0
1.5
1.0
0.5
0.0
Water injected
Oocytes expressing hOCT1
0.9μM [14C]Sucrose (0% ion-pairs)
+ 8μM Taurodeoxycholate (8.4% ion-pairs)
+ 160μM Taurodeoxycholate (66.1% ion-pairs)

(a)

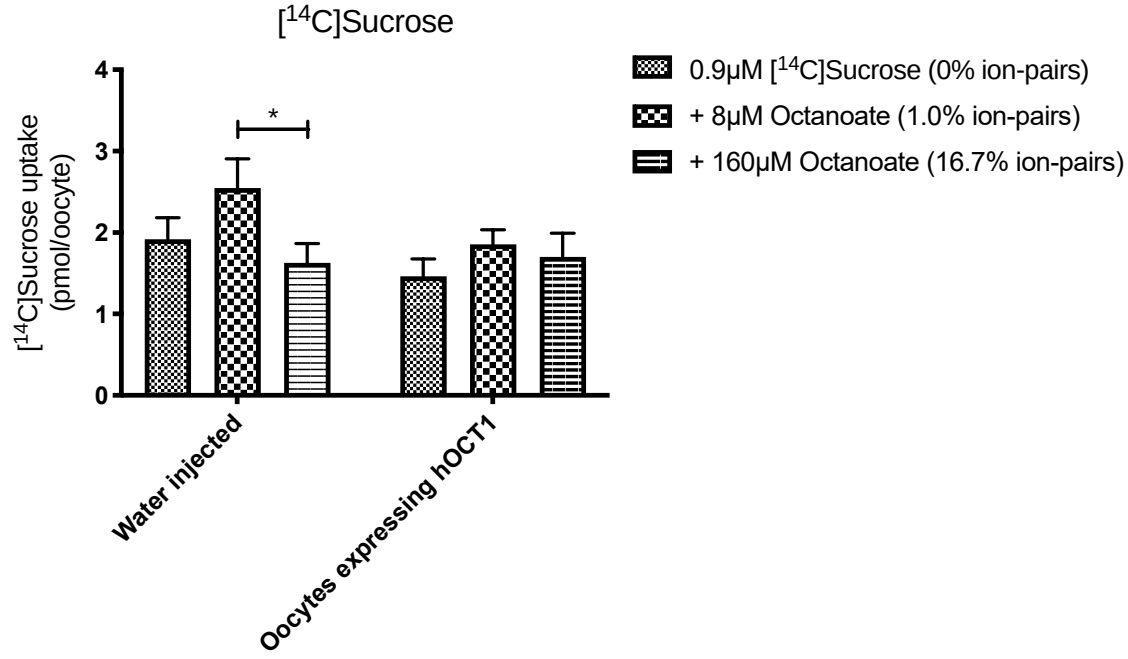
[14C]Sucrose
[14C]Sucrose uptake (pmol/oocyte)
4
3
2
1
0
*
Water injected
Oocytes expressing hOCT1
0.9μM [14C]Sucrose (0% ion-pairs)
+ 8μM Octanoate (1.0% ion-pairs)
+ 160μM Octanoate (16.7% ion-pairs)

(b)

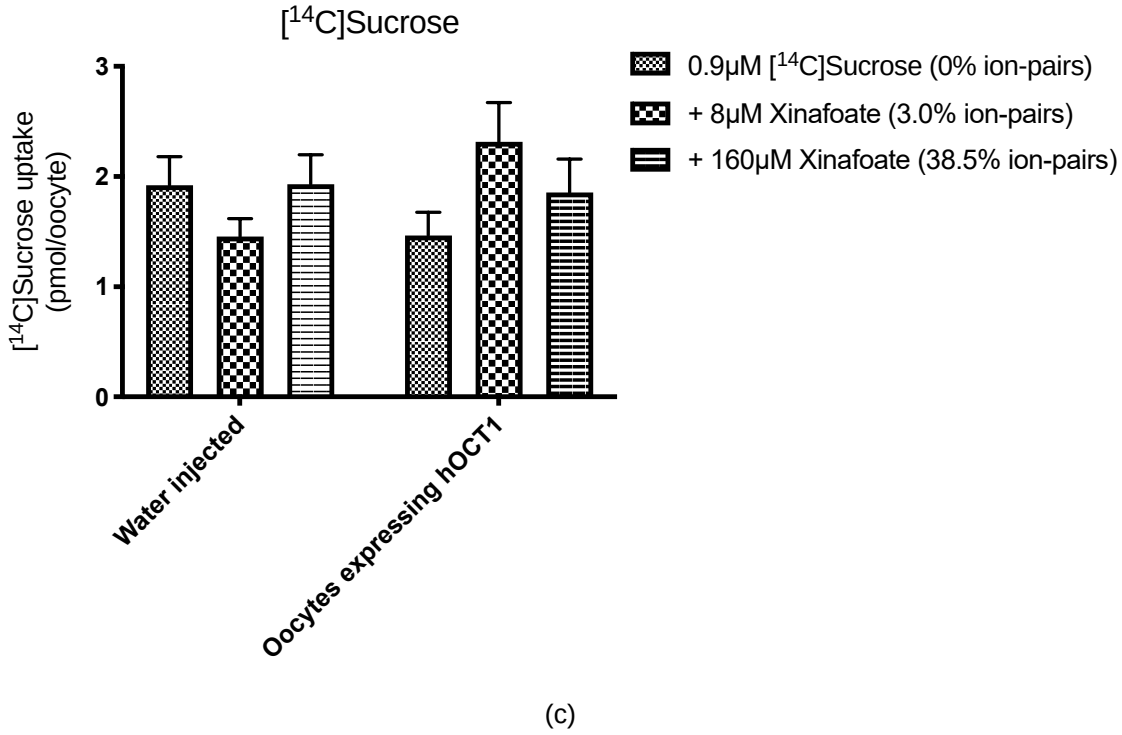

(c)

Figure 3-28 The uptake of [^{14}C]sucrose in water-injected and oocytes expressing hOCT1. The concentration of [^{14}C]sucrose was 0.9 μM and concentrations of counterions were 8 μM or 160 μM. Results were expressed as mean ± SEM, n=21-26 oocytes from 3 different batches/ independent experiments. Data were analysed by one-way ANOVA with GraphPad7.

3.5 Discussion

Human African Trypanosomiasis (HAT) is a neglected disease that affects some of the poorest areas in the world and investing in developing an effective treatment has been demotivated by the high expenses (Barrett, 2000; Barrett *et al.*, 2007). The current drugs for treating HAT are either not effective for late-stage infection when parasites enter the cerebrospinal fluid and brain or cause severe side effects (Legros *et al.*, 2002; Baker and Welburn, 2018). Pentamidine is used only in early-stage of *gambiense* HAT as it is highly ionised in physiological pH and does not cross the BBB well (Bardal *et al.*, 2011). At the BBB, pentamidine is transported into the brain through hOCT1 and effluxed by P-gp (Sekhar *et al.*, 2017). Improving the permeability of pentamidine across the BBB could be key to improving treatment effectiveness for last stage HAT. The ion-pairing method has been successful in improving the entry of ionised molecules into the lung, skin, nasal mucosa and intestinal mucosa (Hatanaka *et al.*, 2000; Benaouda *et al.*, 2018). In chapter 2 we demonstrated that selected counterions improve the lipophilicity of pentamidine as determined using octanol-saline shake flask and HPLC analysis. In this chapter, we explored the possible influence of counterions and ion pair formation on pentamidine transport via passive diffusion and OCT1 using both simple and complex BBB models.

The MTT assay of counterions confirmed that taurodeoxycholate, octanoate, xinafoate, and quercetin of up to 200 µM in hCMEC/D3 cells during the 2 h incubation time did not affect cell viability. This was also assessed by the presence of [^{14}C]sucrose in each of the accumulation assays. There was no effect of 8 or 160 µM counterion on [^{14}C]sucrose uptake at time points of 5, 20, 30 and 60 min, however, there seemed to be loss of membrane integrity at the later time point of 120 min with 9 nM and 160 µM xinafoate. Any increase observed by the presence of counterion with pentamidine at such timepoints was therefore ignored.

The uptake of [^{3}H]pentamidine in hCMEC/D3 cells was either unchanged or reduced with all the counterions, which was contrary to what we expected based on the physicochemical data in Chapter 2. Although pentamidine ion-pairs could improve the lipophilicity of pentamidine as measured by Log D, the complex did not improve the accumulation of [^{3}H]pentamidine in hCMEC/D3 cells. This may be caused by their interactions with other membrane transporters such as hOCT1 and P-gp expressed in hCMEC/D3 cells, or inhibited permeation by the larger

size of pentamidine ion-pair complex. In order to verify these assumptions, we used the single transporter model *xenopus* oocytes which express hOCT1 and studied the interaction of pentamidine ion-pairs with hOCT1.

As the hOCT1 vector had not been used in our lab, the hOCT1 expressed in oocytes model was established and then verified by a series of methods in order to confirm the identity and functionality of hOCT1 in oocytes. The uptake of [^{14}C]D-glucose in oocytes expressing rSGLT was consistent with the results in the thesis of MSc student Reshma Suresh (Suresh, 2013). The DNA sequencing and gel electrophoresis of DNA digestions verified the identity of hOCT1 cDNA. The RNA chip confirmed the size of hOCT1 RNA. The uptake results of the endogenous hOCT1 substrate, [^{3}H]acetylcholine, in oocytes expressing hOCT1 were consistent to the published results by Lips (Lips *et al.*, 2005), This data confirmed the functionality of hOCT1 expressed in oocytes. In the [^{3}H]pentamidine uptake assay, our data suggested that pentamidine is also a substrate of hOCT1, which is consistent to the studies CHO cells and in hCMEC/D3 cells (Xin Ming *et al.*, 2009; Sekhar *et al.*, 2017). In our experiments [^{14}C]sucrose data was generated along with [^{3}H]pentamidine data but was not used as a baseline value to calculate the K_m of [^{3}H]pentamidine uptake by hOCT1 in oocytes. Instead, [^{14}C]sucrose was used as an internal control to measure the membrane integrity of oocytes throughout and between the experiment(The oocytes with extremely high accumulation of [^{14}C]sucrose were excluded from the analyses). Further validation experiments could have been performed to improve the rigour and assurance of the functional expression of hOCT1 in oocytes. For example, OCT1 inhibitors and/or an OCT1 mutated transporter could have been used.

The K_m of pentamidine by hOCT1 transporter in *xenopus* oocytes in this study was 279.9±112.4 µM. This value is higher than 36.4 µM generated by Ming (et al. 2009) utilising transfected Chinese hamster ovary (CHO) cells. This discrepancy may be explained by non-identical expression levels of the transfected OCT1 as well as the different sizes of the *xenopus* oocytes and CHO cells.

Importantly, as human OCT1 was expressed in *xenopus* oocytes, the glycosylation of proteins may have influenced its transport activity in oocytes. Glycosylation affecting the transport activity of transporters has previously been observed as discussed below for the human erythrocyte anion

transporter (band 3) and the proton-coupled amino acid transporter 1 (PAT-1). Glycosylation is a common post-translation modification in protein biosynthesis that affects the thermodynamic stabilization, folding, and kinetics of proteins (Shental-Bechor and Levy, 2008). Glycosylation is a complex process that involves the formation of the sugar-amino acid linkage of carbohydrate components of glycoproteins (Spiro, 2002). Glycosylation affects the membrane expression and transport activity of membrane transporters expressing in *xenopus* oocytes. The human erythrocyte anion transporter (band 3) has a glycosylation site N-glycan at the amino residue. The glycosylated band 3 had more band 3 transported chloride into oocytes compared to the unglycosylated band 3. This suggested that glycosylation may play an important role in allowing the correct folding of protein in oocytes and thereby affecting its transport activity (Groves and Tanner, 1994). The proton-coupled amino acid transporter 1 (PAT1, SLC36A1) when expressed in *xenopus* oocytes is glycosylated at asparagine residues. A study has revealed that changes to the asparagine residues causes reduced transport and less expression on the plasma membrane (Dorn *et al.*, 2009).

The influx of [^{3}H]pentamidine ion-pairs in water-injected oocytes indicated the passive diffusion in simple cell membranes as no membrane transporters were involved. Interestingly, the improvement of lipophilicity of pentamidine by counterions (taurodeoxycholate> octanoate> xinafoate) in octanol-shake flask method (Chapter 2) did not correlate with the influx of [^{3}H]pentamidine with these counterions (xinafoate>octanoate>taurodeoxycholate) in water-injected oocytes. To understand the differences, we compared lipophilicity from the shake-flask method and the uptake of [^{3}H]pentamidine with each counterion in water-injected oocytes (Figure 3-28 below). These comparisons indicate that counterions with larger molecular weight impede pentamidine to pass through cell membranes. One thing to be aware of is that the water-injected oocyte model is not ideal for studying passive diffusion properties, because injecting water into oocytes could damage the integrity of membranes. Thus, drugs could fall into oocytes through the hole on the membrane rather than by lipophilicity.

Also, in the octanol-saline shake-flask methods (Chapter 2), the total pentamidine in the octanol phase was calculated by mass balance method and the total pentamidine in saline phase was quantified by HPLC. The increased log D meant there were more pentamidine in the octanol phase compared to the saline phase, with the introduction of counterions. It did not, however,

reflect the percentage of pentamidine in ion-pair complexes. In other words, more pentamidine could have transported to the octanol phase without forming ion-pairs with counterions.

Pentamidine + Taurodeoxycholate

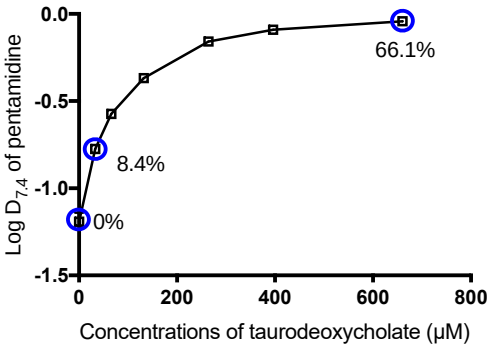

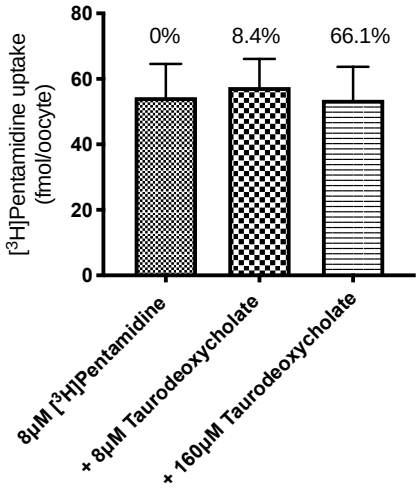

MW of pentamidine: 340.4 g/mol
MW of sodium taurodeoxycholate: 521.7 g/mol

Pentamidine + Octanoate

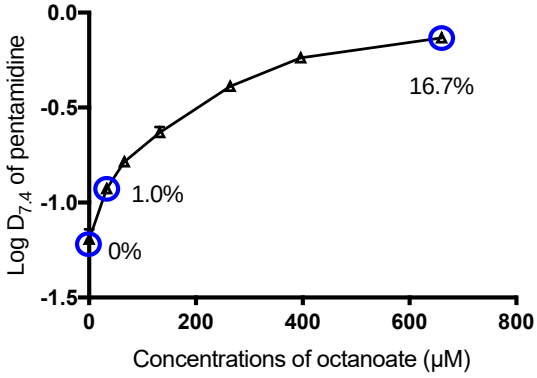

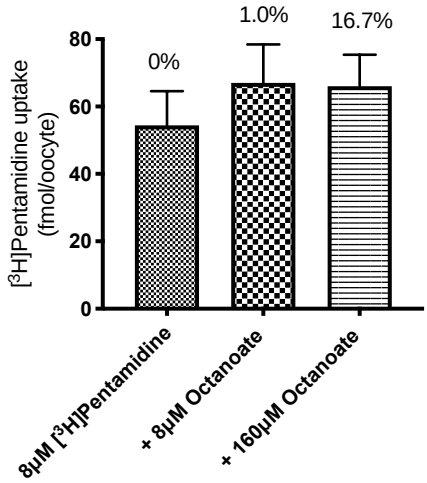

MW of pentamidine: 340.4 g/mol
MW of sodium octanoate: 166.19 g/mol

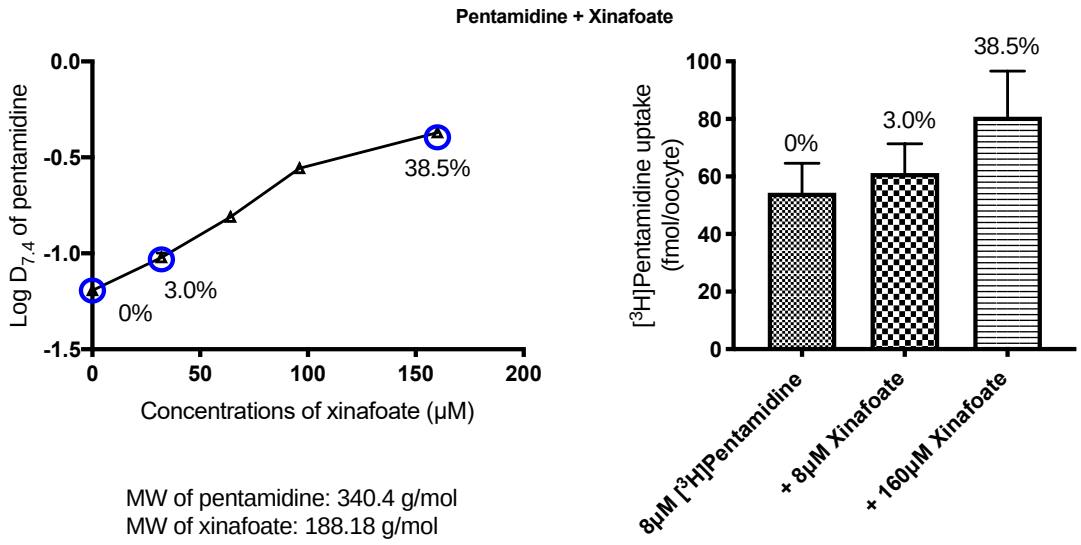

Figure 3-29 Comparisons of the distribution coefficient of pentamidine at pH 7.4 measured by octanol-saline shake flask and HPLC methods (left) and uptake of [^{3}H]pentamidine in water-injected oocytes (right) with counterions (taurodeoxycholate, octanoate, xinafoate). The percentage labels on the figures are percentage of pentamidine in ion-pairs predicted from the HYSS simulations (Chapter 2 Section 2.4.7). For the distribution coefficient of pentamidine, the pentamidine concentration was 20 μg/ml (33 μM) for ion-pairing with taurodeoxycholate and octanoate, or 5 μg/ml (8 μM) for pairing with xinafoate. Results were expressed as mean ± standard deviation at each point (n=3, with 3 replicates each). Some of the error bars were too small to be seen in the figure. For the uptake of [^{3}H]pentamidine in water-injected oocytes, the concentration of pentamidine was 8 μM (31 nM [^{3}H]pentamidine and 8 μM unlabelled pentamidine) and the concentration of counterions was 8 μM or 160 μM. Results were expressed as mean ± SEM, n=21-26 oocytes from 3 different batches/ independent experiments. Data were analysed by one-way ANOVA with GraphPad7.

The net influence of hOCT1 on the uptake of [^{3}H]pentamidine was significantly lower for pentamidine-xinafoate ion pairs in oocytes, which suggested that pentamidine-xinafoate ion-pairs interacted with hOCT1 and this new formation may have impeded the uptake of [^{3}H]pentamidine. This may be related to the change of binding site of pentamidine with hOCT1 when forming pentamidine-xinafoate ion-pairs. The molecular docking simulation indicated that the hydrogen in the amine group of pentamidine interacted with hOCT1. The amidine group on pentamidine is also the binding site of pentamidine with xinafoate, as suggested in the NMR results (chapter 2). Therefore, it is likely that xinafoate blocked the binding site of pentamidine to the hOCT1 influx transporter in oocytes expressing hOCT1.

hOCT1 of the SLC22 transporter family is a polyspecific facilitated transporter that mediates the absorption and the clearance of xenobiotics in liver, kidney, brain (Couroussé and Gautron, 2015). Most of the hOCT1 substrates are cations, although some neutral and weak anionic compounds are also transported by hOCT1 (Koepsell, 2013). A previous study demonstrated that relatively elongated cationic molecules might have stronger binding to hOCT1 (Bednarczyk, 2003). This is

consistent with our finding that pentamidine ion-pair made the chemical structure “fatter” and therefore less likely to be transported by hOCT1. Also, as shown in the literature review in Chapter 2, half of the 26 published OCT1 substrates have a molecular weight in 101-200 g/mol, and with the further beyond 200 g/mol molecular weight, the less likely the molecules to be substrates of hOCT1. Pentamidine has a molecular weight of 340 g/mol, while pairing with the selected counterions in this study would deviate the molecular weight of complexes from the ideal range for hOCT1 substrates.

3.6 Conclusion

The data generated in this chapter confirmed the role of hOCT1 in the uptake of pentamidine.

For pentamidine ion-pairs, we proposed that the transport of pentamidine ion-pairs across the BBB was a dynamic process. When there were no counterions, pentamidine was taken across the BBB by hOCT1. When pentamidine was in the ion-pair complexes, more pentamidine could be taken across the BBB by passive diffusion due to improved lipophilicity, but only if the counterion had a small molecular weight. For example, xinafoate and octanoate. Interestingly, less pentamidine interacted with hOCT1 when pentamidine formed ion-pairs with xinafoate. This may be because the size of pentamidine-xinafoate ion-pairs is outside the normal molecular weight of hOCT1 substrates. It may also be because forming ion-pairs with xinafoate affects the ability of pentamidine to interact with the binding pocket of hOCT1.

Chapter 4 Interaction of pentamidine ion-pairs with P-gp

4.1 Chapter overview

In this chapter, we will examine the interaction of pentamidine ion-pairs with biological membranes using Madin-Darby Canine Kidney (MDCK) cells and *xenopus* oocytes expressing human P-gp. We will first establish and verify these cell models and then study the interaction of pentamidine ion-pairs with P-gp.

4.2 Introduction

The blood-brain barrier is known to express a high density of efflux transporters, as mentioned in Chapter 1, including the P-gp (ABCB1; MDR1), MRP1 (ABCC1), BCRP (ABCG2). These efflux transporters interact with large molecules (i.e. molecular weights over 600 Daltons). Both P-gp and BCRP are expressed at the luminal side of the brain endothelial cells (Löscher and Potschka, 2005b; Hoosain *et al.*, 2015). MRP exists in multiple isoforms and different isoforms are located on different membranes. It has been widely recognised that the P-gp transporter is a key restrictive factor for the cerebral uptake of drugs in CNS (Jonker *et al.*, 1999; Montanari and Ecker, 2015). Therefore, understanding the role of P-gp in the transport of drugs at the blood-brain barrier (BBB) has been and remains of great importance in drug design and development (Hoosain *et al.*, 2015).

Pentamidine was found to be effluxed by P-gp at the BBB (L. Sanderson *et al.*, 2009; Watson *et al.*, 2012; Sekhar *et al.*, 2017). Its inability to treat the late stage of Human African Trypanosomiasis is related to its efflux by P-gp and possibly MRP at the BBB (L. Sanderson *et al.*, 2009). Although the physicochemical studies discussed in Chapter 2 and Chapter 3 revealed that the ion-pairing method significantly improved the lipophilicity of pentamidine and resulted in enhanced passive diffusion across biological membranes, the interaction of pentamidine ion-pairs with P-gp at the BBB is unknown.

As summarized by Hoosain (*et al.*, 2015), currently there are three major models explaining the mechanisms of drugs efflux by the P-gp transporter: the pore model, vacuum cleaner model, and the flippase model. (i) The pore model. It hypothesizes that drugs interact with P-gp on the interior membrane and then is effluxed out of cells through protein channels; (ii) The vacuum cleaner

model (figure 4-1). This model suggests that substrates are first recognised and bound with P-gp at the inner leaflet (one sheet of the lipid bilayer) of plasma membranes, then pumped out of the cells through protein channels. (iii) The flippase model (figure 4-1). It is the most accepted model. It hypothesizes that drugs are first flipped from the inner leaflet (inner sheet of the lipid bilayer) to the outer leaflet (outer sheet of the lipid bilayer) against concentration gradients before reaching the extracellular space through passive diffusion.

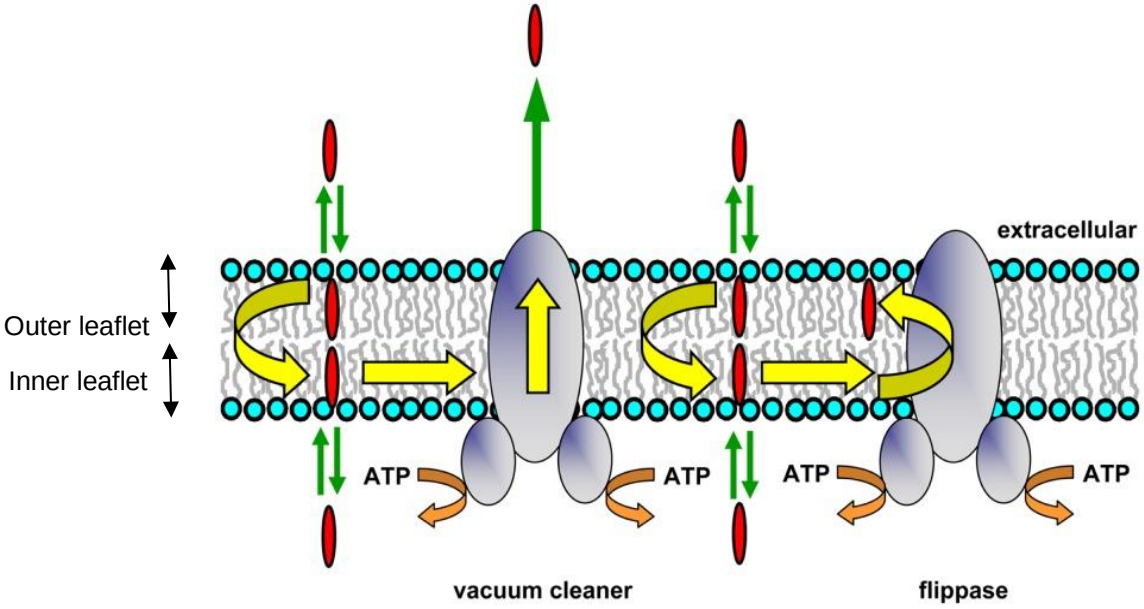

Figure 4-1 The hypothesized structure of P-gp, and mechanisms of the vacuum cleaner and flippase model for P-gp efflux. The image modified from (Sharom, 2014).

There are a few methods developed to either inhibit or bypass the P-gp transporter so that drugs absorption across the BBB can be improved, such as the use of a P-gp inhibitor, nanocarrier, or liposomes (Hoosain *et al.*, 2015). Among these, the combination with a P-gp inhibitor is the most widely studied method and some inhibitors have been successfully used in the clinic. For example, the third generation of P-gp inhibitors including tariquidar, zosuquidar, laniquidar, and ONT-093 have been used in chemotherapy regimens (Thomas and Coley, 2003). However, there is little evidence that the inhibition can be achieved at non-toxic concentrations (Löscher and Potschka, 2005a). Thus, a safer and more effective drug delivery method is of great interest to overcome the issue of drug effluxed by P-gp.

The ion-pairing method is a non-invasive and effective way to improve the absorption of drugs through multiple routes, including oral, parenteral, transdermal, and ocular (Suresh and Paul, 2011a). It is also generally accepted that ion-pairing can only modify physicochemical properties

of drugs, rather than interactions with membrane transporters (Neubert, 1989; Suresh and Paul, 2011a). For example, Miller (*et al.*, 2009) found that phenformin-HNAP ion-pairing method increased the permeability of phenformin by 4.9 folds in Caco-2 cells. He also found that the enhancement of phenformin membrane permeability in Caco-2 cells was in relation to the concentrations of the counterion HNAP and was not saturable. More specifically, the log flux of phenformin was in a linear relationship with the log HNAP concentration. The Caco-2 cell is known to express the P-gp transporter (Brück et al., 2017) and phenformin is a substrate for P-gp (Choi and Song, 2016). So if the P-gp interfered with the ion-pair in addition to the passive diffusion, then the efflux of phenformin would most likely not have a linear relationship with the increased concentration of the counterion HNAP. Therefore, it seems that there was no relationship between P-gp and phenformin-HNAP ion-pairs.

More recently, there was evidence that membrane transporters could have been involved in the transport of ion-pair drugs. Benaouda (*et al.*, 2018) applied theophylline-spermine ion-pair on A549 epithelial cells. The permeability of theophylline was increased by forming theophylline-spermine ion-pair at 37 ˚C. However, when the temperature was lower at 4 ˚C, the permeability of theophylline was suppressed. This hinted that active transport was involved in the process. In our pentamidine ion-pairs study (chapter 3), the accumulation of [^{3}H]pentamidine ion-pairs in hCMEC/D3 cells was inhibited. This could be due to inhibition of influx transport and/or increased pentamidine efflux.

By analysing 28 published P-gp substrates (Figure 4-2) and 38 published P-gp inhibitors (Figure 4-3), we found that the majority of P-gp substrates and inhibitors are neutral or positively charged at pH 7.4 with a wide range of molecular weights from 200 to over 600 g/mol. It is not known whether modifying the charge of pentamidine through ion-pairing would have a direct impact on the dynamics of pentamidine interactions with P-gp.

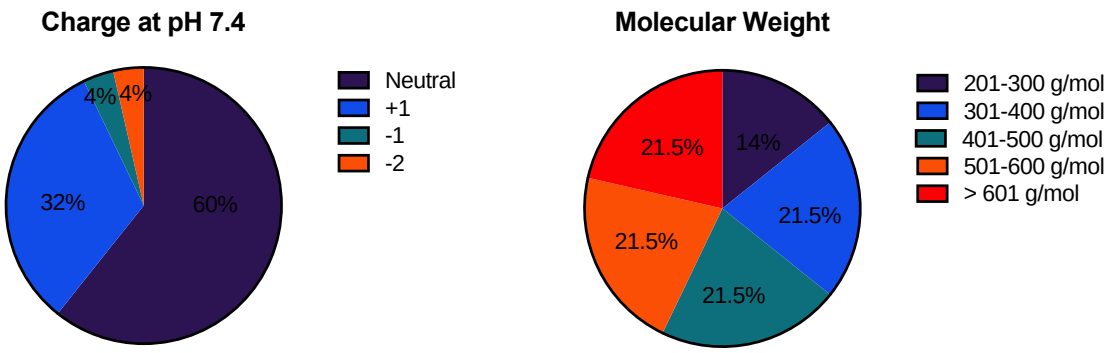

Figure 4-2 Charge and molecular weight of 28 published P-gp substrates (source: NCBI database, 1989-2016).

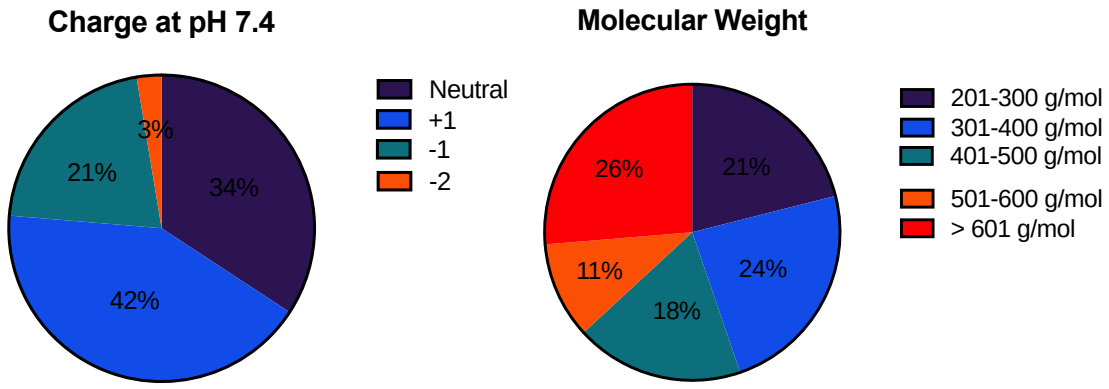

Figure 4-3 Charge and molecular weight of 38 published P-gp inhibitors (source: NCBI database, 1989-2016).

The hypothesis of this chapter is that ion-pairing of pentamidine with a counterion would affect the efflux of pentamidine by the P-gp transporter and therefore change delivery of pentamidine to the brain.

The aim of this chapter is to understand the dynamics between pentamidine ion-pairs and P-gp. The pentamidine-xinafoate ion-pair was chosen as the model ion-pair to study the interaction of ion-pairs with the P-gp transporter, as this counterion was extensively researched in chapter 2 and chapter 3 and we have generated a robust set of physicochemical and biological data for xinafoate. In addition, xinafoate is more lipophilic than the other two counterions taurodeoxycholate and octanoate, so it is more likely to form ion-pairs with pentamidine that could improve the passive diffusion of pentamidine across membranes and result in a more efficacious drug formulation.

The objectives are as follows:

- To determine the specific interactions of pentamidine with P-gp using *in silico* molecular docking and compare the results with known P-gp substrates (e.g. dexamethasone)
- To confirm suitability of the MDCK and MDCK-hMDR1 cell lines for exploring pentamidine ion pairs interaction with human MDR1 by determining the toxicity of pentamidine-taurodeoxycholate, pentamidine-octanoate, pentamidine-quercetin, and pentamidine-xinafoate in these cells using the MTT assay
- To examine the impact of counterions on the interaction of pentamidine with P-gp using Madin-Darby Canine Kidney (MDCK-WT) and MDCK-hMDR1
- To establish a P-gp single transporter expressing model utilising *xenopus* oocytes
- To confirm the identity and functional expression of P-gp in *xenopus* oocytes through DNA sequencing, gel electrophoresis of DNA and RNA, influx (accumulation) and efflux transport of P-gp substrates [^{3}H]dexamethasone and [^{3}H]corticosterone
- To determine the interaction of [^{3}H]pentamidine-xinafoate ion-pair with P-gp by measuring the efflux of [^{3}H]pentamidine extruded from xenopus oocytes expressing P-gp

4.3 Materials and Methods

4.3.1 Materials

Ampicillin sodium salt was purchased from Calbiochem, gentamicin sulphate from Apollo Scientific, HiSpeed Plamid Midi Kit was purchased from Qiagen (Manchester, UK), mMESSAGE mMACHINE T7 Transcription Kit, 3M Sodium Acetate (pH 5.5), 100mm square petri dishes were purchased from Thermo Fisher Scientific (Paisley, UK), 100mM Sodium Pyruvate, tris base were purchased from Fisher Scientific (Leicestershire, UK), Collagenase Type IV was purchased from Gibco, UltraPure Agarose from Invitrogen Life Technologies, 0.5M EDTA solution was purchased from Severn Biotech (Worcestershire, UK), magnesium sulphate heptahydrate (>=99.5%), potassium chloride were bought from AnalaR, calcium chloride dihydrate (>=99.0%), sodium chloride (>=99.5%), sodium dodecyl sulfate (>=92.5%), quinine were purchased from Sigma-Aldrich, sodium octanoate (>=99.0%), calcium nitrate tetrahydrate, quercetin (>=95.0%), HEPES (>=99.5%), sodium taurodeoxycholate hydrate (>=95.0%), LB Agar, boric acid (>=99.5%) were from Sigma Life Science, 1-Hydroxy-2-naphthoic acid (>=97.0%) from Aldrich Chemistry. Ethidium Bromide Solution (10mg/ ml) was bought from Alfa Aesar, 3.5'' tubes from Drummond

Scientific, Ultima Gold was purchased from PerkinElmer (Bucks, UK), 1kb DNA ladder, 6x loading dye, SalI and NcoI enzymes were purchased from Promega, hydrochloric acid and sodium hydroxide standard solution were purchased from Fluka Analytical.

Radiolabelled compounds

[^{3}H]pentamidine (31.9 Ci/mmol, 31 µM) was custom radiolabelled from Moravek Biochemicals, [^{14}C] D-glucose (250-360 mCi/mmol) was purchased from PerkinElmer (Bucks, UK), [^{3}H]Dexamethasone (89 Ci/mmol, 11.2 µM) was purchased from GE Healthcare, UK and has a specific activity of 3.29 TBq/mmol, [^{3}H]corticosterone (75.0 Ci/mmol, 13 µM) has a specific activity of 2.78 TBq/mmol and was purchased from GE Healthcare, UK.

4.3.2 Cell Culture

Two different types of cells: wild type MDCK (MDCK-WT) and human MDR1 highly expressing MDCK (MDCK-hMDR1) cells were utilised in the study, in order to examine the interaction of P-gp (MDR1) with pentamidine ion-pair complexes. (Source of WT MDCK cells and the MDCK-MDR1 cells were a gift from Dr David Begley received from GSK (Ware, UK)). This cell line was prepared by transfecting the MDCK (Madin-Darby Canine Kidney) cells with human P-gp (MDR1) transporter. The passages of cells for wild type MDCK and MDCK-hMDR1 were among P21-26 and P35-42, respectively. Both cells lines were seeded onto 96-well plates less than 10 generations after thawing from the liquid nitrogen, as required to maintain the function of cells (Kuteykin-Teplyakov *et al.*, 2010; Wang *et al.*, 2013).

For cell culture, both cell lines were grown in T-75 flasks with high glucose Dulbecco's Modified Eagle Medium (DMEM) which consists of 4,500 mg/L-glucose, L-glutamine, sodium, pyruvate, and sodium bicarbonate with 10% fetal bovine serum (FBS), 1% penicillin-streptomycin, and 1% 1x non-essential amino acids (Sigma Aldrich, UK). The cells were kept in a 37 °C incubator with 5% CO_2. The media were changed every 2 to 3 days. Both cell lines were passaged when they reached 80-90% confluency. The cells were seeded in a density of 20,000 cells/cm^2. After splitting, the cells reached 80-90% confluency in 2-3 days. For cell accumulation assays, the cells were left for a further two days to differentiate further.

4.3.3 Cytotoxicity Assay

The viability of MDCK-WT and MDCK-MDR1 cells was measured by MTT (3-(4,5-dimethylthiazol-2-yl)-2,5-diphenyltetrazolium bromide) to assess the cytotoxicity of taurodeoxycholate, octanoate, quercetin and xinafoate. Confluent MDCK-WT (P21-23) and MDCK-MDR1 cells (P35-37) were incubated with different concentrations (0, 50, 100 and 200 µM) of counterions in the accumulation buffer for 2 h at 37 ˚C. At the end of this incubation time, the buffer was aspirated, and the wells were refilled with pre-warmed MTT (1 mg/ml) in DMEM without phenol red and the plates placed in an incubator with 5% CO_2 at 37 ˚C for 4 h. Following this, the MTT solutions were replaced with 100 µl propan-2-ol. After 5 min, the viability of cells could be determined by measuring the absorbance of samples at 540 nm using a Labsystems Multiscan reader with the Ascent software. The absorbance was corrected by protein concentrations with BCA assay. Cells viability was compared to the control (i.e. cells in accumulation buffer) and results were expressed as percentage viability.

4.3.4 Accumulation of [^{3}H]pentamidine in wild type MDCK and MDCK-MDR1 cells

The objective of the accumulation assay was to evaluate if the MDCK-WT and MDCK-MDR1 cells could be utilised to isolate the impact of P-gp transporter on the transport of pentamidine ion-pairs. The accumulation assay of [^{3}H]pentamidine (9 nM) in the presence or absence of unlabelled (8 µM) was performed on confluent MDCK-WT or MDCK-MDR1 cells in 96-well plates. The [^{14}C]sucrose (0.9 µM) acted as a marker for non-specific binding, membrane integrity and measurement of extracellular space. The plates were shaken at 120 rpm over 2 h at 37 °C. The accumulation buffer was removed at the 5, 20, 30, 60 and 120-min time points, immediately followed with three times of washes with ice-cold PBS^+ to terminate the transport. Then the cells were lysed in 200 µl 1% Triton x-100 and shaken at 120 rpm for 1 h. The 100 µl of the lysates were transferred to a scintillation vial with 4 ml of scintillation solution to count for radioactivity. The radioactivity was measured as disintegrations per min (dpm) by Packard Tri-Carb 2900TR liquid scintillation counter (Perkin-Elmer, Beaconsfield, UK). The radioactivity of the lysates was corrected with protein concentrations measured by Bicinchoninic acid (BCA) and background dpm of the accumulation buffer.

4.3.5 Bicinchoninic acid (BCA) assay

See section 3.3.5 for details.

4.3.6 Expression of results

The accumulated radioactivity was expressed as a volume of distribution (V_d) which was calculated by the ratio of dpm/mg protein to dpm/µl buffer. Results were expressed as the mean value of V_d from not less than three different passages of cells/ independent experiments. The calculation method can be found in chapter 3 Section 3.3.6.

4.3.7 Molecular Docking of pentamidine onto P-gp

Computer modelling was utilized to study the specific interactions of pentamidine, dexamethasone (positive control i.e. known P-gp substrate), sucrose (negative control i.e. non-P-gp substrate) and mannitol (negative control i.e. non-P-gp substrate) with the P-gp transporter and was completed by Dr Khondaker Miraz Rahman from the medicinal chemistry group at King's College London. Molecular docking was performed using CDOCKER (Discovery studio version 4.0), a CHARMm based docking tool, where annealing molecular dynamics were simulated to each orientation. P-gp contains 2 active ATPase sites, and both binding sites were used for docking. Based on the CDOCKER energy, the ligand poses were sorted and then the most favorable binding (the most negative value) was retained.

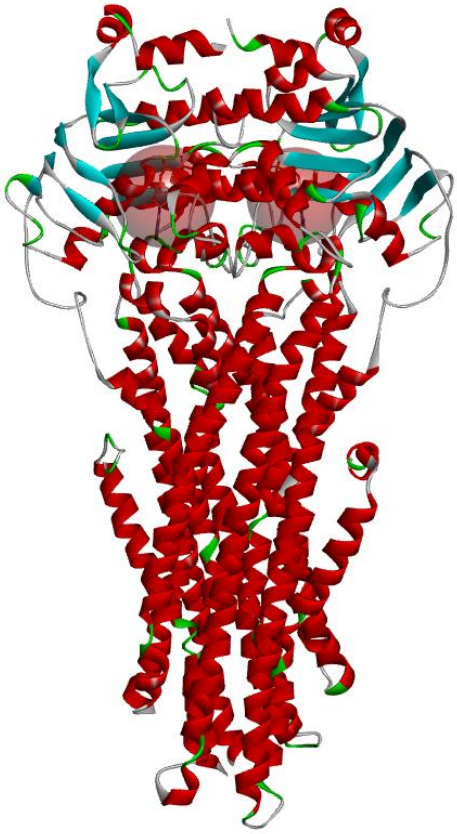

Figure 4-4 Molecular structure of human P-glycoprotein in the ATP bound, outward-facing conformation (Kim and Chen, 2018).

4.3.8 Method to Express P-gp transporter in the *lavies xenopus* oocytes

In order to express the P-gp transporter in *xenopus* oocytes, the cDNA of P-gp vector was amplified and verified through DNA sequencing and restriction enzyme digestion. Then the P-gp RNA was synthesised and verified by gel electrophoresis. Finally, the P-gp RNA was injected into oocytes and the functional expression of P-gp was confirmed by radiolabelled P-gp substrates.

4.3.8.1 Plasmid and inserts

Human ABCB1 *(P-gp)* cDNA plasmid (Accession: NM_000927) was purchased from Stratech (catalogue number: HG12030-G, Suffolk, UK) manufactured by Sino Biological Inc (Drake *et al.*, 2018). The *P-gp* cDNA was cloned into the pGEM-T vector with ampicillin resistance gene for selection. The size of the *P-gp* cDNA is 3843 base pairs.

4.3.8.2 Preparation of agar plates

See section 3.3.10.2 for details

4.3.8.3 Amplification of P-gp cDNA

See section 3.3.10.3 for details.

4.3.8.4 Sequencing of P-gp cDNA insert

The following customised primers (oligonucleotides), as shown in Table 4-1, were purchased from Sigma-Aldrich Company Ltd (Dorset, UK) to sequence the full-length *P-gp* cDNA insert. The primers and the *P-gp* vector cDNA template were diluted to 10 µM and then posted to GENEWIZ (Essex, UK) for Sanger Sequencing.

Table 4-1 Oligonucleotides for Sanger Sequencing

Primers	Sequence
1	GCCAGGGTTTTCCCAGTCACGAC
2	GAGCGGATAACAATTTCACACAGG
3	GGCCATCAGTCCTGTTCTTG
4	GCTGTCAAGGAAGCCAATGC
5	CGCCAATGATGCTGCTCAAG

4.3.8.5 Restriction Enzyme Digestion of *P-gp* cDNA

The *P-gp* cDNA plasmid was digested by enzymes to confirm the identity of the insert. *P-gp* cDNA was digested by SalI and NcoI enzymes at 37 ˚C for overnight. Then sizes of the fragments were checked with agarose gel electrophoresis. The agarose was dissolved in 75 ml of 1xTBE buffer at a final concentration of 1% (m/v). Ethidium Bromide (4 µl) was used to stain the DNA. 1 kb DNA ladder was loaded in parallel with the samples as a reference. 500 ng DNA samples in loading buffer were loaded in each well and run at 100 V for 1 h. Then results were visualized under UV and images were captured by GeneSnap.

4.3.8.6 Plasmid linearization

The *P-gp* plasmid was linearized with the restriction enzyme SalI at 37 ˚C overnight. The linearization process was terminated with 1/20th volume of 0.5 M EDTA, 1/10th volume of 3 M Na acetate and 2 volumes of ethanol. Then the sample was mixed well and chilled at -20 ˚C overnight for precipitation.

4.3.8.7 Synthesis of *P-gp* RNA

See section 3.3.10.7 for details.

4.3.8.8 Poly-A-tailing *P-gp* RNA

The Poly-A tailing Kit (Applied Biosystems) could add a poly-A tail (≥150 bases) to the RNA prepared with the Ambion® mMESSAGE mMACHINE® Kit. This capped and tailed RNA may increase mRNA stability and therefore could enhance translation following micro-injection experiments (Bernstein and Ross, 1989; Gallie, 1991). The procedures of preparing the poly-a tailed RNA start with a complete and DNase-treated mMESSAGE mMACHINE reaction (20 µl). At room temperature, the tailing reagents: nuclease-free water (36 µl), 5X E-PAP Buffer (20 µl), 25 mM $MnCl_2$ (10 µl), 10 mM ATP (10 µl) were added to the reaction. After the assembling, a 0.5 µl of the mix solution was taken out as a control, prior to the addition of 4 µl of E-PAP. Then the reaction and the control were incubated at 37 ˚C for 1 h.

4.3.8.9 Verification of RNA

The un-tailed *P-gp* RNA can be verified using Agilent RNA 6000 Nano Kit with 2100 Bioanalyzer, as described in Chapter 3 Section 3.3.9.10. The poly-a tailed *P-gp* RNA was verified on a denaturing agarose-formaldehyde gel, since the components in the Poly-A tailing Kit could disrupt the signal of the 2100 Bioanalyzer. To prepare for a denaturing agarose-formaldehyde gel, 1 g of agarose in 72 ml water was heated until dissolved, then cooled to 60°C. Then 10ml 10X MOPS (3-(N-morpholino) propanesulfonic acid) which is composed of 0.4 M MOPS at pH 7.0, 0.1 M sodium acetate, 0.01 M EDTA running buffer and 18 ml 37% formaldehyde were mixed with the agarose solution, before it was immediately poured to a tank with a comb to form wells. After the gel was solidified, the comb was carefully removed from the tank. The gel was covered by 1X MOPS running buffer. For samples, 0.5 µl of the RNA marker (Millennium Markers, P/N AM7150) and RNA samples were mixed with 4 µl gel loading dye with EDTA containing 50 µg/ml ethidium bromide, before heated at 75 °C for 10 min. The samples were loaded into the wells of the gel, and then run at 5 volts/cm for 1 h. Then bands of samples were examined under UV light.

4.3.8.10 Preparation of *xenopus* oocytes expressing P-gp

The details of preparing for *xenopus* oocytes can be found in chapter 3 section 3.3.9.11. Briefly, stage V and VI oocytes were selected for micro-injection. Each oocyte was injected with 50nl

RNA-free water or *P-gp* cRNA, then placed in MBM with 1 mM sodium pyruvate. The injected oocytes were stored at 19-20 ˚C for 3 days before the uptake assay. The MBM was changed every day, and broken oocytes were discarded.

4.3.8.11 Verification of P-gp functional expression in oocytes by [^{3}H]dexamethasone and [^{3}H]corticosterone

The functionality of P-gp in oocytes was verified by measuring the influx and efflux transport of two P-gp substrates [^{3}H]dexamethasone (Régina *et al.*, 1999) and [^{3}H]corticosterone (Wolf and Horwitz, 1992a). The use of P-gp substrates to demonstrate transporter functionality shows considerable variation dependent upon binding affinity, membrane partitioning considerations. It is important to note that some molecules are inhibitors of P-gp transport and not substrates. We utilised two types of experimental design for [^{3}H]dexamethasone and [^{3}H]corticosterone: Influx (uptake/accumulation) and efflux intraoocyte injection) assay. For influx (accumulation) assay, water-injected oocytes or oocytes expressing P-gp were incubated in MBM with radiolabelled drug for up to 1 h, after that the oocytes were washed and the intra-oocyte DPM of radiolabelled drug was measured. For efflux assay, the radiolabelled drug was injected into each oocyte at the beginning of the experiment, then the amount of radiolabelled drug that went out of the oocyte was measured. Note both the influx and efflux assay here are the overall effect by passive diffusion and interaction with P-gp.

For influx assay, 8-10 of water-injected oocytes or oocytes expressing P-gp were placed in vials with MBM. The MBM was aspirated just before 9 nM [^{3}H]dexamethasone or 13 nM [^{3}H]corticosterone in 500 µl of MBM was filled in the vials. Each group of oocytes was incubated with the transport buffer for 1 h and then the transport was stopped with three times of washes with ice-cold MBM. Each of the oocytes was lysed in 500 µl 10% SDS. Then 4 ml of scintillation fluid was added to the each of the oocyte lysates and the DPM was counted on a Packard Tri-Carb 2900TR liquid scintillation counter (Perkin-Elmer, Beaconsfield, UK). Results were expressed as the mean uptake ± standard errors of [^{3}H]dexamethasone or [^{3}H]corticosterone in each oocyte (fmol/oocyte). For the calculation method, see 4.2.10.

For efflux assay, oocytes were injected with 30 µg P-gp RNA in 50 nl water or 50 nl RNA-free water and then incubated in MBM with pyruvate for 3 days. The average intra-volume of each

xenopus oocyte was assumed at 500 nl for the ease of calculation. On the day of efflux assay, water-injected oocytes and oocytes expressing P-gp were injected with [^{3}H]dexamethasone or [^{3}H]corticosterone in MBM with 1 mM ATP to give final intra-oocyte concentrations of 4 nM for [^{3}H]dexamethasone and 25 nM for [^{3}H]corticosterone. After injection, each oocyte was placed in a well of a 96-well plate with 100 µl MBM. At the 15, 60, and 120-min time points, the efflux buffer was carefully drawn by a fine tip without breaking the oocytes. The efflux buffer from each oocyte was placed in scintillation vials. Then 4ml of scintillation solution was added and the DPM was counted by Packard Tri-Carb 2900TR liquid scintillation counter (Perkin-Elmer, Beaconsfield, UK). Results were expressed as the mean efflux ± standard errors of [^{3}H]dexamethasone or [^{3}H]corticosterone from each oocyte (pmol or fmol/oocyte). For calculation method, see 4.3.10.

4.3.9 Efflux of [^{3}H]pentamidine and [^{3}H]pentamidine-xinafoate ion-pairs in oocytes expressing P-gp

Oocytes were injected with 30 µg P-gp or 50 nl RNA-free water, and then incubated in MBM with pyruvate for 3 days. The average intra-volume of each *xenopus* oocyte was assumed at 500 nl for the ease of calculation. For the efflux of [^{3}H]pentamidine, on the day of efflux assay, water-injected oocytes and oocytes expressing P-gp were injected with [^{3}H]pentamidine to give final intra-oocyte concentrations of 31 nM for [^{3}H]pentamidine. For the efflux of [^{3}H]pentamidine-xinafoate ion-pairs, the final intra-oocyte concentration of [^{3}H]pentamidine was 8 µM (31 nM radiolabeled and 8 µM unlabeled pentamidine), while the final intra-oocyte concentration of xinafoate was 8 µM and 160 µM (pentamidine: xinafoate = 1:1 and 1:20). After injection, each oocyte was placed in a well of a 96-well plate with 100 µl MBM. At the 60-min time point, the efflux buffer was carefully drawn by a fine tip without breaking the oocytes. The efflux buffer from each oocyte was placed in scintillation vials. Then 4ml of scintillation solution was added and the DPM was counted by Packard Tri-Carb 2900TR liquid scintillation counter (Perkin-Elmer, Beaconsfield, UK). Results were expressed as the mean efflux ± standard errors of [^{3}H]pentamidine from 3-4 different batches of oocytes. See calculation method in 4.3.10.

4.3.10 Calculation methods for influx and efflux assay

Step 1: The specific activity of 10 µl uptake or efflux media was calculated.

For example, 10 µl of 10 mM drug has 100 nMoles/10 µl,

10 mM= 10, 000 µM/l=10,000 µM/1000 ml= 10 µM/ml = 10,000 nM/1000 µl = 100 nMoles/10 µl

Step 2: Count 10 µl of uptake media - X dpm/ 100 nMoles

e.g. 1000 DPM/100 nMoles = 100 pmols/DPM

Step 3: Y DPMs is converted to pmols in each oocyte.

The counted DPM in each oocyte was converted to pmols using the conversion ratio in step 2.

4.3.11 Statistical analysis

Results were expressed as mean ± standard errors (S.E.M). The data for uptake assay were analysed by one-way ANOVA or two-way ANOVA with GraphPad 7. Significant differences were assumed when $p<0.05$.

4.4 Results

4.4.1 Molecular docking of pentamidine onto P-gp

For the ATPase binding site with the lowest energy, all interactions between pentamidine and P-gp are hydrogen bonds (figure 4-5): the ether group on pentamidine interacts with ARG262 on P-gp; the benzene ring on pentamidine attracts to the GLN535 and ALA529 on P-gp; the hydrogen on the amidine of pentamidine attaches to the GLU1119 on P-gp.

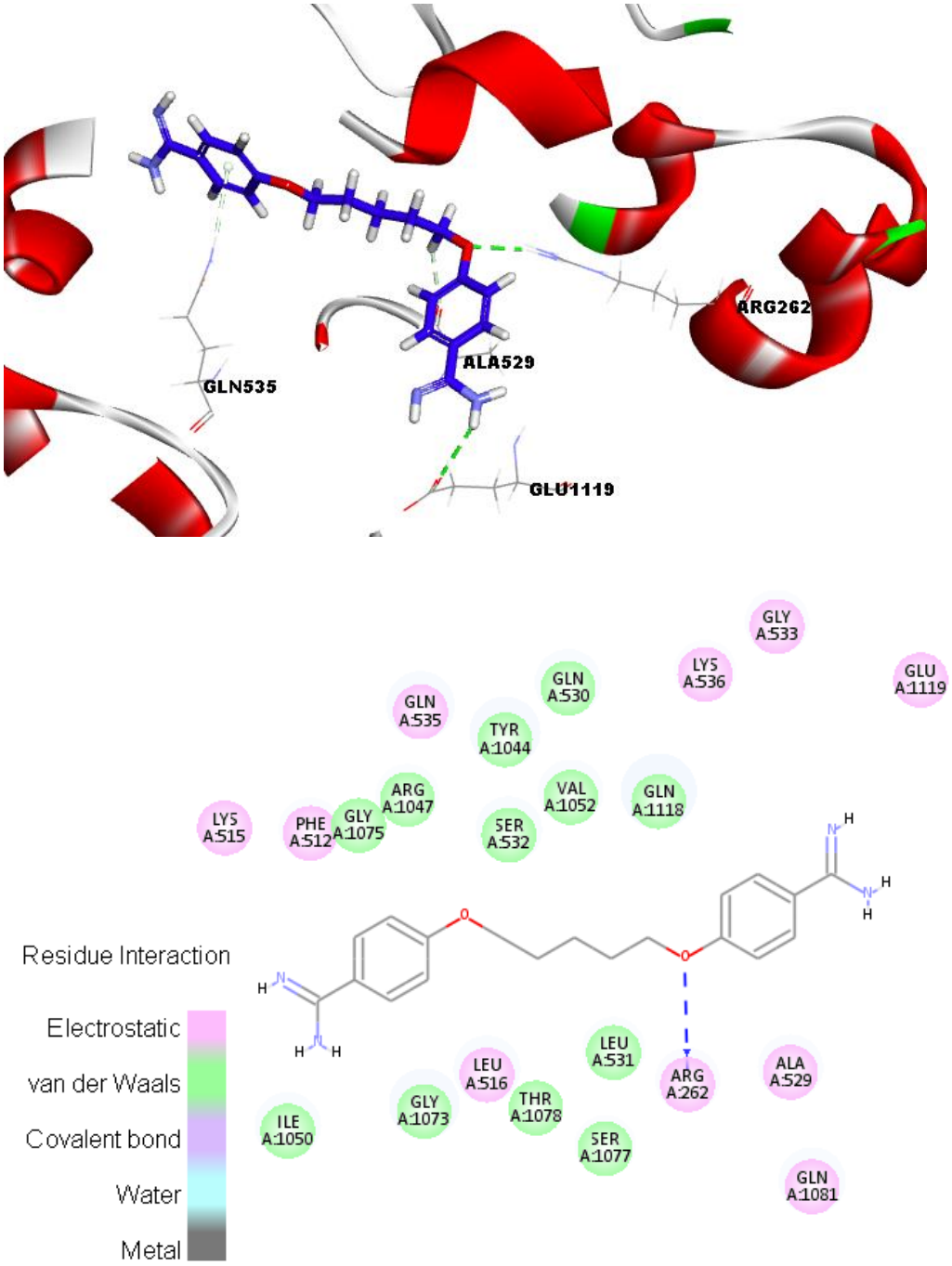

Figure 4-5 Molecular docking of pentamidine onto P-gp transporter. The image was provided by Dr Khondaker Miraz Rahman's group from Medicinal Chemistry at King's College London.

For dexamethasone (a P-gp substrate), its oxo group forms a hydrogen bond with GLN724 on P-gp. Its hydroxy groups also interact MET985, GLU874, GLN346 on P-gp through a hydrogen bond. The methyl group on dexamethasone interacts with MET875 on P-gp through hydrophobic attraction (figure 4-6).

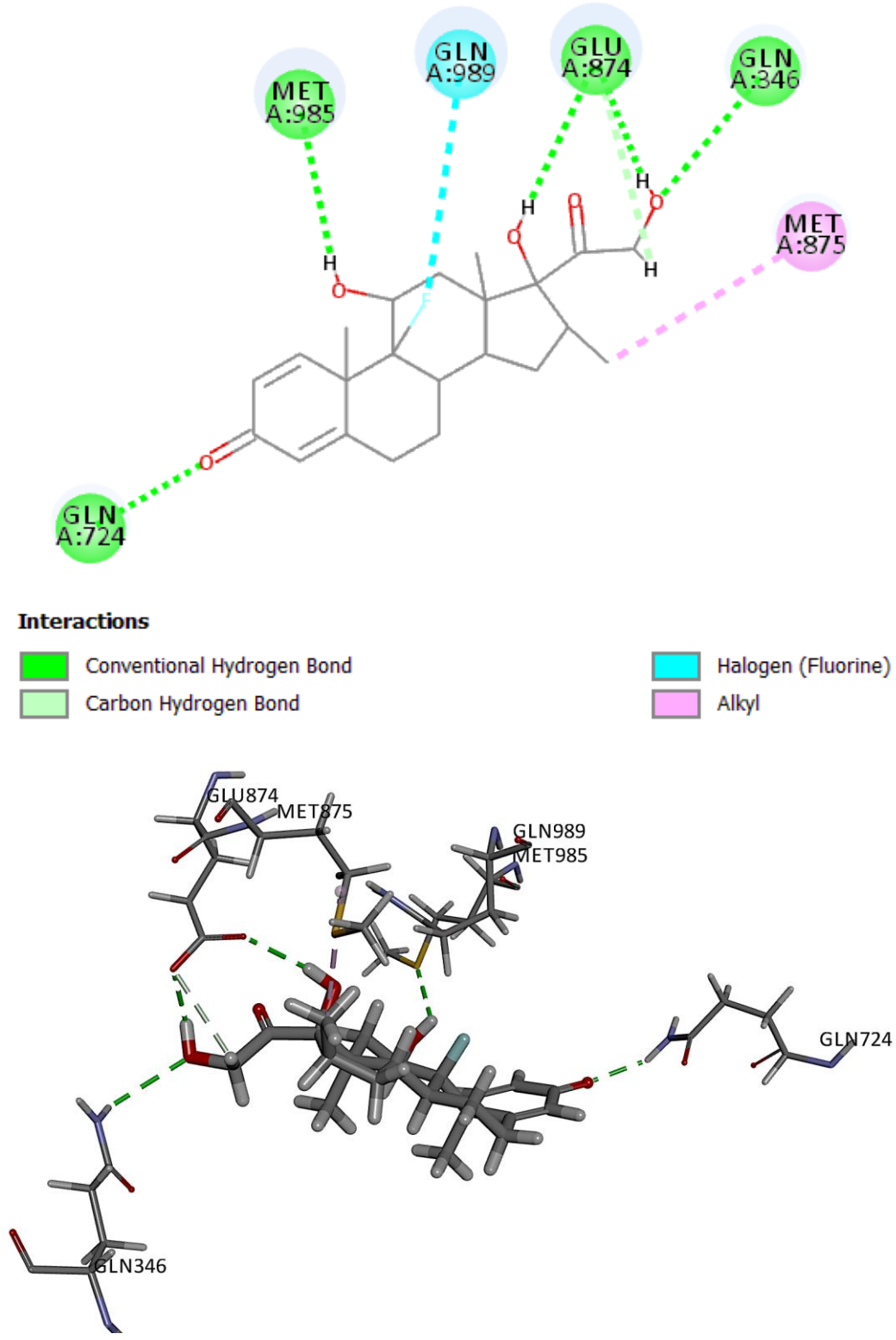

Figure 4-6 Molecular docking of dexamethasone onto P-gp transporter. The image was provided by Dr Khondaker Miraz Rahman's group from Medicinal Chemistry at King's College London.

For mannitol, its hydroxyl functional groups interact with ARG262, TYR1044, and ALA529 on P-gp with hydrogen bond (figure 4-7).

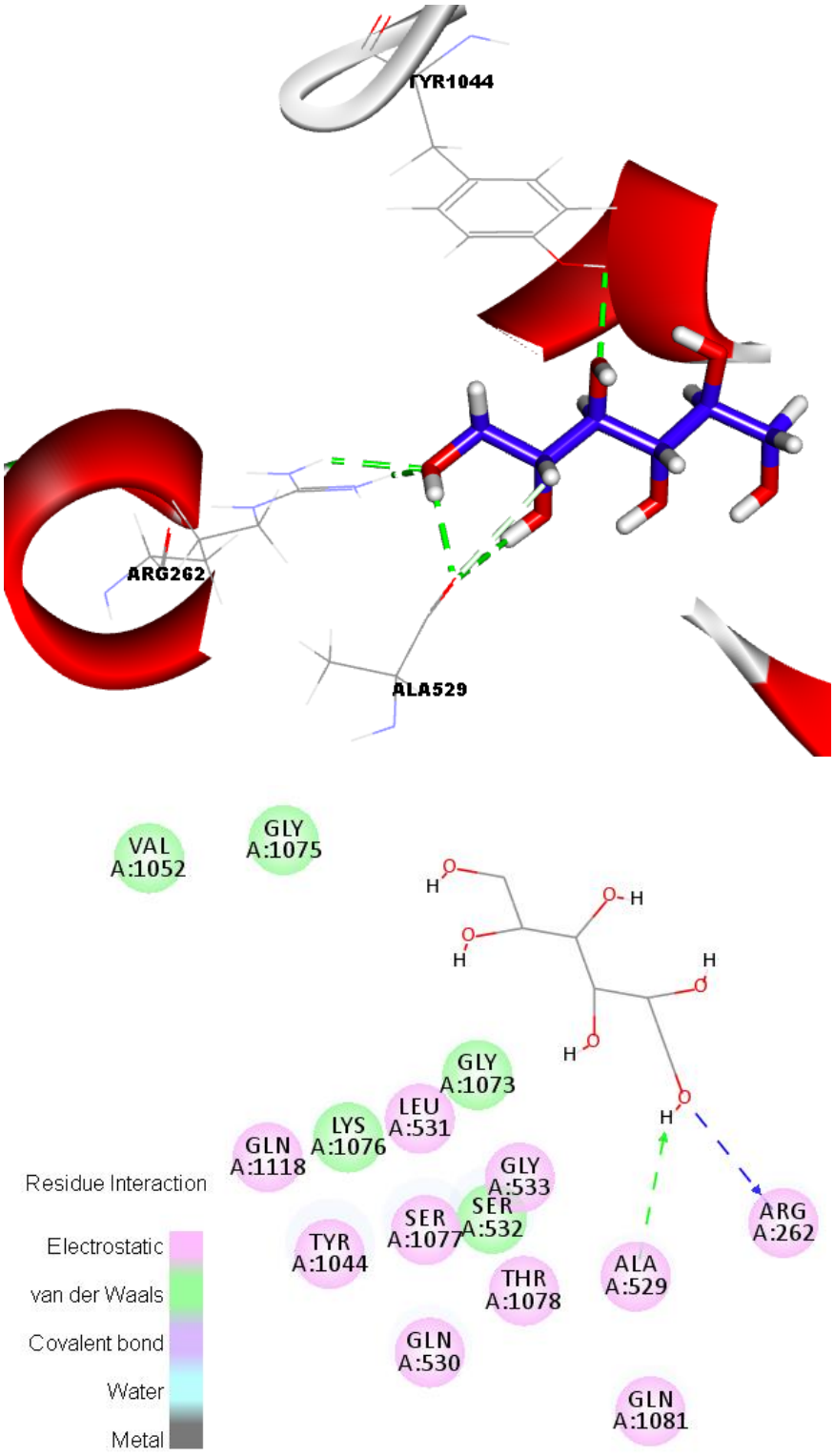

Figure 4-7 Molecular docking of mannitol into P-gp transporter binding site 1. The image was provided by Dr Khondaker Miraz Rahman's group from Medicinal Chemistry at King's College London.

Similar to mannitol, the hydroxyl functional groups of sucrose interact with ARG404, ARG905, GLN1180, SER1177, GLY430, GLN1175, SER434, TYR401 on P-gp through hydrogen bonds (figure 4-8).

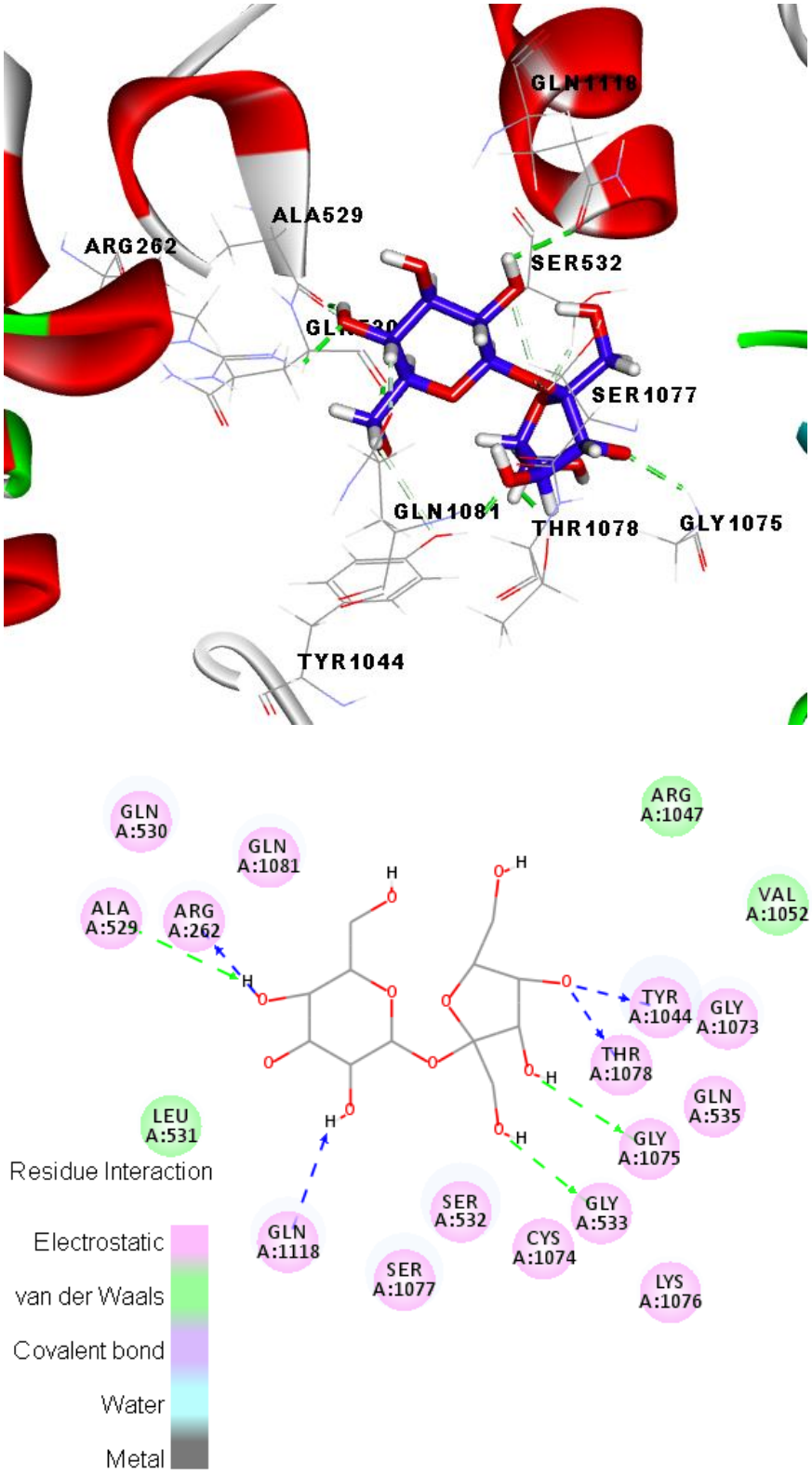

Figure 4-8 Molecular docking of sucrose into P-gp transporter binding site 1. The image was provided by Dr Khondaker Miraz Rahman's group from Medicinal Chemistry at King's College London.

As shown in table 4-2, the best pose of pentamidine and dexamethasone interacts with the binding site of P-gp with a free energy of -31.01 kcal/mol and -31.83 kcal/mol, respectively. The negative controls mannitol and sucrose have a free energy of -12.64 kcal/mol and +2.95 kcal/mol.

Table 4-2 CDOCKER energy of pentamidine, dexamethasone, mannitol and sucrose with P-gp

Ligand	Pose	CDOCKER energy	Average energy for 5 poses
Pentamidine	Pose 1	-32.9931	-31.01458 kcal/mol
	Pose 2	-30.8081	
	Pose 3	-30.6151	
	Pose 4	-30.396	
	Pose 5	-30.2606	
Dexamethasone (P-gp substrate)	Pose 1	-32.9386	-31.8297 kcal/mol
	Pose 2	-32.748	
	Pose 3	-32.5801	
	Pose 4	-32.5596	
	Pose 5	-32.2865	
	Pose 6	-31.7978	
	Pose 7	-31.4883	
	Pose 8	-31.4354	
	Pose 9	-30.9809	
	Pose 10	-29.482	
Mannitol (non-substrate)	Pose 1	-17.1204	-12.64257 kcal/mol
	Pose 2	-13.6015	
	Pose 3	-13.0657	
	Pose 4	-10.2716	
	Pose 5	-9.15363	
Sucrose (non-substrate)	Pose 1	+0.40632	+2.95041 kcal/mol
	Pose 2	+1.80311	
	Pose 3	+2.29536	
	Pose 4	+4.48916	
	Pose 5	+5.75812	

4.4.2 Cytotoxicity of taurodeoxycholate, octanoate, quercetin, and xinafoate on MDCK-WT and MDCK-hMDR1 cells

The cytotoxicity of the four counterions (taurodeoxycholate, octanoate, quercetin, and xinafoate) on MDCK-WT and MDCK-hMDR1 cells were examined by MTT assay. For both MDCK-WT and MDCK-hMDR1 cells, as displayed in figure 4-9 and 4-10, the viability of the cells did not change significantly with 50-200 μM of the four counterions at the 2-h incubation time point. The viability of cells in MBM (the buffer used to dissolve counterions) did not change compared to the untreated cells in cells media. As expected, the positive control (1%triton) significantly decreased the viability of cells compared to the cells in MBM (control).

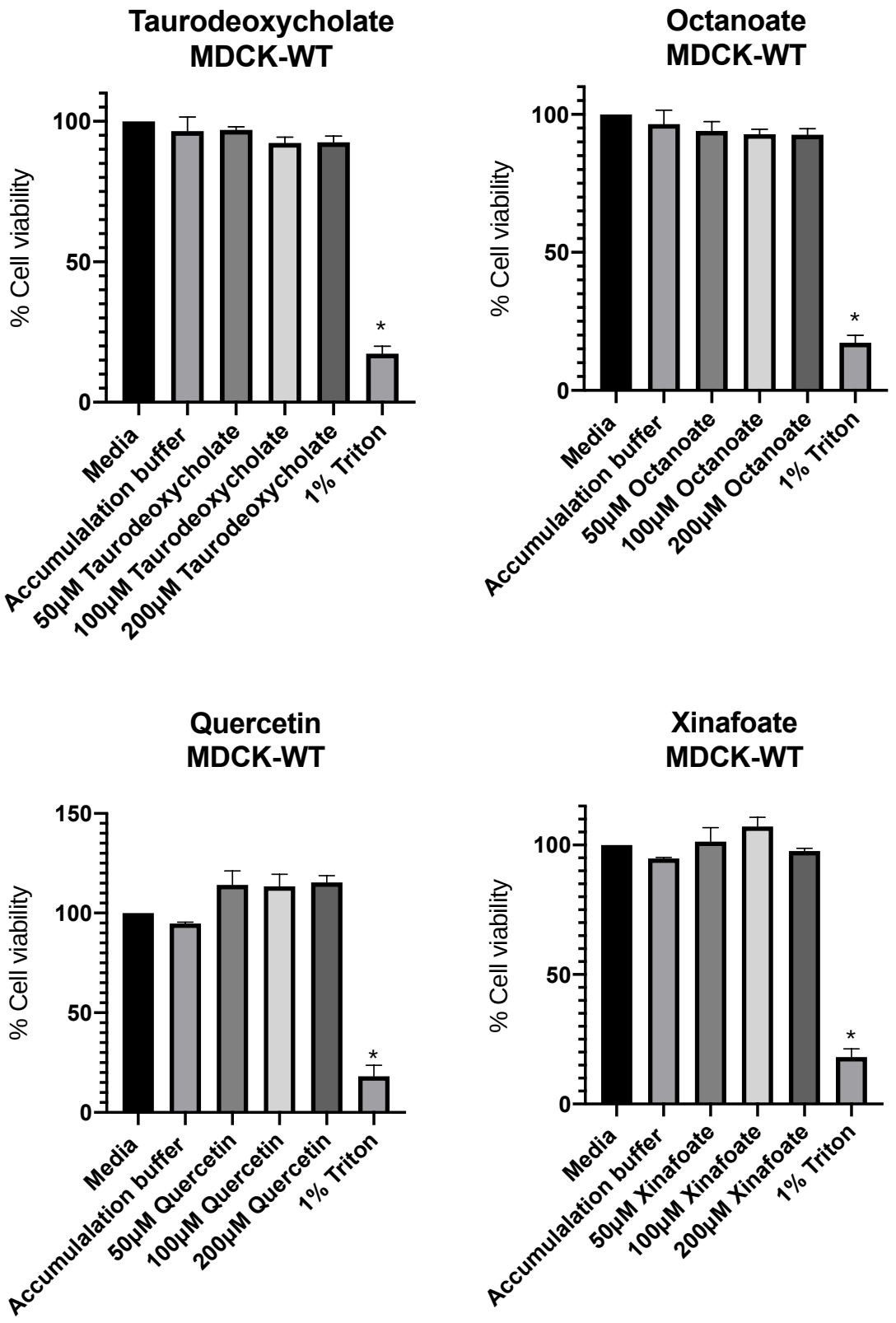

Figure 4-9 Cytotoxicity of taurodeoxycholate, octanoate, quercetin, and xinafoate (50-200 µM) in MDCK-WT cells at 2 h incubation time point. Results were corrected by protein from BCA assay and expressed as percentage viability of cells ± SEM (n=3 passages from P21-23/ independent experiments with 6 replicates per plate) compared to the viability of cells in accumulation buffer. Data were analysed by one-way ANOVA with GraphPad Prism 7 (*$p<0.05$).

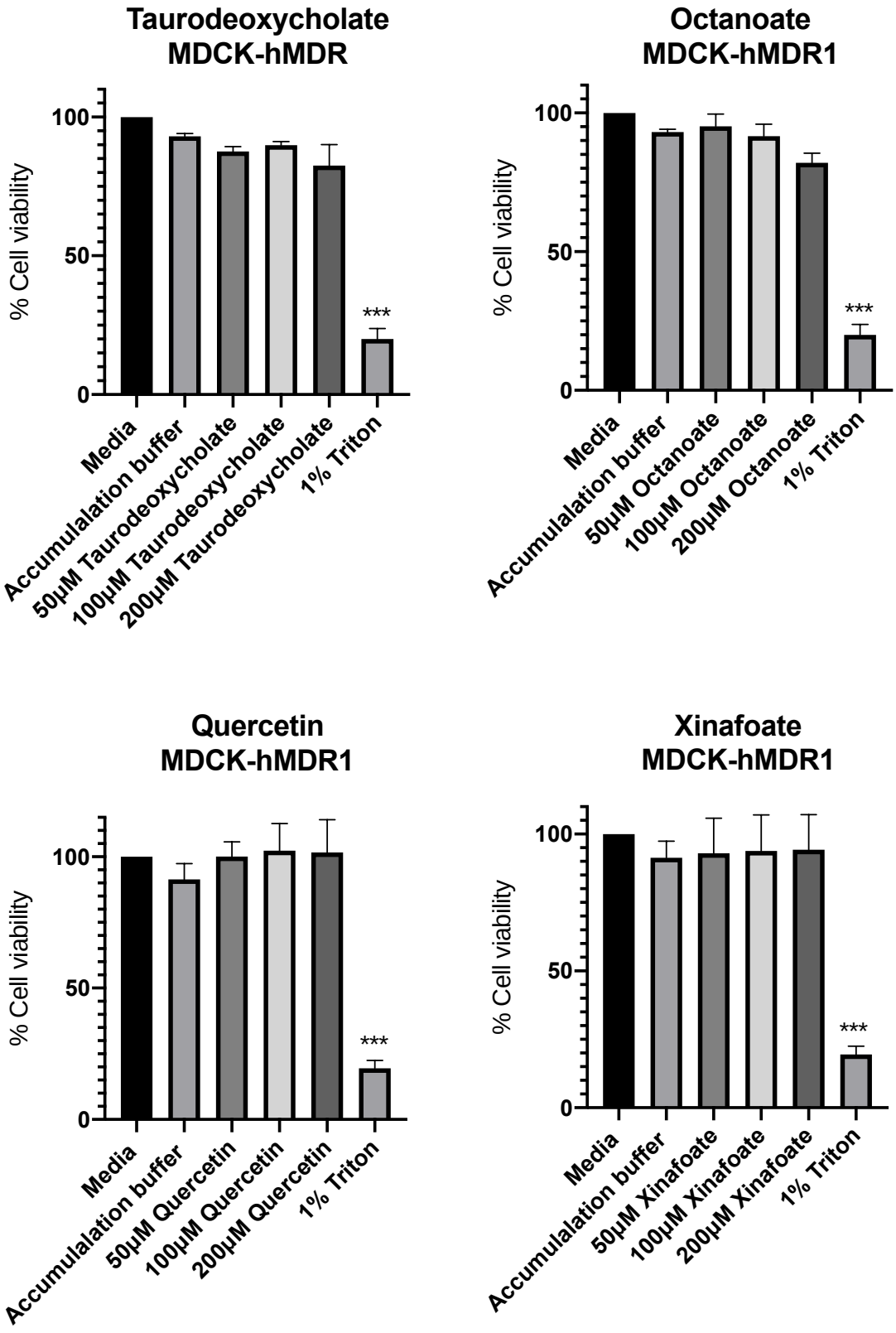

Figure 4-10 Cytotoxicity of taurodeoxycholate, octanoate, quercetin, and xinafoate (50-200 µM) in MDCK-hMDR1 cells at 2 h incubation time point. Results were corrected by protein from BCA assay and expressed as percentage viability of cells ± SEM (n=3 passages from P35-37/ independent experiments with 6 replicates per plate) compared to the viability of cells in accumulation buffer. Data were analysed by one-way ANOVA with GraphPad Prism 7 (***p<0.001).

4.4.3 Accumulation of [^{3}H]pentamidine in MDCK-WT and MDCK-hMDR1 cells

4.4.3.1 Accumulation in MDCK-WT cells

The [^{14}C]sucrose (0.9 μM) acted as a marker for non-specific binding, membrane integrity and measurement of extracellular space. As shown in figure 4-11, no significant difference was seen in the accumulation of [^{14}C]sucrose with 8 μM pentamidine. This indicated that the cells membrane integrity was intact within the 120-min time point.

The accumulation of [^{3}H]pentamidine corrected by sucrose dropped by 90.2% at the 5-min ($P<0.01$), 78.7% at the 20-min ($P<0.05$), 80.5% at the 30-min ($P<0.05$), 76.2% at the 60-min ($P<0.05$), and 36.4% at the 120-min time points in the presence of 8 μM unlabelled pentamidine. This indicated that influx transporters were involved.

(a)

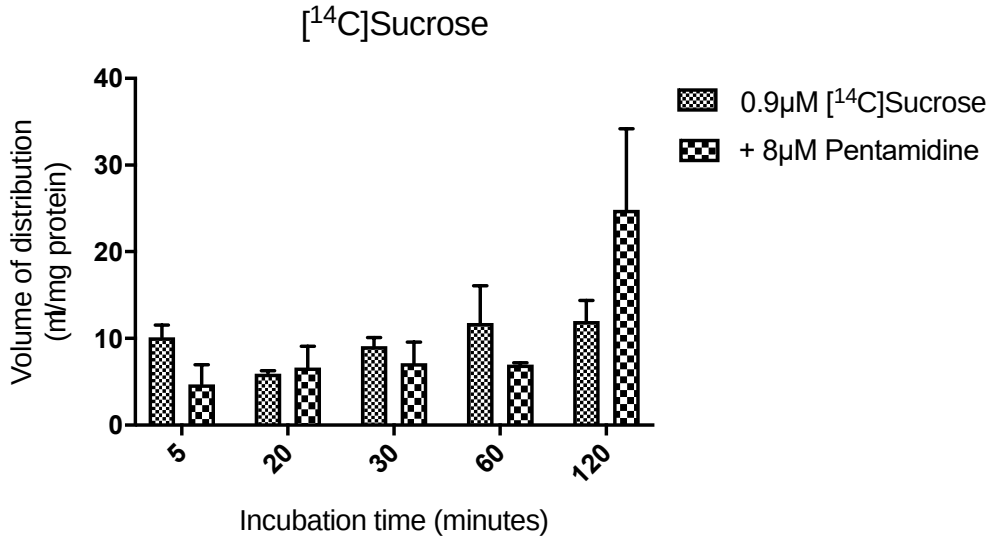

(b)

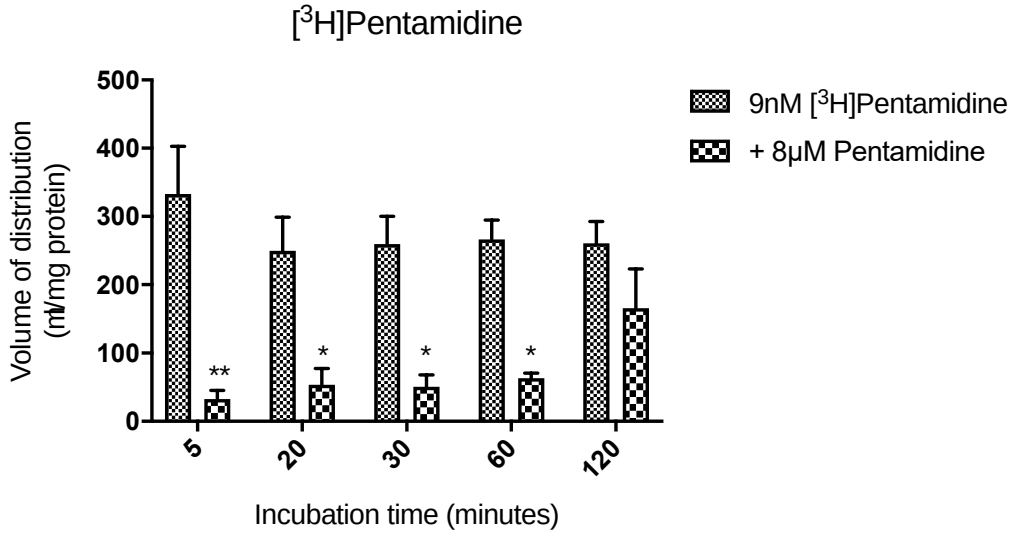

Figure 4-11 Accumulation of 0.9 μM [^{14}C]sucrose and 9 nM [^{3}H]pentamidine corrected by sucrose in MDCK-WT cells. The data were corrected by protein concentrations. Results were expressed as mean ± SEM from 3 passages of cells/ independent experiments (n=P24, 25, 26) with 6 replicates per time point. Data were analysed by two-way ANOVA with Sidak's multiple comparison test by GraphPad Prism 7.

4.4.3.2 Accumulation in MDCK-hMDR1 cells

The accumulation of [^{14}C]sucrose was significantly higher by 157.3% ($P<0.05$) with 8 μM pentamidine at the 120-min time point (figure 4-12). This indicated that the cell membrane integrity was damaged. Therefore, the data for [^{3}H]pentamidine accumulation in MDCK-MDR1 cells at the 120-min time point was considered invalid and excluded for analyses.

For [^{3}H]pentamidine, its accumulation with 8 μM unlabelled pentamidine was much lower but did not achieve statistical significance. The accumulation of [^{3}H]pentamidine corrected by sucrose

decreased by 88.3% at the 5-min, 80.7% at the 20-min, 72.1% at the 30-min, 64.4% at the 60-min time points.

(a)

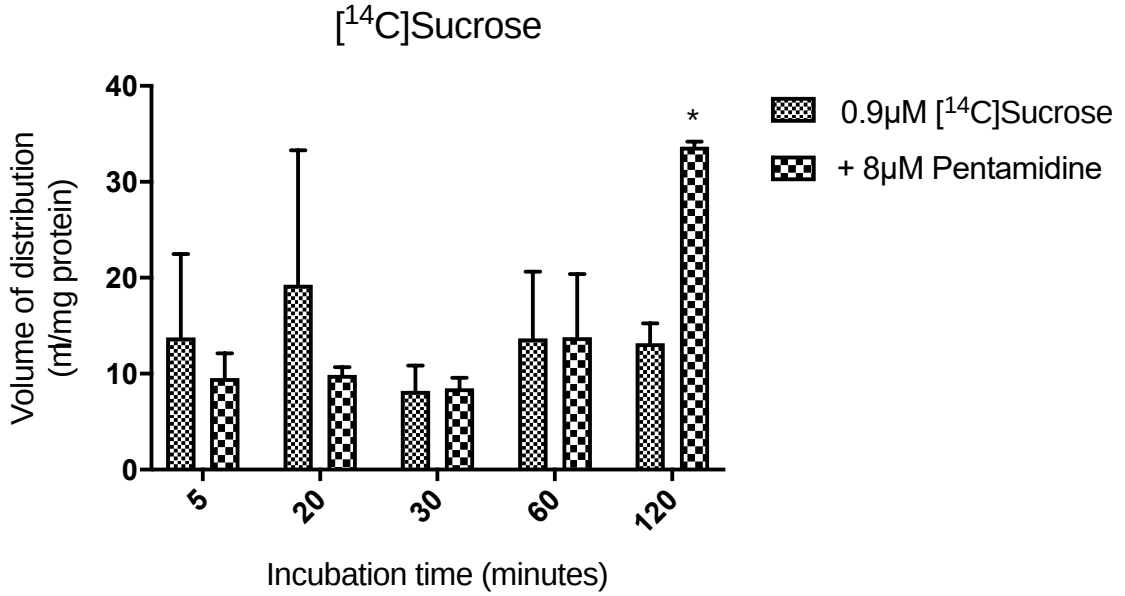

(b)

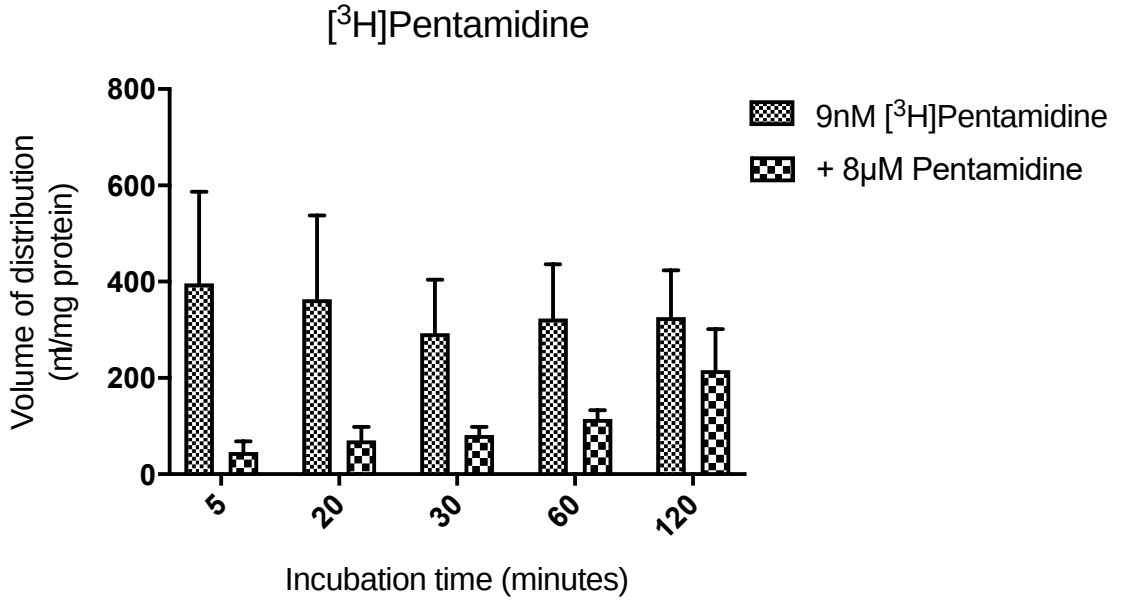

Figure 4-12 Accumulation of 0.9 μM [^{14}C]sucrose and 9 nM [^{3}H]pentamidine corrected by sucrose in MDCK-hMDR1 cells. The data were corrected by protein concentrations. Results were expressed as mean ± SEM from 3 passages of cells/ independent experiments (n=39, 41,42 for MDCK-hMDR1) with 6 replicates per time point. Data were analysed by two-way ANOVA with Sidak's multiple comparison test by GraphPad Prism 7.

4.4.3.3 Comparison of [^{3}H]pentamidine accumulation in MDCK-WT and MDCK-hMDR1 cells

As shown in figure 4-13, the efflux of [^{3}H]pentamidine by the highly expressed hMDR1 transporter could not be detected, as there was no significant difference in the accumulation of [^{3}H]pentamidine in between the MDCK-WT and MDCK-hMDR1 cells. This is likely to be caused

by the presence of multiple influx and efflux transporters in the MDCK-WT and MDCK-hMDR1 cells. Therefore, the MDCK-WT and MDCK-hMDR1 cells are not suitable to study the specific interaction of pentamidine ion-pairs with the P-gp transporter.

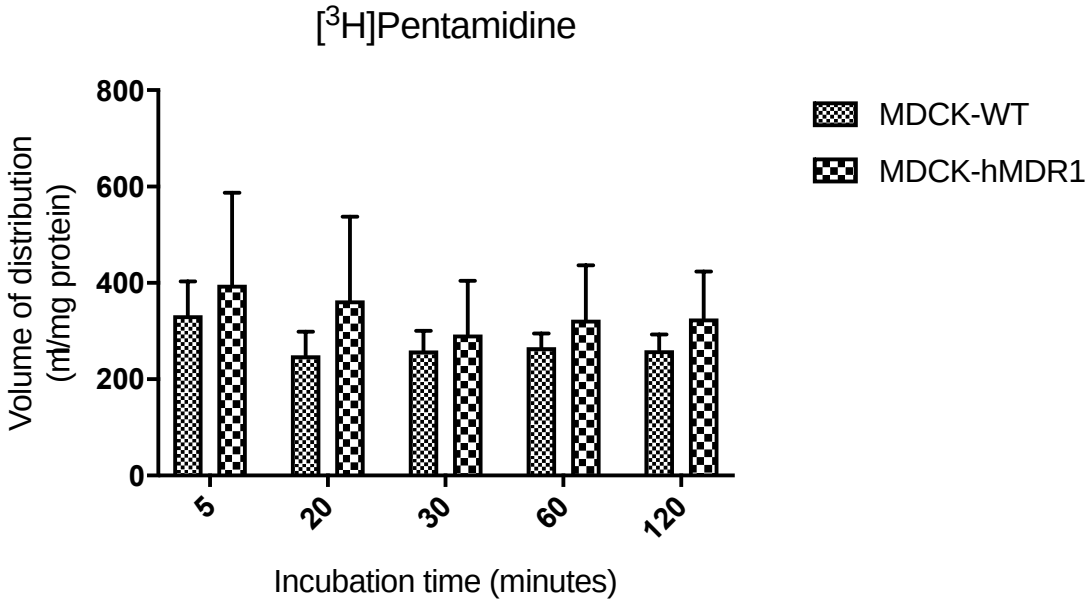

Figure 4-13 Accumulation of 9nM [^{3}H]pentamidine corrected by sucrose in MDCK-WT and MDCK-hMDR1 cells. The data were corrected by protein concentrations. Results were expressed as mean ± SEM from 3 passages of cells/ independent experiments (n=P24, 25, 26 for MDCK - WT and n=39, 41, 42 for MDCK-MDR1) with 6 replicates per time point. Data were analysed by two-way ANOVA with Sidak's multiple comparison test by GraphPad Prism 7.

4.4.4 Method verification

The P-gp expressing *lavies xenopus* oocyte model was verified in three ways: (a) confirming the sequence and size of *P-gp* cDNA; (b) verifying the size and integrity *P-gp* RNA; (c) testing the functional expression of P-gp transporter in oocytes with [^{3}H]dexamethasone and [^{3}H]corticosterone.

4.4.4.1 *P-gp* vector sequence and vector map

The amino acid sequences of the P-gp vector were aligned to the published P-gp sequences (NM_000927) from the National Centre for biotechnology Information (NCBI) database. During the alignment, a mutation was revealed at the point of 3435 (T>C), as highlighted in red colour in figure 4-14. This mutation does not change the resulting amino acid, as noted in the product information (catalogue number: HG12030-G) of Sino Biological Inc. The translated amino acids sequence was also compared to the U.S. NCBI database and confirmed that they were identical to the amino acids sequence of multidrug resistance protein 1 (MDR1) variance 2 (Sequence ID: NP_000918.2). There is only one isoform of human P-gp: ABCB1. In mice, there are two isoforms:

Abcb1a and Abcb1b and their proteins are 87.3% and 80.5% to the human ABCB1 (Kalabis *et al.*, 2005; Krohn *et al.*, 2018). Their sequences can be found in the NCBI database. After confirmation of the identity of the *P-gp* sequence, this vector was utilised for all the following experiments.

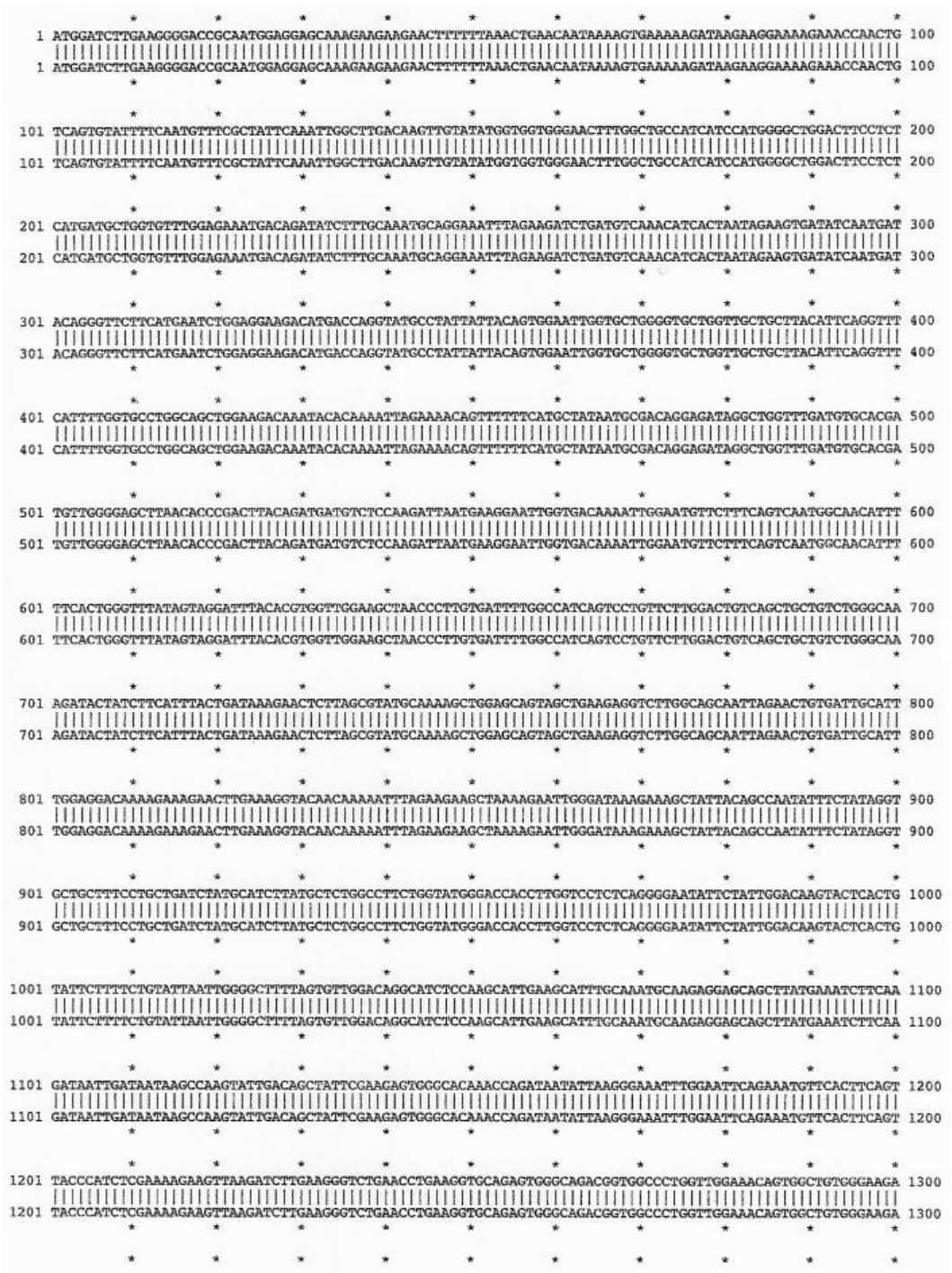

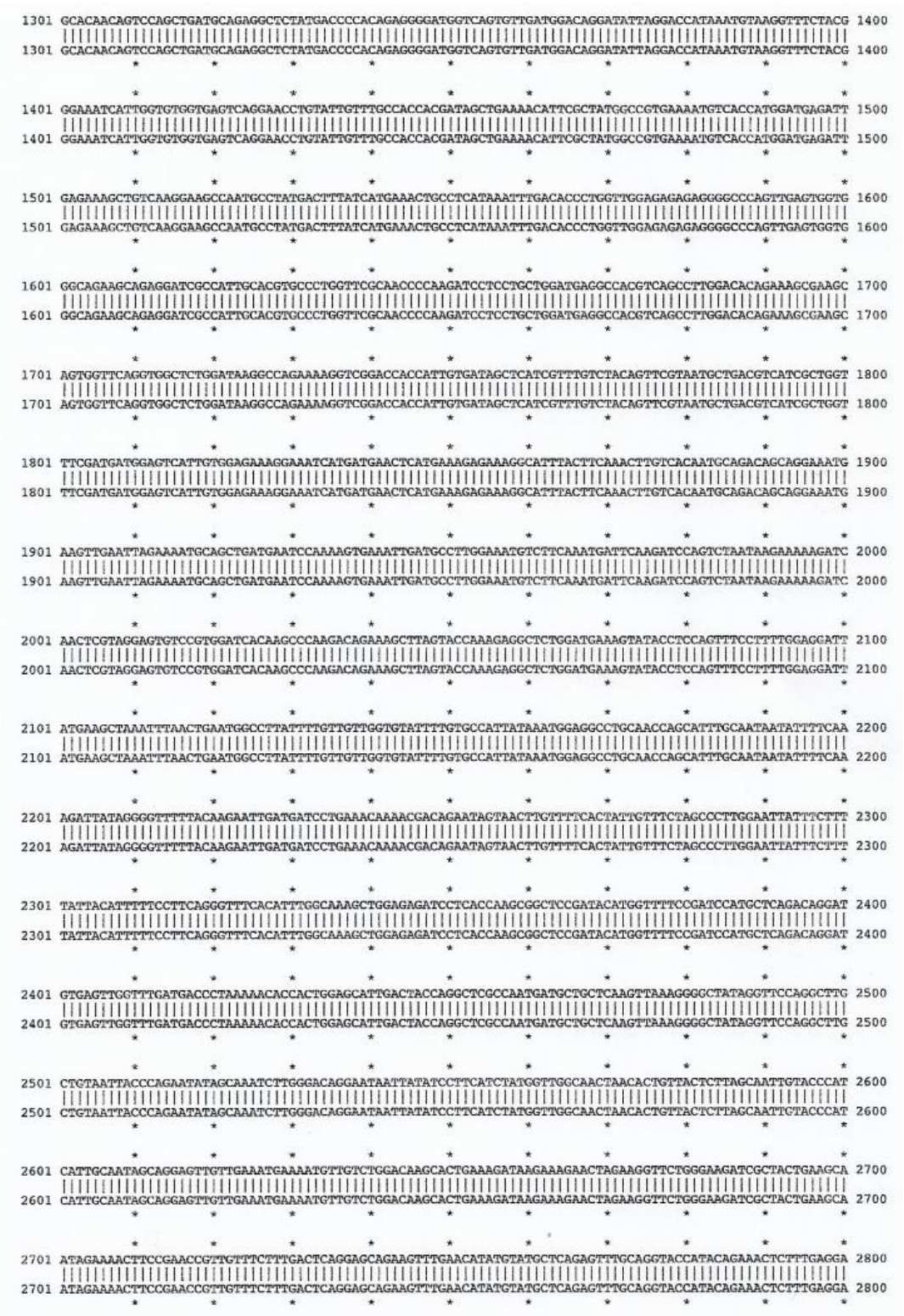

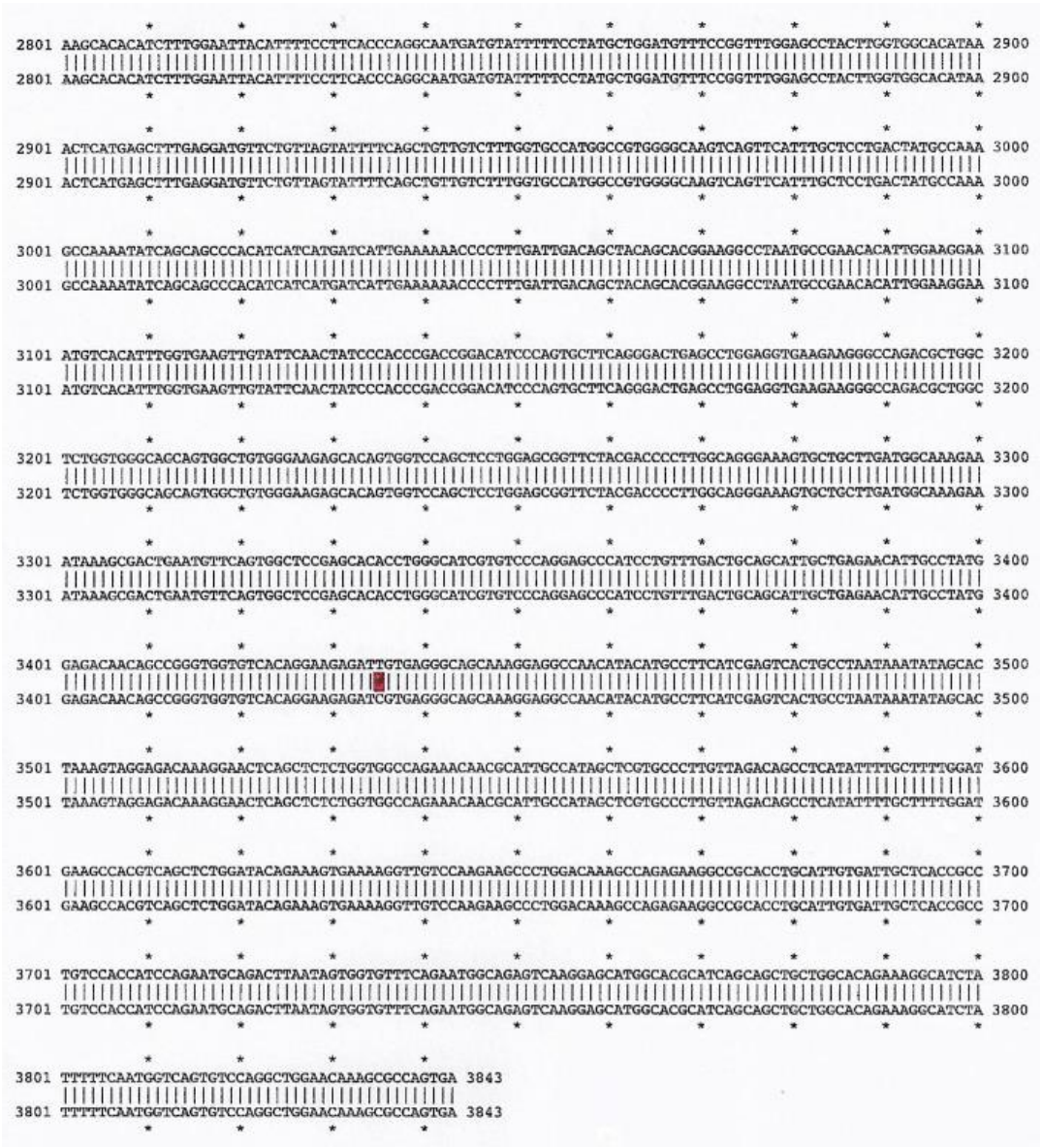

Figure 4-14 Comparison of the *P-gp* vector sequences to *P-gp* sequence (NM_000927) from the NCBI database. A (adenine), T (thymine), C (cytosine), G (guanine) are the four bases of DNA. The upper rows of the alignment are the sequences from NCBI database (NM_000927), and lower rows are the P-gp vector cDNA sequences. The mismatch (mutation) is highlighted in red colour.

As mentioned earlier, sequencing *P-gp* cDNA can verify the identity of P-gp vector. It can also be used to select restriction enzymes for DNA linearization. As shown in figure 4-15, the *P-gp* (ABCBA1) gene was inserted in the location from 52-3894 in the vector. The restriction enzyme SalI can be used to linearize the *P-gp* cDNA.

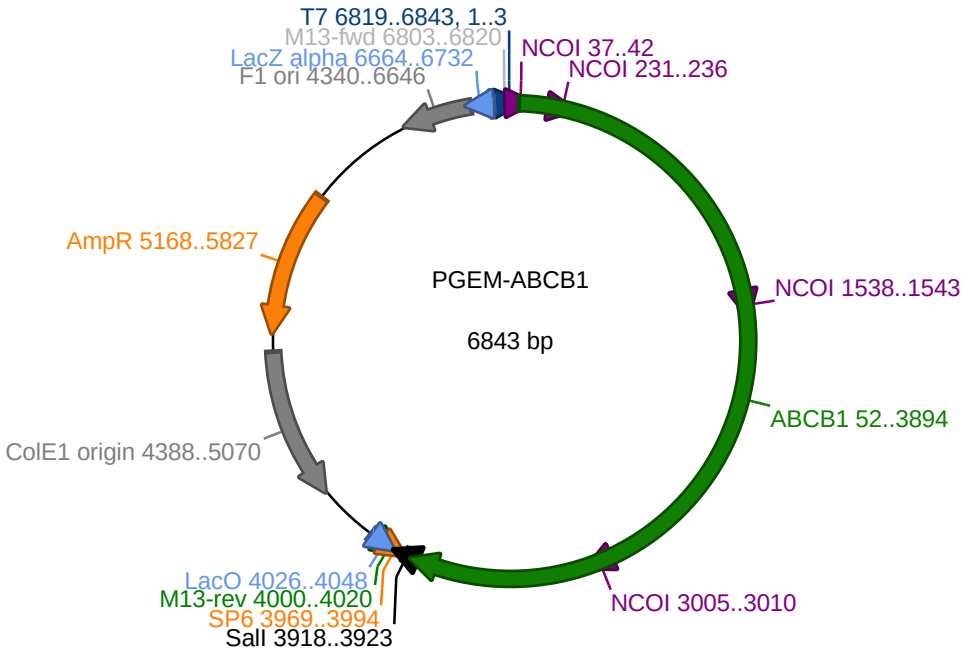

Figure 4-15 *P-gp (ABCB1)* vector map. The 6843 bp shows the location of ABCBA1 gene in T7 sense orientation, the ampicillin selection gene, and the NcoI and SalI restriction sites. The vector map was drawn with ApE software (version 2.0.52a).

4.4.4.2 Restriction enzyme digestion of *P-gp* cDNA

As shown in Figure 4-16, the identity of the *P-gp* cDNA was confirmed by gel electrophoresis after digested with SalI and NcoI restriction enzymes. The number of fragments and size of bands shown on the gel are compared to the P-gp cDNA vector map (figure 4-13) and verified. The band for linearization of *P-gp* cDNA by SalI appeared at the expected size (6843 bp). The bands for cDNA double digestion by SalI and NcoI appeared at the expected locations (2962, 1467, 1307, 913). It is also expected to have a band at 195 bp but it was very light and invisible on the gel.

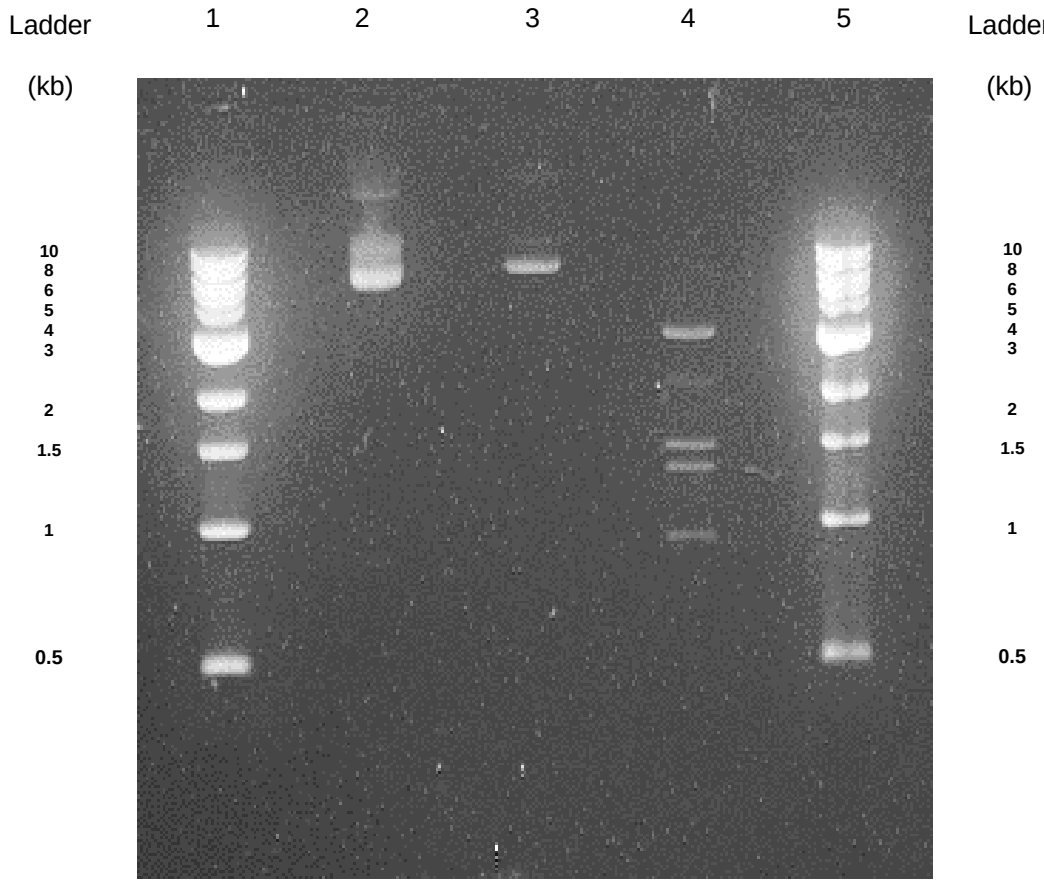

Figure 4-16 Restriction enzyme digestion of *P-gp*. Band 1: 1 kb DNA ladder, band 2: uncut *P-gp* cDNA, band 3: *P-gp* linearised by SalI, band 4: *P-gp* digested by SalI and NcoI, band 5: 1 kb DNA ladder. The digestion was repeated each time before RNA sysnthesis.

Prior to RNA synthesis, the concentration and purity of the linearized *P-gp* cDNA were measured. The figure 4-17 below was an exemplary result measured with Nanodrop. The concentration of the *P-gp* cDNA was 418 ng/µl, which was high enough for the following RNA synthesis which usually requires at least 200 ng/µl of pure cDNA. The 260/280 ratio shows the purity of DNA and value of ~1.8 is considered pure for DNA. The 260/230 ratio is a secondary measure of nucleic acid purity with an expected range of 2.0-2.2. The result of the *P-gp* cDNA nanodrop revealed that the *P-gp* DNA was pure as its 260/280 was at 1.8. The 260/230 ratio was at 1.56 which was

lower than expected. This was usually caused by the residual ethanol that was used to wash cDNA. A slightly lower value of 260/230 ratio normally does not affect the success of following RNA synthesis. However, if this ratio was too low, then the efficiency of RNA synthesis may be affected.

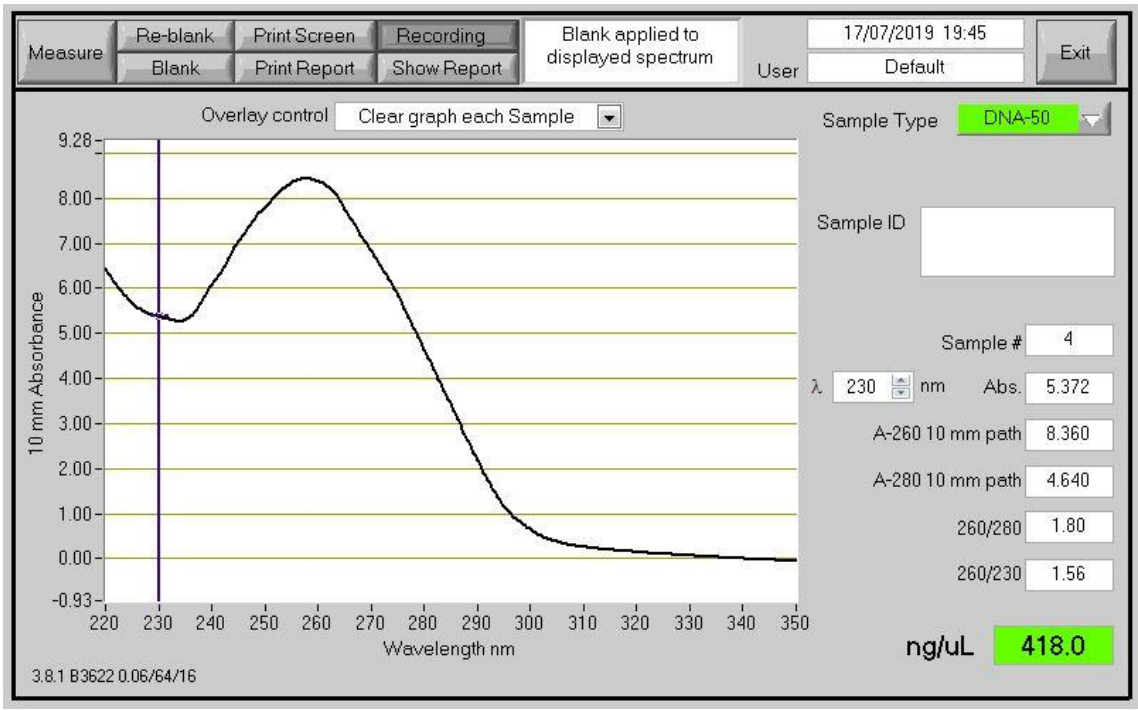

Figure 4-17 *P-gp* cDNA measured by Nanodrop.

4.4.4.3 Verification of *P-gp* RNA

The size and integrity of the synthesized *P-gp* RNA was confirmed by Agilent RNA 6000 Nano Kit with 2100 Bioanalyzer. As shown in figure 4-18, the size of *P-gp* RNA band on the RNA gel was at around 3.8 kb, which was the expected size of the *P-gp* inserted clone (3843 bp). The *pTRI-Xef*, a control RNA provided in the Invitrogen MEGAscript® T7 Kit, appeared at the expected transcript size of 1.89 kb on the gel. a

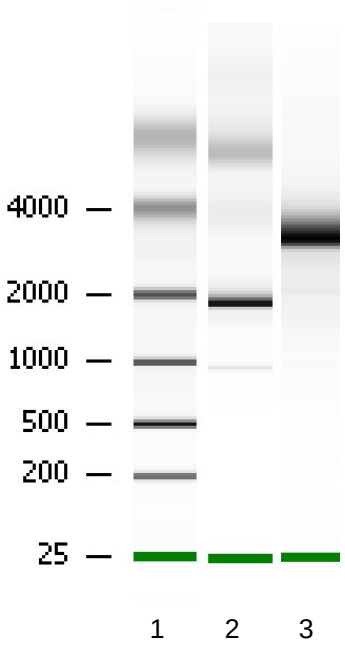

(a)

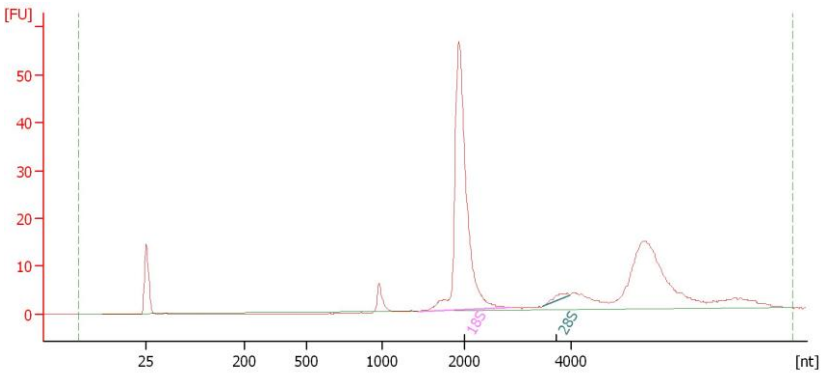

(b)

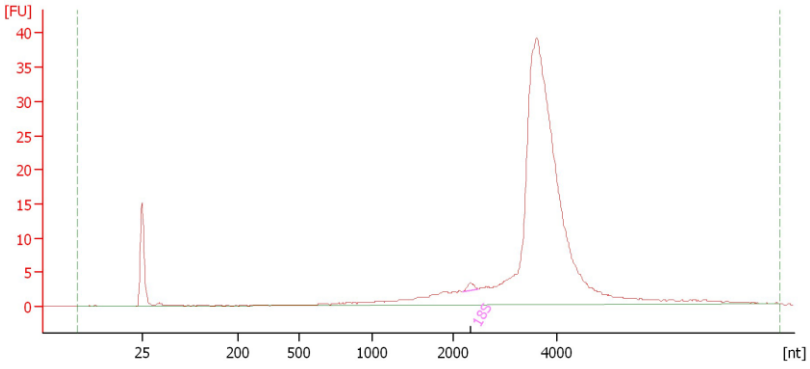

(c)

Figure 4-18 RNA Nanochip electrophoresis of *P-gp* RNA. The x-axis represents the size of RNA (nucleotide) and y-axis represents fluorescence intensity. (a) Image of the RNA chip. Band 1: RNA ladder, band 2: *pTRI-Xef* control RNA, band 3: *P-gp* RNA; (b) Electropherogram of *pTRI-Xef* control RNA, (c) Electropherogram of *P-gp* RNA.

4.4.4.4 Verification of poly-A tailed *P-gp* RNA on denaturing agarose-formaldehyde gel

The poly-A tailing kit could add a tail to RNA samples, and the tailed RNA would have a trailing band on the denaturing agarose-formaldehyde gel. As shown in figure 4-19, the untailed *P-gp* RNA had an expected size (6843 bp) on the gel (band 2, figure 4-19). The tailed *P-gp* RNA (band 3, figure 4-19) was trailing on the gel and started with a bigger size compared to the untailed P-gp RNA. The *pTRI-Xef* control RNA (band 4, figure 4-19), provided in the Invitrogen MEGAscript® T7 Kit, appeared at the expected transcript size of 1.89 kb on the gel. The tailed pTRI-Xef RNA also had a trailing shape and started with a bigger size compared to the untailed pTRI-Xef RNA. The results on the denaturing agarose-formaldehyde gel proved that the poly-A tailing of P-gp RNA was successful.

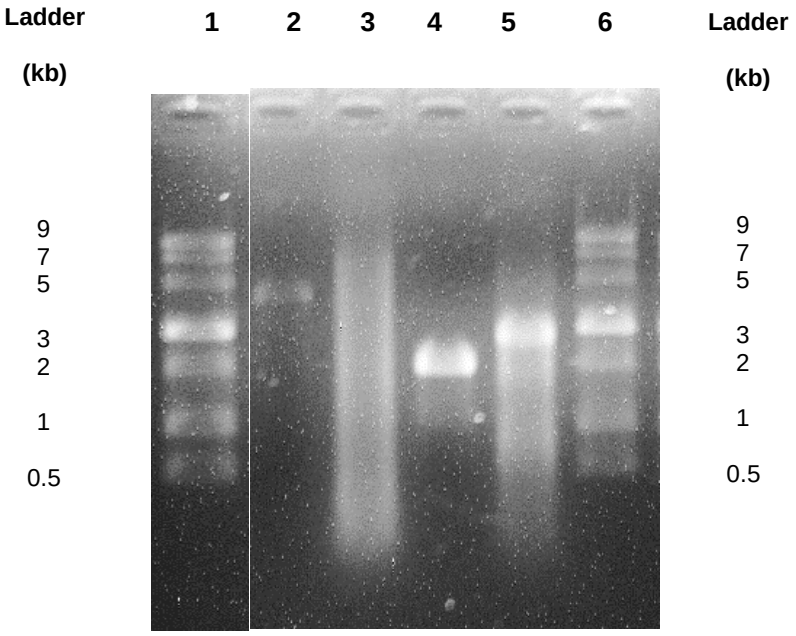

Figure 4-19 Verification of poly-a tailed *P-gp* RNA on a denaturing agarose-formaldehyde gel. Band 1: 9 kb RNA ladder, 2: *P-gp* RNA, 3: poly-A tailed RNA, 4: *TRI-Xef* RNA, 5: poly-a tailed *pTRI-Xef* RNA, 6: 9 kb RNA ladder.

4.4.4.5 Transport of [^{3}H]dexamethasone in *xenopus* oocytes expressing P-gp

The purpose of the influx (accumulation) and efflux of [^{3}H]dexamethasone in oocytes expressing P-gp was to verify the functional expression of P-gp transporter. For the influx of [^{3}H]dexamethasone, the water-injected oocytes and oocytes expressing P-gp were incubated in MBM with [^{3}H]dexamethasone. There was no significant difference observed at the 1 h incubation time point between the water-injected oocytes and oocytes expressing P-gp (figure 4-20).

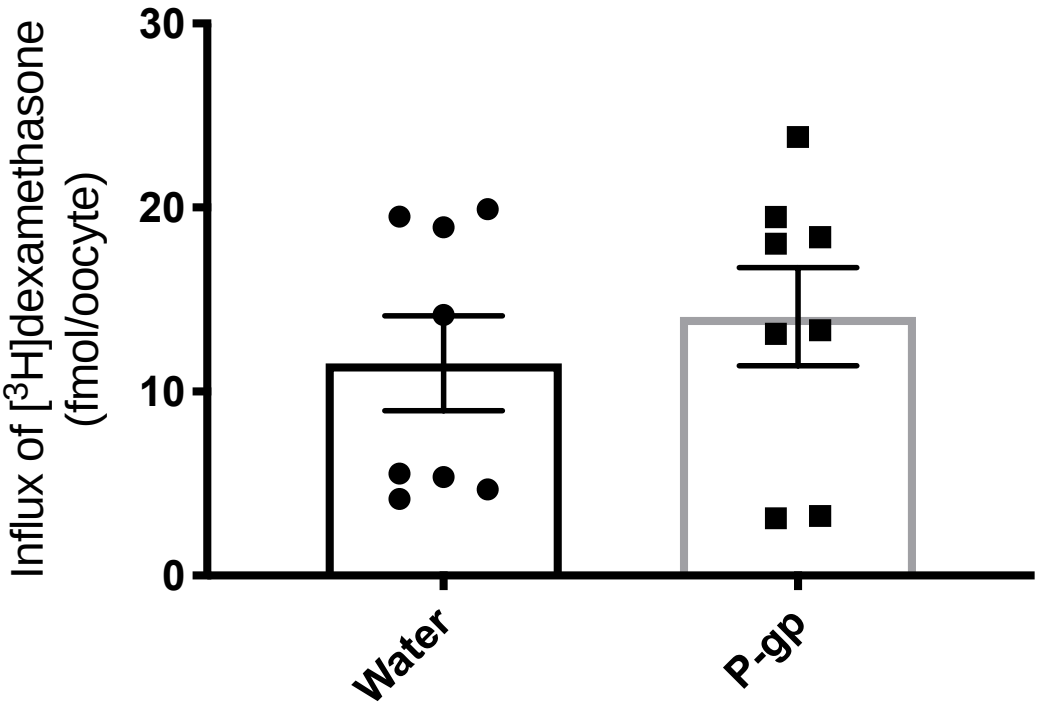

Figure 4-20 Accumulation of [^{3}H]dexamethasone (9 nM) in water-injected and oocytes expressing P-gp after 1 h. Oocytes were incubated with [^{3}H]dexamethasone (9 nM) buffer. Data were expressed as mean ± standard errors (n= 8-10, from one batch of oocytes/ experiment) and analysed using unpaired t-test with Prism GraphPad 7.

Unlike the influx assay, for efflux assay the [^{3}H]dexamethasone was injected into each oocyte and the efflux of [^{3}H]dexamethasone was measured. As can be seen from figure 4-21, the oocytes injected with P-gp RNA and extra ATP significantly increased the efflux of [^{3}H]dexamethasone compared to water-injected oocytes at the 120-min time point. The oocytes injected with poly-A tailed P-gp RNA and extra ATP also increased the efflux of [^{3}H]dexamethasone, although it did not make much difference compared to the non-tailed P-gp RNA with ATP. Therefore, it was clear that the key-driven factor was ATP for the efflux of [^{3}H]dexamethasone in oocytes expressing P-gp.

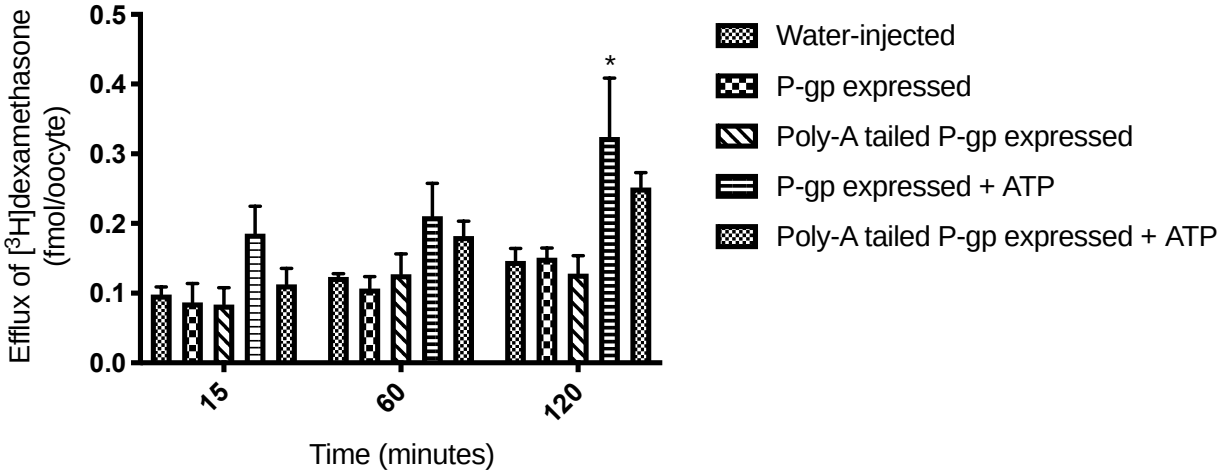

Figure 4-21 Efflux of [^{3}H]dexamethasone in oocytes expressing P-gp. Intra-oocytes buffer consisted of 4 nM [^{3}H]dexamethasone. Data were expressed as mean ± SEM (n= 4-6 from 1 batch of oocytes) and analysed by two-way ANOVA.

4.4.4.6 Transport of [^{3}H]corticosterone in *xenopus* oocytes expressing P-gp

Corticosterone is a substrate for P-gp (Wolf and Horwitz, 1992b). The purpose of the influx assay of [^{3}H]corticosterone in oocytes injected with RNA-free water (control), P-gp RNA, or Poly-A tailed P-gp RNA was to verify if P-gp was expressed in the correct direction. The results showed that no significant difference of [^{3}H]corticosterone influx in oocytes was observed that were injected into cells with RNA-free water (control), P-gp RNA, or Poly-A tailed P-gp RNA (figure 4-22).

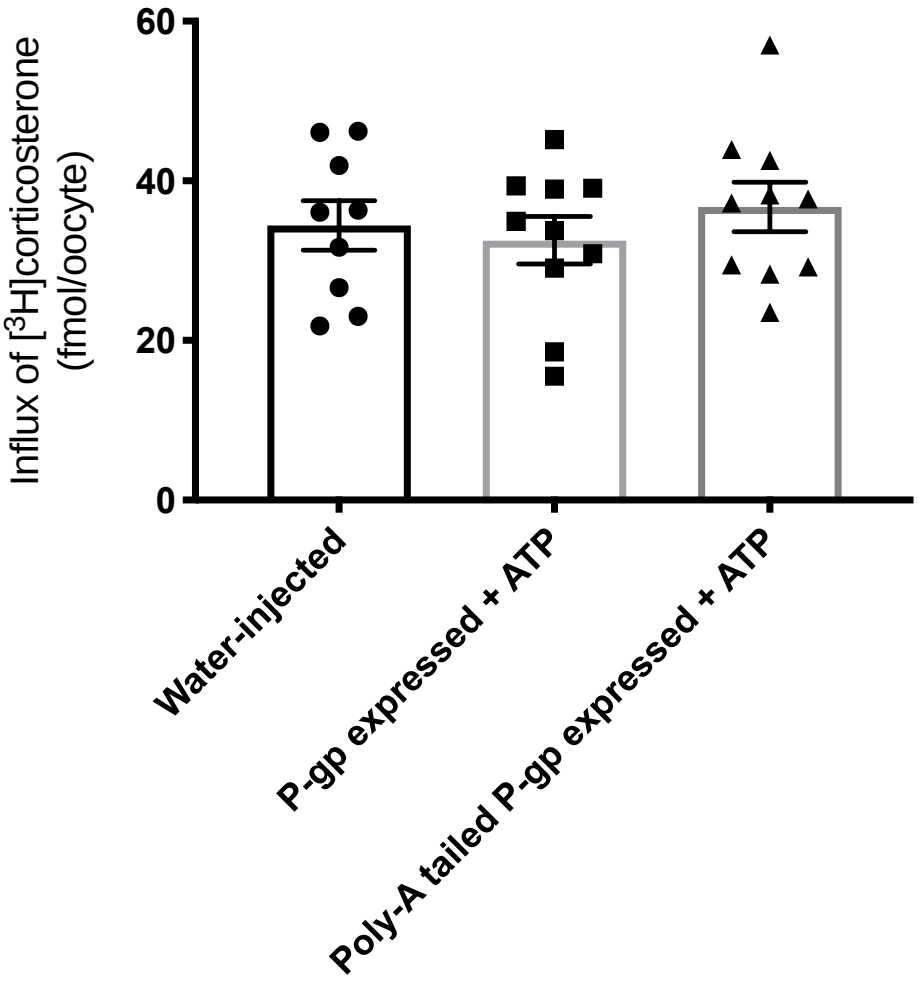

Figure 4-22 Influx of 13nM [^{3}H]corticosterone in oocytes injected with water, P-gp RNA and, and Poly-A tailed P-gp RNA. The accumulation buffer for the influx assay consisted of 13 nM [^{3}H]corticosterone and extra ATP. Incubation time was 1h. Expressed were expressed as mean ± S.E.M (n=10) from 1 batch of oocytes.

The efflux of [^{3}H]corticosterone in oocytes expressing P-gp with additional ATP was significantly higher by 60.7% compared to the efflux in water-injected oocytes (figure 4-23).

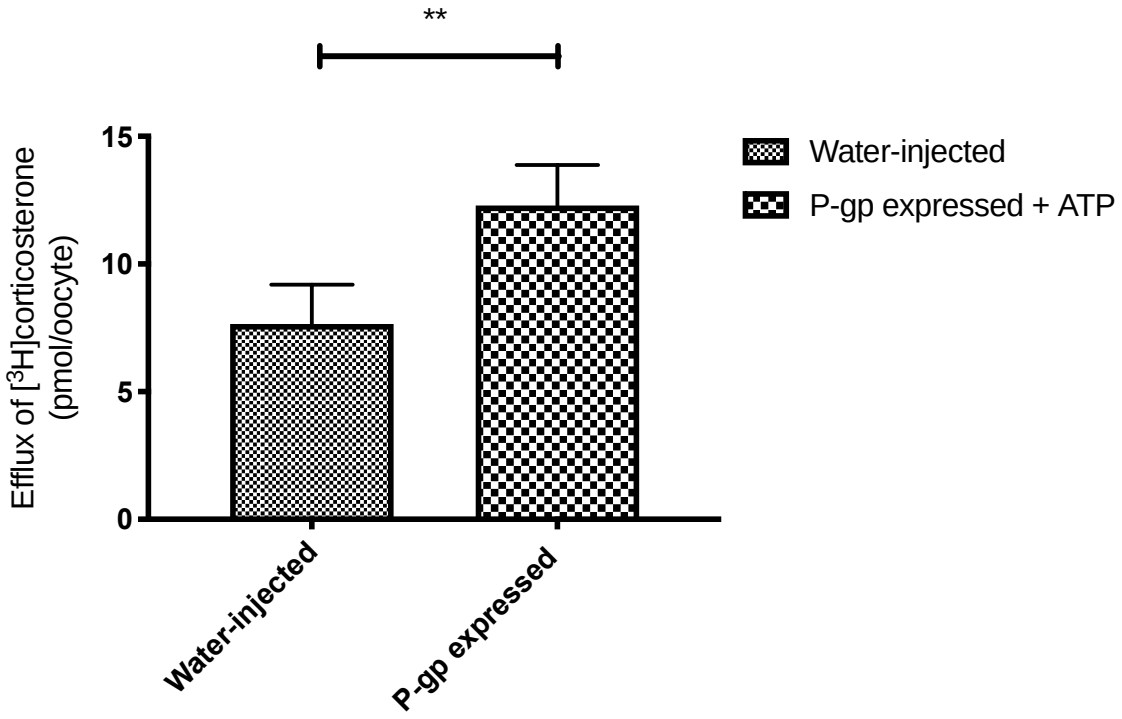

Figure 4-23 Efflux of [^{3}H]corticosterone in oocytes expressing P-gp. Intra-oocytes buffer consisted of 25nM [^{3}H]corticosterone. Incubation time was 1h. Data were expressed as mean ± SEM (n= 10 from 1 batch of oocytes) and analysed by unpaired t-test.

4.4.5 Efflux of [^{3}H]pentamidine in *xenopus* oocytes expressing P-gp

As can be seen in figure 4-24, the efflux of [^{3}H]pentamidine from oocytes expressing P-gp was not significantly different compared to the water-injected oocytes. Also, the presence of 8μM unlabelled pentamidine did not seem to suppress the efflux of [^{3}H]pentamidine as the change was not statistically significant.

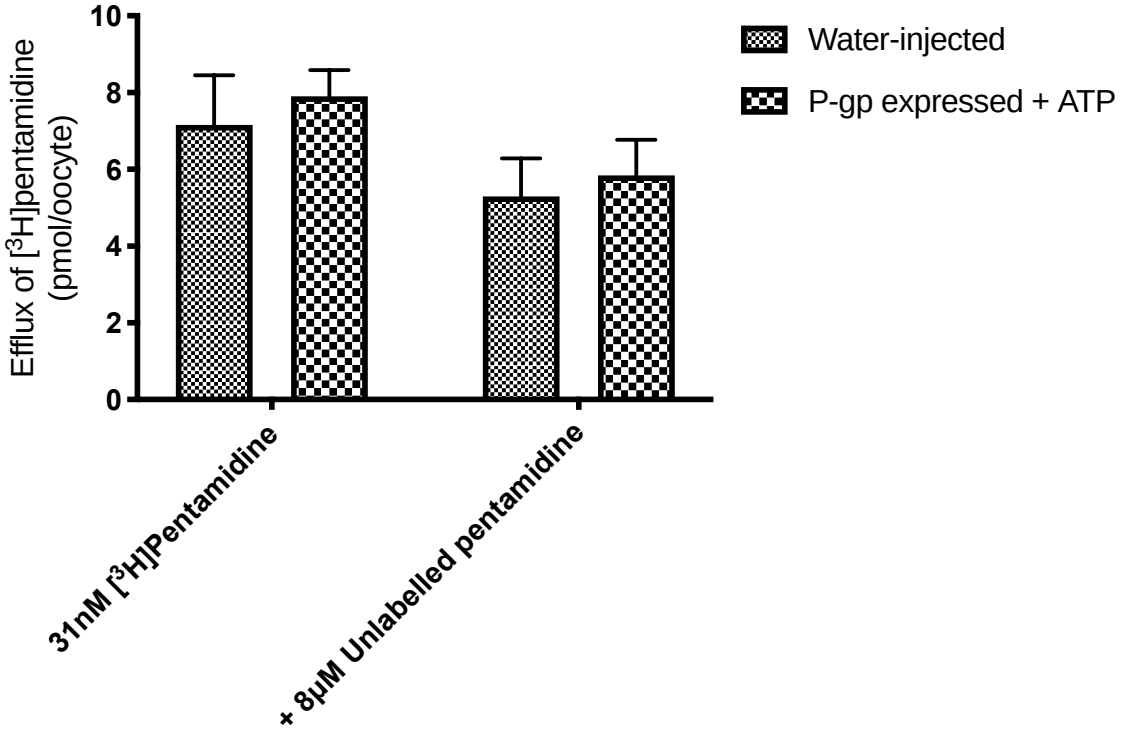

Figure 4-24 Efflux of 31nM [^{3}H]pentamidine in water-injected and P-gp expressed xenopus oocytes. Data were analysed by two-way ANOVA (n=3 batches / independent experiments with 7-12 oocytes/replicates per treatment).

4.4.6 Efflux of [^{3}H]pentamidine-xinafoate ion-pairs by P-gp in oocytes

As shown in figure 4-25, the presence of 38.5% pentamidine-xinafoate ion-pairs significantly increased the efflux of [^{3}H]pentamidine for both oocytes injected with water and oocytes expressing P-gp. Comparing the water-injected group and the oocytes expressing P-gp with extra ATP, the pattern for the efflux of [^{3}H]pentamidine with 3% and 38.5% pentamidine-xinafoate ion-pairs looks very similar and does not seem to differentiate when P-gp was in the system.

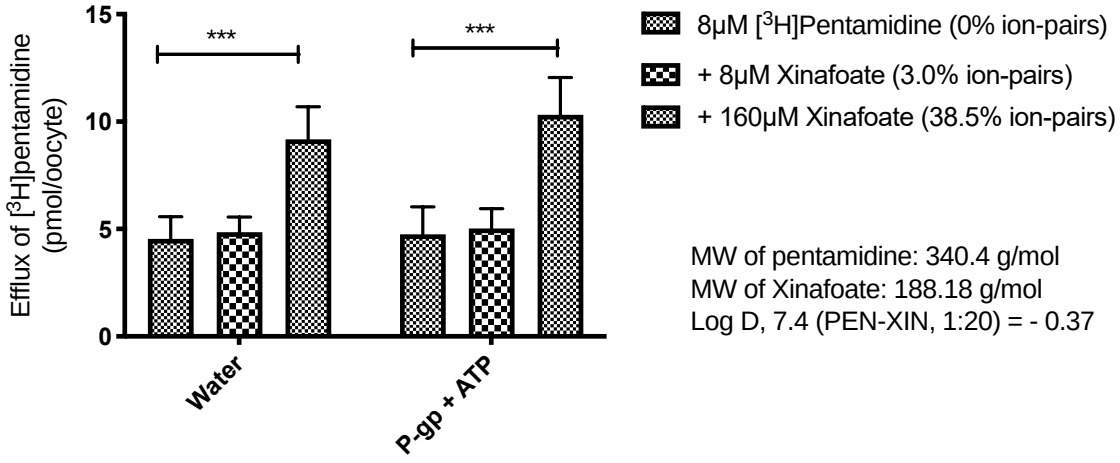

Figure 4-25 Efflux of [^{3}H]pentamidine in water-injected and P-gp expressed *xenopus* oocytes. Data were analysed by two-way ANOVA (n=4 batches / independent experiments with 6-8 oocytes/replicates per treatment). The percentage of [^{3}H]pentamidine in ion-pair form was predicted from the HYSS simulations (Chapter Section 2.4.7.3). The Log D was measured by shake flask method and HPLC analysis (Chapter 2 Section 2.4.3). For ease of comparison, these values have been included in this figure.

4.5 Discussion

The molecular docking simulated the potential binding sites of pentamidine with P-gp transporter and confirmed that pentamidine was a P-gp substrate. This corresponds to the results in previous *in vivo* experiments where the distribution of [^{3}H]pentamidine was found to be 2-3 folds higher in the brain of P-glycoprotein-deficient (FVB-mdr1a/1b(-/-) type) mice compared to wild-type mice (Lisa Sanderson *et al.*, 2009).

The MDCK-hMDR1 cells can be used to study drug delivery as a BBB model. It has been found that there is a positive correlation between drugs permeability measured with transwell to be transported across the MDCK-hMDR1 cells and their ability to reach CNS (Wang *et al.*, 2005; Hellinger *et al.*, 2012), so the MDCK-hMDR1 cells were used to explore the permeability of pentamidine ion-pairs across the BBB. MDCK-WT cells do express endogenous P-gp. However, the highest expressing isoforms of P-gp in MDCK-WT and MDCK-hMDR1 are different. Tang, Horie and Borchardt (2002) found that the MDCK-hMDR1 cells expressed a high level of the 150

kDa isoform of human P-gp transporter, while the MDCK-WT cells had more of 170 kDa endogenous isoform of canine P-gp than the 150 kDa isoform. MDCK-WT expresses quite a high level of endogenous P-gp. Whilst MDCK-hMDR1 also expresses a high level of P-gp, it expresses less endogenous (canine) P-gp compared to MDCK-WT. As the human P-gp is expressed in MDCK cells, the amount of P-gp in MDCK might have reached the protein threshold and down-regulated the endogenous P-gp in MDCK-MDR1. Also, the interspecies variance on the binding sites and binding affinities with substrates may have a mixed impact on the transport of substrates. As a result, the different expression of P-gp in the two cell lines may complicate the transport analysis of P-gp substrates in MDCK-WT and MDCK-hMDR1 and sometimes even provide misleading results (Kuteykin-Teplyakov *et al.*, 2010).

While the information regarding the exact passages of cells used was not provided by Tang, Horie and Borchardt (2002), it was stated that the MDCK-hMDR1 cells used in their study were within two months of thawing from liquid nitrogen, with lower passages of MDCK-hMDR1 cells expressing more 150 kDa isoform of P-gp. It is unknown that if the different expression of P-gp isoforms would affect the transport of P-gp substrates in the two cell lines.

In our study, initially, we intended to isolate the impact of P-gp on the transport of pentamidine ion-pairs by leveraging the different levels of P-gp expression in MDCK-WT and MDCK-hMDR1 cells. Therefore, the two cells lines were validated and the toxicity of different concentrations of counterions was tested. The MTT assay of counterions confirmed that taurodeoxycholate, octanoate, xinafoate, and quercetin of up to 200µM did not affect the viability of MDCK-WT and MDCK-MDR1 cells within 2h incubation time. Thus, the four counterions at concentrations up to 200µM were safe for the two cell lines.

In the accumulation assay in MDCK-WT and MDCK-hMDR1 cells, no difference of [^{3}H]pentamidine accumulation corrected by [^{14}C]sucrose was seen in the two cell lines. This suggests that there is no difference in membrane integrity/and or extracellular space between the two cell lines/monolayers. The accumulation of [^{14}C]sucrose did not show significant difference with 9nM [^{3}H]pentamidine in both MDCK-WT and MDCK-hMDR1 cells during the 2h incubation, which indicated that changes in membrane integrity did not affect the [^{3}H]pentamidine accumulation. Thus, we suspect that the efflux of [^{3}H]pentamidine by P-gp could have been

masked by its interactions with other transporters in MDCK-WT and MDCK-hMDR1 cells. This speculation was supported by the results of 9nM [^{3}H]pentamidine accumulation in the presence of 8 µM unlabelled pentamidine, where the accumulation of [^{3}H]pentamidine corrected by [^{14}C]sucrose decreased with 8 µM unlabelled pentamidine in both MDCK-WT and MDCK-hMDR1 cells. This indicated that there influx transporters involved in the accumulation of [^{3}H]pentamidine. Quan (*et al.*, 2012) conducted a systematic study on the gene expression of MDCK cells on both plastic and transwell formats. A small number of genes encoding ABCs, SLCs, and CYPs were detected in MDCK cells, and their level of expression was much higher in the cells grown on transwell membranes than cell culture flasks. Among these, ABCB1 (MDR1) and SLC22A2 (OCT2) were detected. It is possible that the accumulation format that we used in this study for MDCK-WT and MDCK-hMDR1 did not allow MDCK-hMDR1 cells to generate a high level of P-gp transporter to be able to efflux more [^{3}H]pentamidine than MDCK-WT cells. Although SLC22A1 (OCT1) was not detected by Quan (*et al.*, 2012), we intended to double-check that if there was SLC22A1 (OCT1) expressing in the MDCK-WT and MDCK-hMDR1 cells. As explained in Chapter 3, OCT1 is an influx transporter that is known to interact with pentamidine (X. Ming *et al.*, 2009; Sekhar *et al.*, 2017). However, we could not confirm if OCT1 is expressed in MDCK-WT and MDCK-hMDR1 as we could not locate a suitable antibody which would be cross-reactive with canine proteins. Therefore, the influence of P-gp on the accumulation of [^{3}H]pentamidine ion-pairs could, therefore, not be determined with MDCK-WT and MDCK-hMDR1 cells.

In order to address our objective, we, therefore, established a P-gp single transporter expressing model in *xenopus laevies* oocytes. P-gp has been successfully expressed in *xenopus laevies* oocytes to study the efflux of [^{3}H]vinblastine and [^{3}H]digoxin (Castillo *et al.*, 1990; Jutabha *et al.*, 2010). Similar to the process of establishing oocytes expressing hOCT1 in chapter 3, the P-gp expressing oocytes was also verified by various methods. The DNA sequencing and gel electrophoresis of DNA digestions verified the identity of P-gp cDNA. The RNA chip confirmed the size and integrity of P-gp RNA. The gel electrophoresis on the denaturing agarose-formaldehyde gel proved that the poly-A tailed P-gp RNA was successfully prepared.

In order to confirm the functional expression of P-gp in oocytes as well as to optimize the experimental methods for [^{3}H]pentamidine, we utilised the P-gp substrates, [^{3}H]dexamethasone and [^{3}H]corticosterone (Wolf and Horwitz, 1992a; Régina *et al.*, 1999; Mason, Pariante and

Thomas, 2008; Narang *et al.*, 2008), in oocytes expressing the P-gp transporter. The P-gp transporter is an ATP-dependent efflux transporter and is expected to transport its substrates out of the oocytes (Jutabha *et al.*, 2010).

Our experiments confirmed that the P-gp was inserted in the correct direction at the oocytes membrane because there were no difference in the influx of [^{3}H]dexamethasone and [^{3}H]corticosterone in oocytes expressing P-gp compared to the water-injected oocytes. The efflux assay of [^{3}H]dexamethasone and [^{3}H]corticosterone confirmed the functional of P-gp transporter in oocytes. It also revealed that ATP was a key driver for the efflux of P-gp substrates in oocytes. In addition, whether the P-gp RNA was poly-A tailed or not did significantly change the efflux of [^{3}H]dexamethasone and [^{3}H]corticosterone from oocytes. However, a lack of post-translational P-gp modifications, (e.g. glycosylation) may have affected the ability of the human P-gp transporter to fully function when it was expressed in *xenopus* oocytes. This has previously been observed for the transporters, band 3 and PAT-1.

For [^{3}H]pentamidine, its efflux in oocytes expressing P-gp did not differ significantly from oocytes injected with water. This was likely due to the fact that pentamidine and dexamethasone bound to different binding sites at the P-gp transporter. The P-gp transporter is a transmembrane glycoprotein which contains two transmembrane domains and two ATP binding regions, with a broad range of substrates (Hoosain *et al.*, 2015; Kim and Chen, 2018). As predicted by molecular docking, dexamethasone interacts with GLN724, MET985, GLU874, GLN346, MET875, while pentamidine attracts to ARG262, GLN535, ALA529, GLU1119 on P-gp. Although the functional expression of P-gp was verified by the efflux of [^{3}H]dexamethasone, it was possible that the binding sites on P-gp for [^{3}H]pentamidine did not work functionally in oocytes.

In order to examine the interaction of P-gp with [^{3}H]pentamidine-xinafoate ion-pairs, the efflux of [^{3}H]pentamidine-xinafoate ion-pairs in oocytes expressing P-gp was measured. The presence of 38.5% [^{3}H]pentamidine-xinafoate ion-pairs significantly increased the efflux of [^{3}H]pentamidine in both water-injected and oocytes expressing P-gp by a similar extent. Therefore, it seems like that the [^{3}H]pentamidine-xinafoate ion-pairs facilitated the efflux of [^{3}H]pentamidine through modifying the physicochemical properties of pentamidine (i.e. lipophilicity) rather than interacting with the P-gp transporter.

More validation experiments could have been taken place to prove the functional expression of P-gp in oocytes. For example, P-gp inhibitors and mutated P-gp transporter could have been used in this study. Also, the glycosylation of P-gp in oocytes can be tested with glycosylation mutants of P-gp.

4.6 Conclusion

Based on these data, we propose that pentamidine-xinafoate can improve the ability of pentamidine to cross plasma membranes by passive diffusion, but does not affect the efflux of pentamidine by P-gp. This may be because the size of the pentamidine-xinafoate ion-pair (i.e. MW is 528) is within the range of P-gp substrates (i.e. MW ranges from 200 to over 600 g/mol).

Chapter 5 General Discussion and Future Studies

5.1 General discussion

The rate of clinical approval for central nervous system (CNS) drugs is the lowest among all diseases. This is mainly due to the difficulty in developing drug candidates which cross the blood-brain barrier (BBB). It takes an average of 12-16 years to bring a CNS drug from preclinical development through to clinical trials and finally to market, much longer than the average duration of 10-12 years for non-CNS drugs. Around 98% of failure of CNS drug development is attributed to their inability to cross the BBB (C. Trippier, 2016).

In this PhD project, we proposed using pentamidine ion-pairs to overcome the limited permeability of pentamidine across the BBB and so reformulate pentamidine to be a CNS active drug. In this study, we tested the hypothesis that a -1 charged counterion can bind to the +2 pentamidine and form a +1 charged ion-pair and in doing so make pentamidine more lipophilic and improve its passive transport across the BBB. We also hypothesized that pentamidine ion-pairs would improve its influx by hOCT1 and decrease its efflux by P-gp, which are both expressed at the BBB.

This study of pentamidine ion-pairs is divided into physicochemical characterisation and interactions with biological membranes and the human BBB transporters, hOCT1 and P-gp. The physicochemical characterisation of pentamidine was explained in chapter 2, and the interactions of pentamidine ion-pairs with hOCT1 and P-gp were addressed in chapter 3 and chapter 4, respectively.

Our methodological approach for each arm of the study is outlined in the form of a screening cascade and can be found in Figure 5-1.

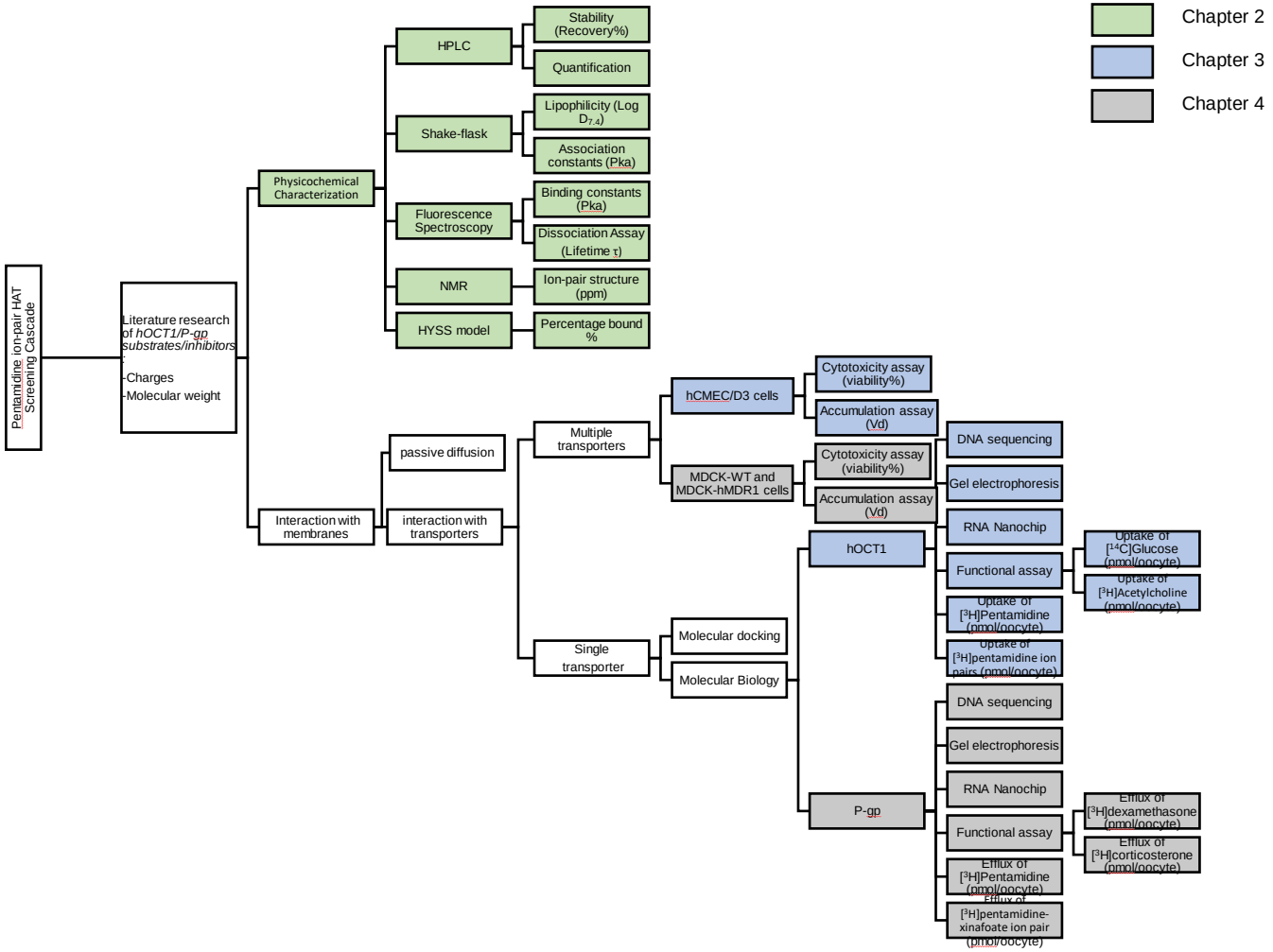

Figure 5-1 Screening cascade of the project. The colour of the blocks represents the different chapters of this thesis.

The physicochemical properties of pentamidine ion-pairs were examined in chapter 2. The lipophilicity (log D) of pentamidine (8 µM or 33 µM), as determined by octanol-saline shake flask at pH 7.4, in the presence of 20 times molar ratio of taurodeoxycholate, octanoate, and xinafoate increased by 1.15, 1.06 and 0.82, respectively compared to pentamidine alone suggesting the presence of ion-pairs. The lipophilicity of pentamidine was only slightly improved in the presence of quercetin. The binding constants (pK_a) of pentamidine with taurodeoxycholate, octanoate, and xinafoate ranged from 3.1 - 4.1 and were determined by HPLC. The binding of pentamidine with counterions is relatively weak, compared to the reported highly stable metal complexes: $pK_{Cu^{2+}\text{-}EDTA}$= 18.8, $pK_{Mg^{2+}\text{-}EDTA}$= 8.8 (Wang and Tomasella, 2016). The NMR and fluorescence data further confirmed the existence of pentamidine-xinafoate ion-pairs and indicated that the binding site of pentamidine with the counterion xinafoate was through the amidine groups of pentamidine (figure 5-2). It is reasonable to conclude that pentamidine is unable to form significant numbers of ion-pairs with quercetin (<0.1%), due to the minimal lipophilicity improvement of pentamidine with quercetin in the shake-flask experiment, as well as the unfit regression of pentamidine - quercetin binding constants analysis. They may, however, have other forms of unknown interactions rather than ion-pairing. Therefore, the percentage of pentamidine bound to quercetin was not predicted by HySS.

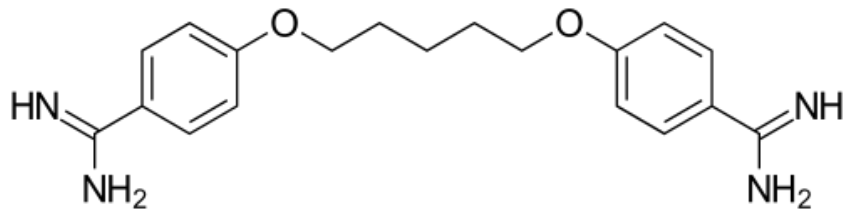

Figure 5-2 The chemical structure of pentamidine

The percentage of pentamidine existing as an ion pair with the counterions taurodeoxycholate, octanoate, or xinafoate was estimated by HySS. It is clear that if we maintain the molar ratio of pentamidine to counterion but increase the actual concentrations of pentamidine and counterions in solution, the percentage of pentamidine ion-pairs increases dramatically, according to Le Châtelier's Principle. For example, for the pentamidine-xinafoate ion-pair, 99.9% of the pentamidine existed as an ion-pair when pentamidine is 8 mM and xinafoate is 160 mM. However, when the concentration of pentamidine is decreased to 8 µM and 9 nM and the molar ratio is maintained at 1:20, the percentage of pentamidine bound in ion-pairs drops to 38.5% and 0.07%,

respectively. Thus higher concentrations of pentamidine and counterions allow the formation of a higher percentage of ion pairs as the individual molecules are more likely to come into contact.

From a clinical perspective, the human plasma concentration of pentamidine peaks at 1h after intramuscular administration (3.5-4.5 mg pentamidine /kg body weight) and varies from 0.42µM (142.8 µg/L) to 13.42µM (4562.8 µg/L) with a median plasma concentration of pentamidine at day 7 of 4 nM (2.4 µg/L) (Bronner *et al.*, 1991). This could be a concern in the development of pentamidine ion-pair formulations for clinical use as it means the percentage of pentamidine remaining bound in ion-pairs would be very low after administration as the concentration of pentamidine would be reduced as it is distributed and diluted in the different body compartments. It would be useful to gain insight into the dissociation rate of pentamidine ion-pairs; unfortunately, due to the detection limits of fluorescence lifetime imaging microscopy, the dissociation of pentamidine ion-pairs could not be measured.

The interactions of pentamidine ion-pairs with biological membranes and the hOCT1 transporter were examined in chapter 3. The accumulation of [^{3}H]pentamidine (9 M and 8 µM) in the human blood-brain barrier (hCMEC/D3) cells did not increase in the presence of the counterions taurodeoxycholate, octanoate, quercetin and xinafoate. This is contrary to what would be expected based on the physicochemical data described in chapter 2. As the lipophilicity (log D) of pentamidine at pH 7.4 was improved with the counterions taurodeoxycholate, octanoate, and xinafoate you would predict that increasing the lipophilicity of pentamidine by reformulation as an ion pair should improve its accumulation in hCMEC/D3 cells. The inability of the counterions to improve pentamidine BBB permeability may be caused by several factors: (a) pentamidine ion-pair formation increases the size of pentamidine. The large size hindering the amount of [^{3}H]pentamidine ion-pairs able to pass through the BBB; (b) The ion environment of the accumulation buffer in which [^{3}H]pentamidine ion-pairs were dissolved for cell accumulation assay was more complicated than the simple saline solution used in the octanol-saline shake flask method and reduced the percentage of ion pairs that could be formed. In other words as the ion-pairs are formed non-covalently, and the binding is relatively weak any competition from ions in the complex cell accumulation buffer could dampen the effect of pentamidine ion-pairing. Based on the binding constants of ion-pairs and the molecular weights of the counterions, pentamidine is more likely to form a stable ion-pair which can be transported across biological membranes

more easily with xinafoate than taurodeoxycholate and octanoate. (c) the transport of [^{3}H]pentamidine ion-pairs may be intervened by membrane transporters such as hOCT1 and P-gp;

In order to test these possibilities, the influx of [^{3}H]pentamidine ion-pairs in control oocytes (oocytes injected with RNA-free water) and oocytes expressing hOCT1 was tested. The net impact of hOCT1 on the transport of [^{3}H]pentamidine ion-pairs was calculated by subtracting the influx of [^{3}H]pentamidine in water oocytes (representing the passive diffusion of [^{3}H]pentamidine) from the influx of [^{3}H]pentamidine in oocytes expressing hOCT1 (representing both passive diffusion and transport by hOCT1 of [^{3}H]pentamidine). For pentamidine-taurodeoxycholate ion-pair, the [^{3}H]pentamidine influx in water-injected oocytes did not increase with taurodeoxycholate. Thus passive diffusion of the more lipophilic ion pair may be inhibited by the large molecular weight of taurodeoxycholate (MW=521.7 g/mol). The influx of [^{3}H]pentamidine by hOCT1 was not influenced by forming ion-pairs with taurodeoxycholate. For pentamidine-octanoate ion-pair, the passive diffusion of [^{3}H]pentamidine with octanoate (MW: 166.16 g/mol) was increased. For pentamidine-xinafoate ion-pair, the passive diffusion of [^{3}H]pentamidine by forming ion-pairs with xinafoate (MW:188.18 g/mol) was increased. However, there was a tendency for the influx of [^{3}H]pentamidine to be decreased by hOCT1 with octanoate and xinafoate in oocytes.

The interactions of pentamidine ion-pairs with P-gp was studied in chapter 4. In our study, initially, we intended to isolate the impact of P-gp on the transport of pentamidine ion-pairs by leveraging the different levels of P-gp expression in MDCK-WT and MDCK-hMDR1 cells. However, no difference in the accumulation of [^{3}H]pentamidine was seen between the two cell lines. This may be because the efflux of [^{3}H]pentamidine by human P-gp was masked by its interactions with other transporters expressed in the MDCK-WT and MDCK-hMDR1 cells. Therefore, to assess the interactions of pentamidine ion-pairs with P-gp, we expressed human P-gp transporter in *xenopus* oocytes. Pentamidine-xinafoate ion-pair was selected as our model ion-pair. In oocytes expressing P-gp, no significant change in the efflux of [^{3}H]pentamidine was observed by forming 38.5% [^{3}H]pentamidine-xinafoate ion-pairs (predicted by HySS). This indicated that the efflux of [^{3}H]pentamidine by forming ion-pairs with xinafoate was not influenced by human P-gp expressing in oocytes.

It is worth mentioning that more validation experiments could have been performed to improve the rigour and assurance of the functional expression of hOCT1 and P-gp transporters in oocytes. For example, transporter inhibitors can be used to verify the functional expression of hOCT1 and P-gp in oocytes. Also, the data generated in this study may have been affected by protein glycosylation in oocytes when transporters were expressed. This can be verified using mass spectrometry in which the glycosylation site and its microheterogeneity of proteins can be checked. A more detailed description can be found in (An, Froehlich and Lebrilla, 2009).

Based on the results obtained in this PhD project: (a) The passive diffusion of pentamidine is improved by forming ion-pairs with taurodeoxycholate (+96.5%), octanoate (+89.1%) and xinafoate (+68.9%). (b) When pentamidine forms ion-pairs with xinafoate and octanoate, its influx across the BBB by hOCT1 is decreased. This might be caused by the change of binding site of pentamidine with hOCT1 when forming pentamidine-xinafoate or pentamidine-octanoate ion-pairs. The NMR study (Chapter 2) and the molecular docking simulation (Chapter 3) suggested that the amidine group on pentamidine was the binding site for both hOCT1 and xinafoate. So xinafoate might have blocked the binding site of pentamidine to hOCT1. This may also be true for pentamidine-octanoate ion pairs and pentamidine-taurocholate ion pairs. Although pentamidine-taurocholate ion pairs did not change the overall influx by OCT1. (c) Pentamidine is still effluxed by P-gp and its efflux by P-gp is not changed by forming ion-pairs with xinafoate. This might be caused by two factors: (i) Forming ion-pairs with xinafoate could prevent the interaction of pentamidine with the specific binding pocket of hOCT1 but not P-gp. (ii) the MW of the pentamidine-xinafoate (MW: 528 Da) ion pair is outside the normal MW range for OCT1 (<400 Da) but is still within the range for P-gp substrates (200-600 Da).

Table 5-1 Key findings of this PhD project

Chapter	Hypothesis	Objectives	Parameters	Key findings
2	The passive diffusion of pentamidine across the blood-brain barrier is improved by ion pairing.	To measure the lipophilicity (Log D) of pentamidine alone and when bound to a counterion (i.e. the ion-pair) by shake-flask and fluorescence methods.	Lipophilicity (log D)	Ion pairing increased the lipophilicity of pentamidine. The magnitude of change: taurodeoxycholate > octanoate > xinafoate > quercetin
		To determine the association constants (binding constants, pK_a) of pentamidine ion-pairs using HPLC and fluorescence methods.	Binding constants (pK_a)	Pentamidine forms ions pairs with Pentamidine-taurodeoxycholate > pentamidine-xinafoate> pentamidine-octanoate Pentamidine does not form ion pairs with quercetin.
		To investigate the binding site of the counterion with pentamidine with ^{13}C-NMR and ^{1}H-NMR by assessing the chemical shift of H and C assigned to pentamidine in the presence of counterions.	Binding sites (only xinafoate was assessed)	The amidine groups on pentamidine could bind to xinafoate and form ion-pairs.

		To estimate the percentage of pentamidine (%) bound with counterions (taurodeoxycholate, octanoate and xinafoate) in solutions using Hyperquad Simulation and Speciation (HySS) software.	Percentage bound	The percentage of pentamidine existing as an ion pair is extremely low (<1%) when pentamidine is at 9nM, even in the presence of excess counterions; The percentage of pentamidine bound with counterions ranges from 1% to 66%, depending on the type and concentrations of counterions.
		To further confirm the presence of pentamidine ion-pairs and understand the dissociation (pK_d) of pentamidine ion-pairs with fluorescence-lifetime imaging microscopy (FLIM).	Dissociation rate (only xinafoate was assessed)	Not determined due to method limitations, however FLIM confirmed formation of ion-pairs

3	The ion-pairing of pentamidine increases the transport of pentamidine by hOCT1.	To measure the toxicity of pentamidine-taurodeoxycholate, pentamidine-octanoate, pentamidine-quercetin, and pentamidine-xinafoate in hCMEC/D3 cells using MTT assay.	% cell viability	0.1-200 µM of the four counterions do not affect membrane integrity of hCMEC/D3 cells.
		To determine the retention of [^{3}H]pentamidine with taurodeoxycholate, octanoate, quercetin, and xinafoate in hCMEC/D3 cells by measuring the volume of distribution (V_d) of [^{3}H]pentamidine with drug accumulation assay and the concentrations of protein with bicinchoninic acid (BCA) assay.	Volume of distribution (Vd)	The accumulation of [^{3}H]pentamidine (9M and 8µM) in human blood-brain barrier (hCMEC/D3) cells did not increase in the presence of the counterions taurodeoxycholate, octanoate, quercetin and xinafoate.
		To simulate the interaction of pentamidine with hOCT1 membrane transporter using *in silico* molecular docking.	CDOCKER free energy (kcal/mol)	The result confirmed that pentamidine was a substrate for hOCT1.

		To confirm the identity and functional expression of hOCT1 in *xenopus* oocytes through DNA sequencing, gel electrophoresis of DNA and RNA, and influx of the hOCT1 substrate - [^{3}H]acetylcholine into xenopus oocytes expressing hOCT1	DNA sequencing, size of DNA and RNA, uptake of [^{3}H]acetylcholine into xenopus oocytes expressing hOCT1	The identity and functional expression of hOCT1 were confirmed.

		To determine the interaction of [^{3}H]pentamidine ion-pairs with hOCT1 by measuring the influx of [^{3}H]pentamidine into *xenopus* oocytes expressing hOCT1	Uptake of [^{3}H]pentamidine (fmol/oocyte) into oocytes	[^{3}H]pentamidine-xinafoate and ^{3}H]pentamidine-octanoate ion-pairs inhibited the uptake of [^{3}H]pentamidine by hOCT1. The formation of [^{3}H]pentamidine-taurodeoxycholate had no impact on the influx of [^{3}H]pentamidine by hOCT1.
4	Pentamidine ion-pairs inhibit the efflux of pentamidine by P-gp transporter expressed at the blood-brain barrier.	To determine the specific interactions of pentamidine with P-gp using *in silico* molecular docking and compare the results with known P-gp substrates (e.g. dexamethasone).	CDOCKER free energy binding (kcal/mol)	Pentamidine is a substrate for P-gp.
		To confirm the suitability of the MDCK and MDCK-hMDR1 cell lines for exploring pentamidine ion	% cell viability	50-200 µM of the four selected counterions should not cause measurable cytotoxicity

		pairs interaction with human MDR1 by determining the toxicity of pentamidine-taurodeoxycholate, pentamidine-octanoate, pentamidine-quercetin, and pentamidine-xinafoate in these cells using the MTT assay.		issues that may influence the interpretation of the data obtained from confluent monolayers of MDCK and MDCK-hMDR1 cells in this study.
		To examine the impact of counterions on the interaction of pentamidine with P-gp using Madin-Darby Canine Kidney (MDCK-WT) and MDCK-hMDR1.	The volume of distribution (V_d) of [^{3}H]pentamidine corrected by [^{14}C]sucrose	The V_d of [^{3}H]pentamidine corrected by [^{14}C]sucrose dropped significantly within 60 mins of incubation when 8μM of unlabelled pentamidine was present in MDCK-WT cells. These indicated influx transporters were involved. The efflux of [^{3}H]pentamidine by the highly expressed hMDR1 transporter could not be detected, as there was no significant difference in the accumulation of [^{3}H]pentamidine in between the MDCK-WT and MDCK-hMDR1 cells.

		To confirm the identity and functional expression of P-gp in *xenopus* oocytes through DNA sequencing, gel electrophoresis of DNA and RNA, influx (accumulation) and efflux transport of P-gp substrates [^{3}H]dexamethasone and [^{3}H]corticosterone.	Sequencing alignment, Size of enzyme digestion of *P-gp* DNA, Size of *P-gp* RNA, Efflux of [^{3}H]dexamethasone and [^{3}H]corticosterone in oocytes expressing Pgp (fmol/oocyte)	The identity and functional of P-gp in oocytes were confirmed.
		To determine the interaction of [^{3}H]pentamidine-xinafoate ion-pair with P-gp by measuring the efflux of [^{3}H]pentamidine extruded from *xenopus* oocytes expressing P-gp.	Efflux of [^{3}H]pentamidine (pmol/oocyte) out of oocytes	Pentamidine is still effluxed by P-gp and its efflux by P-gp is not changed by forming ion-pairs with xinafoate.

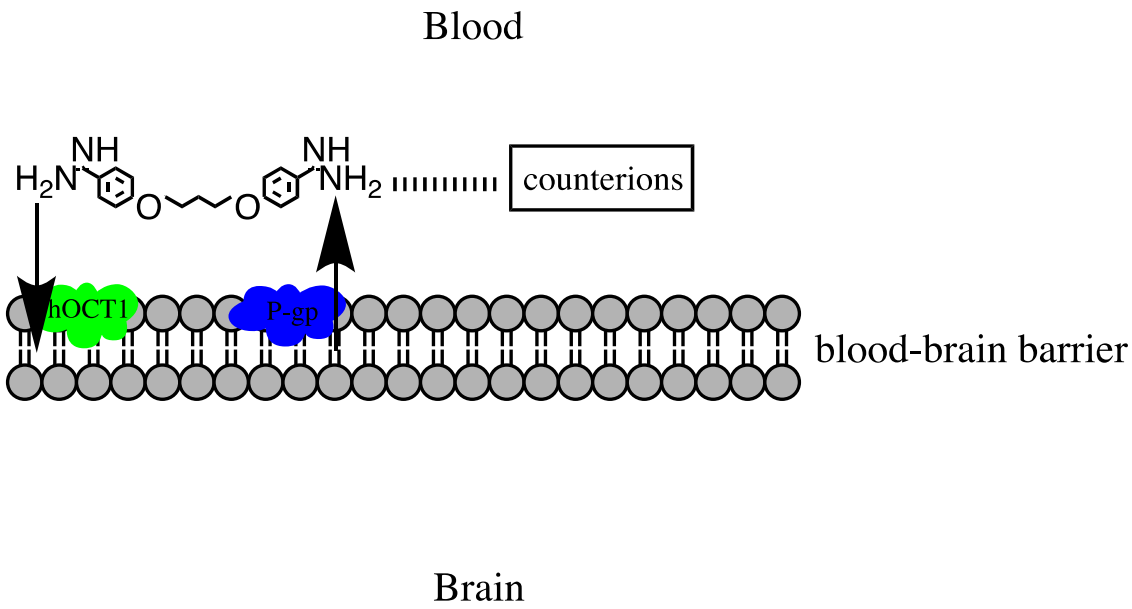

Figure 5-3 Transport of pentamidine ion-pairs cross the blood-brain barrier.

From the results acquired in this project, we can state that there are several advantages of pentamidine ion-pair method for drug delivery across the BBB. Firstly, ion-pairing is a non-invasive method and safer as it does not force the BBB to open like the focused ultrasound method. Pentamidine is also less toxic than current drugs for CNS stage HAT. Importantly pentamidine was recently screened against 40 CNS targets, and no major neurotoxicity issues were found (Sanderson *et al.*, 2019). Ion-pairing is an inexpensive method, with the potential to scale into massive production for therapeutic drugs. As 98% of drug molecules are not able to cross the BBB (Pardridge, 2005), ion-pairing could be a potential solution for these molecules. Thirdly, ion-pairing is easy to prepare and is effective in improving the lipophilicity of molecules (Suresh and Paul, 2011b).

The disadvantages of pentamidine ion-pairing for drug delivery across the BBB are summarized as follows: Firstly, pentamidine would not be able to form ion-pairs at the plasma concentrations achieved clinically. It is known that the percentage of pentamidine bound in ion-pairs is largely dependent on the concentration of pentamidine. The percentage of pentamidine bound in ion-pairs would be negligible (<0.1%) when the concentration of pentamidine is 9nM, which is within the range of pentamidine in cerebrospinal fluid (1.7-3.9 nM) (Bronner *et al.*, 1991). Secondly, pentamidine ion-pairs might be unstable in the human body as they face enormous competition from ions in the biological environment. Thirdly, although the efflux transporter P-gp does not

accelerate the excretion of pentamidine ion-pairs out of the BBB, the influx of pentamidine by hOCT1 transporter at the BBB may be hindered by forming ion-pairs.

5.2 Future studies

In this study we confirmed that pentamidine could form ion-pairs with specific counterions and its lipophilicity was improved. Ion-pairs could also enhance the ability of pentamidine to cross plasma membranes by passive diffusion. We also evaluated the ability of the pentamidine ion-pairs to interact with cell membranes and transporters using simple and complex BBB models *in vitro*.

In the future further studies could be designed:

(i) To overcome the instability of pentamidine ion-pairs and allow ion-pairs to reach the BBB *in vivo*, ion-pairs could be wrapped with liposomes or cyclodextrins to improve drug delivery. Liposomes are well-established nanocarriers which can encapsulate hydrophilic and lipophilic compounds for targeted drug delivery and improved stability (Sercombe *et al.*, 2015). Cyclodextrins are cyclic oligosaccharides and have been used for increasing solubility, bioavailability, and stability of drugs (Tiwari, Tiwari and Rai, 2010). We could explore the possibility of forming pentamidine ion-pairs with liposomes and cyclodextrins to increase the stability of pentamidine ion-pairs in future studies. In addition, focused ultrasound could be used to target the delivery of encapsulated pentamidine ion-pairs into the CNS. Focused ultrasound has been applied successfully in delivering chemotherapeutic agents, nanoparticles, and peptides across the BBB (Chen, Wei and Liu, 2019). Other strategies can also be used to improve the delivery of pentamidine ion-pairs across the BBB. For example, nanocarriers or artificial peptides with fatty acid residues might be introduced in future studies to overcome the stability issue of pentamidine ion-pairs (Bors and Erdő, 2019).

(ii) To explore if ion pairs could be designed to reduce the penetration of a drug into any target tissue /organ. This may reduce toxicity issues and any resulting adverse effects. For example, hypoglycaemia and diabetes mellitus associated with increasing doses of pentamidine may be prevented (BURRI, 2010).

(iii) To further explore the interaction of pentamidine ion-pairs with hOCT1 and P-gp using *in silico* assessment. To do this, we can compare the free energy binding of pentamidine ion-pair with transporters to that of pentamidine alone.

(iv) To determine if pentamidine ion pairs could be formed with other counterions or to assess if the selected counterions can form ion-pairs with other drugs (e.g. antipsychotic drugs and cancer therapies) whose entry into the CNS is also limited by the BBB and interact with the same and different transporters. The selected counterions taurodeoxycholate, octanoate, and xinafoate showed promising effect as they improve the lipophilicity of pentamidine. These counterions have also previously been used in the production of pharmaceutical products and do not cause major side effects at the concentrations used in this study.

(v) To test if ion-pairing could improve the permeability of pentamidine or other drug across the BBB using *in vivo methods*. For example*, in vivo* whole body distribution, brain microdialysis and *in situ* brain perfusion studies on mice could be performed.

(vi) To explore the ability of ion pairs to cross other blood-tissue interfaces e.g, choroid plexus.

References

Abbott, N. J. *et al.* (2010) 'Structure and function of the blood-brain barrier.', *Neurobiology of disease*, 37(1), pp. 13–25. doi: 10.1016/j.nbd.2009.07.030.

Ahlin, G. *et al.* (2008) 'Structural Requirements for Drug Inhibition of the Liver Specific Human Organic Cation Transport Protein 1', *Journal of Medicinal Chemistry*, 51(19), pp. 5932–5942. doi: 10.1021/jm8003152.

Ajay, Bemis, G. W. and Murcko, M. A. (1999) 'Designing libraries with CNS activity.', *Journal of medicinal chemistry*, 42(24), pp. 4942–51. doi: 10.1021/jm990017w.

Aksoy, S. (2003) 'Control of tsetse flies and trypanosomes using molecular genetics.', *Veterinary parasitology*, 115(2), pp. 125–45. doi: 10.1016/s0304-4017(03)00203-6.

Aksoy, S. *et al.* (2017) 'Human African trypanosomiasis control: Achievements and challenges.', *PLoS neglected tropical diseases*. Public Library of Science, 11(4), p. e0005454. doi: 10.1371/journal.pntd.0005454.

Alderighi, L. *et al.* (1999) 'Hyperquad simulation and speciation (HySS): a utility program for the investigation of equilibria involving soluble and partially soluble species', *Coordination Chemistry Reviews*. Elsevier, 184(1), pp. 311–318. doi: 10.1016/S0010-8545(98)00260-4.

Alebouyeh, M. *et al.* (2003) 'Expression of Human Organic Anion Transporters in the Choroid Plexus and Their Interactions With Neurotransmitter Metabolites', *Journal of Pharmacological Sciences*, 93(4), pp. 430–436. doi: 10.1254/jphs.93.430.

Alirol, E. *et al.* (2013) 'Nifurtimox-Eflornithine Combination Therapy for Second-Stage Gambiense Human African Trypanosomiasis: Médecins Sans Frontières Experience in the Democratic Republic of the Congo', *Clinical Infectious Diseases*. Narnia, 56(2), pp. 195–203. doi: 10.1093/cid/cis886.

Allen, J. D. *et al.* (1999) 'The mouse Bcrp1/Mxr/Abcp gene: amplification and overexpression in cell lines selected for resistance to topotecan, mitoxantrone, or doxorubicin.', *Cancer research*, 59(17), pp. 4237–41. doi: Published September 1999.

Allen, T. D. *et al.* (2007) 'A protocol for isolating Xenopus oocyte nuclear envelope for visualization

and characterization by scanning electron microscopy (SEM) or transmission electron microscopy (TEM)', *Nature Protocols*, 2(5), pp. 1166–1172. doi: 10.1038/nprot.2007.137.

Amaral, J. D. *et al.* (2009) 'Bile acids: regulation of apoptosis by ursodeoxycholic acid', *Journal of Lipid Research*, 50(9), pp. 1721–1734. doi: 10.1194/jlr.R900011-JLR200.

An, H. J., Froehlich, J. W. and Lebrilla, C. B. (2009) 'Determination of Glycosylation Sites and Site-specific Heterogeneity in Glycoproteins', *Current opinion in chemical biology*. NIH Public Access, 13(4), p. 421. doi: 10.1016/J.CBPA.2009.07.022.

Arimany-Nardi, C. *et al.* (2014) 'Nucleoside transporters and human organic cation transporter 1 determine the cellular handling of DNA-methyltransferase inhibitors.', *British journal of pharmacology*. Wiley-Blackwell, 171(16), pp. 3868–80. doi: 10.1111/bph.12748.

Armulik, A. *et al.* (2010) 'Pericytes regulate the blood-brain barrier.', *Nature*, 468(7323), pp. 557–61. doi: 10.1038/nature09522.

Arnott, J. A., Kumar, R. and Planey, S. L. (2013) *Lipophilicity Indices for Drug Development*, *Journal of Applied Biopharmaceutics and Pharmacokinetics*. doi: 10.14205/2309-4435.2013.01.01.6.

Aslantürk, Ö. S. (2018) 'In Vitro Cytotoxicity and Cell Viability Assays: Principles, Advantages, and Disadvantages', in *Genotoxicity - A Predictable Risk to Our Actual World*. InTech. doi: 10.5772/intechopen.71923.

Atwal, J. K. *et al.* (2011) 'A therapeutic antibody targeting BACE1 inhibits amyloid-β production in vivo.', *Science translational medicine*, 3(84), p. 84ra43. doi: 10.1126/scitranslmed.3002254.

Avdeef, A. (2012) *Absorption and drug development solubility, permeability, and charge state*. John Wiley & Sons.

Babokhov, P. *et al.* (2013) 'A current analysis of chemotherapy strategies for the treatment of human African trypanosomiasis.', *Pathogens and global health*. Taylor & Francis, 107(5), pp. 242–52. doi: 10.1179/2047773213Y.0000000105.

Bacchi, C. J. (2009) 'Chemotherapy of human african trypanosomiasis.', *Interdisciplinary perspectives on infectious diseases*. Hindawi, 2009, p. 195040. doi: 10.1155/2009/195040.

Baker, C. H. and Welburn, S. C. (2018) ‘The Long Wait for a New Drug for Human African Trypanosomiasis.’, *Trends in parasitology*. Elsevier, 34(10), pp. 818–827. doi: 10.1016/j.pt.2018.08.006.

van Balkom, B. W. M. *et al.* (2004) ‘Role of cytoplasmic termini in sorting and shuttling of the aquaporin-2 water channel’, *American Journal of Physiology-Cell Physiology*, 286(2), pp. C372–C379. doi: 10.1152/ajpcell.00271.2003.

Ballabh, P., Braun, A. and Nedergaard, M. (2004) ‘The blood-brain barrier: an overview: structure, regulation, and clinical implications.’, *Neurobiology of disease*, 16(1), pp. 1–13. doi: 10.1016/j.nbd.2003.12.016.

Banks, W. A. (2016) ‘From blood-brain barrier to blood-brain interface: new opportunities for CNS drug delivery.’, *Nature reviews. Drug discovery*. Nature Publishing Group, a division of Macmillan Publishers Limited. All Rights Reserved., 15(4), pp. 275–292. doi: 10.1038/nrd.2015.21.

Bardal, S. K. *et al.* (2011) ‘Infectious Diseases’, *Applied Pharmacology*. Content Repository Only!, pp. 233–291. doi: 10.1016/B978-1-4377-0310-8.00018-X.

Barrett, M. P. (2000) ‘Problems for the chemotherapy of human African trypanosomiasis.’, *Current opinion in infectious diseases*, 13(6), pp. 647–651. doi: 10.1097/00001432-200012000-00012.

Barrett, M. P. *et al.* (2007) ‘Human African trypanosomiasis: pharmacological re-engagement with a neglected disease.’, *British journal of pharmacology*. Wiley-Blackwell, 152(8), pp. 1155–71. doi: 10.1038/sj.bjp.0707354.

Bauer, H.-C. *et al.* (2014) ‘“You Shall Not Pass”—tight junctions of the blood brain barrier’, *Frontiers in Neuroscience*. Frontiers, 8, p. 392. doi: 10.3389/fnins.2014.00392.

Beare-Rogers, J., Dieffenbacher, A. and Holm, J. V (2001) *Lexicon of lipid nutrition (IUPAC Technical Report)*, *Pure Appl. Chem*. doi: 73,4,685-774,2001.

Bednarczyk, D. (2003) ‘Influence of Molecular Structure on Substrate Binding to the Human Organic Cation Transporter, hOCT1’, *Molecular Pharmacology*, 63(3), pp. 489–498. doi: 10.1124/mol.63.3.489.

Bellavance, M.-A., Blanchette, M. and Fortin, D. (2008) ‘Recent advances in blood-brain barrier

disruption as a CNS delivery strategy.', *The AAPS journal*. Springer, 10(1), pp. 166–77. doi: 10.1208/s12248-008-9018-7.

Benaouda, F. *et al.* (2018) 'Ion-Pairing with Spermine Targets Theophylline To the Lungs via the Polyamine Transport System', *Molecular Pharmaceutics*, 15(3), pp. 861–870. doi: 10.1021/acs.molpharmaceut.7b00715.

Berberof, M., Pérez-Morga, D. and Pays, E. (2001) 'A receptor-like flagellar pocket glycoprotein specific to Trypanosoma brucei gambiense.', *Molecular and biochemical parasitology*, 113(1), pp. 127–38. doi: 10.1016/s0166-6851(01)00208-0.

Bernstein, P. and Ross, J. (1989) 'Poly(A), poly(A) binding protein and the regulation of mRNA stability.', *Trends in biochemical sciences*, 14(9), pp. 373–7. doi: 10.1016/0968-0004(89)90011-x.

Bertrand, L., Cho, H. J. and Toborek, M. (2019) 'Blood–brain barrier pericytes as a target for HIV-1 infection', *Brain*. Narnia, 142(3), pp. 502–511. doi: 10.1093/brain/awy339.

Bhowmik, A. *et al.* (2015) 'Blood Brain Barrier: A Challenge for Effectual Therapy of Brain Tumors', *BioMed Research International*. Hindawi Publishing Corporation, 2015, pp. 1–20. doi: 10.1155/2015/320941.

Boado, R. J. *et al.* (2009) 'AGT-181: Expression in CHO Cells and Pharmacokinetics, Safety, and Plasma Iduronidase Enzyme Activity in Rhesus Monkeys', *Journal of biotechnology*. NIH Public Access, 144(2), p. 135. doi: 10.1016/J.JBIOTEC.2009.08.019.

Boatright, J. H. *et al.* (2009) 'Bile acids in treatment of ocular disease.', *Journal of ocular biology, diseases, and informatics*. Springer, 2(3), pp. 149–159. doi: 10.1007/s12177-009-9030-x.

Bornstein, R. S. and Yarbro, J. W. (1970) 'An evaluation of the mechanism of action of pentamidine isethionate', *Journal of Surgical Oncology*. John Wiley & Sons, Ltd, 2(4), pp. 393–398. doi: 10.1002/jso.2930020412.

Bors, L. and Erdő, F. (2019) 'Overcoming the Blood–Brain Barrier. Challenges and Tricks for CNS Drug Delivery', *Scientia Pharmaceutica*. Multidisciplinary Digital Publishing Institute, 87(1), p. 6. doi: 10.3390/scipharm87010006.

BOTCHWAY, S. W. *et al.* (2015) ‘A series of flexible design adaptations to the Nikon E-C1 and E-C2 confocal microscope systems for UV, multiphoton and FLIM imaging’, *Journal of Microscopy*. John Wiley & Sons, Ltd (10.1111), 258(1), pp. 68–78. doi: 10.1111/jmi.12218.

Bronner, U. *et al.* (1991) ‘Pentamidine concentrations in plasma, whole blood and cerebrospinal fluid during treatment of Trypanosoma gambiense infection in Côte d’Ivoire’, *Transactions of the Royal Society of Tropical Medicine and Hygiene*. Elsevier, 85(5), pp. 608–611. doi: 10.1016/0035-9203(91)90364-5.

Brown, L. S. *et al.* (2019) ‘Pericytes and Neurovascular Function in the Healthy and Diseased Brain’, *Frontiers in Cellular Neuroscience*. Frontiers, 13, p. 282. doi: 10.3389/fncel.2019.00282.

Brück, S. *et al.* (2017) ‘Caco-2 cells - expression, regulation and function of drug transporters compared with human jejunal tissue’, *Biopharmaceutics & Drug Disposition*. John Wiley & Sons, Ltd, 38(2), pp. 115–126. doi: 10.1002/bdd.2025.

BURRI, C. (2010) ‘Chemotherapy against human African trypanosomiasis: Is there a road to success?’, *Parasitology*. Cambridge University Press, 137(14), pp. 1987–1994. doi: 10.1017/S0031182010001137.

Burri, C. and Blum, J. (2017) ‘Human African Trypanosomiasis’, *Infectious Diseases*. Elsevier, pp. 966-970.e1. doi: 10.1016/B978-0-7020-6285-8.00110-6.

Burri, C. and Brun, R. (2003) ‘Eflornithine for the treatment of human African trypanosomiasis’, *Parasitology Research*, 90(S1), pp. S49–S52. doi: 10.1007/s00436-002-0766-5.

C. Trippier, P. (2016) ‘Selecting Good “Drug-Like” Properties to Optimize Small Molecule Blood-Brain Barrier Penetration’, *Current Medicinal Chemistry*, 23(14), pp. 1392–1407. doi: 10.2174/0929867323666160405112353.

Cabezas, R. *et al.* (2014) ‘Astrocytic modulation of blood brain barrier: perspectives on Parkinson’s disease.’, *Frontiers in cellular neuroscience*. Frontiers Media SA, 8, p. 211. doi: 10.3389/fncel.2014.00211.

Castillo, G. *et al.* (1990) ‘Functional expression of murine multidrug resistance in Xenopus laevis oocytes.’, *Proceedings of the National Academy of Sciences of the United States of America*. National Academy of Sciences, 87(12), pp. 4737–41. doi: 10.1073/pnas.87.12.4737.

Castro Dias, M. *et al.* (2019) 'Claudin-12 is not required for blood–brain barrier tight junction function', *Fluids and Barriers of the CNS*. BioMed Central, 16(1), p. 30. doi: 10.1186/s12987-019-0150-9.

Ceña, V. and Játiva, P. (2018) 'Nanoparticle crossing of blood–brain barrier: a road to new therapeutic approaches to central nervous system diseases', *Nanomedicine*. Future Medicine Ltd London, UK , 13(13), pp. 1513–1516. doi: 10.2217/nnm-2018-0139.

Chatham, J. C. and Blackband, S. J. (2001) 'Nuclear Magnetic Resonance Spectroscopy and Imaging in Animal Research', *ILAR Journal*. Narnia, 42(3), pp. 189–208. doi: 10.1093/ilar.42.3.189.

Chen, K.-T., Wei, K.-C. and Liu, H.-L. (2019) 'Theranostic Strategy of Focused Ultrasound Induced Blood-Brain Barrier Opening for CNS Disease Treatment', *Frontiers in Pharmacology*. Frontiers, 10, p. 86. doi: 10.3389/fphar.2019.00086.

Chen, X. *et al.* (2014) 'Effect of transporter inhibition on the distribution of cefadroxil in rat brain', *Fluids and Barriers of the CNS*. BioMed Central, 11(1), p. 25. doi: 10.1186/2045-8118-11-25.

Chen, Y. and Liu, L. (2012) 'Modern methods for delivery of drugs across the blood-brain barrier.', *Advanced drug delivery reviews*, 64(7), pp. 640–65. doi: 10.1016/j.addr.2011.11.010.

Chikhale, E. G. *et al.* (1994) 'Hydrogen Bonding Potential as a Determinant of the in Vitro and in Situ Blood–Brain Barrier Permeability of Peptides', *Pharmaceutical Research*. Kluwer Academic Publishers-Plenum Publishers, 11(3), pp. 412–419. doi: 10.1023/A:1018969222130.

Choi, M.-K. and Song, I.-S. (2016) 'Blockade of P-Glycoprotein Decreased the Disposition of Phenformin and Increased Plasma Lactate Level.', *Biomolecules & therapeutics*. Korean Society of Applied Pharmacology, 24(2), pp. 199–205. doi: 10.4062/biomolther.2015.087.

Cipolla, M. J. (2009) *The Cerebral Circulation*, *The Cerebral Circulation*. Morgan & Claypool Life Sciences.

Cisternino, S. *et al.* (2003) 'Apparent Lack of Mrp1-Mediated Efflux at the Luminal Side of Mouse Blood-Brain Barrier Endothelial Cells', *Pharmaceutical Research*. Kluwer Academic Publishers-Plenum Publishers, 20(6), pp. 904–909. doi: 10.1023/A:1023895404929.

Clark, D. E. (2003) ‘In silico prediction of blood–brain barrier permeation’, *Drug Discovery Today*, 8(20), pp. 927–933. doi: 10.1016/S1359-6446(03)02827-7.

Coomber, B. L. and Stewart, P. A. (1985) ‘Morphometric analysis of CNS microvascular endothelium’, *Microvascular Research*, 30(1), pp. 99–115. doi: 10.1016/0026-2862(85)90042-1.

Cooray, H. C. *et al.* (2002) ‘Localisation of breast cancer resistance protein in microvessel endothelium of human brain’, *NeuroReport*, 13(16), pp. 2059–2063. doi: 10.1097/00001756-200211150-00014.

Correale, J. and Villa, A. (2009) ‘Cellular Elements of the Blood-Brain Barrier’, *Neurochemical Research*. Springer, 34(12), pp. 2067–2077. doi: 10.1007/s11064-009-0081-y.

Couroussé, T. and Gautron, S. (2015) ‘Role of organic cation transporters (OCTs) in the brain’, *Pharmacology & Therapeutics*, 146, pp. 94–103. doi: 10.1016/j.pharmthera.2014.09.008.

Daneman, R. and Prat, A. (2015) ‘The blood-brain barrier.’, *Cold Spring Harbor perspectives in biology*. Cold Spring Harbor Laboratory Press, 7(1), p. a020412. doi: 10.1101/cshperspect.a020412.

Daood, M. *et al.* (2008) ‘ABC Transporter (P-gp/ABCB1, MRP1/ABCC1, BCRP/ABCG2) Expression in the Developing Human CNS’, *Neuropediatrics*. © Georg Thieme Verlag KG Stuttgart · New York, 39(04), pp. 211–218. doi: 10.1055/s-0028-1103272.

Davis, J. M., Murphy, E. A. and Carmichael, M. D. (2009) ‘Effects of the Dietary Flavonoid Quercetin Upon Performance and Health’, *Current Sports Medicine Reports*, 8(4), pp. 206–213. doi: 10.1249/JSR.0b013e3181ae8959.

Deeks, E. D. (2019) ‘Fexinidazole: First Global Approval’, *Drugs*, 79(2), pp. 215–220. doi: 10.1007/s40265-019-1051-6.

DeMars, K. M. *et al.* (2017) ‘Spatiotemporal Changes in P-glycoprotein Levels in Brain and Peripheral Tissues Following Ischemic Stroke in Rats.’, *Journal of experimental neuroscience*. SAGE Publications, 11, p. 1179069517701741. doi: 10.1177/1179069517701741.

Demeule, M., Régina, A., *et al.* (2008) ‘Identification and Design of Peptides as a New Drug Delivery System for the Brain’, *Journal of Pharmacology and Experimental Therapeutics*.

American Society for Pharmacology and Experimental Therapeutics, 324(3), pp. 1064–1072. doi: 10.1124/JPET.107.131318.

Demeule, M., Currie, J.-C., *et al.* (2008) 'Involvement of the low-density lipoprotein receptor-related protein in the transcytosis of the brain delivery vector Angiopep-2', *Journal of Neurochemistry*, 106(4), pp. 1534–1544. doi: 10.1111/j.1471-4159.2008.05492.x.

Demeule, M. *et al.* (2014) 'Conjugation of a brain-penetrant peptide with neurotensin provides antinociceptive properties', *The Journal of Clinical Investigation*. American Society for Clinical Investigation, 124(3), pp. 1199–1213. doi: 10.1172/JCI70647.

Deng, D. *et al.* (2015) 'Molecular basis of ligand recognition and transport by glucose transporters', *Nature*. Nature Publishing Group, 526(7573), pp. 391–396. doi: 10.1038/nature14655.

Deracinois, B. *et al.* (2015) 'Tissue Non-specific Alkaline Phosphatase (TNAP) in Vessels of the Brain', in *Sub-cellular biochemistry*, pp. 125–151. doi: 10.1007/978-94-017-7197-9_7.

Dong, X. (2018) 'Current Strategies for Brain Drug Delivery.', *Theranostics*. Ivyspring International Publisher, 8(6), pp. 1481–1493. doi: 10.7150/thno.21254.

Dorn, M. *et al.* (2009) 'The role of N-glycosylation in transport function and surface targeting of the human solute carrier PAT1', *FEBS Letters*. No longer published by Elsevier, 583(10), pp. 1631–1636. doi: 10.1016/J.FEBSLET.2009.04.037.

Doyle, L. A. *et al.* (1998) 'A multidrug resistance transporter from human MCF-7 breast cancer cells.', *Proceedings of the National Academy of Sciences of the United States of America*. National Academy of Sciences, 95(26), pp. 15665–70. doi: 10.1073/pnas.95.26.15665.

Drake, P. M. *et al.* (2018) 'CAT-02-106, a Site-Specifically Conjugated Anti-CD22 Antibody Bearing an MDR1-Resistant Maytansine Payload Yields Excellent Efficacy and Safety in Preclinical Models', *Molecular Cancer Therapeutics*, 17(1), pp. 161–168. doi: 10.1158/1535-7163.MCT-17-0776.

Dutton, B. L. (2018) 'Using ion-pairs to modify salbutamol delivery to the lungs'. King's College London.

ElShaer, A., Hanson, P. and Mohammed, A. R. (2014) ‘A novel concentration dependent amino acid ion pair strategy to mediate drug permeation using indomethacin as a model insoluble drug.’, *European journal of pharmaceutical sciences : official journal of the European Federation for Pharmaceutical Sciences*, 62, pp. 124–31. doi: 10.1016/j.ejps.2014.05.022.

Fan, Y. and Liu, X. (2018) ‘Alterations in Expression and Function of ABC Family Transporters at Blood-Brain Barrier under Liver Failure and Their Clinical Significances’, *Pharmaceutics*. Multidisciplinary Digital Publishing Institute, 10(3), p. 102. doi: 10.3390/pharmaceutics10030102.

Fanning, A. S., Ma, T. Y. and Anderson, J. M. (2002) ‘Isolation and functional characterization of the actin-binding region in the tight junction protein ZO-1’, *The FASEB Journal*. Federation of American Societies for Experimental Biology, 16(13), pp. 1–23. doi: 10.1096/fj.02-0121fje.

Fazary, A. E. and Ramadan, A. M. (2014) ‘Stability constants and complex formation equilibria between iron, calcium, and zinc metal ions with vitamin B9 and glycine’, *Complex Metals*. Taylor & Francis, 1(1), pp. 139–148. doi: 10.1080/2164232X.2014.941115.

Fischer, H., Gottschlich, R. and Seelig, A. (1998) ‘Blood-brain barrier permeation: molecular parameters governing passive diffusion.’, *The Journal of membrane biology*, 165(3), pp. 201–11. doi: 10.1007/s002329900434.

da Fonseca, A. C. C. *et al.* (2014) ‘The impact of microglial activation on blood-brain barrier in brain diseases’, *Frontiers in Cellular Neuroscience*. Frontiers, 8, p. 362. doi: 10.3389/fncel.2014.00362.

Franco, J. R. *et al.* (2014) ‘Epidemiology of human African trypanosomiasis.’, *Clinical epidemiology*. Dove Press, 6, pp. 257–75. doi: 10.2147/CLEP.S39728.

Fredericks, W. R. and Rapoport, S. I. (1988) ‘Reversible osmotic opening of the blood-brain barrier in mice.’, *Stroke*, 19(2), pp. 266–268. doi: 10.1161/01.STR.19.2.266.

Gallie, D. R. (1991) ‘The cap and poly(A) tail function synergistically to regulate mRNA translational efficiency.’, *Genes & Development*, 5(11), pp. 2108–2116. doi: 10.1101/gad.5.11.2108.

Gao, B. *et al.* (2000) ‘Organic anion-transporting polypeptides mediate transport of opioid peptides across blood-brain barrier.’, *The Journal of pharmacology and experimental*

therapeutics, 294(1), pp. 73–9. doi: 294(1):73-9.

Gao, B. *et al.* (2015) 'Differential cellular expression of organic anion transporting peptides OATP1A2 and OATP2B1 in the human retina and brain: implications for carrier-mediated transport of neuropeptides and neurosteriods in the CNS', *Pflügers Archiv - European Journal of Physiology*, 467(7), pp. 1481–1493. doi: 10.1007/s00424-014-1596-x.

Geier, E. G. *et al.* (2013) 'Profiling solute carrier transporters in the human blood-brain barrier.', *Clinical pharmacology and therapeutics*. NIH Public Access, 94(6), pp. 636–9. doi: 10.1038/clpt.2013.175.

Gerhart, D. Z. *et al.* (1997) 'Expression of monocarboxylate transporter MCT1 by brain endothelium and glia in adult and suckling rats', *American Journal of Physiology-Endocrinology and Metabolism*, 273(1), pp. E207–E213. doi: 10.1152/ajpendo.1997.273.1.E207.

Ghosh, C. *et al.* (2011) 'Blood-brain barrier P450 enzymes and multidrug transporters in drug resistance: a synergistic role in neurological diseases.', *Current drug metabolism*. NIH Public Access, 12(8), pp. 742–9. doi: 10.2174/138920011798357051.

Gibson, W., Backhouse, T. and Griffiths, A. (2002) 'The human serum resistance associated gene is ubiquitous and conserved in Trypanosoma brucei rhodesiense throughout East Africa.', *Infection, genetics and evolution : journal of molecular epidemiology and evolutionary genetics in infectious diseases*, 1(3), pp. 207–14. doi: 10.1016/s1567-1348(02)00028-x.

Gleeson, M. P. (2008) 'Generation of a Set of Simple, Interpretable ADMET Rules of Thumb', *Journal of Medicinal Chemistry*. American Chemical Society, 51(4), pp. 817–834. doi: 10.1021/jm701122q.

Gorboulev, V. *et al.* (1997) 'Cloning and Characterization of Two Human Polyspecific Organic Cation Transporters'. Mary Ann Liebert, Inc. Pp, 16(7), pp. 871–881. doi: 10.1089/dna.1997.16.871.

Greenwood, J. *et al.* (1988) 'Hyperosmolar Opening of the Blood-Brain Barrier in the Energy-Depleted Rat Brain. Part 1. Permeability Studies', *Journal of Cerebral Blood Flow & Metabolism*, 8(1), pp. 9–15. doi: 10.1038/jcbfm.1988.2.

Gribkoff, V. K. and Kaczmarek, L. K. (2017) 'The need for new approaches in CNS drug discovery:

Why drugs have failed, and what can be done to improve outcomes.', *Neuropharmacology*. NIH Public Access, 120, pp. 11–19. doi: 10.1016/j.neuropharm.2016.03.021.

Grieb, P. *et al.* (1985) 'O2 exchange between blood and brain tissues studied with 18O2 indicator-dilution technique.', *Journal of applied physiology (Bethesda, Md. : 1985)*, 58(6), pp. 1929–41. doi: 10.1152/jappl.1985.58.6.1929.

Gronbeck, K. R. *et al.* (2016) 'Application of Tauroursodeoxycholic Acid for Treatment of Neurological and Non-neurological Diseases: Is There a Potential for Treating Traumatic Brain Injury?', *Neurocritical Care*. Springer US, 25(1), pp. 153–166. doi: 10.1007/s12028-015-0225-7.

Groves, J. D. and Tanner, M. J. A. (1994) 'Role of *N* -glycosylation in the expression of human band 3-mediated anion transport', *Molecular Membrane Biology*, 11(1), pp. 31–38. doi: 10.3109/09687689409161027.

Guan, L. *et al.* (2019) 'ADMET-score - a comprehensive scoring function for evaluation of chemical drug-likeness.', *MedChemComm*. Royal Society of Chemistry, 10(1), pp. 148–157. doi: 10.1039/c8md00472b.

Gupta, D. *et al.* (2018) 'Salts of Therapeutic Agents: Chemical, Physicochemical, and Biological Considerations', *Molecules*, 23(7), p. 1719. doi: 10.3390/molecules23071719.

Hatanaka, T. *et al.* (2000) 'Ion pair skin transport of a zwitterionic drug, cephalexin', *Journal of Controlled Release*, 66(1), pp. 63–71. doi: 10.1016/S0168-3659(99)00259-X.

Hellinger, É. *et al.* (2012) 'Comparison of brain capillary endothelial cell-based and epithelial (MDCK-MDR1, Caco-2, and VB-Caco-2) cell-based surrogate blood–brain barrier penetration models', *European Journal of Pharmaceutics and Biopharmaceutics*. Elsevier, 82(2), pp. 340–351. doi: 10.1016/J.EJPB.2012.07.020.

Herrero-Martínez, J. M. *et al.* (2005) 'Determination of dissociation constants of flavonoids by capillary electrophoresis', *ELECTROPHORESIS*, 26(10), pp. 1886–1895. doi: 10.1002/elps.200410258.

Hervé, F., Ghinea, N. and Scherrmann, J.-M. (2008) 'CNS Delivery Via Adsorptive Transcytosis', *The AAPS Journal*. Springer, 10(3), p. 455. doi: 10.1208/S12248-008-9055-2.

Hollenstein, K., Dawson, R. J. and Locher, K. P. (2007) 'Structure and mechanism of ABC transporter proteins', *Current Opinion in Structural Biology*. Elsevier Current Trends, 17(4), pp. 412–418. doi: 10.1016/J.SBI.2007.07.003.

Hoosain, F. G. *et al.* (2015) 'Bypassing P-Glycoprotein Drug Efflux Mechanisms: Possible Applications in Pharmacoresistant Schizophrenia Therapy', *BioMed Research International*. Hindawi, 2015, pp. 1–21. doi: 10.1155/2015/484963.

Hori, S. *et al.* (2004) 'Functional expression of rat ABCG2 on the luminal side of brain capillaries and its enhancement by astrocyte-derived soluble factor(s)', *Journal of Neurochemistry*, 90(3), pp. 526–536. doi: 10.1111/j.1471-4159.2004.02537.x.

Hoshi, Y. *et al.* (2013) 'Quantitative Atlas of Blood–Brain Barrier Transporters, Receptors, and Tight Junction Proteins in Rats and Common Marmoset', *Journal of Pharmaceutical Sciences*. Elsevier, 102(9), pp. 3343–3355. doi: 10.1002/jps.23575.

Hu, C. *et al.* (2019) 'The solute carrier transporters and the brain: physiological and pharmacological implications', *Asian Journal of Pharmaceutical Sciences*. Elsevier. doi: 10.1016/J.AJPS.2019.09.002.

Huai-Yun, H. *et al.* (1998) 'Expression of Multidrug Resistance-Associated Protein (MRP) in Brain Microvessel Endothelial Cells', *Biochemical and Biophysical Research Communications*, 243(3), pp. 816–820. doi: 10.1006/bbrc.1997.8132.

Hui, M. *et al.* (2016) 'The effect of ion-pair formation combined with penetration enhancers on the skin permeation of loxoprofen.', *Drug delivery*, 23(5), pp. 1550–7. doi: 10.3109/10717544.2014.981768.

Hurtado-Alvarado, G., Cabañas-Morales, A. M. and Gómez-Gónzalez, B. (2013) 'Pericytes: brain-immune interface modulators', *Frontiers in Integrative Neuroscience*. Frontiers Media SA, 7. doi: 10.3389/FNINT.2013.00080.

Hynynen, K. *et al.* (2003) 'Non-invasive opening of BBB by focused ultrasound', in *Brain Edema XII*. Vienna: Springer Vienna, pp. 555–558. doi: 10.1007/978-3-7091-0651-8_113.

ICH Topic Q 2 (R1) Validation of Analytical Procedures (1995).

Jackson, S. *et al.* (2017) 'The effect of regadenoson on the integrity of the human blood–brain barrier, a pilot study', *Journal of Neuro-Oncology*, 132(3), pp. 513–519. doi: 10.1007/s11060-017-2404-1.

Janzer, R. C. and Raff, M. C. (1987) 'Astrocytes induce blood-brain barrier properties in endothelial cells.', *Nature*, 325(6101), pp. 253–7. doi: 10.1038/325253a0.

Ji, J.-J. *et al.* (2013) 'Quercetin: a potential natural drug for adjuvant treatment of rheumatoid arthritis.', *African journal of traditional, complementary, and alternative medicines : AJTCAM*. African Traditional Herbal Medicine Supporters Initiative, 10(3), pp. 418–21. doi: 10.4314/ajtcam.v10i3.5.

Jonker, J. W. *et al.* (1999) 'Role of blood-brain barrier P-glycoprotein in limiting brain accumulation and sedative side-effects of asimadoline, a peripherally acting analgaesic drug.', *British journal of pharmacology*. Wiley-Blackwell, 127(1), pp. 43–50. doi: 10.1038/sj.bjp.0702497.

Jutabha, P. *et al.* (2010) 'Xenopus laevis oocytes expressing human P-glycoprotein: Probing trans- and cis-inhibitory effects on [3H]vinblastine and [3H]digoxin efflux', *Pharmacological Research*, 61(1), pp. 76–84. doi: 10.1016/j.phrs.2009.07.002.

Kalabis, G. M. *et al.* (2005) 'Multidrug Resistance Phosphoglycoprotein (ABCB1) in the Mouse Placenta: Fetal Protection1', *Biology of Reproduction*. Narnia, 73(4), pp. 591–597. doi: 10.1095/biolreprod.105.042242.

Kanai, Y. *et al.* (1998) 'Expression Cloning and Characterization of a Transporter for Large Neutral Amino Acids Activated by the Heavy Chain of 4F2 Antigen (CD98)', *Journal of Biological Chemistry*, 273(37), pp. 23629–23632. doi: 10.1074/jbc.273.37.23629.

Kapuscinski, J. (1995) 'DAPI: a DNA-specific fluorescent probe.', *Biotechnic & histochemistry : official publication of the Biological Stain Commission*, 70(5), pp. 220–33. doi: 10.3109/10520299509108199.

Kasinathan, N. *et al.* (2015) 'Strategies for drug delivery to the central nervous system by systemic route', *Drug Delivery*. Informa Healthcare, 22(3), pp. 243–257. doi: 10.3109/10717544.2013.878858.

Kemper, E. M. *et al.* (2004) 'The influence of the P-glycoprotein inhibitor zosuquidar

trihydrochloride (LY335979) on the brain penetration of paclitaxel in mice', *Cancer Chemotherapy and Pharmacology*, 53(2), pp. 173–178. doi: 10.1007/s00280-003-0720-y.

Kennedy, P. G. (2013) 'Clinical features, diagnosis, and treatment of human African trypanosomiasis (sleeping sickness)', *The Lancet Neurology*. Elsevier, 12(2), pp. 186–194. doi: 10.1016/S1474-4422(12)70296-X.

Kennedy, P. G. E. (2004) 'Human African trypanosomiasis of the CNS: current issues and challenges.', *The Journal of clinical investigation*. American Society for Clinical Investigation, 113(4), pp. 496–504. doi: 10.1172/JCI21052.

Kim, R. B. *et al.* (1998) 'The drug transporter P-glycoprotein limits oral absorption and brain entry of HIV-1 protease inhibitors.', *The Journal of clinical investigation*. American Society for Clinical Investigation, 101(2), pp. 289–94. doi: 10.1172/JCI1269.

Kim, Y. and Chen, J. (2018) 'Molecular structure of human P-glycoprotein in the ATP-bound, outward-facing conformation', *Science*. American Association for the Advancement of Science, 359(6378), pp. 915–919. doi: 10.1126/SCIENCE.AAR7389.

Koepsell, H. (2013) 'The SLC22 family with transporters of organic cations, anions and zwitterions', *Molecular Aspects of Medicine*. Pergamon, 34(2–3), pp. 413–435. doi: 10.1016/J.MAM.2012.10.010.

Kong, W., Engel, K. and Wang, J. (2004) '(Section A: Molecular, Structural, and Cellular Biology of Drug Transporters) Mammalian Nucleoside Transporters', *Current Drug Metabolism*, 5(1), pp. 63–84. doi: 10.2174/1389200043489162.

Koutcher, J. A. and Burt, C. T. (1984) 'Principles of nuclear magnetic resonance.', *Journal of nuclear medicine : official publication, Society of Nuclear Medicine*. Society of Nuclear Medicine, 25(1), pp. 101–11.

Kovac, A., Erickson, M. A. and Banks, W. A. (2011) 'Brain microvascular pericytes are immunoactive in culture: cytokine, chemokine, nitric oxide, and LRP-1 expression in response to lipopolysaccharide.', *Journal of neuroinflammation*. BioMed Central, 8, p. 139. doi: 10.1186/1742-2094-8-139.

Kovacs, Z. I. *et al.* (2017) 'Disrupting the blood-brain barrier by focused ultrasound induces sterile

inflammation.', *Proceedings of the National Academy of Sciences of the United States of America*. National Academy of Sciences, 114(1), pp. E75–E84. doi: 10.1073/pnas.1614777114.

Krohn, M. *et al.* (2018) 'Humanization of the Blood-Brain Barrier Transporter ABCB1 in Mice Disrupts Genomic Locus - Lessons from Three Unsuccessful Approaches.', *European journal of microbiology & immunology*. Akadémiai Kiadó, 8(3), pp. 78–86. doi: 10.1556/1886.2018.00008.

Kubotera, H. *et al.* (2019) 'Astrocytic endfeet re-cover blood vessels after removal by laser ablation', *Scientific Reports*. Nature Publishing Group, 9(1), p. 1263. doi: 10.1038/s41598-018-37419-4.

Kuteykin-Teplyakov, K. *et al.* (2010) 'Differences in the expression of endogenous efflux transporters in MDR1-transfected versus wildtype cell lines affect P-glycoprotein mediated drug transport.', *British journal of pharmacology*. Wiley-Blackwell, 160(6), pp. 1453–63. doi: 10.1111/j.1476-5381.2010.00801.x.

Lagas, J. S. *et al.* (2009) 'Brain Accumulation of Dasatinib Is Restricted by P-Glycoprotein (ABCB1) and Breast Cancer Resistance Protein (ABCG2) and Can Be Enhanced by Elacridar Treatment', *Clinical Cancer Research*, 15(7), pp. 2344–2351. doi: 10.1158/1078-0432.CCR-08-2253.

Lajoie, J. M. and Shusta, E. V. (2015) 'Targeting Receptor-Mediated Transport for Delivery of Biologics Across the Blood-Brain Barrier', *Annual Review of Pharmacology and Toxicology*. Annual Reviews , 55(1), pp. 613–631. doi: 10.1146/annurev-pharmtox-010814-124852.

LeBleu, V. S., Macdonald, B. and Kalluri, R. (2007) 'Structure and function of basement membranes.', *Experimental biology and medicine (Maywood, N.J.)*. SAGE Publications, 232(9), pp. 1121–9. doi: 10.3181/0703-MR-72.

Lee, E. J. D., Lean, C. B. and Limenta, L. M. G. (2009) 'Role of membrane transporters in the safety profile of drugs', *Expert Opinion on Drug Metabolism & Toxicology*. Taylor & Francis, 5(11), pp. 1369–1383. doi: 10.1517/17425250903176421.

Lee, J. H. *et al.* (1988) 'Enhanced Entrapment of Isopropamide Iodide in Liposomes by Ion-Pairing with Sodium Taurodeoxycholate', *Drug Development and Industrial Pharmacy*. Taylor & Francis, 14(4), pp. 451–463. doi: 10.3109/03639048809151876.

Lee, J. Y. *et al.* (2017) 'Overcoming Monocarboxylate Transporter 8 (MCT8)-Deficiency to Promote Human Oligodendrocyte Differentiation and Myelination', *EBioMedicine*. Elsevier, 25, pp. 122–135. doi: 10.1016/J.EBIOM.2017.10.016.

Legros, D. *et al.* (2002) 'Treatment of human African trypanosomiasis--present situation and needs for research and development.', *The Lancet. Infectious diseases*, 2(7), pp. 437–40. doi: 10.1016/s1473-3099(02)00321-3.

Leino, R. L., Gerhart, D. Z. and Drewes, L. R. (1999) 'Monocarboxylate transporter (MCT1) abundance in brains of suckling and adult rats: a quantitative electron microscopic immunogold study.', *Brain research. Developmental brain research*, 113(1–2), pp. 47–54. doi: 10.1016/s0165-3806(98)00188-6.

Levin, V. A. (1980) 'Relationship of octanol/water partition coefficient and molecular weight to rat brain capillary permeability', *Journal of Medicinal Chemistry*, 23(6), pp. 682–684. doi: 10.1021/jm00180a022.

Lin-Moshier, Y. and Marchant, J. S. (2013) 'The Xenopus oocyte: a single-cell model for studying Ca2+ signaling.', *Cold Spring Harbor protocols*. NIH Public Access, 2013(3). doi: 10.1101/pdb.top066308.

Lin, L. *et al.* (2015) 'SLC transporters as therapeutic targets: emerging opportunities', *Nature Publishing Group*, 14. doi: 10.1038/nrd4626.

Lipinski, C. A. *et al.* (2001) 'Experimental and computational approaches to estimate solubility and permeability in drug discovery and development settings', *Advanced Drug Delivery Reviews*. Elsevier, 46(1–3), pp. 3–26. doi: 10.1016/S0169-409X(00)00129-0.

Lips, K. S. *et al.* (2005) 'Polyspecific Cation Transporters Mediate Luminal Release of Acetylcholine from Bronchial Epithelium', *American Journal of Respiratory Cell and Molecular Biology*, 33(1), pp. 79–88. doi: 10.1165/rcmb.2004-0363OC.

Liu, S. *et al.* (2012) 'The Role of Pericytes in Blood-Brain Barrier Function and Stroke', *Current Pharmaceutical Design*, 18(25), pp. 3653–3662. doi: 10.2174/138161212802002706.

Loo, T. W. and Clarke, D. M. (1999) 'Molecular dissection of the human multidrug resistance P-glycoprotein.', *Biochemistry and cell biology = Biochimie et biologie cellulaire*, 77(1), pp. 11–23.

doi: 10.1139/o99-014.

Löscher, W. and Potschka, H. (2005a) 'Blood-brain barrier active efflux transporters: ATP-binding cassette gene family.', *NeuroRx : the journal of the American Society for Experimental NeuroTherapeutics*. Am. Soc. for Experimental NeuroTherapeutics, 2(1), pp. 86–98. doi: 10.1602/neurorx.2.1.86.

Löscher, W. and Potschka, H. (2005b) 'Drug resistance in brain diseases and the role of drug efflux transporters', *Nature Reviews Neuroscience*. Nature Publishing Group, 6(8), pp. 591–602. doi: 10.1038/nrn1728.

Lu, C.-T. *et al.* (2014) 'Current approaches to enhance CNS delivery of drugs across the brain barriers.', *International journal of nanomedicine*. Dove Press, 9, pp. 2241–57. doi: 10.2147/IJN.S61288.

Luissint, A.-C. *et al.* (2012) 'Tight junctions at the blood brain barrier: physiological architecture and disease-associated dysregulation.', *Fluids and barriers of the CNS*. BioMed Central, 9(1), p. 23. doi: 10.1186/2045-8118-9-23.

M.S. Hartz, A. and Bauer, B. (2011) 'ABC Transporters in the CNS – An Inventory', *Current Pharmaceutical Biotechnology*, 12(4), pp. 656–673. doi: 10.2174/138920111795164020.

Mahringer, A. and Fricker, G. (2010) 'BCRP at the Blood−Brain Barrier: Genomic Regulation by 17β-Estradiol', *Molecular Pharmaceutics*. American Chemical Society, 7(5), pp. 1835–1847. doi: 10.1021/mp1001729.

Marchant, J. S. (2018) 'Heterologous Protein Expression in the *Xenopus* Oocyte', *Cold Spring Harbor Protocols*, 2018(4), p. pdb.prot096990. doi: 10.1101/pdb.prot096990.

Markovich, D. (2008a) 'Expression cloning and radiotracer uptakes in Xenopus laevis oocytes', *Nature Protocols*, 3(12), pp. 1975–1980. doi: 10.1038/nprot.2008.151.

Markovich, D. (2008b) 'Expression cloning and radiotracer uptakes in Xenopus laevis oocytes', *Nature Protocols*. Nature Publishing Group, 3(12), pp. 1975–1980. doi: 10.1038/nprot.2008.151.

Mason, B. L., Pariante, C. M. and Thomas, S. A. (2008) 'A revised role for P-glycoprotein in the brain distribution of dexamethasone, cortisol, and corticosterone in wild-type and ABCB1A/B-

deficient mice.', *Endocrinology*. Europe PMC Funders, 149(10), pp. 5244–53. doi: 10.1210/en.2008-0041.

Masserini, M. (2013) 'Nanoparticles for Brain Drug Delivery', *ISRN Biochemistry*. Hindawi, 2013, pp. 1–18. doi: 10.1155/2013/238428.

Mathiisen, T. M. *et al.* (2010) 'The perivascular astroglial sheath provides a complete covering of the brain microvessels: An electron microscopic 3D reconstruction', *Glia*. John Wiley & Sons, Ltd, 58(9), pp. 1094–1103. doi: 10.1002/glia.20990.

Mikitsh, J. L. and Chacko, A.-M. (2014) 'Pathways for small molecule delivery to the central nervous system across the blood-brain barrier.', *Perspectives in medicinal chemistry*. Libertas Academica, 6, pp. 11–24. doi: 10.4137/PMC.S13384.

Miller, D. (2015) 'Regulation of ABC transporters at the blood-brain barrier', *Clinical Pharmacology & Therapeutics*, 97(4), pp. 395–403. doi: 10.1002/cpt.64.

Miller, J. M. *et al.* (2009a) 'Quasi-equilibrium analysis of the ion-pair mediated membrane transport of low-permeability drugs.', *Journal of controlled release : official journal of the Controlled Release Society*, 137(1), pp. 31–7. doi: 10.1016/j.jconrel.2009.02.018.

Miller, J. M. *et al.* (2009b) 'Quasi-equilibrium analysis of the ion-pair mediated membrane transport of low-permeability drugs.', *Journal of controlled release : official journal of the Controlled Release Society*, 137(1), pp. 31–7. doi: 10.1016/j.jconrel.2009.02.018.

Miller, J. M. *et al.* (2010) 'Enabling the intestinal absorption of highly polar antiviral agents: ion-pair facilitated membrane permeation of zanamivir heptyl ester and guanidino oseltamivir.', *Molecular pharmaceutics*. NIH Public Access, 7(4), pp. 1223–34. doi: 10.1021/mp100050d.

Ming, Xin *et al.* (2009) 'Transport of Dicationic Drugs Pentamidine and Furamidine by Human Organic Cation Transporters', *Drug Metabolism and Disposition*, 37(2).

Ming, X. *et al.* (2009) 'Transport of Dicationic Drugs Pentamidine and Furamidine by Human Organic Cation Transporters', *Drug Metabolism and Disposition*, 37(2), pp. 424–430. doi: 10.1124/dmd.108.024083.

Mogi, M. *et al.* (2003) 'Akt signaling regulates side population cell phenotype via Bcrp1

translocation.', *The Journal of biological chemistry*. American Society for Biochemistry and Molecular Biology, 278(40), pp. 39068–75. doi: 10.1074/jbc.M306362200.

Mohammed, A. F. A. *et al.* (2018) 'Promising Use of Cyclodextrin-Based Non-Viral Vectors for Gene and Oligonucleotide Drugs', in *Cyclodextrin - A Versatile Ingredient*. InTech. doi: 10.5772/intechopen.74614.

Montanari, F. and Ecker, G. F. (2015) 'Prediction of drug-ABC-transporter interaction--Recent advances and future challenges.', *Advanced drug delivery reviews*, 86, pp. 17–26. doi: 10.1016/j.addr.2015.03.001.

van Montfoort, J. E. *et al.* (2001) 'Comparison of "Type I" and "Type II" Organic Cation Transport by Organic Cation Transporters and Organic Anion-Transporting Polypeptides', *Journal of Pharmacology and Experimental Therapeutics*, 298(1).

Moriyama, Y. *et al.* (2008) 'Multidrug and toxic compound extrusion (MATE)-type proteins as anchor transporters for the excretion of metabolic waste products and xenobiotics', *Xenobiotica*. Taylor & Francis, 38(7–8), pp. 1107–1118. doi: 10.1080/00498250701883753.

Morris, M. E., Rodriguez-Cruz, V. and Felmlee, M. A. (2017) 'SLC and ABC Transporters: Expression, Localization, and Species Differences at the Blood-Brain and the Blood-Cerebrospinal Fluid Barriers', *The AAPS Journal*. Springer US, 19(5), pp. 1317–1331. doi: 10.1208/s12248-017-0110-8.

Mulenga, C. *et al.* (2001) 'Trypanosoma brucei brucei crosses the blood-brain barrier while tight junction proteins are preserved in a rat chronic disease model', *Neuropathology and Applied Neurobiology*, 27(1), pp. 77–85. doi: 10.1046/j.0305-1846.2001.00306.x.

Nakanishi, T. and Ross, D. D. (2012) 'Breast cancer resistance protein (BCRP/ABCG2): its role in multidrug resistance and regulation of its gene expression.', *Chinese journal of cancer*. BioMed Central, 31(2), pp. 73–99. doi: 10.5732/cjc.011.10320.

Narang, V. S. *et al.* (2008) 'Dexamethasone increases expression and activity of multidrug resistance transporters at the rat blood-brain barrier.', *American journal of physiology. Cell physiology*. American Physiological Society, 295(2), pp. C440-50. doi: 10.1152/ajpcell.00491.2007.

Neubert, R. (1989) ‘Ion Pair Transport Across Membranes’, *Pharmaceutical Research*. Kluwer Academic Publishers-Plenum Publishers, 06(9), pp. 743–747. doi: 10.1023/A:1015963128124.

Neuwelt, E. A. *et al.* (2011) ‘Engaging neuroscience to advance translational research in brain barrier biology.’, *Nature reviews. Neuroscience*. NIH Public Access, 12(3), pp. 169–82. doi: 10.1038/nrn2995.

Ni, Z. *et al.* (2010) ‘Structure and function of the human breast cancer resistance protein (BCRP/ABCG2).’, *Current drug metabolism*. NIH Public Access, 11(7), pp. 603–17. doi: 10.2174/138920010792927325.

Nies, A. T. *et al.* (2004) ‘Expression and immunolocalization of the multidrug resistance proteins, MRP1–MRP6 (ABCC1–ABCC6), in human brain’, *Neuroscience*. Pergamon, 129(2), pp. 349–360. doi: 10.1016/J.NEUROSCIENCE.2004.07.051.

Niewoehner, J. *et al.* (2014) ‘Increased Brain Penetration and Potency of a Therapeutic Antibody Using a Monovalent Molecular Shuttle’, *Neuron*. Cell Press, 81(1), pp. 49–60. doi: 10.1016/J.NEURON.2013.10.061.

Nigam, S. K. *et al.* (2015) ‘The Organic Anion Transporter (OAT) Family: A Systems Biology Perspective’, *Physiological Reviews*. American Physiological Society Bethesda, MD, 95(1), pp. 83–123. doi: 10.1152/physrev.00025.2013.

Nikolskaia, O. V. *et al.* (2006) ‘Blood-brain barrier traversal by African trypanosomes requires calcium signaling induced by parasite cysteine protease’, *Journal of Clinical Investigation*. American Society for Clinical Investigation, 116(10), p. 2739. doi: 10.1172/JCI27798.

Nikolskaia, O. V. *et al.* (2008) ‘Blood-brain barrier traversal by African trypanosomes requires calcium signaling induced by parasite cysteine protease’, *Journal of Clinical Investigation*, 118(5), pp. 1974–1974. doi: 10.1172/JCI27798C1.

Nitta, T. *et al.* (2003) ‘Size-selective loosening of the blood-brain barrier in claudin-5–deficient mice’, *The Journal of Cell Biology*, 161(3), pp. 653–660. doi: 10.1083/jcb.200302070.

Ohtsuki, S. and Terasaki, T. (2007) ‘Contribution of Carrier-Mediated Transport Systems to the Blood–Brain Barrier as a Supporting and Protecting Interface for the Brain; Importance for CNS Drug Discovery and Development’, *Pharmaceutical Research*. Springer US, 24(9), pp. 1745–

1758. doi: 10.1007/s11095-007-9374-5.

Oksanen, M. *et al.* (2019) ‘Astrocyte alterations in neurodegenerative pathologies and their modeling in human induced pluripotent stem cell platforms’, *Cellular and Molecular Life Sciences*. Springer International Publishing, 76(14), pp. 2739–2760. doi: 10.1007/s00018-019-03111-7.

Oldendorf, W. H. *et al.* (1972) ‘Blood-Brain Barrier: Penetration of Morphine, Codeine, Heroin, and Methadone after Carotid Injection’, *Science*, 178(4064), pp. 984–986. doi: 10.1126/science.178.4064.984.

Oldendorf, W. H., Cornford, M. E. and Brown, W. J. (1977) ‘The large apparent work capability of the blood-brain barrier: a study of the mitochondrial content of capillary endothelial cells in brain and other tissues of the rat.’, *Annals of neurology*, 1(5), pp. 409–17. doi: 10.1002/ana.410010502.

Oldendorf, W. and Szabo, J. (1976) ‘Amino acid assignment to one of three blood-brain barrier amino acid carriers’, *American Journal of Physiology-Legacy Content*. American Physiological Society, 230(1), pp. 94–98. doi: 10.1152/ajplegacy.1976.230.1.94.

Omura, Y. *et al.* (2011) ‘Caprylic Acid in The Effective Treatment of Intractable Medical Problems of Frequent Urination, Incontinence, Chronic Upper Respiratory Infection, Root Canalled Tooth Infection, ALS, etc., Caused By Asbestos & Mixed Infections of *Candida albicans, Helicobacter pylori & Cytomegalovirus* With or Without Other Microorganisms & Mercury’, *Acupuncture & Electro-Therapeutics Research*, 36(1), pp. 19–64. doi: 10.3727/036012911803860886.

Paine, M. F. *et al.* (2010) ‘Diamidines for human African trypanosomiasis.’, *Current opinion in investigational drugs (London, England : 2000)*, 11(8), pp. 876–83.

Pajouhesh, H. and Lenz, G. R. (2005) ‘Medicinal chemical properties of successful central nervous system drugs.’, *NeuroRx : the journal of the American Society for Experimental NeuroTherapeutics*. Am. Soc. for Experimental NeuroTherapeutics, 2(4), pp. 541–53. doi: 10.1602/neurorx.2.4.541.

Pangeni, R. *et al.* (2018) ‘Preparation, Characterization, and In Vivo Evaluation of an Oral Multiple Nanoemulsive System for Co-Delivery of Pemetrexed and Quercetin.’, *Pharmaceutics*. Multidisciplinary Digital Publishing Institute (MDPI), 10(3). doi: 10.3390/pharmaceutics10030158.

Pardridge, W. M. (2005) ‘The blood-brain barrier: bottleneck in brain drug development.’, *NeuroRx : the journal of the American Society for Experimental NeuroTherapeutics*. Am. Soc. for Experimental NeuroTherapeutics, 2(1), pp. 3–14. doi: 10.1602/neurorx.2.1.3.

Pardridge, W. M. (2012) ‘Drug Transport across the Blood–Brain Barrier’, *Journal of Cerebral Blood Flow & Metabolism*, 32(11), pp. 1959–1972. doi: 10.1038/jcbfm.2012.126.

Pardridge, W. M., Kumagai, A. K. and Eisenberg, J. B. (1987) ‘Chimeric peptides as a vehicle for peptide pharmaceutical delivery through the blood-brain barrier’, *Biochemical and Biophysical Research Communications*. Academic Press, 146(1), pp. 307–313. doi: 10.1016/0006-291X(87)90726-1.

Patel, A. *et al.* (2016) ‘Using Salt Counterions to Modify β2-Agonist Behavior in Vivo’, *Molecular Pharmaceutics*. American Chemical Society, 13(10), pp. 3439–3448. doi: 10.1021/acs.molpharmaceut.6b00448.

Patel, M. M. and Patel, B. M. (2017) ‘Crossing the Blood–Brain Barrier: Recent Advances in Drug Delivery to the Brain’, *CNS Drugs*, 31(2), pp. 109–133. doi: 10.1007/s40263-016-0405-9.

Pelfrene, E. *et al.* (2019) ‘The European Medicines Agency’s scientific opinion on oral fexinidazole for human African trypanosomiasis.’, *PLoS neglected tropical diseases*. Public Library of Science, 13(6), p. e0007381. doi: 10.1371/journal.pntd.0007381.

Pérez-Martínez, F. C., Carrión, B. and Ceña, V. (2012) ‘The Use of Nanoparticles for Gene Therapy in the Nervous System’, *Journal of Alzheimer’s Disease*, 31(4), pp. 697–710. doi: 10.3233/JAD-2012-120661.

Persidsky, Y. *et al.* (2006) ‘Blood–brain Barrier: Structural Components and Function Under Physiologic and Pathologic Conditions’, *Journal of Neuroimmune Pharmacology*. Springer US, 1(3), pp. 223–236. doi: 10.1007/s11481-006-9025-3.

Pieters, L. A. C. and Vlietinck, A. J. (1989) ‘Applications of quantitative 1H- and 13C-NMR spectroscopy in drug analysis’, *Journal of Pharmaceutical and Biomedical Analysis*, 7(12), pp. 1405–1417. doi: 10.1016/0731-7085(89)80145-1.

Pike, S. *et al.* (2019) ‘Using *Xenopus laevis* Oocytes to Functionally Characterize Plant Transporters’, *Current Protocols in Plant Biology*. John Wiley & Sons, Ltd, 4(1), p. e20087. doi:

10.1002/cppb.20087.

Poller, B. *et al.* (2008) 'The human brain endothelial cell line hCMEC/D3 as a human blood-brain barrier model for drug transport studies', *Journal of Neurochemistry*. Blackwell Publishing Ltd, 107(5), pp. 1358–1368. doi: 10.1111/j.1471-4159.2008.05730.x.

Prados, M. D. *et al.* (2003) 'A randomized, double-blind, placebo-controlled, phase 2 study of RMP-7 in combination with carboplatin administered intravenously for the treatment of recurrent malignant glioma', *Neuro-Oncology*, 5(2), pp. 96–103. doi: 10.1093/neuonc/5.2.96.

Priotto, G. *et al.* (2008) 'Safety and effectiveness of first line eflornithine for *Trypanosoma brucei gambiense* sleeping sickness in Sudan: cohort study', *BMJ*, 336(7646), pp. 705–708. doi: 10.1136/bmj.39485.592674.BE.

Pulgar, V. M. (2019) 'Transcytosis to Cross the Blood Brain Barrier, New Advancements and Challenges', *Frontiers in Neuroscience*. Frontiers, 12, p. 1019. doi: 10.3389/fnins.2018.01019.

Qosa, H. *et al.* (2015) 'Regulation of ABC efflux transporters at blood-brain barrier in health and neurological disorders.', *Brain research*. NIH Public Access, 1628(Pt B), pp. 298–316. doi: 10.1016/j.brainres.2015.07.005.

Quan, Y. *et al.* (2012) 'Expression Profile of Drug and Nutrient Absorption Related Genes in Madin-Darby Canine Kidney (MDCK) Cells Grown under Differentiation Conditions.', *Pharmaceutics*. Multidisciplinary Digital Publishing Institute (MDPI), 4(2), pp. 314–33. doi: 10.3390/pharmaceutics4020314.

Radwanska, M. *et al.* (2002) 'The serum resistance-associated gene as a diagnostic tool for the detection of Trypanosoma brucei rhodesiense.', *The American Journal of Tropical Medicine and Hygiene*, 67(6), pp. 684–690. doi: 10.4269/ajtmh.2002.67.684.

Ramakrishnan, P. (2003) 'The Role of P-glycoprotein in the Blood-Brain Barrier'.

Rapoport, S., Hori, M. and Klatzo, I. (1972) 'Testing of a hypothesis for osmotic opening of the blood-brain barrier', *American Journal of Physiology-Legacy Content*. American Physiological Society, 223(2), pp. 323–331. doi: 10.1152/ajplegacy.1972.223.2.323.

Rapoport, S. I. (2000) 'Osmotic Opening of the Blood–Brain Barrier: Principles, Mechanism, and

Therapeutic Applications', *Cellular and Molecular Neurobiology*. Kluwer Academic Publishers-Plenum Publishers, 20(2), pp. 217–230. doi: 10.1023/A:1007049806660.

Rautio, J., Laine, K., *et al.* (2008) 'Prodrug approaches for CNS delivery.', *The AAPS journal*. Springer, 10(1), pp. 92–102. doi: 10.1208/s12248-008-9009-8.

Rautio, J., Kumpulainen, H., *et al.* (2008) 'Prodrugs: design and clinical applications', *Nature Reviews Drug Discovery*, 7(3), pp. 255–270. doi: 10.1038/nrd2468.

Redzic, Z. B. *et al.* (2005) 'Polarized distribution of nucleoside transporters in rat brain endothelial and choroid plexus epithelial cells', *Journal of Neurochemistry*, 94(5), pp. 1420–1426. doi: 10.1111/j.1471-4159.2005.03312.x.

Régina, A. *et al.* (1999) 'Dexamethasone regulation of P-glycoprotein activity in an immortalized rat brain endothelial cell line, GPNT.', *Journal of neurochemistry*, 73(5), pp. 1954–63.

Ribeiro, M. M. B. *et al.* (2012) 'Translocating the blood-brain barrier using electrostatics', *Frontiers in Cellular Neuroscience*. Frontiers, 6, p. 44. doi: 10.3389/fncel.2012.00044.

Ristroph, K. D. and Prud'homme, R. K. (2019) 'Hydrophobic ion pairing: encapsulating small molecules, peptides, and proteins into nanocarriers', *Nanoscale Advances*. Royal Society of Chemistry, 1(11), pp. 4207–4237. doi: 10.1039/C9NA00308H.

Sanchez-Covarrubias, L. *et al.* (2014) 'Transporters at CNS barrier sites: obstacles or opportunities for drug delivery?', *Current pharmaceutical design*. NIH Public Access, 20(10), pp. 1422–49. Available at: http://www.ncbi.nlm.nih.gov/pubmed/23789948 (Accessed: 28 February 2017).

Sanderson, L. *et al.* (2008) 'The blood–brain barrier significantly limits eflornithine entry into Trypanosoma brucei brucei infected mouse brain1', *Journal of Neurochemistry*. Wiley-Blackwell, 107(4), p. 1136. doi: 10.1111/J.1471-4159.2008.05706.X.

Sanderson, Lisa *et al.* (2009) 'Pentamidine movement across the murine blood-brain and blood-cerebrospinal fluid barriers: effect of trypanosome infection, combination therapy, P-glycoprotein, and multidrug resistance-associated protein.', *The Journal of pharmacology and experimental therapeutics*. American Society for Pharmacology and Experimental Therapeutics, 329(3), pp. 967–77. doi: 10.1124/jpet.108.149872.

Sanderson, L. *et al.* (2009) ‘Pentamidine Movement across the Murine Blood-Brain and Blood-Cerebrospinal Fluid Barriers: Effect of Trypanosome Infection, Combination Therapy, P-Glycoprotein, and Multidrug Resistance-Associated Protein’, *Journal of Pharmacology and Experimental Therapeutics*, 329(3), pp. 967–977. doi: 10.1124/jpet.108.149872.

Sanderson, L. *et al.* (2019) ‘Drug reformulation for a neglected disease. The NANOHAT project to develop a safer more effective sleeping sickness drug’, *bioRxiv*. Cold Spring Harbor Laboratory, p. 573329. doi: 10.1101/573329.

Sanderson, L., Khan, A. and Thomas, S. (2007) ‘Distribution of suramin, an antitrypanosomal drug, across the blood-brain and blood-cerebrospinal fluid interfaces in wild-type and P-glycoprotein transporter-deficient mice.’, *Antimicrobial agents and chemotherapy*. American Society for Microbiology Journals, 51(9), pp. 3136–46. doi: 10.1128/AAC.00372-07.

Saraiva, C. *et al.* (2016) ‘Nanoparticle-mediated brain drug delivery: Overcoming blood–brain barrier to treat neurodegenerative diseases’, *Journal of Controlled Release*. Elsevier, 235, pp. 34–47. doi: 10.1016/J.JCONREL.2016.05.044.

Schinkel, A. H. and Jonker, J. W. (2003) ‘Mammalian drug efflux transporters of the ATP binding cassette (ABC) family: an overview’, *Advanced Drug Delivery Reviews*. Elsevier, 55(1), pp. 3–29. doi: 10.1016/S0169-409X(02)00169-2.

Segawa, H. *et al.* (1999) ‘Identification and Functional Characterization of a Na^+-independent Neutral Amino Acid Transporter with Broad Substrate Selectivity’, *Journal of Biological Chemistry*, 274(28), pp. 19745–19751. doi: 10.1074/jbc.274.28.19745.

Sekhar, G. N. *et al.* (2017) ‘Organic cation transporter 1 (OCT1) is involved in pentamidine transport at the human and mouse blood-brain barrier (BBB)’, *PLOS ONE*. Edited by H. W. van Veen. Public Library of Science, 12(3), p. e0173474. doi: 10.1371/journal.pone.0173474.

Sekhar, G. N. *et al.* (2019) ‘Region-specific blood-brain barrier transporter changes leads to increased sensitivity to amisulpride in Alzheimer’s disease’, *bioRxiv*. Cold Spring Harbor Laboratory, p. 582387. doi: 10.1101/582387.

Sercombe, L. *et al.* (2015) ‘Advances and Challenges of Liposome Assisted Drug Delivery.’, *Frontiers in pharmacology*. Frontiers Media SA, 6, p. 286. doi: 10.3389/fphar.2015.00286.

Sharom, F. J. (2014) ‘Complex Interplay between the P-Glycoprotein Multidrug Efflux Pump and the Membrane: Its Role in Modulating Protein Function.’, *Frontiers in oncology*. Frontiers Media SA, 4, p. 41. doi: 10.3389/fonc.2014.00041.

Shental-Bechor, D. and Levy, Y. (2008) ‘Effect of glycosylation on protein folding: a close look at thermodynamic stabilization.’, *Proceedings of the National Academy of Sciences of the United States of America*. National Academy of Sciences, 105(24), pp. 8256–61. doi: 10.1073/pnas.0801340105.

Shim, C.-K. (1986) ‘Effect of ion-pair complexation with bile acids on the biliary excretion and systemic distribution of organic cationic drugs’, *Archives of Pharmacal Research*. Pharmaceutical Society of Korea, 9(1), pp. 49–54. doi: 10.1007/BF02857707.

Smith, P. K. *et al.* (1985) ‘Measurement of protein using bicinchoninic acid’, *Analytical Biochemistry*, 150(1), pp. 76–85. doi: 10.1016/0003-2697(85)90442-7.

Song, T. *et al.* (2016) ‘Regulating the Skin Permeation Rate of Escitalopram by Ion-pair Formation with Organic Acids.’, *AAPS PharmSciTech*. doi: 10.1208/s12249-015-0474-y.

Spiro, R. G. (2002) ‘Protein glycosylation: nature, distribution, enzymatic formation, and disease implications of glycopeptide bonds’, *Glycobiology*. Oxford Academic, 12(4), pp. 43R-56R. doi: 10.1093/glycob/12.4.43R.

Stamatovic, S. M. *et al.* (2016) ‘Junctional proteins of the blood-brain barrier: New insights into function and dysfunction.’, *Tissue barriers*. Taylor & Francis, 4(1), p. e1154641. doi: 10.1080/21688370.2016.1154641.

Stamatovic, S. M., Keep, R. F. and Andjelkovic, A. V (2008) ‘Brain endothelial cell-cell junctions: how to "open" the blood brain barrier.’, *Current neuropharmacology*. Bentham Science Publishers, 6(3), pp. 179–92. doi: 10.2174/157015908785777210.

Stich, A., Abel, P. M. and Krishna, S. (2002) ‘Human African trypanosomiasis.’, *BMJ (Clinical research ed.)*. BMJ Publishing Group, 325(7357), pp. 203–6. Available at: http://www.ncbi.nlm.nih.gov/pubmed/12142311 (Accessed: 12 October 2017).

Su, W. and Pasternak, G. W. (2013) ‘The role of multidrug resistance-associated protein in the blood-brain barrier and opioid analgesia.’, *Synapse (New York, N.Y.)*. NIH Public Access, 67(9),

pp. 609–19. doi: 10.1002/syn.21667.

Sumpio, B. E., Timothy Riley, J. and Dardik, A. (2002) ‘Cells in focus: endothelial cell’, *The International Journal of Biochemistry & Cell Biology*, 34(12), pp. 1508–1512. doi: 10.1016/S1357-2725(02)00075-4.

Sun, H. *et al.* (2003) ‘Drug efflux transporters in the CNS’, *Advanced Drug Delivery Reviews*. Elsevier, 55(1), pp. 83–105. doi: 10.1016/S0169-409X(02)00172-2.

Suresh, P. and Paul, S. (2011a) ‘Ion-paired Drug Delivery: An Avenue for Bioavailability Improvement’, *Sierra Leone Journal of Biomedical Research*. College of Medicine and Allied Health Sciences, University of Sierra Leone, 3(2), pp. 70–76. doi: 10.4314/sljbr.v3i2.71806.

Suresh, P. and Paul, S. (2011b) ‘Ion-paired Drug Delivery: An Avenue for Bioavailability Improvement’, *Sierra Leone Journal of Biomedical Research*. College of Medicine and Allied Health Sciences, University of Sierra Leone, 3(2), pp. 70–76. doi: 10.4314/sljbr.v3i2.71806.

Sweeney, M. D. *et al.* (2019) ‘Blood-Brain Barrier: From Physiology to Disease and Back’, *Physiological Reviews*. American Physiological Society Bethesda, MD , 99(1), pp. 21–78. doi: 10.1152/physrev.00050.2017.

Tan, Z. *et al.* (2009) ‘The enhancing effect of ion-pairing on the skin permeation of glipizide.’, *AAPS PharmSciTech*. Springer, 10(3), pp. 967–76. doi: 10.1208/s12249-009-9283-5.

Tang, F., Horie, K. and Borchardt, R. T. (2002) ‘Are MDCK Cells Transfected with the Human MDR1 Gene a Good Model of the Human Intestinal Mucosa?’, *Pharmaceutical Research*. Kluwer Academic Publishers-Plenum Publishers, 19(6), pp. 765–772. doi: 10.1023/A:1016140429238.

Tao-Cheng, J. H., Nagy, Z. and Brightman, M. W. (1987) ‘Tight junctions of brain endothelium in vitro are enhanced by astroglia.’, *The Journal of neuroscience : the official journal of the Society for Neuroscience*. Society for Neuroscience, 7(10), pp. 3293–9. doi: 10.1523/JNEUROSCI.07-10-03293.1987.

Tarral, A. *et al.* (2014) ‘Determination of an optimal dosing regimen for fexinidazole, a novel oral drug for the treatment of human African trypanosomiasis: First-in-human studies’, *Clinical Pharmacokinetics*, 53(6), pp. 565–580. doi: 10.1007/s40262-014-0136-3.

Thomas, H. and Coley, H. M. (2003) ‘Overcoming Multidrug Resistance in Cancer: An Update on the Clinical Strategy of Inhibiting P-Glycoprotein’, *Cancer Control*, 10(2), pp. 159–165. doi: 10.1177/107327480301000207.

Thomas, J. A. *et al.* (2018) ‘Insights into antitrypanosomal drug mode-of-action from cytology-based profiling.’, *PLoS neglected tropical diseases*. Public Library of Science, 12(11), p. e0006980. doi: 10.1371/journal.pntd.0006980.

Thompson, S. N. (1990) ‘NMR spectroscopy: Its basis, biological application and use in studies of insect metabolism’, *Insect Biochemistry*. Pergamon, 20(3), pp. 223–237. doi: 10.1016/0020-1790(90)90039-W.

Thomsen, M. S., Routhe, L. J. and Moos, T. (2017) ‘The vascular basement membrane in the healthy and pathological brain.’, *Journal of cerebral blood flow and metabolism : official journal of the International Society of Cerebral Blood Flow and Metabolism*. SAGE Publications, 37(10), pp. 3300–3317. doi: 10.1177/0271678X17722436.

Ticehurst, M. D. and Marziano, I. (2015) ‘Integration of active pharmaceutical ingredient solid form selection and particle engineering into drug product design’, *Journal of Pharmacy and Pharmacology*. John Wiley & Sons, Ltd (10.1111), 67(6), pp. 782–802. doi: 10.1111/jphp.12375.

Tiwari, G., Tiwari, R. and Rai, A. K. (2010) ‘Cyclodextrins in delivery systems: Applications.’, *Journal of pharmacy & bioallied sciences*. Wolters Kluwer -- Medknow Publications, 2(2), pp. 72–9. doi: 10.4103/0975-7406.67003.

Tsuji, A. and Tamai, I. (1997) ‘Blood-brain barrier function of P-glycoprotein’, *Advanced Drug Delivery Reviews*, 25(2–3), pp. 287–298. doi: 10.1016/S0169-409X(97)00504-8.

Vijay, N. and Morris, M. E. (2014) ‘Role of Monocarboxylate Transporters in Drug Delivery to the Brain’, *Current pharmaceutical design*. NIH Public Access, 20(10), p. 1487. Available at: https://www.ncbi.nlm.nih.gov/pmc/articles/PMC4084603/ (Accessed: 1 December 2019).

Walpole, S. C. *et al.* (2012) ‘The weight of nations: An estimation of adult human biomass’, *BMC Public Health*. BioMed Central, 12(1), p. 439. doi: 10.1186/1471-2458-12-439.

Wang, D. Q.-H. and Carey, M. C. (2014) ‘Therapeutic uses of animal biles in traditional Chinese medicine: An ethnopharmacological, biophysical chemical and medicinal review’, *World Journal*

of Gastroenterology, 20(29), p. 9952. doi: 10.3748/wjg.v20.i29.9952.

Wang, G. and Tomasella, F. P. (2016) 'Ion-pairing HPLC methods to determine EDTA and DTPA in small molecule and biological pharmaceutical formulations $'. doi: 10.1016/j.jpha.2016.01.002.

Wang, J. (2016) 'The plasma membrane monoamine transporter (PMAT): Structure, function, and role in organic cation disposition.', *Clinical pharmacology and therapeutics*. NIH Public Access, 100(5), pp. 489–499. doi: 10.1002/cpt.442.

Wang, Q. *et al.* (2005) 'Evaluation of the MDR-MDCK cell line as a permeability screen for the blood–brain barrier', *International Journal of Pharmaceutics*. Elsevier, 288(2), pp. 349–359. doi: 10.1016/J.IJPHARM.2004.10.007.

Wang, Z. *et al.* (2013) 'Influence of overexpression of efflux proteins on the function and gene expression of endogenous peptide transporters in MDR-transfected MDCKII cell lines.', *International journal of pharmaceutics*. NIH Public Access, 441(1–2), pp. 40–9. doi: 10.1016/j.ijpharm.2012.12.011.

Waring, M. J. (2010) 'Lipophilicity in drug discovery', *Expert Opinion on Drug Discovery*, 5(3), pp. 235–248. doi: 10.1517/17460441003605098.

Warren, K. E. (2018) 'Beyond the Blood:Brain Barrier: The Importance of Central Nervous System (CNS) Pharmacokinetics for the Treatment of CNS Tumors, Including Diffuse Intrinsic Pontine Glioma', *Frontiers in Oncology*. Frontiers, 8, p. 239. doi: 10.3389/fonc.2018.00239.

Watson, C. P. *et al.* (2012) 'The transport of nifurtimox, an anti-trypanosomal drug, in an in vitro model of the human blood-brain barrier: evidence for involvement of breast cancer resistance protein.', *Brain research*, 1436, pp. 111–21. doi: 10.1016/j.brainres.2011.11.053.

Wegener, G. and Rujescu, D. (2013) 'The current development of CNS drug research', *International Journal of Neuropsychopharmacology*. Narnia, 16(7), pp. 1687–1693. doi: 10.1017/S1461145713000345.

Weiss, N. *et al.* (2009) 'The blood-brain barrier in brain homeostasis and neurological diseases', *Biochimica et Biophysica Acta (BBA) - Biomembranes*, 1788(4), pp. 842–857. doi: 10.1016/j.bbamem.2008.10.022.

Wenzler, T. *et al.* (2009) ‘New treatment option for second-stage African sleeping sickness: in vitro and in vivo efficacy of aza analogs of DB289.’, *Antimicrobial agents and chemotherapy*. American Society for Microbiology Journals, 53(10), pp. 4185–92. doi: 10.1128/AAC.00225-09.

‘WHO | WHO interim guidelines for the treatment of gambiense human African trypanosomiasis’ (2019) *WHO*. World Health Organization. Available at: https://www.who.int/trypanosomiasis_african/resources/9789241550567/en/ (Accessed: 28 November 2019).

Wolf, D. C. and Horwitz, S. B. (1992a) ‘P-glycoprotein transports corticosterone and is photoaffinity-labeled by the steroid’, *International Journal of Cancer*, 52(1), pp. 141–146. doi: 10.1002/ijc.2910520125.

Wolf, D. C. and Horwitz, S. B. (1992b) ‘P-glycoprotein transports corticosterone and is photoaffinity-labeled by the steroid’, *International Journal of Cancer*, 52(1), pp. 141–146. doi: 10.1002/ijc.2910520125.

Yang, S. *et al.* (2014) ‘Pharmacokinetic comparison to determine the mechanisms underlying the differential efficacies of cationic diamidines against first- and second-stage human African trypanosomiasis.’, *Antimicrobial agents and chemotherapy*. American Society for Microbiology (ASM), 58(7), pp. 4064–74. doi: 10.1128/AAC.02605-14.

Yenari, M. A. *et al.* (2006) ‘Microglia potentiate damage to blood-brain barrier constituents: improvement by minocycline in vivo and in vitro.’, *Stroke*, 37(4), pp. 1087–93. doi: 10.1161/01.STR.0000206281.77178.ac.

ZHANG, W. *et al.* (2003) ‘The expression and functional characterization of ABCG2 in brain endothelial cells and vessels’, *The FASEB Journal*, 17(14), pp. 2085–2087. doi: 10.1096/fj.02-1131fje.

Zlokovic, B. V. (2009) ‘Blood–Brain Barrier and Neurovascular Mechanisms of Neurodegeneration and Injury’, *Encyclopedia of Neuroscience*. Academic Press, pp. 265–271. doi: 10.1016/B978-008045046-9.00491-5.

Appendix A. **Poster for Pharmacology 2016.**

Transporter interaction of warfarin, a traditional oral vitamin K antagonist with the mouse blood-brain barrier *in vitro*: evidence for BCRP involvement.

H. Wang1, P. Muresan1, G. Sekhar1, R. Brown1, J. P. Patel1,2, R. Arya2, S. A. Jones1, S. A. Thomas1
1Institute of Pharmaceutical Science, Faculty of Life Sciences and Medicine, King's College London, London, UNITED KINGDOM, 2King's Thrombosis Centre, Department of Haematological Medicine, King's College Hospital NHS Foundation Trust, London, UNITED KINGDOM.

Introduction

Warfarin is a vitamin K antagonist that has been traditionally used for prophylaxis and treatment of thrombosis. An adverse event associated with warfarin treatment is intracranial haemorrhage. To explore the interaction of warfarin with the brain vasculature we investigated the ability of warfarin to interact with transporters expressed at the blood-brain barrier (BBB) by means of a commercially available immortalized adult mouse brain cell line, b.End3 cells.

Methods

The accumulation of [^{3}H]warfarin into bEnd.3 cells was investigated at five different time points: 5 min, 20 min, 30 min, 60 min and 120 min. Different transporter inhibitors/ substrates were added to the accumulation buffer and the results compared to [^{3}H]warfarin alone (control). Raw data were corrected for protein content and extracellular space ([^{14}C]sucrose). Results were expressed as the mean (Vd, µl/mg of protein)±SEM, n =4-6 plates, with 6 replicates per plate, passage number 16-29. Comparisons were made between control and test plates of cells at each time point by one-way ANOVA. Differences at p <0.05 were considered significant.

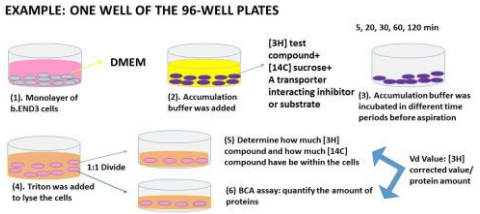

Fig 1. Experimental procedures

Results

The accumulation of [^{3}H]warfarin (34 nM) was significantly decreased by the presence of unlabelled warfarin (Figure 2). However, there was no effect on [^{3}H]warfarin accumulation in the presence of P-glycoprotein (P-gp; ABCB1) inhibitors and substrates (Figure 2). There was a significant increase with breast cancer resistance-associated protein (BCRP; ABCG2) inhibitors (Figure 3) although no significant change has been observed in the presence of multidrug resistance-associated proteins (MRPs; ABCC group) inhibitor (data not shown). The significant increase in the presence of ATP depletion method indicated the consistency of ABC transporters involvements in the transport of warfarin (Figure 4). Incubation with organic anion transporting peptides (OATP; SLC21A) substrate significantly increased the accumulation of warfarin (Figure 5).

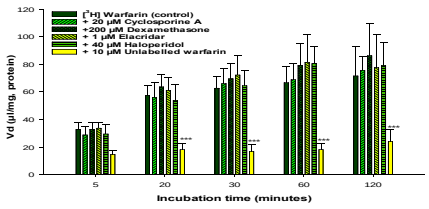

Fig 2. Accumulation of [^{3}H]warfarin in the absence and presence of P-gp inhibitors/substrates and self-inhibition (*p< 0.05,**p<0.01,***p<0.001). All [^{3}H]warfarin data are corrected for protein content and expressed as means±SEM, n=6 plates with 6 replicates per plate.

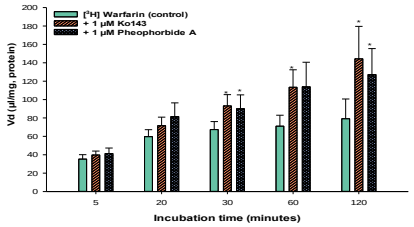

Fig 3. Accumulation of [^{3}H]warfarin in the absence and presence of BCRP inhibitors/substrates and self-inhibition (*p< 0.05,**p<0.01,***p<0.001). All [^{3}H]warfarin data are corrected for protein content and expressed as means±SEM, n=6 plates with 6 replicates per plate.

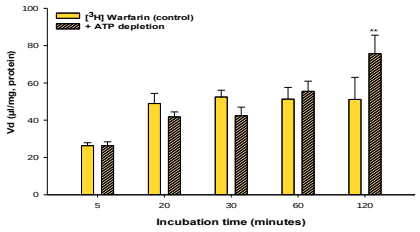

Fig 4. Accumulation of [^{3}H]warfarin in the absence and presence of ATP depletion (*p< 0.05,**p<0.01,***p<0.001). All [^{3}H]warfarin data are corrected for protein content and expressed as means±SEM, n=4 plates with 6 replicates per plate.

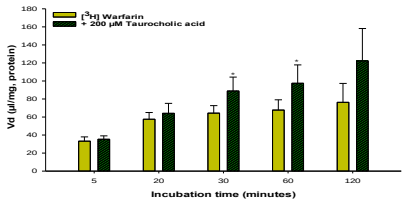

Fig 5. Accumulation of [^{3}H]warfarin in the absence and presence of OATP substrate (*p< 0.05,**p<0.01,***p<0.001). All [^{3}H]warfarin data are corrected for protein content and expressed as means±SEM, n=4 plates with 6 replicates per plate.

Discussions and Conclusions

Taken together these results suggest that warfarin is a substrate for BCRP and OATP and that an influx transporter is involved (identity unknown). Amongst the group of ABC transporters, P-gp and/or BCRP are thought to be the dominant players and are expressed on the luminal (blood-facing) membrane of the BBB, whereas the OATPs of the SLC transporters are localized on both the luminal and abluminal (brain-facing) sides of the BBB. Furthermore, the effects on BCRP and OATP were not significant until later time points which suggested a time dependent effect. It may be that the effect was occurring at an intracellular membrane of an organelle.

References

1. Shaik AN *et al.* (2016). *Journal of Pharmaceutical Sciences* 105: 1976-1986.
2. Wessler JD *et al.* (2013). *Journal of the American College of Cardiology* 61: 2495-2502.

Appendix B. **Uptake of [^{3}H]pentamidine with quercetin by hOCT1 in oocytes**

No significant difference in the uptake of [^{3}H]pentamidine was found between water-injected or oocytes expressing hOCT1 with quercetin. The transport of [^{3}H]pentamidine via hOCT1 was reduced when 160µM of quercetin was present although this did not attain statistical significance. The increase in the uptake of [^{14}C]sucrose in water-injected oocytes in the presence of 160µM of quercetin suggested that this counterion caused membrane damage which resulted in loss of membrane integrity .

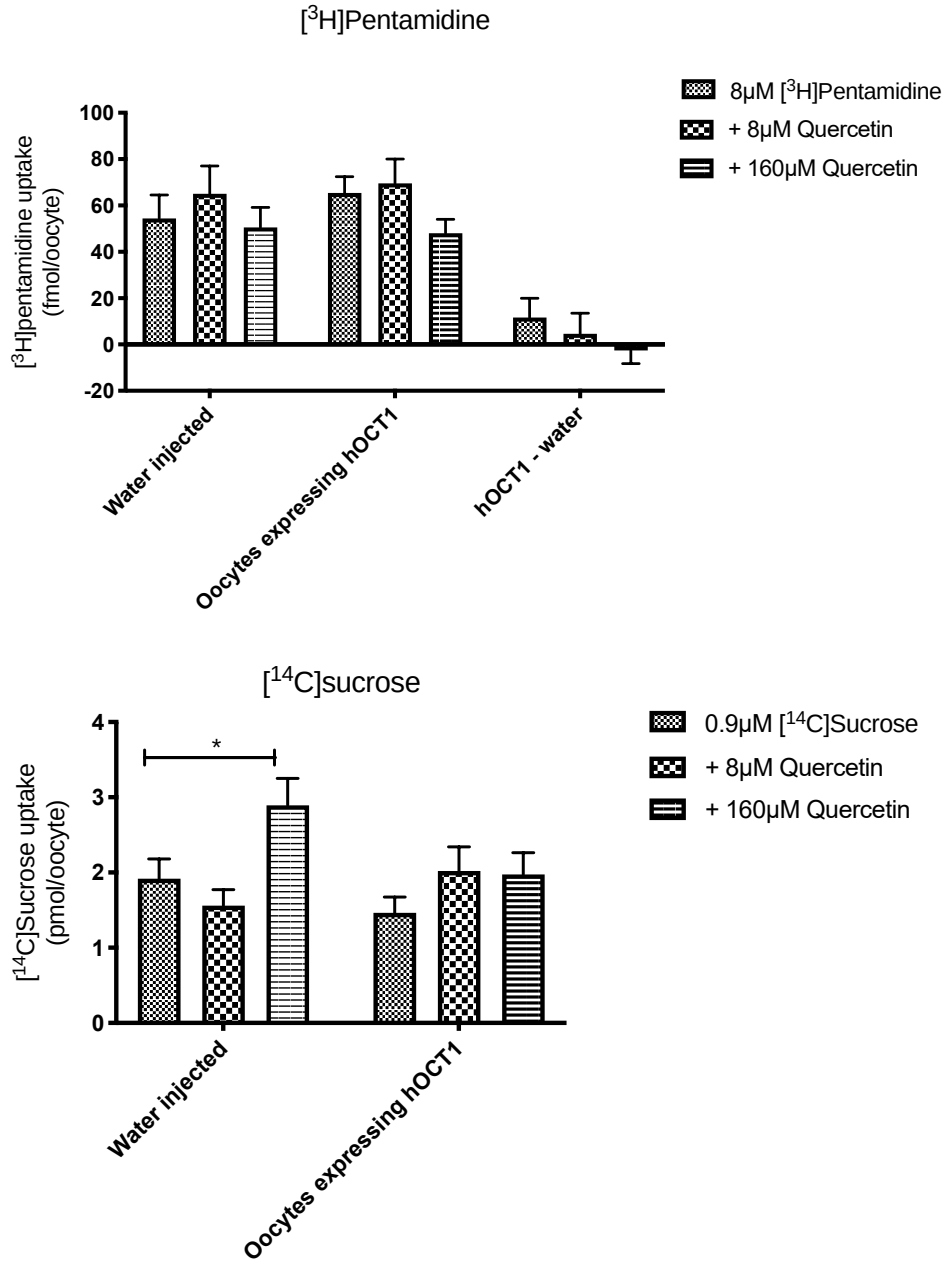

Figure A1. The uptake of [^{3}H]pentamidine and [^{14}C]sucrose by hOCT1 transporter. The concentration of pentamidine was 8µM (31nM [^{3}H]pentamidine and 8µM unlabelled pentamidine) and the concentration of quercetin was 8µM or 160µM. Data were expressed as mean ± SEM, n=24-26 oocytes from 3 different batches/ independent experiments. Data were analysed by one-way ANOVA with GraphPad7.

Appendix C. **Sequence Alignment between hOCT1 and GLUT3**

```
SP|O15245|S22A1_HUMAN MPTVDDILEQVGESGWFQKQAFLILCLLSAAFAPICVGIVFLGFTPDHHCQSPGVAELSQ 60
SP|P11169|GTR3_HUMAN  ------------------------------------------------------MGT----- 3
                                                                                *.

SP|O15245|S22A1_HUMAN RCGWSPAEELNYTVPGLGPAGEAFLGQCRRYEVDWNQSALSCVDPLASLATNRSHLPLGP 120
SP|P11169|GTR3_HUMAN  -QKVTPALIFAITVAT-----------IGSFQFGYNTGVINAPEKIIKEFINKTLT---- 47
                          :**  :  **               ::..:* ..:.. : : .   *::

SP|O15245|S22A1_HUMAN CQDGWVYDTPGSSIVTEFNLVCADSWKLDLFQSCLNAGFLFGSLGVGYFADRFGRKLCLL 180
SP|P11169|GTR3_HUMAN  --------DKGNA--PPSEVLLTSLWSLSV--AIFSVGGMIGSFSVGLFVNRFGRRNSML 95
                              *.:     ::: :. *.*.:  : :..* ::**:.** *.:****: .:*

SP|O15245|S22A1_HUMAN GTVLVNAVSGVLMAFSPNYMSM---LLFRLLQGLVSKGNWMAGYTLITEFVGS----GSR 233
SP|P11169|GTR3_HUMAN  IVNLLAVTGGCFMGLCKVAKSVEMLILGRLVIGLFCG--LCTGF--VPMYIGEISPTALR 151
                       . *: ...* :*.:.    *:   :* **: **..     :*:  :  ::*.    . *

SP|O15245|S22A1_HUMAN RTVAIMYQMAFTVGLV--ALTGLAYAL---PHWRWLQLAVSLPTFLFLLYYWCVPESPRW 288
SP|P11169|GTR3_HUMAN  GAFGTLNQLGIVVGILVAQIFGLEFILGSEELWPLLLGFTILPAILQSAALPFCPESPRF 211
                       :.. : *:.:.**::   : ** : *     *  *   . **::*        *****:

SP|O15245|S22A1_HUMAN LLSQKRNTEAIKIM-DHIAQKNGKLPPADLKMLSLEEDVTEKLSPSFADLFRTPRLRKRT 347
SP|P11169|GTR3_HUMAN  LLINRKEEENAKQILQRLWGT-QDVSQDIQEMKDESARMSQEKQVTVLELFRVSSYRQPI 270
                      ** :::: *  * : :::  .  .:     :* . .  :::: . :. :***.   *:

SP|O15245|S22A1_HUMAN FILMYLWFTDS------VLY-QGLILHMGATSGNLYLDFLYSALVEIPGAFIALITIDRV 400
SP|P11169|GTR3_HUMAN  IISIVLQLSQQLSGINAVFYYSTGIFKDAGVQEPIYATIG-AGVVNTIFTVVSLFLVERA 329
                      :* : * :::.      *:* .  *:: ....  :*  :  :.:*:   :.::*: ::*.

SP|O15245|S22A1_HUMAN GRIYPMAMSNLLAGAACLVMIFI--SPDLHWLNIIIMCVGRMGITIAIQMI------CLV 452
SP|P11169|GTR3_HUMAN  GRRTL-HMIGLGGMAFCSTLMTVSLLLKDNYNGMSFVCIGAILVFVAFFEIGPGPIPWFI 388
                      **     * .* . * * .:: :    . :: .: ::*:* : : :*:  *       ::

SP|O15245|S22A1_HUMAN NAELYPTFVRN--LGVMVCSSLCD--IGGIITPFIVFRLREVWQALPLILFAV-LGLLAA 507
SP|P11169|GTR3_HUMAN  VAELFSQGPRPAAMAVAGCSNWTSNFLVGLLFPSAA----HYLGAYVFIIFTGFLITFLA 444
                       ***:    *   :.*  **.  .  : *:: *  .    .   *  :*:*:  *  : *

SP|O15245|S22A1_HUMAN GVTLLLPETKGVALPETMKDAENLGRKAKPKENTIYLKVQTSEPSGT----- 554
SP|P11169|GTR3_HUMAN  FTFFKVPETRGRTFEDITRAFEGQAHGADRSGKDGVMEMNSIEPAKETTTNV 496
                       . : :***:* :: :  :  *. .: *. . :   ::::: **:
```

Figure A2 Alignment using the universal protein resource (Uniprot) between S22A1_HUMAN and GTR3_HUMAN (https://www.uniprot.org assessed 9.7.2020). S22A1_HUMAN represents human OCT1 (SLC22A1) (Uniprot accession: O15245). GTR3_HUMAN (Our chosen pdb code 4ZW9) represents human GLUT3 (SLC2A3) (Uniprot accession: P11169). There are 99 identical (identified by *) positions and 184 similar positions (very similar identified by **:**, somewhat similar identified by **.**).

The universal protein resource (Uniprot) cluster omega program allowed us to align the protein sequences (https://www.uniprot.org assessed 9.7.2020). This analysis revealed that there was a 57% sequence homology between OCT1 (Uniprot accession: O15245) and 4ZW9 (Uniprot accession: P11169) (Figure A2).

Appendix D. **Sites of the primers selection for P-gp**

AAACACTTGTATTACCATTTTAAAGGCTATCATTACTCTTTACCTGTGAAGAGTAGAACA

TGAAGAAATCTACTTTATTCAGATATTCTCCAGATTCCTAAAGATTAGAGATCATTTCTCA

TTCTCCTAGGAGTACTCACTTCAGGAAGCAACCAGATAAAAGAGAGGTGCAACGGAAG

CCAGAACATTCCTCCTGGAAATTCAACCTGTTTCGCAGTTTCTCGAGGAATCAGCATTC

AGTCAATCCGGGCCGGGAGCAGTCATCTGTGGTGAGGCTGATTGGCTGGGCAGGAAC

AGCGCCGGGGCGTGGGCTGAGCACAGCCGCTTCGCTCTCTTTGCCACAGGAAGCCTG

AGCTCATTCGAGTAGCGGCTCTTCCAAGCTCAAAGAAGCAGAGGCCGCTGTTCGTTTC

CTTTAGGTCTTTCCACTAAAGTCGGAGTATCTTCTTCCAAAATTTCACGTCTTGGTGGCC

GTTCCAAGGAGCGCGAGGTCGGAATGGATCTTGAAGGGGACCGCAATGGAGGAGCAA

AGAAGAAGAACTTTTTTAAACTGAACAATAAAAGTGAAAAAGATAAGAAGGAAAAGAAAC

CAACTGTCAGTGTATTTTCAATGTTTCGCTATTCAAATTGGCTTGACAAGTTGTATATGG

TGGTGGGAACTTTGGCTGCCATCATCCATGGGGCTGGACTTCCTCTCATGATGCTGGT

GTTTGGAGAAATGACAGATATCTTTGCAAATGCAGGAAATTTAGAAGATCTGATGTCAA

ACATCACTAATAGAAGTGATATCAATGATACAGGGTTCTTCATGAATCTGGAGGAAGAC

ATGACCAGGTATGCCTATTATTACAGTGGAATTGGTGCTGGGGTGCTGGTTGCTGCTTA

CATTCAGGTTTCATTTTGGTGCCTGGCAGCTGGAAGACAAATACACAAAATTAGAAAAC

AGTTTTTTCATGCTATAATGCGACAGGAGATAGGCTGGTTTGATGTGCACGATGTTGGG

GAGCTTAACACCCGACTTACAGATGATGTCTCCAAGATTAATGAAGGAATTGGTGACAA

AATTGGAATGTTCTTTCAGTCAATGGCAACATTTTTCACTGGGTTTATAGTAGGATTTAC

ACGTGGTTGGAAGCTAACCCTTGTGATTTT**GGCCATCAGTCCTGTTCTTG**GACTGTCAG

CTGCTGTCTGGGCAAAGATACTATCTTCATTTACTGATAAAGAACTCTTAGCGTATGCAA

AAGCTGGAGCAGTAGCTGAAGAGGTCTTGGCAGCAATTAGAACTGTGATTGCATTTGG

AGGACAAAAGAAAGAACTTGAAAGGTACAACAAAAATTTAGAAGAAGCTAAAAGAATTG

GGATAAAGAAAGCTATTACAGCCAATATTTCTATAGGTGCTGCTTTCCTGCTGATCTATG

CATCTTATGCTCTGGCCTTCTGGTATGGGACCACCTTGGTCCTCTCAGGGGAATATTCT

ATTGGACAAGTACTCACTGTATTCTTTTCTGTATTAATTGGGGCTTTTAGTGTTGGACAG

GCATCTCCAAGCATTGAAGCATTTGCAAATGCAAGAGGAGCAGCTTATGAAATCTTCAA

GATAATTGATAATAAGCCAAGTATTGACAGCTATTCGAAGAGTGGGCACAAACCAGATA

ATATTAAGGGAAATTTGGAATTCAGAAATGTTCACTTCAGTTACCCATCTCGAAAAGAAG

TTAAGATCTTGAAGGGTCTGAACCTGAAG

GTGCAGAGTGGGCAGACGGTGGCCCTGGTTGGAAACAGTGGCTGTGGGAAGAGCAC

AACAGTCCAGCTGATGCAGAGGCTCTATGACCCCACAGAGGGGATGGTCAGTGTTGAT

GGACAGGATATTAGGACCATAAATGTAAGGTTTCTACGGGAAATCATTGGTGTGGTGAG

TCAGGAACCTGTATTGTTTGCCACCACGATAGCTGAAAACATTCGCTATGGCCGTGAAA

ATGTCACCATGGATGAGATTGAGAAA**GCTGTCAAGGAAGCCAATGC**CTATGACTTTAT

CATGAAACTGCCTCATAAATTTGACACCCTGGTTGGAGAGAGAGGGGCCCAGTTGAGT

GGTGGGCAGAAGCAGAGGATCGCCATTGCACGTGCCCTGGTTCGCAACCCCAAGATC

CTCCTGCTGGATGAGGCCACGTCAGCCTTGGACACAGAAAGCGAAGCAGTGGTTCAG

GTGGCTCTGGATAAGGCCAGAAAAGGTCGGACCACCATTGTGATAGCTCATCGTTTGT

CTACAGTTCGTAATGCTGACGTCATCGCTGGTTTCGATGATGGAGTCATTGTGGAGAAA

GGAAATCATGATGAACTCATGAAAGAGAAAGGCATTTACTTCAAACTTGTCACAATGCA

GACAGCAGGAAATGAAGTTGAATTAGAAAATGCAGCTGATGAATCCAAAAGTGAAATTG

ATGCCTTGGAAATGTCTTCAAATGATTCAAGATCCAGTCTAATAAGAAAAAGATCAACTC

GTAGGAGTGTCCGTGGATCACAAGCCCAAGACAGAAAGCTTAGTACCAAAGAGGCTCT

GGATGAAAGTATACCTCCAGTTTCCTTTTGGAGGATTATGAAGCTAAATTTAACTGAATG

GCCTTATTTTGTTGTTGGTGTATTTTGTGCCATTATAAATGGAGGCCTGCAACCAGCATT

TGCAATAATATTTTCAAAGATTATAGGGGTTTTTACAAGAATTGATGATCCTGAAACAAA

ACGACAGAATAGTAACTTGTTTTCACTATTGTTTCTAGCCCTTGGAATTATTTCTTTTATT

ACATTTTTCCTTCAGGGTTTCACATTTGGCAAAGCTGGAGAGATCCTCACCAAGCG**GCT**

CCGATACATGGTTTTCCGATCCATGCTCAGACAGGATGTGAGTTGGTTTGATGACCCT

AAAAACACCACTGGAGCATTGACTACCAGGCT**CGCCAATGATGCTGCTCAAG**TTAAAG

GGGCTATAGGTTCCAGGCTTGCTGTAATTACCCAGAATATAGCAAATCTTGGGACAGGA

ATAATTATATCCTTCATCTATGGTTGGCAACTAACACTGTTACTCTTAGCAATTGTACCC

ATCATTGCAATAGCAGGAGTTGTTGAAATGAAAATGTTGTCTGGACAAGCACTGAAAGA

TAAGAAAGAACTAGAAGGTTCTGGGAAGATCGCTACTGAAGCAATAGAAAACTTCCGAA

CCGTTGTTTCTTTGACTCAGGAGCAGAAGTTTGAACATATGTATGCTCAGAGTTTGCAG

GTACCATACAGAAACTCTTTGAGGAAAGCACACATCTTTGGAATTACATTTTCCTTCACC

CAGGCAATGATGTATTTTTCCTATGCTGGATGTTTCCGGTTTGGAGCCTACTTGGTGGC

ACATAAACTCATGAGCTTTGAGGATGTTCTGTTAGTATTTTCAGCTGTTGTCTTTGGTGC

CATGGCCGTGGGGCAAGTCAGTTCATTTGCTCCTGACTATGCCAAAGCCA

AAATATCAGCAGCCCACATCATCATGATCATTGAAAAAACCCCTTTGATTGACAGCTAC

AGCACGGAAGGCCTAATGCCGAACACATTGGAAGGAAATGTCACATTTGGTGAAGTTG

TATTCAACTATCCCACCCGACCGGACATCCCAGTGCTTCAGGGACTGAGCCTGGAGGT

GAAGAAGGGCCAGACGCTGGCTCTGGTGGGCAGCAGTGGCTGTGGGAAGAGCACAG

TGGTCCAGCTCCTGGAGCGGTTCTACGACCCCTTGGCAGGGAAAGTGCTGCTTGATG

GCAAAGAAATAAAGCGACTGAATGTTCAGTGGCTCCGAGCACACCTGGGCATCGTGTC

CCAGGAGCCCATCCTGTTTGACTGCAGCATTGCTGAGAACATTGCCTATGGAGACAAC

AGCCGGGTGGTGTCACAGGAAGAGATTGTGAGGGCAGCAAAGGAGGCCAACATACAT

GCCTTCATCGAGTCACTGCCTAATAAATATAGCACTAAAGTAGGAGACAAAGGAACTCA

GCTCTCTGGTGGCCAGAAACAACGCATTGCCATAGCTCGTGCCCTTGTTAGACAGCCT

CATATTTTGCTTTTGGATGAAGCCACGTCAGCTCTGGATACAGAAAGTGAAAAGGTTGT

CCAAGAAGCCCTGGACAAAGCCAGAGAAGGCCGCACCTGCATTGTGATTGCTCACCG

CCTGTCCACCATCCAGAATGCAGACTTAATAGTGGTGTTTCAGAATGGCAGAGTCAAG

GAGCATGGCACGCATCAGCAGCTGCTGGCACAGAAAGGCATCTATTTTTCAATGGTCA

GTGTCCAGGCTGGAACAAAGCGCCAGTGAACTCTGACTGTATGAGATGTTAAATACTT

TTTAATATTTGTTTAGATATGACATTTATTCAAAGTTAAAAGCAAACACTTACAGAATTAT

GAAGAGGTATCTGTTTAACATTTCCTCAGTCAAGTTCAGAGTCTTCAGAGACTTCGTAA

TTAAAGGAACAGAGTGAGAGACATCATCAAGTGGAGAGAAATCATAGTTTAAACTGCAT

TATAAATTTTATAACAGAATTAAAGTAGATTTTAAAAGATAAAATGTGTAATTTTGTTTAT

ATTTTCCCATTTGGACTGTAACTGACTGCCTTGCTAAAAGATTATAGAAGTAGCAAAAA

GTATTGAAATGTTTGCATAAAGTGTCTATAATAAAACTAAACTTTCATGTGAAA

Appendix E. **Reagents used throughout the thesis**

Product name	**Company bought**	**Catalogue code**
1kb DNA Ladder	Promega Uk Ltd	G5711
ssRNA Ladder	New England Biolabs (Uk) Ltd	N0362S
TRYPSIN-EDTA SOLUTION 10X, 0.5% TRYPSIN	Merck Life Science Uk Limited	59418C-100ML
DPBS, no calcium, no magnesium-1,000 mL	Thermo Fisher Scientific (Life Technologies)	14190136
Ultima Gold XR, 2x5L	Perkin Elmer	6013119
NotI	Promega Uk Ltd	R6435
HindIII	Promega Uk Ltd	R6041
EcoRI	Promega Uk Ltd	R6011
NcoI	New England Biolabs (Uk) Ltd	R0193T
SalI	New England Biolabs (Uk) Ltd	R0138S
TBE BUFFER (10X)	Applichem Lifescience	A0972.1000
Collagenase, Type IV, powder-1 g	Gibco	17104019
DULBECCO'S MODIFIED EAGLES MEDIUM	Sigma-Aldrich	D1145-500ML

Publications

Journal articles

Hao Wang, Christopher P. Corpe, David Barlow, Doaa Farag, Khondaker Miraz Rahman, Stuart A. Jones, Sarah A. Thomas. Targeting the hOCT1 transporter at blood-brain barrier for the delivery of pentamidine ion-pairs: Mechanism and Strategy. Intended journal submission: Journal of Controlled Release (*In preparation*).

Hao Wang, Christopher P. Corpe, Ahmed Sedky, David Barlow, Doaa Farag, Khondaker Miraz Rahman, Stuart A. Jones, Sarah A. Thomas. Targeted delivery of pentamidine across the blood-brain barrier using ion-pairs: physicochemical characterisation and efflux by P-gp. Intended journal submission: International Journal of Pharmaceutics (*In preparation*).

Gayathri Nair Sekhar, Alice L. Fleckney, Sevda Tomova Boyanova, Huzefa Rupawala, Rachel Lo, **Hao Wang**, Doaa B. Farag, Khondaker Miraz Rahman, Martin Broadstock, Suzanne Reeves & Sarah Ann Thomas (2019) 'Region-specific blood–brain barrier transporter changes leads to increased sensitivity to amisulpride in Alzheimer's disease', Fluids and Barriers of the CNS. BioMed Central, 16(1), p. 38. doi: 10.1186/s12987-019-0158-1.

Abstracts

Hao Wang, Christopher P. Corpe, Doaa Farag, Khondaker Miraz Rahman, Stuart A. Jones and Sarah A. Thomas. (2018). Modifying Pentamidine Blood-Brain Barrier transport through Ion-Pair Formation. 8th Annual UK and Ireland Early Career Blood-Brain Barrier Symposium. Oxford.

Hao Wang, Christopher P. Corpe, Stuart A. Jones, Sarah A. Thomas. (2018). Modifying pentamidine blood-brain barrier transport through Ion-pair formation. Europhysiology. London.

Hao Wang, Paula Muresan, Gayathri Sekhar, Rachel Brown, Jignesh Patel, Stuart A. Jones and Sarah A. Thomas. (2016). Transporter interaction of warfarin, a traditional oral vitamin K antagonist with the mouse blood-brain barrier in vitro: evidence for BCRP involvement. Pharmacology 2016. London.

S. Boyanova, S., **Wang, H**., Fleckney, A., Reeves, S. J. and Thomas, S.A. (2019). The role of solute carrier transporters in the translocation of the antipsychotic amisulpride at the blood-brain barrier in Alzheimer's disease and in normal ageing. ARUK Network Day, London.

S. Boyanova, S., **Wang, H.**, Reeves, S. J. and Thomas, S.A. (2018). The role of solute carrier transporters in the translocation of the antipsychotic amisulpride at the blood-brain barrier in Alzheimer's disease and in normal ageing. 8th Early Career BBB meeting, Oxford.

.

S. Boyanova, S., **Wang, H.**, Reeves, S. J. and Thomas, S.A. (2018). The role of solute carrier transporters in the translocation of the antipsychotic amisulpride at the blood-brain barrier in Alzheimer's disease and in normal ageing. BIRAX, London.

S. Boyanova, S., **Wang, H.**, Reeves, S. J. and **Thomas, S.A.** (2018). The role of solute carrier transporters in the translocation of the antipsychotic amisulpride at the blood-brain barrier in Alzheimer's disease and in normal ageing. Europhysiology (London). PCA279, 248P.